

Block Polymer Self-assembly and Applications

A DISSERTATION
SUBMITTED TO THE FACULTY OF THE GRADUATE SCHOOL
OF THE UNIVERSITY OF MINNESOTA
BY

Morgan W. Schulze

IN PARTIAL FULFILLMENT OF THE REQUIREMENTS
FOR THE DEGREE OF
DOCTOR OF PHILOSOPHY

Marc A. Hillmyer

June 2016

© MORGAN W. SCHULZE 2016

ALL RIGHTS RESERVED

Acknowledgements

I have much to be thankful for during my time at the University of Minnesota, and I owe so much to my adviser, Professor Marc Hillmyer. Marc generously invested his time to help me grow as both a person and a scientist, and as a dear mentor, he sincerely cared about my personal well-being. His enthusiasm and encouragement picked me up when I was down from the numerous challenges of research and motivated me to continually explore new ideas. I hope that I will be a positive reflection of him and his group in my future endeavors.

Many individuals across all denominations of the Polymer Group have helped me throughout graduate school, and I have only gained skills and expertise through their teaching. I am grateful to Josh Speros who taught me organic synthesis and to Myung Seo and Justin Kennemur who taught me many characterization techniques. I also want to express gratitude to Debbie Schneiderman, Tim Gillard, Matt Irwin, Rob Hickey, Megan Matta, Justin Bolton, Marie Vanderlaan, Li Yao, Leo Oquendo and Sam Dalsin for their friendship and helpful discussion. Mark Martello, Liz Jackson, Yuanyan Gu, and Brian Habersberger also deserve thanks for their advice and help in diverse but all challenging tasks. Professor Christophe Sinturel deserves special recognition for his collaborative efforts during his sabbatical leave spent in our laboratories. Lastly, I am grateful to Chris Fretham and David Giles who kindly assisted and trained me on many of the tools and instruments that made this work possible.

There is a distinct sense of community within the Polymer Group that, in leaving, I worry I will find nowhere else. Somehow I have enjoyed not one, but two, excellent and

close collaborations that bridge its research groups. I am grateful to Lucas McIntosh for all his contributions and leadership in many aspects of our work together, and it has been an incredibly fun experience to work with Ron Lewis. The teachings and mentorship of Professors Frank Bates and Tim Lodge during these projects has had a tremendous impact on me scientifically.

Lastly, I am fortunate to be able to share both the personal and the technical side of life with my fiancée, Chris, who has been supportive of me throughout graduate school. It means the world to me that he is proud of me and what I do, and I will cherish many fond memories of being with his family, who have formed an integral part of my time here.

Dedication

For my brother, Troy.

Abstract

Block polymers have grown beyond a niche field of polymer science and engineering to enable a diverse and seemingly ever-expanding range of practical applications. Their utility is derived from a molecular architecture containing discrete sequences of chemically distinct units that segregate into periodic nanoscale structures of various domain geometries. A primary focus of this thesis is to connect meso- and macroscopic structural properties to molecular design, a goal that broadly informs a variety of contemporary topics in polymer science. These works include facile polymerization strategies to achieve domain co-continuity, new block chemistries to circumvent the domain size limitations of preceding materials, and the discovery and understanding of new equilibrium morphologies in block polymer melts.

The design strategy imparted by the block polymer molecular motif effectively combines the material properties of each block segment. In this work, we decouple the orthogonal properties of conductivity and modulus for the advancement of polymer electrolyte membranes through a facile synthetic strategy coined polymerization-induced microphase separation (PIMS). The produced electrolytes achieved the highest contemporary record of conductivity and modulus, attributes owed to a bicontinuous microstructure comprising a low- T_g , highly conductive domain and a mechanically robust crosslinked domain. This work was then extended through an adaptation of PIMS to the preparation of nanoporous materials that benefit from the continuity of a percolating pore structure in a thermally and mechanically stable crosslinked matrix. The reaction parameters that control the porous properties were elucidated.

Technologies employed in modern fabrication and nanolithography must constantly improve the resolution of patterned structures. Block polymer self-assembly can serve as an alternative patterning strategy to overcome the resolution limitations that thwart the extension of current optical lithography processes. Because domain size is tied to block polymer molar mass, the design of new materials that can self-assemble at lower molar masses, and hence smaller length-scales, is needed. In this work, a new polymer,

poly(cyclohexylethylene)-*block*-poly(ethylene oxide) (PCHE-PEO) was synthesized and found to self-assemble at exceptionally low molar mass due to the high incompatibility of block segments. Block-specific interactions between the inorganic precursors and the polar PEO block then enabled the templating of dense arrays of metal oxide structures on silicon wafers through simple spin coating techniques.

The geometries assumed by block polymer mesophases have been a subject of intensive experimental and theoretical investigation. Discovery of the complex, low-symmetry Frank-Kasper σ phase in compositionally-asymmetric diblock copolymers emphasized a relationship between melt thermodynamics and domain geometry not captured by previous theoretical frameworks. Our experimental work supports recent theoretical conclusions that *conformational* asymmetry underpins the formation of new complex phases in block polymer materials. Through the synthesis and characterization of two different block polymers systems of low molar mass, far below the entanglement molar mass of either block segment, we enable facile assembly that is poised to probe the effect of conformational asymmetry and offer new insights into nanostructure formation in soft materials.

Table of Contents

Acknowledgements.....	i
Dedication.....	iii
Abstract.....	iv
List of Tables.....	ix
List of Figures.....	xi
List of Schemes.....	xx
1 BACKGROUND: BLOCK POLYMER SELF-ASSEMBLY AND APPLICATIONS.....	1
1.1 Introduction.....	2
1.2 Microphase Separation and the Phase Diagram.....	2
1.3 The Interaction Parameter χ	4
1.4 Fluctuations and the Structure of the Disordered Phase.....	6
1.5 General Comment on Material Design Strategies.....	8
1.6 Overview.....	16
1.7 References.....	18
2 HIGH-MODULUS, HIGH-CONDUCTIVITY NANOSTRUCTURED POLYMER ELECTROLYTES VIA POLYMERIZATION-INDUCED MICROPHASE SEPARATION.....	22
2.1 Introduction.....	23

2.2 Experimental Section	25
2.3 Results and Discussion	31
2.4 Conclusions.....	47
2.5 References.....	49
3 EVOLUTION OF MORPHOLOGY, MODULUS, AND CONDUCTIVITY IN POLYMER	
ELECTROLYTES PREPARED VIA POLYMERIZATION-INDUCED MICROPHASE SEPARATION 52	
3.1 Introduction.....	53
3.2 Experimental Section.....	55
3.3 Results.....	59
3.4 Discussion.....	72
3.5 Conclusions.....	85
3.6 References.....	86
4 CROSSLINKED NANOPOROUS POLYMER MONOLITHS FROM POLYMERIZATION-INDUCED	
MICROPHASE SEPARATION	
4.1 Introduction.....	91
4.2 Experimental Procedures and Characterization	93
4.3 Results and Discussion	97
4.4 Conclusions.....	117
4.5 References.....	118
5 POLY(CYCLOHEXYLETHYLENE)- <i>BLOCK</i> -POLY(ETHYLENE OXIDE) BLOCK POLYMERS FOR	
METAL OXIDE TEMPLATING	
5.1 Introduction.....	122

5.2 Experimental Procedures and Characterization	123
5.3 Results and Discussion	129
5.4 Conclusions.....	151
5.5 References.....	152
6 INFLUENCE OF CONFORMATIONAL ASYMMETRY ON THE FORMATION OF FRANK-KASPER PHASES IN DIBLOCK COPOLYMER MELTS	155
6.1 Introduction.....	156
6.2 Experimental Section.....	157
6.3 Results and Discussion	159
6.4 Conclusions.....	193
6.5 References.....	194
BIBLIOGRAPHY	196

List of Tables

Table 2.1 Properties of polymer electrolyte samples	32
Table 2.2 Thermal transitions of PIPS PEM and PEO homopolymer/BMITFSI electrolyte samples shown in Figure 2.5.....	42
Table 2.3 VFT Parameters for the conductivity profiles in Figure 2.6.....	43
Table 3.1 Composition (vol%) of polymer electrolyte samples.	56
Table 3.2 Molar mass and dispersity for SEC traces in Figure 3.4	62
Table 3.3 Calculation of the number of styrene and DVB repeat units polymerized per PEO-CTA from ¹ H-NMR analysis of soluble polymers.....	64
Table 3.4 Rate constants obtained from fitting the data in Figure 3.5.....	64
Table 3.5 Characteristic timescales associated with the in situ experiments in Figure 3.13	82
Table 4.1 Molecular characterization of PLA-CTA precursors.....	95
Table 4.2 Porous characteristics of samples prepared using precursor PLA-CTA-18 ...	102
Table 4.3 Porous characteristics of samples prepared using precursor PLA-CTA-8	109
Table 4.4 Porous characteristics of samples prepared using <i>p</i> -DVB.....	113
Table 5.1 Hydroxyl-terminated poly(cyclohexylethylene) and the corresponding polystyrene precursor data	130
Table 5.2 Molecular characteristics of all synthesized PCHE–PEO block polymers.....	134
Table 5.3 Thermal characteristics of all PCHE–PEO block polymers	135

Table 5.4 Summary of domain dimensions of the templating block polymer film, CEO (5.9, 0.42), and deposited precursors as observed via AFM.....	149
Table 6.1 Molecular characterization data for poly(ethylene)- <i>block</i> -poly(lactide) block polymers.....	161
Table 6.2 Molecular characterization data for poly(ethylene- <i>alt</i> -propylene)- <i>block</i> - poly(lactide) block polymers	187

List of Figures

Figure 1.1 The sequence of morphologies observed in diblock copolymer melts.....	3
Figure 1.2 Phase diagram for melts of AB diblock copolymers, showing the stability regions of the ordered phases constructed using SCFT	4
Figure 1.3 Schematic representation of the space-filling characteristics for PVCH-PEE, PEP-PVCH, and PE-PVCH	12
Figure 1.4 Mean-field phase diagrams for diblock copolymer melts for a series of conformational asymmetries	14
Figure 1.5 Depiction of the AB interface in the BCC phase	15
Figure 2.1 ¹ H-NMR spectra (CDCl ₃ , 500 MHz, 20 °C) of (a) the chain-transfer agent DDMAT and (b) macromolecular PEO-CTA.....	26
Figure 2.2 ¹ H-NMR spectrum (CD ₂ Cl ₂ , 500 MHz, 20 °C) of BMITFSI	27
Figure 2.3 Photographs of the macrophase separation observed in samples	33
Figure 2.4 SAXS data of PEM samples prepared with (a) 5 and (b) 28 kg mol ⁻¹ PEO-CTA (32 wt%) and BMITFSI.....	34
Figure 2.5 SAXS data of PEM samples prepared with (a) 5 and (b) 28 kg mol ⁻¹ PEO-CTA (32 wt%) and increasing concentrations of LiTFSI in BMITFSI	35
Figure 2.6 Comparison of PEM scattering profiles prepared using 5 kg mol ⁻¹ PEO-CTA at concentrations of 42 and 32 wt% in the initial monomer mixture.....	36
Figure 2.7 Representative FTIR spectra of PIMS PEM samples and BMITFSI.....	37

Figure 2.8 Morphology of PIMS PEM samples prepared with 28 kg mol ⁻¹ PEO-CTA and 21 vol% BMITFSI	38
Figure 2.9 SEMs comparing a PIMS PEM sample prepared with 28 kg mol ⁻¹ PEO-CTA and 21 vol% BMITFSI before and after etching out the PEO/IL domain	39
Figure 2.10 TEMs of PEM samples prepared from 28 kg mol ⁻¹ PEO-CTA without ionic liquid and 21 vol% BMITFSI	40
Figure 2.11 DSC thermograms for PIMS PEMs prepared with (a) 5 kg mol ⁻¹ and (b) 28 kg mol ⁻¹ PEO-CTA (32 wt%) and various concentrations of BMITFSI.....	41
Figure 2.12 Ionic conductivity as a function of temperature for PEMs prepared with 5 kg mol ⁻¹ PEO-CTA.	43
Figure 2.13 Comparison of conductivity in a heterogeneous PEM sample and a PEO/ionic liquid homogeneous electrolyte of the same composition	44
Figure 2.14 Linear viscoelastic master curves of representative PEMs prepared from 5 kg mol ⁻¹ and 28 kg mol ⁻¹ PEO-CTA (a) without IL and (b) with 21 vol% BMITFSI.....	46
Figure 2.15 Temperature dependent linear elastic response of PIMS PEMs prepared with (a) 5 and (b) 28 kg mol ⁻¹ PEO-CTA without IL and with 21 vol% BMITFSI.....	47
Figure 2.16 Trade-off relationship between elastic modulus and ionic conductivity in a solid electrolyte	48
Figure 3.1 Schematic of the PIMS strategy used to prepare PEMs	54
Figure 3.2 Polymerization time versus mass yield in the polymerization of S and DVB in the presence of PEO-CTA and BMITFSI at 120 °C.....	59

Figure 3.3 $^1\text{H-NMR}$ spectra (CDCl_3 , 500 MHz, 20 °C) of the soluble polymers obtained by precipitation in hexanes	60
Figure 3.4 Progression of the size exclusion chromatograms of PEO- <i>b</i> -P(S- <i>co</i> -DVB) isolated at various times following initiation.....	61
Figure 3.5 Number of repeat units per PEO-CTA represented as [PS], [PDVB ₁], and [PDVB ₂] versus polymerization time	63
Figure 3.6 In situ conductivity for a PEO- <i>b</i> -P(S- <i>co</i> -DVB) sample prepared with 21 vol% BMITFSI.....	65
Figure 3.7 Evolution of the elastic, G' , and viscous, G'' , shear moduli	68
Figure 3.8 Time-resolved evolution of the maximum scattered intensity, I_m , of the primary structure factor peak located at wave vector q_m	70
Figure 3.9 In situ time-resolved SAXS data for samples prepared with 0 and 21 vol% BMITFSI.....	71
Figure 3.10 (a) Lamellar d-spacing at 150° C for PS- <i>b</i> -PEO/EMITFSI blends and (b) estimation of the effective interaction parameter, $\chi_{\text{salt}}^{\text{eff}}$	74
Figure 3.11 Segregation strength, χN , as a function of the molar mass of a PS block growing from a 5 kg mol ⁻¹ PEO block	76
Figure 3.12 (a) SAXS data for samples prepared with 5 kg mol ⁻¹ PEO-CTA, 21 vol% BMITFSI, and S/DVB, with varying concentration of DVB. (b) Temperature-dependent conductivity as a function of DVB concentration	78
Figure 3.13 Comparison of (a) SAXS, (b) conductivity, (c) mass yield, and (d) rheology in situ experiments for a sample prepared with 21 vol% BMITFSI.....	81

Figure 4.1 SAXS data of monoliths prepared via PIMS from PLA-CTA-18 before and after etching of the PLA.....	99
Figure 4.2 Nitrogen sorption isotherms obtained under adsorption and desorption for monoliths prepared using 18 kg mol ⁻¹ PLA-CTA-18 and various compositions of the monomer mixture expressed as mol% DVB.....	101
Figure 4.3 Mesopore size distributions based on QSDFT analysis of the adsorption branch of monoliths prepared from ≥ 5 mol% DVB monomer mixtures at 120 °C	103
Figure 4.4 SEMs of etched monoliths derived from PLA-CTA-18 and monomer mixtures of (a) 10, (b) 20, (c) 40, and (d) 80 mol% DVB synthesized at 120 °C	104
Figure 4.5 SEMs of Figure 4.4 visualized at higher magnification	105
Figure 4.6 SAXS of monoliths prepared using 20 and 100 mol% DVB at 120 °C	106
Figure 4.7 Nitrogen sorption isotherms obtained under adsorption and desorption for monoliths prepared using 8 kg mol ⁻¹ PLA-CTA-8 and various compositions of the monomer mixture expressed as mol% DVB.....	108
Figure 4.8 SAXS of monoliths prepared form PLA-CTA-8 before and after etching of the PLA	110
Figure 4.9 (a) Mesopore size distributions of monoliths prepared from PLA-CTA-8 at 120 °C based on QSDFT analysis of the adsorption branch. (b) Comparison of the pore structures produced using solutions of PLA-CTA-18 and PLA-CTA-8 in 100 mol% DVB at 120 °C	111

Figure 4.10 Nitrogen sorption isotherms obtained under adsorption and desorption for monoliths prepared using (a, b, c) PLA-CTA-18 and (d) PLA-CTA-8 dissolved in monomer mixtures using only the <i>p</i> -DVB isomer	114
Figure 4.11 SAXS data of monoliths prepared from PLA-CTA-8 at 60 and 120 °C	115
Figure 4.12 BET equivalent surface area of porous monoliths as a function of DVB content for (a) PLA-CTA-8 synthesized at 60 and 120 °C and (b) PLA-CTA-18 and PLA-CTA-19 synthesized at 60 and 120 °C	116
Figure 5.1 ¹ H-NMR spectra of (a) PSOH (1.5) and (b) PCHEOH (1.6)	131
Figure 5.2 Series of representative SEC traces of PCHEOH polymers and the corresponding PSOH precursors	132
Figure 5.3 Dependence of the T_g on molar mass of the PSOH precursors	133
Figure 5.4 Dependence of the T_g on molar mass of the PCHEOH precursors	133
Figure 5.5 Representative ¹ H-NMR spectrum of a PCHE–PEO block copolymer CEO (3.1, 0.49) in CDCl ₃	135
Figure 5.6 SEC traces of compositionally asymmetric PCHE–PEO block polymers and the corresponding PCHE-OH precursor	136
Figure 5.7 SEC traces of compositionally symmetric PCHE–PEO block polymers and the corresponding PCHE-OH precursor	137
Figure 5.8 Representative TGA thermogram of CEO (3.1, 0.51) heated under nitrogen at a ramp rate of 10 °C/min	138
Figure 5.9 Representative DSC thermograms of CEO block copolymers obtained on the second heating	139

Figure 5.10 Temperature dependence of the low-frequency dynamic elastic shear modulus (G') for four compositionally symmetric samples and the determination of T_{ODT}	140
Figure 5.11 SAXS on cooling through the ODT for the four polymers used to determine the interaction parameter for $N = 39$ (a), 44 (b), 61 (c), and 79 (d).....	142
Figure 5.12 $\chi(T)$ for compositionally symmetric diblock copolymers determined using the first four entries of Table 5.1	143
Figure 5.13 SAXS data and the temperature dependence of the dynamic moduli G' and G'' of CEO (5.9, 0.42) obtained on heating	144
Figure 5.14 1 x 1 μm AFM phase images of CEO (5.9, 0.42) obtained in tapping mode following (a) thermal annealing and (b) solvent annealing with THF.....	144
Figure 5.15 1 x 1 μm AFM images of the (a) CEO (5.9, 0.42) thin film after a 5 min solvent vapor anneal using a THF/cyclohexane mixture (phase image) and the templated (b) silica, (c) titania, and (d) iron oxide nanoparticles (height images)	144
Figure 5.16 1 x 1 μm AFM height images of (a) silica and (b) iron oxide nanoparticles obtained in tapping mode and the corresponding SEM images (c) and (d).....	148
Figure 5.17 (a) AFM height image of the silica nanoparticle array templated using CEO (5.9, 0.42). (b) The line scan provides a height profile of the silica nanoparticles prepared by this method.....	149
Figure 5.18 1 x 0.5 μm AFM phase image of the CEO (4.1, 0.24) thin film after a 4 min solvent vapor anneal using a THF/cyclohexane mixture.....	150

Figure 5.19 (a) Iron oxide and (b) silica nanoparticles templated from CEO (4.1, 0.24) following a selective solvent annealing. The resulting features are 6 ± 1 nm	150
Figure 5.20 (a) AFM height image and (b) SEM image of iron oxide nanoparticles templated from CEO (4.1, 0.24).	151
Figure 6.1 Molecular architecture of the three block polymer systems of varied conformational asymmetry studied.....	157
Figure 6.2 (a) Temperature dependence of the low-frequency dynamic elastic shear modulus (G') for three compositionally symmetric EL samples and the determination of T_{ODT} . (b) $\chi(T)$ for compositionally symmetric EL diblock copolymers	162
Figure 6.3 Representative isothermal synchrotron SAXS patterns obtained from EL block polymers for compositions $f_L \geq 0.26$	163
Figure 6.4 Measurement of the T_{ODT} for EL block polymers of $f_L \leq 0.25$. Linear ($\gamma \leq 1\%$) isochronal (1 rad/s) dynamic shear storage (G') and loss (G'') were monitored on heating at a rate of 1 °C/min	164
Figure 6.5 Representative SAXS patterns of the phases observed in EL-44-21	166
Figure 6.6 Indexing of the EL-44-21 SAXS pattern collected at 55 °C, confirming the formation of the Frank-Kasper σ phase	166
Figure 6.7 Representative SAXS patterns of the phases observed in EL-44-24	169
Figure 6.8 Representative SAXS patterns of the phases observed in EL-63-21.....	170
Figure 6.9 Representative SAXS patterns of the phases observed in EL-63-25.....	171
Figure 6.10 Representative SAXS patterns observed in EL-63-17	172
Figure 6.11 Kinetics of ordering of EL-44-17 at 20 °C as measured by SAXS	173

Figure 6.12 Indexing of the EL-44-17 SAXS pattern collected after 177 days of annealing at 20 °C	174
Figure 6.13 Unit cell representation of the phases observed in EL block polymers	175
Figure 6.14 Indexing of the EL-44-17 SAXS pattern collected after two weeks of annealing at 20 °C.....	176
Figure 6.15 Kinetics of ordering of EL-63-21 at 70 °C as measured by SAXS.....	177
Figure 6.16 Kinetics of ordering of EL-63-21 at 100 °C as measured by SAXS.....	178
Figure 6.17 Kinetics of ordering of EL-63-21 at 135 °C as measured by SAXS.....	179
Figure 6.18 Kinetics of ordering of EL-63-21 at 135 °C following annealing of a disordered phase with LLP	180
Figure 6.19 Kinetics of ordering of EL-44-24 at 20 °C as measured by SAXS	181
Figure 6.20 Kinetics of ordering of EL-44-24 at 45 °C as measured by SAXS	182
Figure 6.21 Kinetics of ordering of EL-44-24 at 55 °C as measured by SAXS	183
Figure 6.22 Ordering of EL-44-24 upon heating	184
Figure 6.23 Kinetics of ordering of EL-44-24 at 70 °C as measured by SAXS	185
Figure 6.24 Kinetics of ordering of EL-44-24 at 85 °C as measured by SAXS	186
Figure 6.25 Isothermal synchrotron SAXS patterns obtained from PL block polymers annealed for 7 days at 45 °C	188
Figure 6.26 Scattering patterns of samples (a) PL-47-15 and (b) PL-29-21 obtained on heating using 10–20 °C increments to the ODT	189
Figure 6.27 Phase diagrams summarizing the phase behavior of compositionally asymmetric (a) PL, (b) IL, and (c) EL block polymers	191

Figure 6.28 SCFT phase diagrams for conformationally asymmetric AB block
polymers..... 192

List of Schemes

Scheme 2.1 Reaction scheme used to prepare PIMS PEMs	25
Scheme 3.1 Proposed reaction kinetics for polymerization of DVB and Styrene	62
Scheme 4.1 Synthetic route to porous polymer monolith via PIMS.....	93
Scheme 5.1 Synthesis of poly(cyclohexylethylene)- <i>block</i> -poly(ethylene oxide).....	130

Chapter 1

Background: Block Polymer Self-assembly and Applications

This chapter provides an overview of fundamental concepts in block polymer physics and phase behavior that apply readily to the work described in later chapters of the thesis. The chapter concludes with a review of the content to follow.

1.1 Introduction

Block polymers inundate contemporary macromolecular research in both advanced synthetic chemistry and applied physics. Motivation stems from the broadening of these materials beyond their initial conception and commercial application as thermoplastic elastomers, upholstery foam, and adhesives to more advanced technologies such as microelectronics,¹⁻⁴ transistors,⁵⁻⁷ photovoltaics,⁸⁻¹⁰ information storage,^{11,12} and drug delivery.^{13,14} As a class of macromolecules, block polymers are defined by the covalent connectivity that bridges distinct polymers, each a chain of identical monomers that may be thermodynamically incompatible. This thermodynamic incompatibility drives the controlled self-assembly of nanostructures into defined morphologies over a precise length-scale. Single component materials can thus be designed with composite physical properties, achieving orthogonal design criteria for myriad applications. The following sections attempt to summarize fundamental concepts in the understanding of these materials as they pertain to this dissertation.

1.2 Microphase Separation and the Phase Diagram

Microphase separation reflects a balance between eliminating enthalpically unfavorable segment-segment contacts and preventing an entropic penalty induced by overly stretched chains.^{15,16} This delicate equilibrium, unavoidable due to the synthetically-imposed molecular structure, limits “microphase” separation to molecular dimensions that is manifest as the periodic arrangement of various classic equilibrium morphologies summarized in Figure 1.1. Equal volume fractions of A and B components ($f_A = 0.5$) leads to the formation of alternating layers of A and B identified as lamellae. Varying the composition away from the symmetric condition induces a phase transition engendering a microstructure of increasing interfacial curvature (e.g. networks, cylinders, and spheres) so that stretching penalties of A and B blocks are balanced.

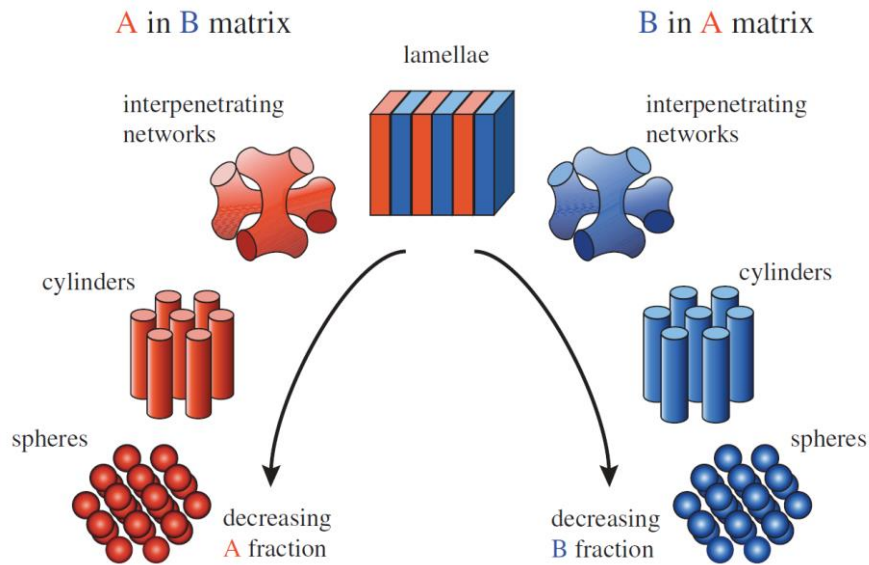


Figure 1.1 The sequence of morphologies observed in diblock copolymer melts. Beginning at low A block content and increasing to high A content, the sequence proceeds from left to right. Note that the surrounding A or B matrix is not depicted. Reproduced with permission from Grason, G. M. *Physics Reports* **2006**, *433*, 1. Copyright 2006 Elsevier.¹⁷

The thermodynamic stability of the ordered phase relative to the disordered state is determined primarily by the segregation strength χN , where N is the volumetric degree of polymerization and χ is the segment-segment interaction parameter. Note that N is a normalized volume (the total volume of a polymer chain, $M_n \rho^{-1} N_A^{-1}$, divided by a reference volume, typically but not always arbitrarily selected as 118 \AA^3)¹⁸ because polymer-polymer phase behavior is framed in terms of Flory-Huggins theory, which places monomers on a lattice, wherein each site occupies a defined volume. At high temperatures or low N , entropic factors dominate, producing a homogeneous disordered melt. The transition from a homogeneous disordered melt to an ordered microstructure is called the order-disorder transition (ODT).

Self-consistent field theory (SCFT) has been the long-standing theoretical approach for the calculation of equilibrium phase diagrams of block copolymers with remarkable success.¹⁹ SCFT enables the free energies of various mesostructures to be computed at a

given segregation strength and composition, $f_A = N_A/(N_A+N_B) = N_A/N$. Consideration of potential morphologies is typically guided by experimental reports, and the morphology of the lowest free energy is accepted as the equilibrium phase. Comparison of the free energies of the disordered phase and all postulated ordered phases produces the theoretical phase diagram of Figure 1.2. Although rigorous accuracy is limited to infinitely long, interpenetrating polymer chains, SCFT is exceptionally versatile and has been progressively expanded through iteration to account for more complex structures and molecular architectures.²⁰⁻²⁴

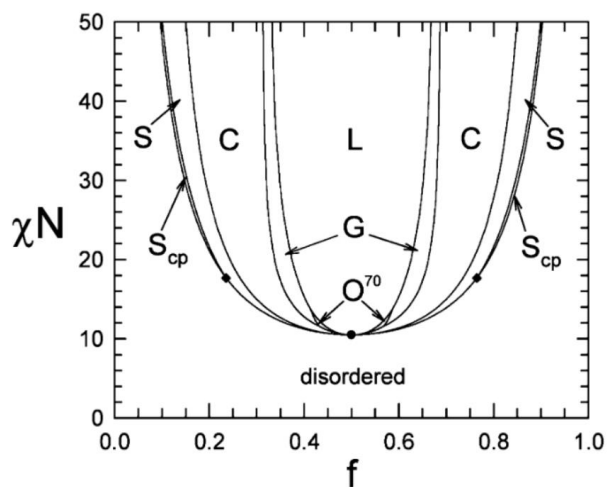


Figure 1.2 Phase diagram for melts of AB diblock copolymers, showing the stability regions of the ordered phases constructed using SCFT. Abbreviations denote the lamellar (L), cylindrical (C), bcc spherical (S), fcc spherical (S_{cp}), gyroid (G), and Fddd (O^{70}) morphologies. The dot denotes a mean-field critical point, and the diamonds mark a couple of the difficult to resolve triple points. Reprinted with permission from Matsen, M. W. *Macromolecules* **2012**, *45*, 2161. Copyright 2012 American Chemical Society.²²

1.3 The Interaction Parameter χ

In theory, the interaction parameter, a dimensionless and purely energetic quantity denoted as χ , defines the exchange energy required to interchange two dissimilar monomers:^{25,26}

$$\chi = \frac{z}{kT} [\epsilon_{AB} - 1/2(\epsilon_{AA} + \epsilon_{BB})] \quad (1.1)$$

Empirically, the quantity is measured through fitting experimental data to a theoretical relation and summarized as²⁷

$$\chi_{eff} = \frac{\alpha}{T} + \beta = \chi_H + \chi_S \quad (1.2)$$

Experimental χ values therefore reflect additional non-idealities necessary to describe the data in addition to the simple exchange energy contribution. This effective interaction parameter is parceled into distinct enthalpic χ_H and entropic χ_S contributions to the excess free energy of mixing. In addition, the empirical parameters α and β that capture these contributions may depend on composition and N , and either may be positive or negative in sign.²⁸ Typical upper critical solution temperature behavior is found in cases where $\alpha > 0$ and $\beta < 0$ such that increases in temperature promote mixing of the two incompatible polymers or block polymer segments.

For block polymers, the effective interaction parameter outlines the preparation of materials with a specified order–disorder transition (ODT) temperature T_{ODT} . In the limit of short-range, isotropic, and generally dispersive van der Waals interactions, estimation of the interaction parameter using solubility parameters may offer reasonable values,²⁸

$$\chi \approx \chi_H = \frac{v_0 (\delta_A - \delta_B)^2}{RT} \quad (1.3)$$

where δ_A and δ_B are the associated segment solubility parameters, v_0 is a common segment reference volume, R is the gas constant, and T is the absolute temperature. However, even for nearly athermal blends, this approach may prove deficient as it ignores changes in polymer conformation or entropic frustration that contribute to the excess free energy of mixing.²⁶

The function $\chi(T)$ for a particular block segment pairing can be extracted experimentally from the temperature dependence of the disordered scattering structure factor²⁹ or from the N dependence of T_{ODT} .²⁵ Measurements of T_{ODT} have been found through a combination of techniques including dynamic mechanical spectroscopy (DMS), small-angle x-ray scattering (SAXS), and differential scanning calorimetry (DSC).³⁰⁻³² Primarily, DMS is used to locate the ODT as the specimen can be heated slowly (0.1–2 C/min) while monitoring the elastic shear modulus, G' , at low frequency ($\omega \sim 1$ rad/s) where the mechanical response is dominated by the microstructure. Abrupt changes in G' are associated with phase transitions. Determination of the temperature dependence of the interaction parameter typically relies on the result $(\chi N)_{ODT} = 10.5$ obtained from SCFT for approximately symmetric volume fractions. Use of this mean-field prediction ignores conformational asymmetry and does not account for the presence of fluctuations that suppress T_{ODT} in the low N block polymers studied in this thesis (Chapters 5 and 6). Note also that analysis of these measurements once again invokes the use of N , and as described above, care must be taken to compare data at constant reference volume. Although recent simulations³³⁻³⁵ have shown that actual $(\chi N)_{ODT}$ values are likely higher than those determined experimentally by an approximate factor of 2–3, the quantitative inaccuracy does not detract from the qualitative features of our results and enables comparisons with other systems in the literature.

1.4 Fluctuations and the Structure of the Disordered Phase

Theoretical treatments of block polymers resort to mean-field approximations.^{19,36} In mean-field descriptions, the disordered state is elucidated as a molecularly mixed homogeneous melt that at the critical point ($\chi N = 10.5$ and $f = 0.5$) gives way to a ordered lamellar phase with a sinusoidally varying composition profile. Experimentally, the ODT deviates from the mean-field prediction due to the presence of compositional fluctuations at finite N that evolve in the vicinity of the ODT phase boundary. These fluctuations produce a transient, locally structured but globally isotropic disordered state characterized by short-range correlations on the order of the radius of gyration of the block polymer.³⁷⁻⁴⁰

The instantaneous structure is thought to resemble the patterns observed for spinodally decomposed binary blends of immiscible liquids.^{39,40} Experimental evidence for the existence of fluctuations has been documented with a variety of techniques, including small-angle X-ray and neutron scattering (SAXS and SANS),⁴¹⁻⁴⁵ transmission electron microscopy (TEM),^{41,42,45} and rheology.^{39,40,46} Chapters 2–4 will highlight a polymerization-induced microphase separation (PIMS) process that is leveraged to produce bicontinuous network structures with small and tunable domain sizes and characteristics. These mesoscale structures are thought to be formed from the structural arrest of a block polymer fluctuating in the disordered state.

The mean-field treatment of Leibler⁴⁷ developed block polymer phase behavior in the limit of weak segregation near the ODT ($\chi N \sim 10$). Within the developed theory, he presented the random phase approximation (RPA) calculation for the structure factor $S(q)$ for diblock copolymer that predicts an inverse peak intensity that depends linearly on χ . Fredrickson and Helfand⁴⁸ proposed a revision to correct for fluctuation effects that reduces to the mean-field result in the limit of $N \rightarrow \infty$. The Fredrickson-Helfand (FH) theory includes a third parameter in addition to χN and f to describe the thermodynamic state of the block polymer. This parameter, termed the invariant degree of polymerization, \bar{N} , gives a measure of the degree of chain overlap in the melt and is defined as $\bar{N} = Nb^6/v_0^2$, where b is the statistical segment length and v_0 is the common segment reference volume. It is equivalent to the square of the ratio of the pervaded volume, $(N^{1/2}b)^3$, to the actual molecular volume of the chain, Nv_0 , which is generally much smaller. It is worth noting that \bar{N} is independent of the chosen reference volume.

FH theory predicts that for a symmetric block polymer ($f_A = 0.5$), a discontinuous weakly first-order ODT occurs at

$$(\chi N)_{ODT} = 10.495 + 41.0 \bar{N}^{-1/3} \quad (1.4)$$

At high \bar{N} , each chain interacts with a large number of neighboring chains such that all interactions for any one chain can be approximated by the averaged interaction of the mean-

field. As \bar{N} is reduced, fluctuation effects become more pronounced, stabilizing the disordered phase and shifting the ODT to lower temperature.

The FH theory provided better qualitative agreement between experimental phase behavior and the developing theoretical phase diagram. It revised the topology of the phase windows to enable direct first-order transitions between the disordered phase and the lamellar and cylindrical phases for asymmetric compositions, which were not permitted in Leibler's mean-field theory. Strictly interpreted, FH theory is a correction to mean-field theory that contains several approximations with validity limited to $\bar{N} \geq 10^4$, a value that remains above that typical for most experiments.³³

Recently, Morse and co-workers^{29,33,34} have attributed the failure of FH theory for $\bar{N} \leq 10^4$ to the assumption of weak-segregation at the ODT. Their findings have utilized advances in renormalized one-loop (ROL) theory⁴⁹ to calculate corrections to Leibler's RPA theory for the structure factor $S(q)$, enabling accurate values of the interaction parameter χ to be extracted from simulation data for various models. Removing ambiguity in the estimation of χ enabled precise comparisons between simulation and theoretical prediction, demonstrating a universal dependence of the free energy and ODT on \bar{N} with improved estimates of $(\chi N)_{ODT}$. Most pertinently, their calculations of the derivative of the free energy enabled a measure of the extent of AB contact in both the ordered and disordered phases. It was found that the disordered phase has a local structure similar to the ordered phase with well-defined A and B domains but lacking long-range order. The structural similarity and the strong-segregation of the disordered phase to the ordered state will be shown to have a large impact on the properties of materials produced from crosslinked and disordered block polymers that form the discussion of Chapters 2–4.

1.5 General Comment on Material Design Strategies

This dissertation primarily investigates and connects molecular design principles with the resulting meso- and macroscopic structural properties. The studies to be reported bridge a variety of contemporary topics in polymer science, including new techniques to access

co-continuous domains, strategies to circumvent the resolution limitations of classical block copolymer chemistries, and discovery of new equilibrium morphologies in block copolymer melts.

1.5.1 Co-continuity

Block polymers have been broadly implemented as polymeric membranes for water purification, gas separation, fuel cells, batteries, and solar cells. The heterogeneous microstructure of block polymers enables the transport and mechanical properties to be independently modulated, as facile transport is often achieved at the expense of mechanical integrity in homogeneous materials. Ideally, three-dimensional domain continuity of the high-modulus A-domain and the high-transport B-domain enables both properties to be maximized. Portions of this thesis will focus on the development of polymer electrolytes that exhibit long-range continuity as a necessary condition for both high conductivity and modulus. The purpose of this discussion is to highlight past studies on co-continuous block polymer structures.

Below the ODT temperature, a microphase-separated state with long-range order is obtained. Body-centered cubic (S), hexagonally close-packed cylinders (C), and lamellae (L) (Figure 1.2) are the predominant equilibrium morphologies for the majority of AB block polymers at strong segregation ($\chi N \gg 10$). These morphologies typically assume a polycrystalline structure of randomly oriented grains with concomitant defects and grain boundaries.^{50,51} None of these mesostructures contain two continuous domains that percolate through the sample in three dimensions, and furthermore, an aligning field (e.g., shear flow,⁵⁰ electric,⁵² magnetic⁵³) provides only two-dimensional continuity for lamellar and one-dimensional continuity for cylindrical microstructures. The alignment procedures necessary to minimize dead-ends and maximize flux through a polymer membrane are also typically costly and/or time-consuming.

Much literature and research has been dedicated to the discovery and evaluation of the stability of network morphologies that exhibit three-dimensional translational order. A variety of network structures with co-continuous domains have been reported in block

polymer melts, mostly within relatively limited compositional space.⁵⁴ Due to the complexity of self-assembly in these regimes, many other systems and strategies have been developed in order to achieve domain continuity.

1.5.2 Tuning Resolution Through Material Design

Chapter 5 will address new materials for lithographic applications that constantly demand smaller structures for high-resolution and economic patterning. Block polymers can self-assemble on the requisite length scale provided they are designed with the appropriate choice of interaction parameter. Since the domain spacing $d \sim \chi^{1/6} N^{2/3}$ scales much more strongly as a function of N than χ (subject to the constraint that $\chi N > 10.5$ to remain ordered), decreasing N at the expense of raising χ will decrease d and provide access to smaller structures. As described above, the interaction parameter is related to the chemical incompatibility between dissimilar blocks, such that selection of disparate polarity blocks will generate a high χ and enable smaller N polymer chains to self-assemble into ordered structures. The intricacies associated with the bulk characterization of these materials and subsequent application in thin films are the focus of the work contained in this thesis.

1.5.3 Conformational asymmetry

Conformational asymmetry can significantly alter the thermodynamic properties of polymer mixtures^{26,55} and block polymers.^{20,21,38,56-61} Macromolecules span a volume that is proportional to R_g^3 , where $R_g = b(N/6)^{1/2}$ is the unperturbed radius of gyration of a chain in a polymer melt, which greatly exceeds the molecular volume, Nv_o . For polymer molecules, a measure of the conformational volume relative to the molecular volume is described using an N -independent parameter

$$\beta^2 = R_g^2/V = b^2/6v_o \quad (1.5)$$

such that conformational asymmetry between block polymer segments A and B can then be defined as

$$\varepsilon = (\beta_A/\beta_B)^2 \quad (1.6)$$

Distinct dimensions of the statistical segment length b give a measure of relative chain flexibility and the excluded-volume interactions that occur over length-scales intermediate to the statistical segment length and the radius of gyration. Typically the effects of conformational asymmetry are considered under the assumption of a common reference volume, reducing the parameter to a simpler ratio $\varepsilon = (b_A/b_B)^2$.

As described by Bates and Fredrickson,²⁶ in polymer mixtures, conformational asymmetry contributes to the excess entropy of mixing because the constraint of maintaining a uniform density in a polymer melt does not allow for the random mixing of conformationally-distinct components. The interchange of one molecule into the vacancy left from removal of a distinct molecule leads to packing frustration. In block polymers, conformational asymmetry also leads to an increase in χ , however, the origin is an enthalpic effect attributed to an increase in the effective coordination, z , when both components have large conformational parameters, β^2 .⁶¹ An illustration of conformational asymmetry in block polymers was initially presented by Gehlsen and Bates⁵⁷ in the study of a series of polyolefins paired with poly(cyclohexylethylene) (PVCH) as shown in Figure 1.3. The image depicts segments of equal molecular volume (compositionally symmetric), while the longer and thinner chains of poly(ethylene-alt-propylene) (PEP) and poly(ethylene) (PE) represent a larger statistical segment length as fewer carbon atoms lie pendant to the backbone.

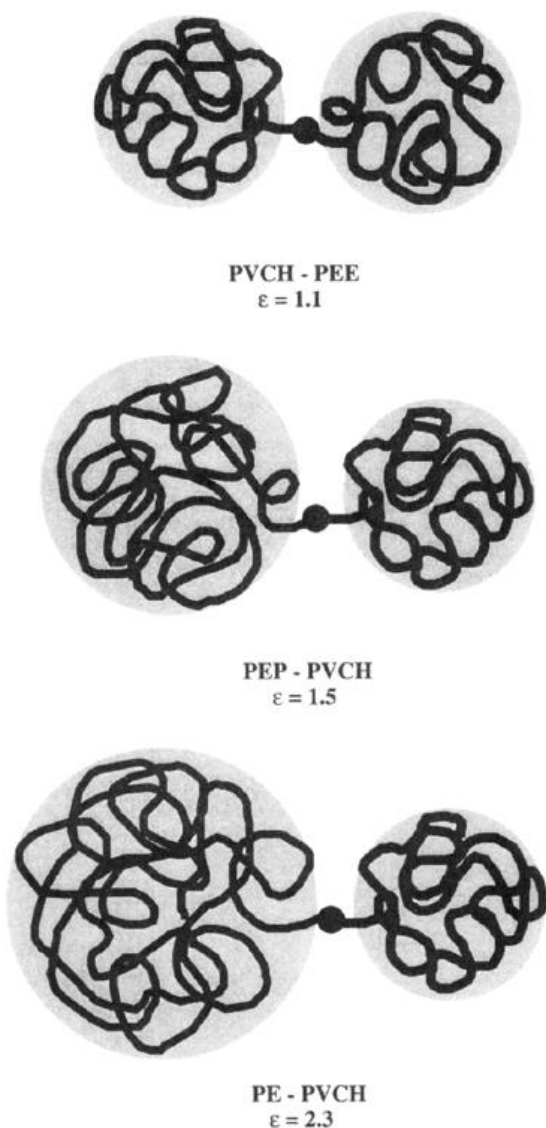


Figure 1.3 Schematic representation of the space-filling characteristics for PVCH-PEE, PEP-PVCH, and PE-PVCH. The thickness and length of each block reflect a common molecular volume. The shaded area represents a cross-sectional view of the coil and is proportional to R_g^2 . For PVCH-PEE ($\epsilon = 1.1$) the volume-filling characteristics are comparable, while for PEP-PVCH ($\epsilon = 1.5$) and PE-PVCH ($\epsilon = 2.3$) the conformational asymmetry becomes more apparent. Reproduced with permission from Gehlsen, M. D.; Bates, F. S. *Macromolecules* **1994**, 27, 3611. Copyright 1994 American Chemical Society.⁵⁷

Because the geometry of the self-assembled microstructure balances interfacial energy and the stretching energies of both A and B blocks, conformational asymmetry can have profound influence on phase boundaries.^{21,22,56,62} SCFT calculations by Matsen assessed the impact of conformational asymmetry for values of $b_A/b_B = 1.0, 1.5$ and 2.0 on the equilibrium phase behavior, which resulted in broken phase symmetry about $f_A = 0.5$ and a shift in the phase boundaries to larger volume fractions of A (Figure 1.4). A simple explanation proposes that as conformational asymmetry increases, i.e. as interfacial curvature balances the stretching penalties of both domains; the A blocks easily stretch to fill the center of the domain so that the strained B blocks can relax. In other words, at a fixed composition, a lamellar morphology will tend to transform to a cylindrical microstructure of A-cylinders in a B-matrix. Notably, the location of the ODT is relatively unaffected since SCFT predicts that the minority A-blocks must pull free of their microdomains to cause the spherical phase to disorder; the energy binding them to their domains $\chi N f_A$ is independent of the statistical segment lengths.

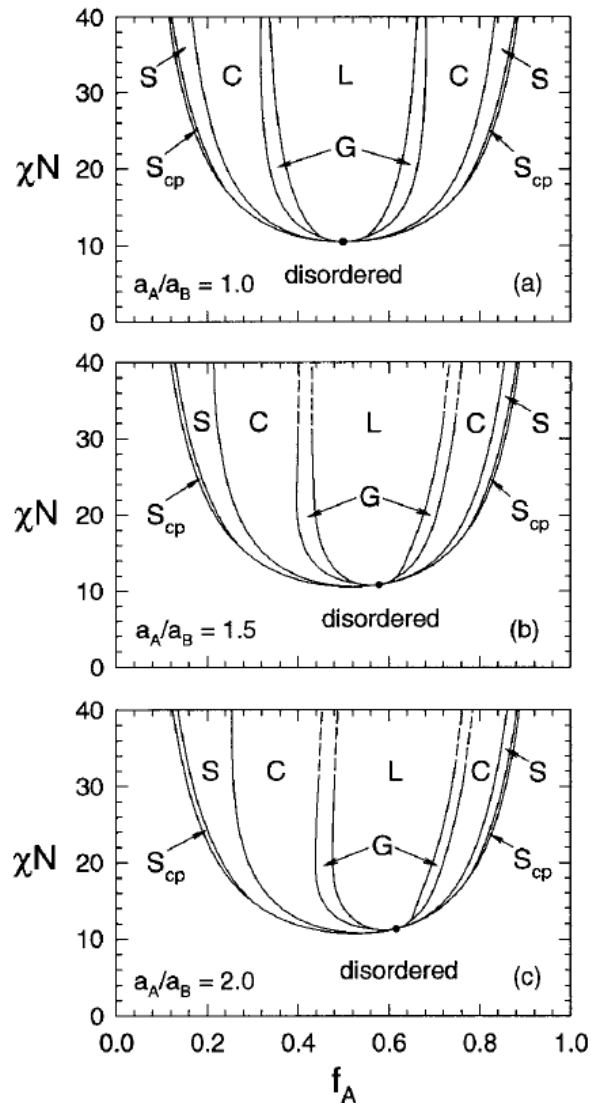


Figure 1.4 Mean-field phase diagrams for diblock copolymer melts for a series of conformational asymmetries expressed as a_A/a_B , a notation equivalent to b_A/b_B employed in the text. The dots denote mean-field critical points, and the dashed curves are extrapolated phase boundaries. In each diagram, the L, C, and S phases extend to the critical point, but the G and S_{cp} phases instead terminate at triple points. Reproduced with permission from Matsen, M. W.; Bates, F. S. *Journal of Polymer Science Part B: Polymer Physics* **1997**, *35*, 945. Copyright 1997 John Wiley & Sons, Inc.⁵⁶

Lee et al.⁶³ recently discovered a new complex spherical morphology, the Frank-Kasper σ phase, in linear poly(isoprene)-*block*-poly(lactide) (PI-PLA) diblock copolymers. The

finding has motivated a theoretical re-examination of the stability of new structures within the augmented sphere-forming window of conformationally asymmetric AB diblocks. The packing of sphere-like particles in block polymer melts deforms micelles toward the shape of the polyhedral unit cell or Voronoi cell of the lattice. As sphere-like phases become more compositionally symmetric, the A/B interface is distorted toward the shape of the Voronoi cell, altering the relative contributions of stretching and interfacial energies (Figure 1.5). Although the potential spherical phases considered by Shi et al.²¹ and Grason et al.²⁰ differ, both theoretical groups valued conformational asymmetry as a critical factor to favor the formation of complex phases such as the σ phase. To date, these theoretical predictions remain unverified experimentally; Chapter 6 reports an experimental inquiry into the spherical phase topology under systematic variation of the conformational asymmetry parameter, validates the theoretical predictions, and discloses the discovery of a new block polymer morphology.

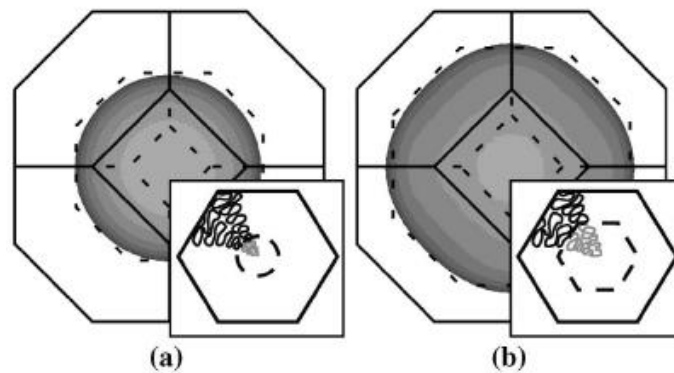


Figure 1.5 Depiction of the AB interface in the BCC phase. Both figures were produced for fixed χN . In (a) the volume fraction of the minority phase, $f = 0.22$ and the interface is almost spherical. In (b) $f = 0.45$ and the interface takes on the shape of the Voronoi cell. The insets depict (a) the spherical interface limit (small f) and (b) the flat interface limit (large f). Reprinted with permission from Grason, G. M.; DiDonna, B. A.; Kamien, R. D. *Physical Review Letters* **2003**, *91*, 058304. Copyright 2003 American Physical Society.²⁰

1.6 Overview

This thesis contributes to five research areas within block polymer science and addresses contemporary challenges in their broad application. The outstanding challenge in the field of polymer electrolyte membranes (PEMs) is to improve mechanical properties without the sacrifice of high conductivity. In Chapter 2, we demonstrate a straightforward, one-pot synthetic strategy to generate high modulus, high conductivity nanostructured polymer electrolytes from an initially homogeneous mixture of poly(ethylene oxide) macromolecular chain transfer agent (macro-CTA), ionic liquid, styrene monomer and crosslinker. The formation of crosslinks within a locally segregated domain of polystyrene kinetically traps a bicontinuous microstructure, enabling these block polymer electrolytes to surpass the conductivity, modulus, and high temperature stability of chemically similar systems in the field. Following an evaluation of their material properties, we study the mechanism of this process, referred to as polymerization-induced microphase separation (PIMS), via a series of in situ, time-resolved experiments (Chapter 3). The findings illustrate a competition between polymerization and concomitant increases in segregation strength that underlies the formation of isotropic composition fluctuations resulting in the observed network morphology. In Chapter 4, the PIMS process is adapted to the generation of nanoporous monoliths, and we present preliminary results that probe and exploit reaction parameters to control the porosity of PIMS monoliths during their preparation.

In Chapter 5, we describe the synthesis and characterization of a new, highly incompatible diblock copolymer, poly(cyclohexylethylene)-*block*-poly(ethylene oxide) characterized by an exceptionally large interaction parameter, χ , that can circumvent the feature size limitations of previously reported low- χ systems based on polystyrene. Furthermore, we demonstrate the utility of this polymer to pattern exceptionally small arrays of metal oxide nanodots via a straightforward, spin-coating process in which the metallo(hydro)philicity of the PEO block allows direct incorporation of metal precursor.

In Chapter 6, two polymeric hydrocarbons are paired with polylactide (PLA) to form highly incompatible, low molar-mass diblock copolymer systems of varied conformational asymmetry. As the statistical segment length of the hydrocarbon block decreases,

conformational asymmetry increases and order-order transitions shift to higher compositions of the PLA-block, resulting in the formation of larger spherical domains of PLA-cores. At relatively high compositions of PLA within the sphere-forming window, complex morphologies such as the Frank-Kasper σ phase are found to be thermodynamically stable, and we present a broad investigation into their formation.

1.7 References

- (1) Gu, X.; Gunkel, I.; Russell, T. P. *Philosophical Transactions of the Royal Society A: Mathematical, Physical and Engineering Sciences* **2013**, 371.
- (2) Bates, C. M.; Maher, M. J.; Janes, D. W.; Ellison, C. J.; Willson, C. G. *Macromolecules* **2013**.
- (3) Bates, C. M.; Seshimo, T.; Maher, M. J.; Durand, W. J.; Cushen, J. D.; Dean, L. M.; Blachut, G.; Ellison, C. J.; Willson, C. G. *Science* **2012**, 338, 775.
- (4) Bang, J.; Jeong, U.; Ryu, D. Y.; Russell, T. P.; Hawker, C. J. *Advanced Materials* **2009**, 21, 4769.
- (5) Lee, J.; Kaake, L. G.; Cho, J. H.; Zhu, X. Y.; Lodge, T. P.; Frisbie, C. D. *The Journal of Physical Chemistry C* **2009**, 113, 8972.
- (6) Kim, S. H.; Hong, K.; Xie, W.; Lee, K. H.; Zhang, S.; Lodge, T. P.; Frisbie, C. D. *Advanced Materials* **2013**, 25, 1822.
- (7) Cho, J. H.; Lee, J.; Xia, Y.; Kim, B.; He, Y.; Renn, M. J.; Lodge, T. P.; Daniel Frisbie, C. *Nat Mater* **2008**, 7, 900.
- (8) Segalman, R. A.; McCulloch, B.; Kirmayer, S.; Urban, J. J. *Macromolecules* **2009**, 42, 9205.
- (9) Sun, S.-S. *Solar Energy Materials and Solar Cells* **2003**, 79, 257.
- (10) Boudouris, B. W.; Frisbie, C. D.; Hillmyer, M. A. *Macromolecules* **2008**, 41, 67.
- (11) Baruth, A.; Rodwogin, M. D.; Shankar, A.; Erickson, M. J.; Hillmyer, M. A.; Leighton, C. *ACS Applied Materials & Interfaces* **2011**, 3, 3472.
- (12) Baruth, A.; Seo, M.; Lin, C. H.; Walster, K.; Shankar, A.; Hillmyer, M. A.; Leighton, C. *ACS Applied Materials & Interfaces* **2014**, 6, 13770.
- (13) Blanazs, A.; Armes, S. P.; Ryan, A. J. *Macromolecular Rapid Communications* **2009**, 30, 267.
- (14) Kataoka, K.; Harada, A.; Nagasaki, Y. *Advanced Drug Delivery Reviews* **2001**, 47, 113.
- (15) Bates, F. S.; Fredrickson, G. H. *Annual Review of Physical Chemistry* **1990**, 41, 525.

- (16) Bates, F. S.; Fredrickson, G. H. *Physics Today* **1999**, *52*, 32.
- (17) Grason, G. M. *Physics Reports* **2006**, *433*, 1.
- (18) Cochran, E. W.; Bates, F. S. *Macromolecules* **2002**, *35*, 7368.
- (19) Matsen, M. W. In *Soft Matter*; Wiley-VCH Verlag GmbH & Co. KGaA: 2007, p 87.
- (20) Grason, G. M.; DiDonna, B. A.; Kamien, R. D. *Physical Review Letters* **2003**, *91*, 058304.
- (21) Xie, N.; Li, W.; Qiu, F.; Shi, A.-C. *ACS Macro Letters* **2014**, *3*, 906.
- (22) Matsen, M. W. *Macromolecules* **2012**, *45*, 2161.
- (23) Matsen, M. W.; Schick, M. *Physical Review Letters* **1994**, *72*, 2660.
- (24) Vavasour, J. D.; Whitmore, M. D. *Macromolecules* **1992**, *25*, 5477.
- (25) Maurer, W. W.; Bates, F. S.; Lodge, T. P.; Almdal, K.; Mortensen, K.; Fredrickson, G. H. *The Journal of Chemical Physics* **1998**, *108*, 2989.
- (26) Bates, F. S.; Fredrickson, G. H. *Macromolecules* **1994**, *27*, 1065.
- (27) Hiemenz, P. C.; Lodge, T. P. *Polymer Chemistry, Second Edition*; CRC Press, 2007.
- (28) Bates, F. S.; Hillmyer, M. A.; Lodge, T. P.; Bates, C. M.; Delaney, K. T.; Fredrickson, G. H. *Science* **2012**, *336*, 434.
- (29) Glaser, J.; Medapuram, P.; Beardsley, T. M.; Matsen, M. W.; Morse, D. C. *Physical Review Letters* **2014**, *113*, 068302.
- (30) Lee, S.; Gillard, T. M.; Bates, F. S. *Aiche J* **2013**, *59*, 3502.
- (31) Voronov, V. P.; Buleiko, V. M.; Podneks, V. E.; Hamley, I. W.; Fairclough, J. P. A.; Ryan, A. J.; Mai, S. M.; Liao, B. X.; Booth, C. *Macromolecules* **1997**, *30*, 6674.
- (32) Kim, J. K.; Lee, H. H.; Gu, Q.-J.; Chang, T.; Jeong, Y. H. *Macromolecules* **1998**, *31*, 4045.
- (33) Medapuram, P.; Glaser, J.; Morse, D. C. *Macromolecules* **2015**, *48*, 819.
- (34) Gillard, T. M.; Medapuram, P.; Morse, D. C.; Bates, F. S. *Macromolecules* **2015**, *48*, 2801.
- (35) Vassiliev, O. N.; Matsen, M. W. *The Journal of Chemical Physics* **2003**, *118*, 7700.

- (36) Matsen, M. W.; Bates, F. S. *Macromolecules* **1996**, *29*, 1091.
- (37) Rosedale, J. H.; Bates, F. S.; Almdal, K.; Mortensen, K.; Wignall, G. D. *Macromolecules* **1995**, *28*, 1429.
- (38) Bates, F. S.; Schulz, M. F.; Khandpur, A. K.; Forster, S.; Rosedale, J. H.; Almdal, K.; Mortensen, K. *Faraday Discussions* **1994**, *98*, 7.
- (39) Bates, F. S.; Rosedale, J. H.; Fredrickson, G. H. *The Journal of Chemical Physics* **1990**, *92*, 6255.
- (40) Hickey, R. J.; Gillard, T. M.; Lodge, T. P.; Bates, F. S. *ACS Macro Letters* **2015**, *4*, 260.
- (41) Sakamoto, N.; Hashimoto, T. *Macromolecules* **1998**, *31*, 3292.
- (42) Sakamoto, N.; Hashimoto, T. *Macromolecules* **1998**, *31*, 3815.
- (43) Bates, F. S.; Rosedale, J. H.; Fredrickson, G. H.; Glinka, C. J. *Physical Review Letters* **1988**, *61*, 2229.
- (44) Koga, T.; Koga, T.; Kimishima, K.; Hashimoto, T. *Physical Review E* **1999**, *60*, R3501.
- (45) Hashimoto, T. *Macromolecular Symposia* **2001**, *174*, 69.
- (46) Kennemur, J. G.; Hillmyer, M. A.; Bates, F. S. *ACS Macro Letters* **2013**, *2*, 496.
- (47) Leibler, L. *Macromolecules* **1980**, *13*, 1602.
- (48) Fredrickson, G. H.; Helfand, E. *The Journal of Chemical Physics* **1987**, *87*, 697.
- (49) Qin, J.; Grzywacz, P.; Morse, D. C. *The Journal of Chemical Physics* **2011**, *135*, 084902.
- (50) Wang, H.; Newstein, M. C.; Krishnan, A.; Balsara, N. P.; Garetz, B. A.; Hammouda, B.; Krishnamoorti, R. *Macromolecules* **1999**, *32*, 3695.
- (51) Balsara, N. P.; Dai, H. J.; Watanabe, H.; Sato, T.; Osaki, K. *Macromolecules* **1996**, *29*, 3507.
- (52) Xu, T.; Zhu, Y.; Gido, S. P.; Russell, T. P. *Macromolecules* **2004**, *37*, 2625.
- (53) Tran, H.; Gopinadhan, M.; Majewski, P. W.; Shade, R.; Steffes, V.; Osuji, C. O.; Campos, L. M. *ACS Nano* **2013**, *7*, 5514.
- (54) Meuler, A. J.; Hillmyer, M. A.; Bates, F. S. *Macromolecules* **2009**, *42*, 7221.

-
- (55) Bates, F. S.; Schulz, M. F.; Rosedale, J. H.; Almdal, K. *Macromolecules* **1992**, *25*, 5547.
- (56) Matsen, M. W.; Bates, F. S. *Journal of Polymer Science Part B: Polymer Physics* **1997**, *35*, 945.
- (57) Gehlsen, M. D.; Bates, F. S. *Macromolecules* **1994**, *27*, 3611.
- (58) Pochan, D. J.; Gido, S. P.; Zhou, J.; Mays, J. W.; Whitmore, M.; Ryan, A. J. *Journal of Polymer Science Part B: Polymer Physics* **1997**, *35*, 2629.
- (59) Lai, C.; Russel, W. B.; Register, R. A.; Marchand, G. R.; Adamson, D. H. *Macromolecules* **2000**, *33*, 3461.
- (60) Mays, J. W.; Kumar, R.; Sides, S. W.; Goswami, M.; Sumpter, B. G.; Hong, K.; Wu, X.; Russell, T. P.; Gido, S. P.; Avgeropoulos, A.; Tsoukatos, T.; Hadjichristidis, N.; Beyer, F. L. *Polymer* **2012**, *53*, 5155.
- (61) Almdal, K.; Hillmyer, M. A.; Bates, F. S. *Macromolecules* **2002**, *35*, 7685.
- (62) Matsen, M. W.; Schick, M. *Macromolecules* **1994**, *27*, 4014.
- (63) Lee, S.; Bluemle, M. J.; Bates, F. S. *Science* **2010**, *330*, 349.

Chapter 2

High-Modulus, High-Conductivity Nanostructured Polymer Electrolytes via Polymerization-Induced Microphase Separation^{†,‡}

The primary challenge in solid-state polymer electrolyte membranes (PEMs) is to enhance properties, such as modulus, toughness, and high temperature stability, without sacrificing ionic conductivity. This chapter describes a remarkably facile one-pot synthetic strategy based on polymerization-induced microphase separation (PIMS) to generate nanostructured PEMs that exhibit an unprecedented combination of high modulus and ionic conductivity. Simple heating of a poly(ethylene oxide) macromolecular chain transfer agent dissolved in a mixture of ionic liquid, styrene and divinylbenzene, leads to a bicontinuous PEM comprising interpenetrating nanodomains of highly crosslinked polystyrene and poly(ethylene oxide)/ionic liquid. Ionic conductivities higher than the 1 mS/cm benchmark were achieved in samples with an elastic modulus approaching 1 GPa at room temperature. Crucially, these samples are robust solids above 100 °C, where the conductivity is significantly higher. This strategy holds tremendous potential to advance lithium-ion battery technology by enabling the use of lithium metal anodes, or to serve as membranes in high temperature fuel cells.

[†] This work was done in collaboration with Lucas D. McIntosh and Timothy P. Lodge.

[‡] Reproduced with permission from Schulze, M. W.;* McIntosh, L. D.;* Hillmyer, M. A.; Lodge, T. P. *Nano Lett.* **2013**, *14*, 122–126. Copyright 2013 American Chemical Society. (* Contributed equally)

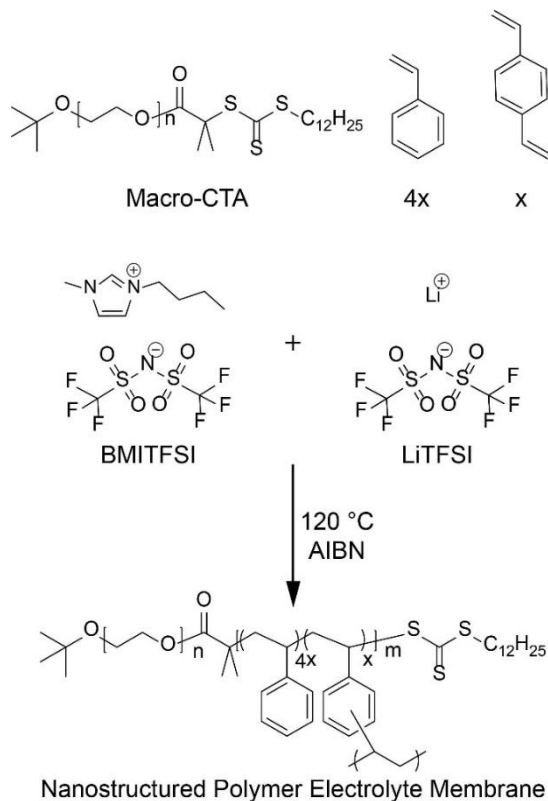
2.1 Introduction

Polymer electrolytes membranes (PEMs) are promising alternatives to conventional liquid electrolytes in energy storage applications such as lithium batteries and high temperature fuel cells.¹⁻⁹ Effective PEMs must maintain a combination of high modulus, toughness, environmental resistance, and high ionic conductivity during use.^{2,10-12} The key challenge is to achieve high mechanical and thermal performance without sacrificing the requisite ionic conductivity. The most successful strategies to date leverage nanostructured AB diblock copolymers, where block A is a glassy, rigid insulator and block B is a low glass transition ion conductor, to independently tune the mechanical and conductivity properties of the membrane.^{9,13-17} Previous studies have suggested that domain alignment is necessary to render pathways continuous for ion transport, and continuity of the mechanically robust phase leads to superior mechanical properties.¹⁸⁻²¹ In this chapter, we demonstrate that nanostructured block polymers with a disordered, bicontinuous morphology are particularly attractive as highly conductive, thermally stable, and mechanically robust PEMs due to the long-range, isotropic continuity of high modulus and ion conducting domains. Our simple, one-step protocol exploits simultaneous *in situ* block copolymer formation and chemical crosslinking such that local segregation of a growing poly(styrene/divinylbenzene) segment from an ionic liquid-swollen poly(ethylene oxide) (PEO) domain is preserved. PEMs with (i) room temperature moduli near 1 GPa, (ii) significantly improved mechanical stability over previously reported systems at high temperature ($E' > 0.1$ GPa for $T < 125$ °C), and (iii) ionic conductivity in excess of 1 mS/cm can be produced by this facile and scalable process. To the best of our knowledge, no other polymer electrolyte reported achieves such combination of modulus ($\geq 10^8$ Pa) and ionic conductivity ($\geq 10^3$ S/cm), nor the high temperature robustness.

Seo and Hillmyer reported that arresting microphase separation during the growth of a diblock copolymer is a simple route to mechanically robust nanostructured materials with a bicontinuous morphology.²² Using a poly(lactide) macro-chain transfer agent (PLA-CTA), the authors prepared nanoporous crosslinked polystyrene monoliths via sequential reversible-addition fragmentation chain transfer (RAFT) and hydrolysis of the PLA

domain. We have extended this polymerization-induced microphase separation (PIMS) approach to the preparation of mechanically rigid block polymer electrolytes via the polymerization of a styrene/divinylbenzene mixture from a macromolecular PEO-CTA in the presence of an ionic liquid (Scheme 2.1). The controlled RAFT polymerization process induces partitioning of growing block polymer chains into nanoscale domains, and concerted chemical crosslinking by divinylbenzene during polymerization of the styrene restrains the coarsening of the resultant bicontinuous morphology. The direct integration of the ionic liquid and/or Li-salt in the liquid precursor obviates post-polymerization salt-doping steps that are common to other dry diblock copolymer-based electrolytes. The principal ionic liquid (IL) utilized, 1-butyl-3-methylimidazolium bis(trifluoromethylsulfonyl)imide (BMITFSI), is immiscible with polystyrene with $M \geq 3$ kg mol⁻¹, thus leading to its partitioning into the PEO domains.^{23,24} The result is the one-step formation of a bicontinuous and nanostructured membrane consisting of a mechanically robust phase (crosslinked PS) and an ion conductive phase (PEO/BMITFSI).

Scheme 2.1 Reaction scheme used to prepare polymerization-induced microphase separation polymer electrolyte membranes.



2.2 Experimental Section

2.2.1 Synthesis of End-functionalized Poly(ethylene oxide) Precursors

Asymmetrically end-capped poly(ethylene oxide) was synthesized by anionic polymerization from a potassium *tert*-butoxide initiator (1.0 M in THF, Sigma Aldrich) using standard Schlenk techniques ($M_n = 28 \text{ kg mol}^{-1}$, $\mathcal{D} = 1.03$). Appendix A provides more detailed information regarding anionic synthesis and reagents used for purification of monomer and solvent. Poly(ethylene glycol) methyl ether was purchased from Sigma Aldrich ($M_n = 5 \text{ kg mol}^{-1}$, $\mathcal{D} = 1.11$). The chain transfer agent, (*S*)-1-dodecyl-(*S'*)-(α,α'-dimethyl-α''-acetic acid) trithiocarbonate (DDMAT), was prepared as previously reported,²⁵ and coupled to the hydroxyl-terminus of each polymer via an acid chloride intermediate to produce macromolecular PEO-CTA.²⁶ SEC traces of linear PS-*b*-PEO

block copolymers prepared and initiated from PEO-CTA in the bulk polymerization of styrene monomer had narrow molar mass distributions. This result supported complete end-functionalization of PEO and agreed with the quantitative end-group analysis performed using $^1\text{H-NMR}$ spectroscopy (Figure 2.1).

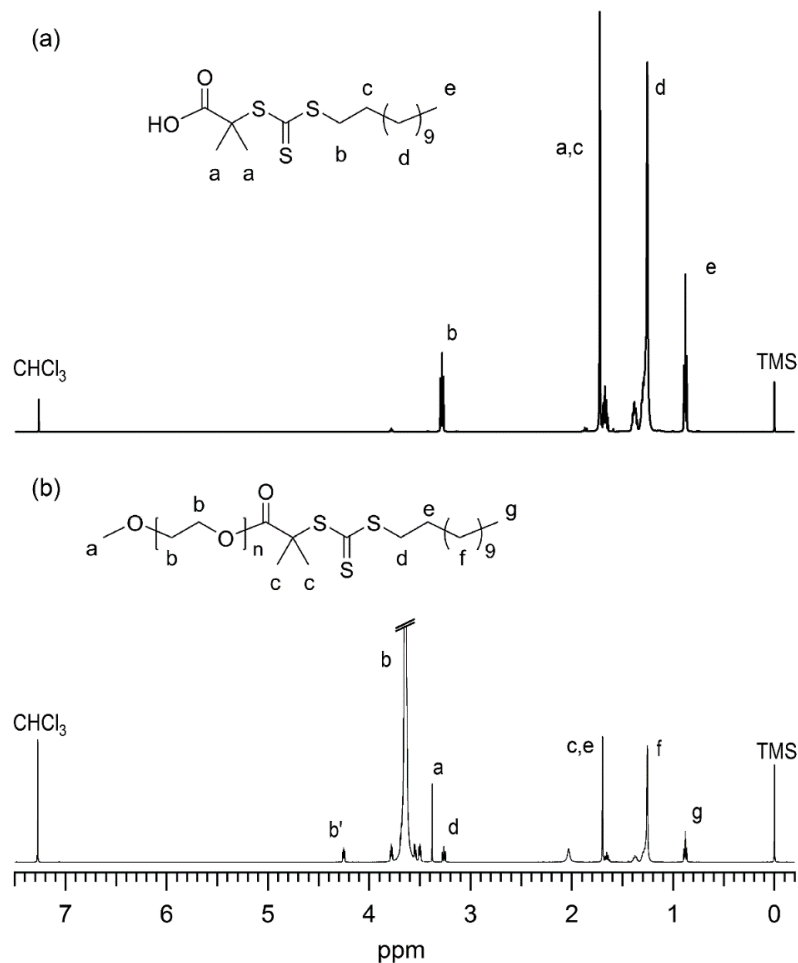


Figure 2.1 $^1\text{H-NMR}$ spectra (CDCl_3 , 500 MHz, 20 $^\circ\text{C}$) of (a) the chain-transfer agent DDMAT and (b) macromolecular PEO-CTA. In (b), the peak denoted as b' at 4.24 ppm refers to the methylene protons of PEO adjacent to the CTA.

2.2.2 Synthesis of 1-butyl-3-methylimidazolium bis(trifluoromethylsulfonyl)imide

The ionic liquid 1-butyl-3-methylimidazolium bis(trifluoromethylsulfonyl)imide (BMITFSI) was prepared following established procedures.^{27,28} A 10% molar excess of 4-chlorobutane was mixed with 1-methylimidazole in a round bottom flask, and cyclohexane was added to the reagents at a volumetric ratio of 10/1. The mixture was heated to reflux conditions and stirred vigorously overnight. Cyclohexane was removed via rotovap and the product, 1-butyl-3-methylimidazole chloride (BMICl), was dried at 60 °C under dynamic vacuum overnight. Lithium bis(trifluoromethylsulfonyl)imide was added to BMICl at 10% molar excess, assuming complete conversion in the first step. DI water was added at a volumetric ratio of 10/1, and the mixture was heated to 70 °C and stirred vigorously for 24 h. The resulting solution phase-separated into BMITFSI and an aqueous phase containing LiCl. BMITFSI was washed with distilled water three times and purified by passing through an alumina column. ¹H-NMR spectroscopy was used to confirm the final product (Figure 2.2). The ionic liquid was dried at elevated temperature under dynamic vacuum for 2 d before use.

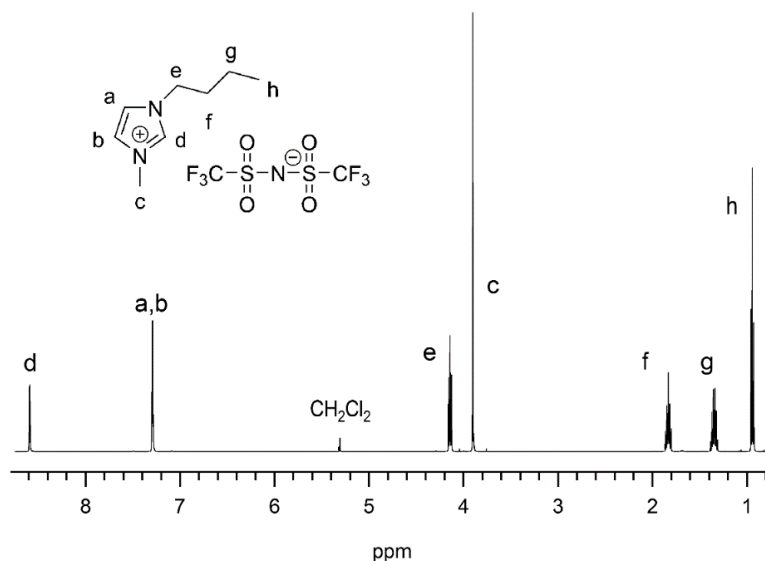


Figure 2.2 ¹H-NMR spectrum (CD₂Cl₂, 500 MHz, 20 °C) of the ionic liquid BMITFSI.

2.2.3 Preparation of Polymer Electrolyte Membranes

Typical reactions to produce polymer electrolyte membranes were performed in a glass vial without degassing. Styrene (99%, Sigma Aldrich) and divinylbenzene (80%, tech., Sigma Aldrich) were passed through activated alumina columns prior to use. A solution maintained at 30 vol% PEO-CTA was prepared by the sequential addition of macro-CTA, styrene, and divinylbenzene, where the monomer molar ratio was maintained at 4/1, respectively. BMITFSI was added to a predetermined concentration, and the entire solution was well-mixed prior to heating to 120 °C to auto-initiate styrene. The use of AIBN as an external initiator (0.05 *eq* to PEO-CTA) was necessary for the uniform generation of radicals to prevent density inhomogeneities that would otherwise induce cracks during polymerization. The resulting transparent, solid monolith could be sanded to a flat surface of ca. 500 μm thickness for additional analysis.

2.2.4 Transmission Electron Microscopy

Bulk samples were microtomed at room temperature on a Leica UC6 Ultramicrotome to obtain sections with a nominal thickness of 70 nm. Sample sections were collected on a 300 mesh copper grid and were stained with the vapor of a 0.5 wt% RuO_4 aqueous solution for 5 min. On this time-scale, RuO_4 preferentially stains poly(ethylene oxide), which appears dark in TEM images. Sections were imaged at room temperature on an FEI Tecnai G2 Spirit Bio-TWIN using an accelerating voltage of 120 kV. Images were collected by a 2048 \times 2048 pixel CCD. ImageJ software was used to generate Fourier transforms (FTs) of TEM images and then azimuthally integrate pixel intensity to generate 1D plots of intensity versus the wave vector, q .

2.2.5 Scanning Electron Microscopy

Nanoporous materials were produced from chemical etching of the poly(ethylene oxide)/IL composite domains. Bulk samples were immersed in 57 wt % aqueous hydroiodic acid (Sigma Aldrich) at 60 °C for 5 days. Each sample was rinsed with copious water and methanol and dried under vacuum at room temperature. Cryo-fractured monoliths of sample were placed on copper tape and coated with a ca. 1 nm thick platinum

layer to reduce sample charging during image acquisition. Micrographs were obtained on a Hitachi S-4900 FE-SEM instrument using a 3–5 kV accelerating voltage.

2.2.6 Small-angle X-ray Scattering

Small-angle X-ray scattering (SAXS) experiments were performed at the Argonne National Lab Advanced Photon Source beamline 5-ID-D, which is maintained by the DuPont-Northwestern-Dow (DND) Collaborative Access Team. Samples were exposed at room temperature to synchrotron-source X-rays with a nominal wavelength of 0.729 Å. Scattered X-rays were collected on a 2D MAR CCD detector at a sample-to-detector distance of 5680 mm. The sample-to-detector distance was calibrated using a silver behenate standard, and intensity was calibrated with glassy carbon. 2D SAXS intensity was reduced to a function of the magnitude of the wave vector, q , by azimuthally integrating the 2D data. q is given by $q = 4\pi \sin(\theta/2)/\lambda$, where λ is the X-ray wavelength and θ is the scattering angle.

2.2.7 Impedance Spectroscopy

Ionic conductivity was measured using 2-point probe impedance spectroscopy on a Solartron 1255B frequency response analyzer connected to a Solartron SI 1287 electrochemical interface. Bulk polymer electrolyte membrane samples were sanded to uniform thickness (ca. 0.5 mm) and sandwiched between stainless steel electrodes. Impedance was measured over the frequency range from 10^6 –1 Hz using a voltage amplitude of 100 mV. Bulk resistance, R , was determined from the frequency-independent plateau of the real part, Z' , of impedance. Ionic conductivity, σ , was calculated as $\sigma = l/(Ra)$, where l is the sample thickness and a is the superficial area. Thickness was measured with a Mitutoyo micrometer (1 μ m resolution) and area was measured using ImageJ software. Samples were stored in either an Ar-filled glovebox or under dynamic vacuum. Each sample was heated under dynamic vacuum (100 mTorr) for at least one day prior to running impedance experiments. Impedance measurements were performed in an open atmosphere at temperatures from 30 to 150 °C in 10 degree increments. Each temperature was maintained for 1 h prior to measurement to ensure

thermal equilibration. Replicate measurements were performed in series to observe the effect of possible water absorption on the conductivity for temperatures below 100 °C. The reproducibility of conductivity measurements over the entire temperature range for polymer electrolyte membranes that contained only ionic liquid indicated that these samples do not exhibit a strong affinity for water. Repeated measurements of the conductivity of LiTFSI-containing samples, however, indicated that these samples were highly absorptive. For this reason, these samples were heated to 100 °C for 3 h prior to measurement and temperatures were restricted to 100–150 °C.

2.2.8 Rheology

Mechanical response was measured in the linear viscoelastic regime using an RSA-G2 Solids Analyzer (TA Instruments). Samples prepared for mechanical response measurements were prepared in Teflon molds sealed using a hydraulic press during polymerization to produce samples with the appropriate geometry. These tensile bars measured approximately 50 × 10 × 1 mm. To generate time-temperature superposition (tTS) master curves, samples were heated to a series of increasing temperatures and thermally equilibrated at a given temperature for at least 10 min. Strain sweeps were performed at a frequency of 10 rad/s to determine the limit of linear viscoelastic response, followed by a frequency sweep performed at fixed strain over the frequency range from 100–0.1 rad/s. Raw data were shifted horizontally by visual alignment of the elastic modulus, E' .

2.2.8 Differential Scanning Calorimetry

Differential scanning calorimetry (DSC) experiments were performed on a TA Instruments Discovery DSC. Samples for measurement were prepared using standard aluminum T-zero pans with standard or hermetic lids. Each sample was annealed at 200 °C for 5 min. Subsequent cooling and heating ramps were applied at 5 °C/min. Heats of fusion were estimated from the endotherm of the second heating and the weight fraction of PEO incorporated into the crosslinked block polymer. Percent crystallinity was calculated in reference to the enthalpy of fusion of 213.4 J/g for pure crystalline PEO.²⁹

2.3 Results and Discussion

As a representative example, homogeneous solutions of 30 vol% PEO-CTA were prepared in a 4/1 molar mixture of styrene/divinylbenzene (S/D). BMITFSI (and mixtures with LiTFSI) could be added to this reaction mixture while retaining homogeneity over a wide compositional window (5–40 overall vol% BMITFSI). Table 2.1 summarizes the resulting composition of the PEMs in terms of the volume percent of conducting phase (PEO + BMITFSI), as well as the concentration of ionic liquid within the conducting phase using 5 and 28 kg mol⁻¹ PEO-CTA. The presence of BMITFSI with the introduction of LiTFSI facilitates the dissolution of the lithium salt in the mixture. Heating the quaternary solution to 120 °C in the presence of radical initiator (AIBN) for at least 20 h resulted in a transparent, insoluble solid PEM. The connectivity between domains resulting from the in situ formation of a block copolymer is critical to the formation of a homogeneous PEM, as illustrated by macrophase separation that results from polymerized mixtures of PEO-OH, monomer and IL (Figure 2.3). Given the immiscibility of PS and BMITFSI, mixtures of monomer and ionic liquid also produced inhomogeneous samples. Additionally, other molar ratios of S/D have been shown to retain bicontinuity, while modulation of the crosslink density does not affect conductivity because mechanical and transport properties are decoupled via microphase-separation.

Table 2.1 Properties of polymer electrolyte samples

M_n	PEO-CTA (kg mol ⁻¹)	$w_{\text{PEO-CTA}}^i$ (wt%)	type of salt	Composition (vol%) ⁱⁱ		
				salt ⁱⁱⁱ	PEO + salt ^{iv}	salt in PEO + salt domain ^v
5	32	32	no salt	0	32	0
5	32	32	BMITFSI	5	35	15
5	32	32	BMI/LiTFSI	7	36	18
5	32	32	BMITFSI	21	47	45
5	32	32	BMI/LiTFSI	21	47	45
5	32	32	BMITFSI	30	52	57
5	42	42	no salt	0	42	0
5	42	42	BMITFSI	12	50	25
5	42	42	BMITFSI	21	54	38
5	42	42	BMITFSI	30	60	50
28	32	32	no salt	0	32	0
28	32	32	BMITFSI	4	32	12
28	32	32	BMITFSI	21	47	46
28	32	32	BMITFSI	30	52	59

ⁱMass fraction of PEO-CTA in the mixture of S/DVB monomer (i.e., excluding the ionic liquid)

ⁱⁱComposition was calculated using the known mass incorporated into the sample and the following densities (in g cm⁻³): $\rho_{\text{PSDVB}} = 1.05$, $\rho_{\text{PEO}} = 1.064$, $\rho_{\text{BMITFSI}} = 1.328$, $\rho_{\text{LiTFSI}} = 1.334$

ⁱⁱⁱOverall volume fraction of ionic liquid or a mixture of ionic liquid and LiTFSI

^{iv}Volume fraction of the conducting phase

^vVolume fraction of salt in the conducting phase

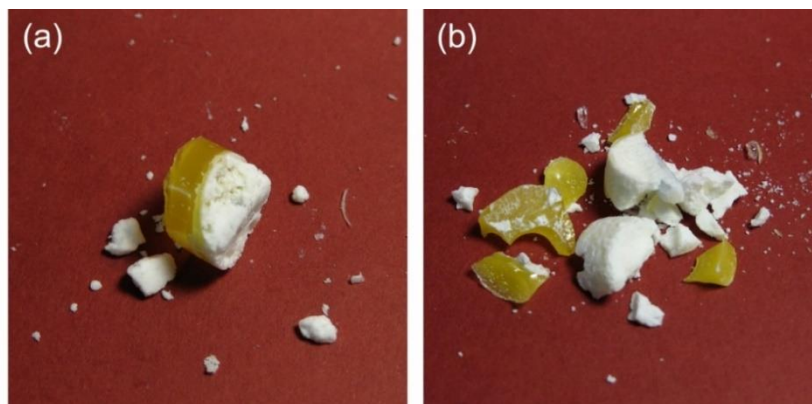


Figure 2.3 Photographs of the macrophase separation observed in samples that are (a) the product of polymerization of styrene and divinylbenzene in the presence of free CTA and no PEO-CTA and (b) the product of polymerization of styrene and divinylbenzene in the presence of free CTA and 5 kg mol^{-1} PEO-OH. These experiments indicate that domain connectivity achieved in the in situ synthesis of a diblock copolymer is necessary to produce a homogeneous structure. Sample sizes are of order 1 cm.

The morphology of PIMS PEMs were characterized using a combination of SAXS, SEM, and TEM. SAXS scattering profiles for samples prepared with 5 and 28 kg mol^{-1} ($w_{\text{PEO-CTA}} \approx 32 \text{ wt}\% \approx 30 \text{ vol}\%$) indicate that nanoscopic structural heterogeneities exist in PEMs prepared by this method (Figures 2.4). The broad principal scattering peak at low wavevector q , typical of microphase-separated but disordered block polymer structures, is accompanied by a secondary shoulder that becomes more pronounced as the ionic liquid concentration is increased. The development of diffuse higher order reflections indicates that the ionic liquid induces greater structural coherence on the length scale of two or more domains (ca. 5–15 nm). The characteristic length scale increases with increasing PEO molar mass, from 10–15 nm for samples prepared with 5 kg mol^{-1} PEO-CTA to 25–35 nm for samples prepared with 28 kg mol^{-1} PEO-CTA. Also, the position of the primary peak shifts to lower wavevector and becomes more intense with increasing ionic liquid content, which is consistent with the introduction of BMITFSI as a selective solvent for the PEO phase and a corresponding increase in the effective degree of segregation between the two domains.²⁴ Inclusion of the lithium salt LiTFSI results in enhanced contrast and possibly greater segregation of the domains as observed by the increases in intensity with increased

molarity of LiTFSI in BMITFSI at constant overall volume fraction of salt for both molar masses of PEO-CTA (Figure 2.5).

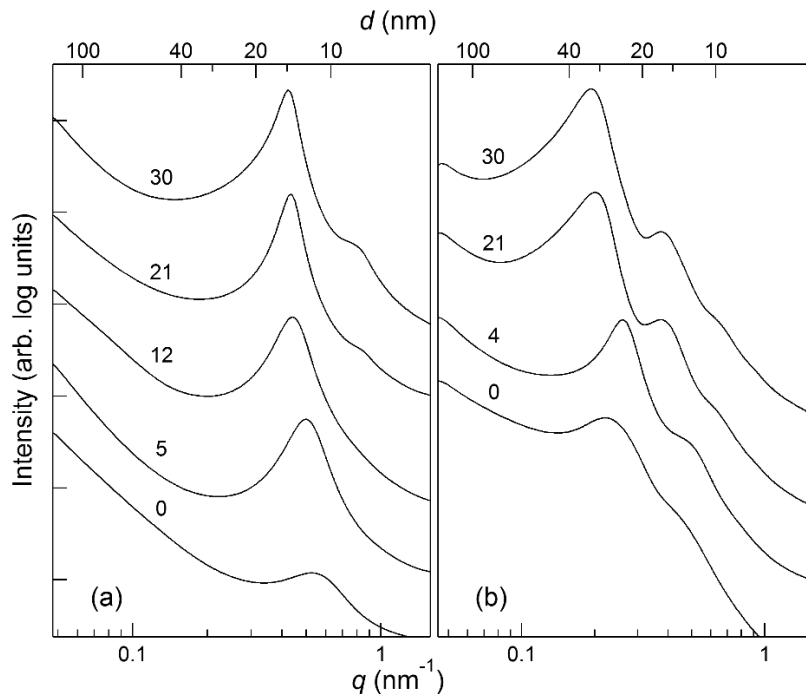


Figure 2.4 Small angle X-ray scattering data of polymer electrolyte membrane samples prepared with (a) 5 and (b) 28 kg mol⁻¹ PEO-CTA (32 wt%) and various concentrations of the ionic liquid BMITFSI. Domain size increases (the primary scattering peak shifts to lower q) with increasing PEO-CTA molar mass and increasing ionic liquid content (reported as overall vol%).

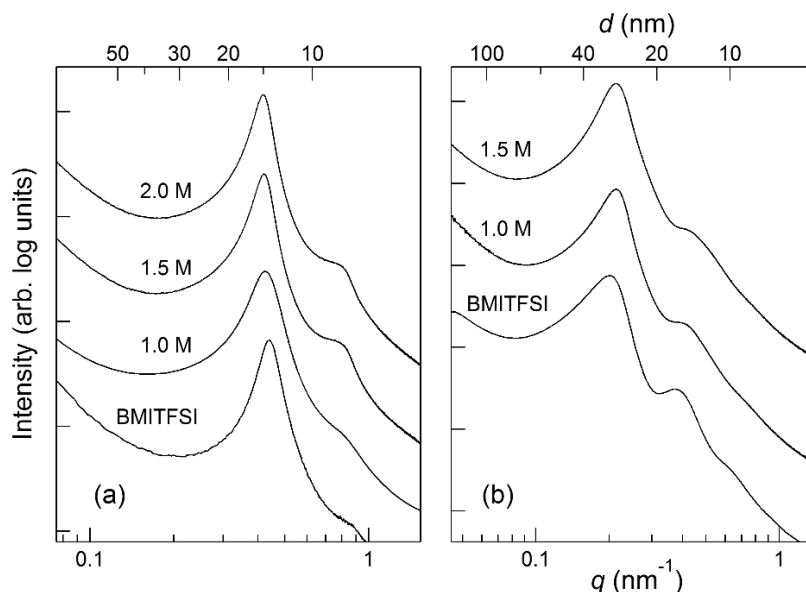


Figure 2.5 Small angle X-ray scattering data of polymer electrolyte membrane samples prepared with (a) 5 and (b) 28 kg mol⁻¹ PEO-CTA (32 wt%) and increasing concentrations of LiTFSI in the ionic liquid BMITFSI. The overall volume fraction of salt is 21 vol% in all samples.

A series of samples were also prepared with 42 wt% PEO-CTA using 5 kg mol⁻¹ PEO-CTA. Figure 2.6 shows that the obtained SAXS data are qualitatively similar to the samples prepared from 32 wt% PEO-CTA. Although these samples were not analyzed further, we anticipate that higher contents of PEO-CTA may enable larger quantities of ionic liquid to be introduced, thereby increasing the conductivity of the resulting PEM. However, increases in the conductivity by such means would lead to a commensurate loss of mechanical integrity as the volume fraction of the crosslinked phase is reduced. Within the compositional limits that allows sufficient continuity of both phases, i.e. a percolation threshold, concentration of PEO-CTA in the initial mixture may serve as an additional handle for tuning the properties of the electrolyte.

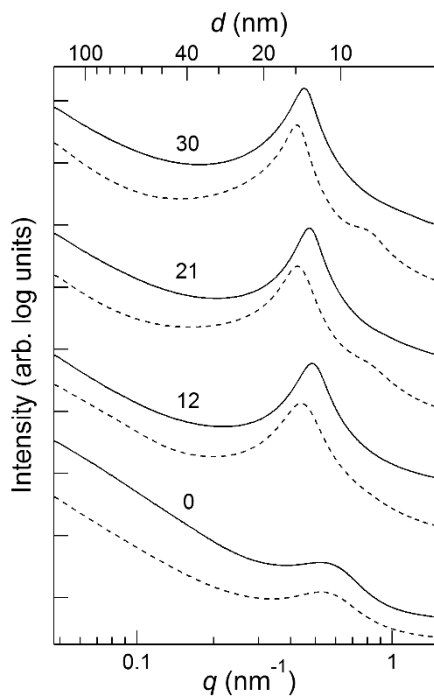


Figure 2.6 Comparison of PEM scattering profiles prepared using 5 kg mol^{-1} PEO-CTA at concentrations of 42 (solid lines) and 32 wt% (dashed lines) in the initial monomer mixture. Concentrations of BMITFSI are reported as overall vol% as indicated.

Exposure of a monolithic PIMS PEM sample to 57 wt% aqueous HI solution at 60°C resulted in quantitative etching of the PEO/IL composite domain, as confirmed gravimetrically and by IR analysis (Figure 2.7). As shown in Figure 2.8, a scanning electron microscopy (SEM) image of the resulting nanoporous structure mirrors the corresponding TEM image of the unetched sample. Figure 2.9 compares scanning electron micrographs of the etched and unetched samples, indicating that the topography observed after treatment with HI comes from the removal of the PEO/IL domain. In addition, analysis of Fourier transform data generated from TEM images are in agreement with SAXS intensity profiles, confirming that the TEM images are representative of the bulk morphology (Figure 2.10).

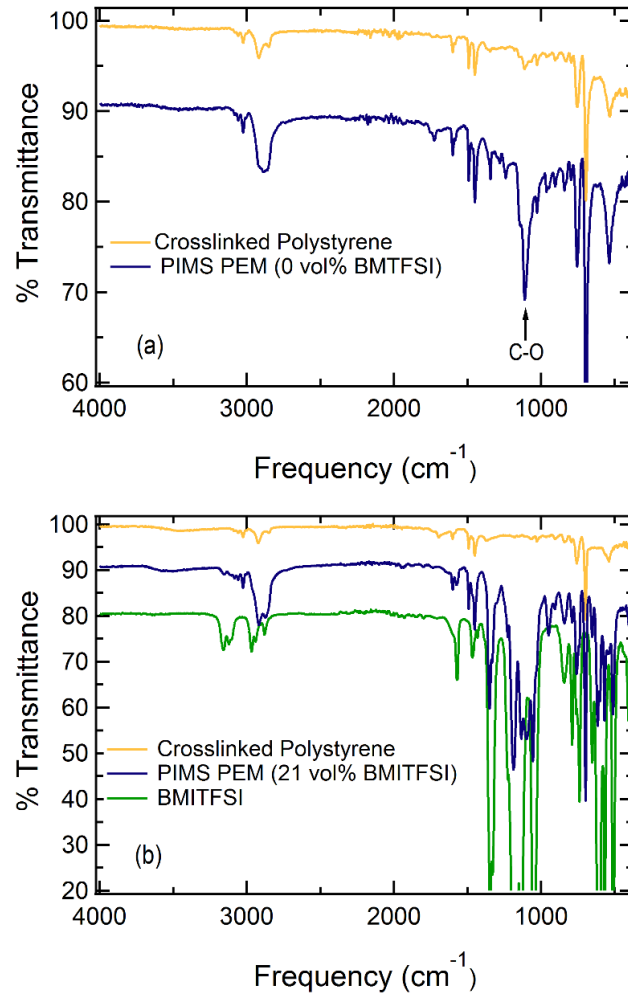


Figure 2.7 Representative FTIR spectra of PIMS PEM samples and ionic liquid BMITFSI. The crosslinked polystyrene sample is formed after the etching of PEO and BMITFSI with 57 wt% aqueous hydroiodic acid.

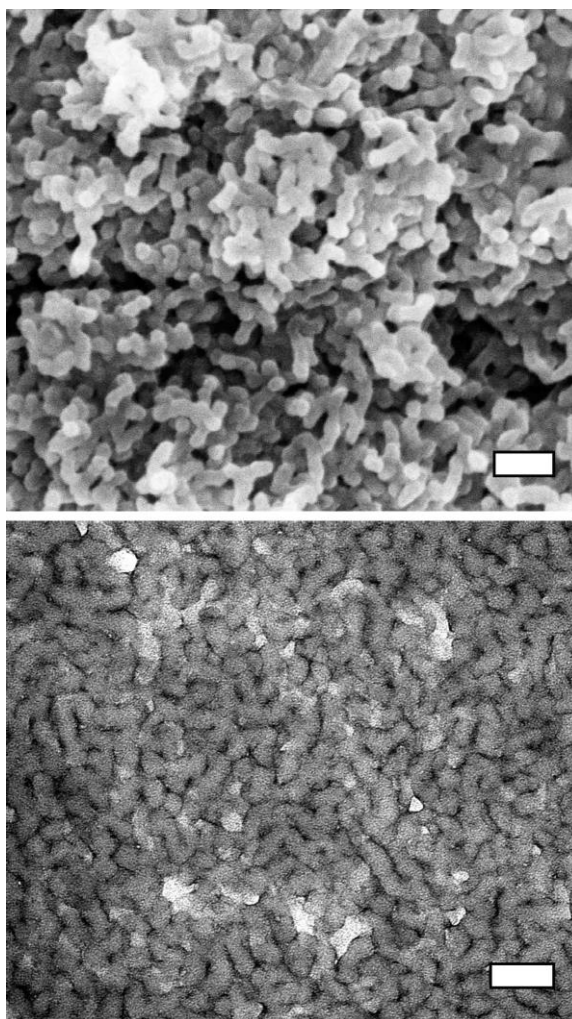


Figure 2.8 Morphology of PIMS PEM samples prepared with 28 kg mol^{-1} PEO-CTA and 21 vol% BMITFSI. Upper panel: Scanning electron micrograph of the sample after the etching of PEO and BMITFSI with 57 wt% aqueous hydroiodic acid. The remaining structure is crosslinked polystyrene. The sample was coated with 1-2 nm of Pt prior to imaging. Lower panel: Transmission electron micrograph of the same sample prior to etching. The PEO/ionic liquid domain appears dark after staining with RuO_4 . Both scale bars represent 100 nm.

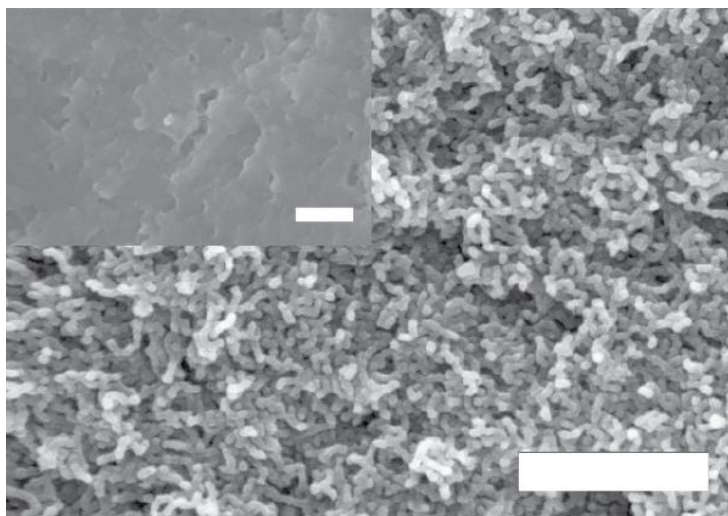


Figure 2.9 Scanning electron micrographs comparing a PIMS PEM sample prepared with 28 kg mol^{-1} PEO-CTA and 21 vol% BMITFSI, before (inset) and after (main panel) etching out PEO/IL with 57 wt% hydroiodic acid. Both samples were freeze-fractured to expose a fresh surface and were coated with 1–2 nm of Pt prior to imaging. Both scale bars represent 500 nm.

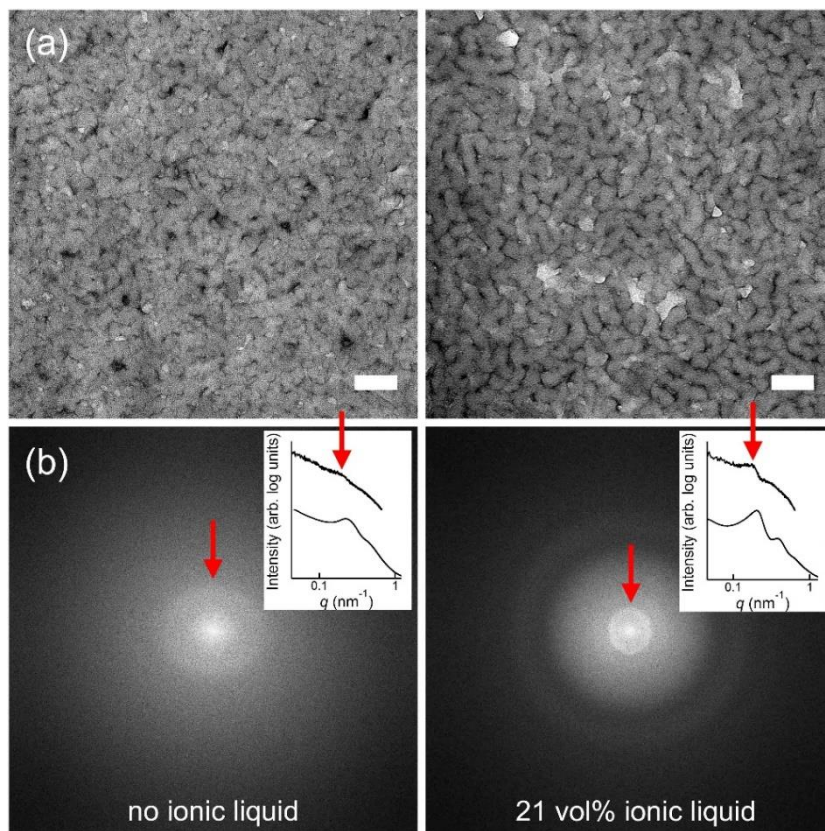


Figure 2.10 (a) Transmission electron micrographs of polymer electrolyte membrane samples prepared from 28 kg mol^{-1} PEO-CTA without ionic liquid and 21 vol% BMITFSI. RuO_4 staining of the PEO/ionic liquid phase was used to enhance contrast. The scale bars represent 100 nm. (b) The corresponding Fourier transform (FT) analysis of the TEM image above. Pixel intensity in the FTs was integrated azimuthally and plotted versus wavevector q in the inset. The upper curve is the integrated FT and the lower curve is the small-angle X-ray scattering (SAXS) data of the sample. The red arrow points to the feature in the FT that appears as a peak in the inset. The close agreement between peaks in the integrated FT and the SAXS data confirms that the TEM images accurately represent the bulk morphology.

Crystallinity has been shown to substantially reduce room temperature conductivity, thwarting broader application of analogous PS-PEO electrolytes.⁴ Importantly, as will be shown, no discontinuity of conductivity is observed at the melting transition of PEO in PIMS PEMs. Even though crystallinity is evident in the DSC chromatograms of Figure 2.11, retention of conductivity at low T is attributed to the relative increase in ion concentration in the amorphous phase that results from the formation of small, dispersed

crystallites that do not occlude ion mobility. Additionally, the DSC data illustrate the dominant interactions of BMITFSI and PEO as crystallinity is suppressed at high concentrations of ionic liquid. Combined, the SAXS, SEM, DSC and TEM analysis of the crosslinked PEM samples support a bicontinuous, nanostructured material with interpenetrating and percolating domains of crosslinked PS and IL-swollen PEO.

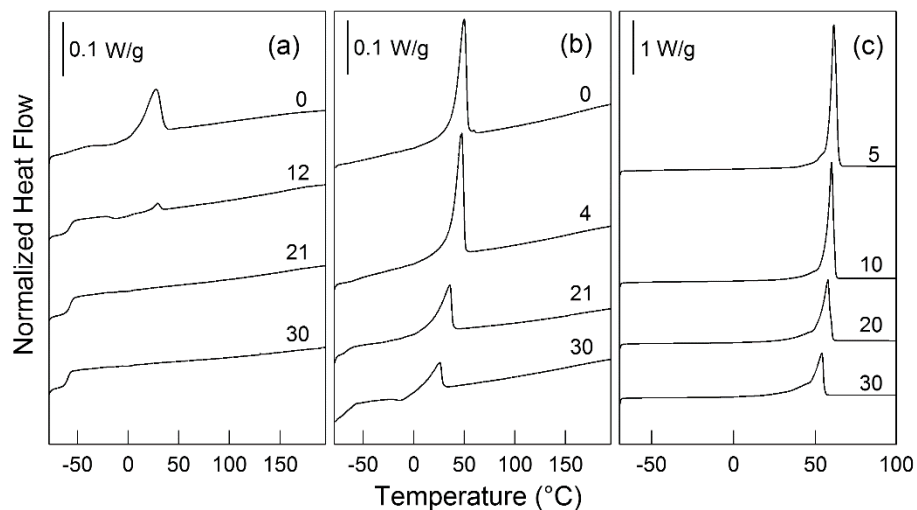


Figure 2.11 Differential scanning calorimetry thermograms (exo down) for PIMS PEMs prepared with (a) 5 kg mol^{-1} and (b) 28 kg mol^{-1} PEO-CTA (32 wt%) and various concentrations of the ionic liquid BMITFSI. (c) Mixture of homopolymer PEO ($M_n = 8 \text{ kg mol}^{-1}$) and BMITFSI. The presented traces were collected during the second heating at a ramp rate of $5 \text{ }^\circ\text{C/min}$.

Table 2.2 Thermal transitions of PIPS PEM and PEO homopolymer/BMITFSI electrolyte samples shown in Figure 2.5.

M_n PEO-CTA (kg mol ⁻¹)	BMITFSI Concentration ⁱ (vol%)	T_g (°C)	$T_{m,max}$ (°C)	crystallinity (wt%)
5	0	-52	26	25
5	12	-58	29	28
5	21	-58	-	-
5	30	-61	-	-
28	0	-	49	42
28	4	-	46	43
28	21	-66	35	32
28	30	-64	25	25
M_n PEO-OH ⁱⁱ				
8	5	-	61	80
8	10	-	60	68
8	20	-	58	52
8	30	-	54	43

ⁱOverall volume fraction of BMITFSI

ⁱⁱ M_{PEO} refers to PEO homopolymer

Ionic conductivity of the resulting PEMs was obtained from measurements of the bulk impedance from 30 to 150 °C (Figure 2.12). The data were fit with excellent agreement to the Vogel-Fulcher-Tammann (VFT) equation,

$$\sigma = \sigma_0 \exp\left(\frac{-B}{T - T_0}\right) \quad (2.1)$$

which describes relaxation processes above the T_g in glass-forming liquids.²⁵ Here, σ_0 is the conductivity at infinite temperature, B is a pseudo-activation energy related to the entropic barrier to ion motion, and T_0 is the temperature at which molecular motion is frozen. The increase in conductivity as ionic liquid concentration is increased, as shown in Figure 2.12, is due primarily to an increase in the number of carrier ions.

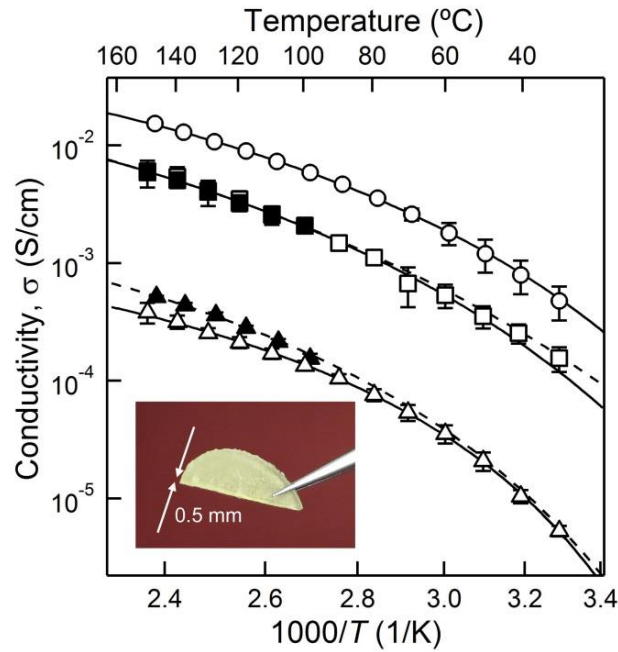


Figure 2.12 Ionic conductivity as a function of temperature for PEMs prepared with 5 kg mol^{-1} PEO-CTA. The inset is a photograph of a typical sample used for conductivity experiments. Open symbols: samples prepared with BMITFSI. Filled symbols: samples prepared with a 1 M mixture of LiTFSI in BMITFSI. Error bars (in some cases under the data points) are one standard deviation based on at least three samples. Overall salt concentrations are 5 (Δ), 7 (\blacktriangle), 21 (\square and \blacksquare), and 40 vol% (\circ). Parameters of the VFT fits are provided in Table 2.2.

Table 2.3 VFT Parameters for the conductivity profiles in Figure 2.6

type of salt	Composition (vol%)			σ_0 (S/cm)	B (K)	T_0 (K)
	salt	PEO + salt	salt in PEO + salt domain			
BMITFSI	40	59	67	0.59	884	178
BMITFSI	21	47	45	0.85	1333	152
BMI/LiTFSI	21	47	45	1.0	1467	136
BMITFSI	5	35	15	0.0064	749	223
BMI/LiTFSI	36	7	18	0.026	841	204

Conductivity is high in these PEMs and exceeds the critical benchmark of 1 mS/cm at 80 °C for the samples containing 21 vol% BMITFSI and 1 M LiTFSI in BMITFSI.¹⁵ The conductivity can be expressed as a fraction of the conductivity achieved in a homogeneous electrolyte of the same PEO/ionic liquid composition, σ_h , by³⁰⁻³²

$$\sigma = \sigma_h \frac{f_c}{\tau} \quad (2.2)$$

where f_c and τ are the volume fraction and the tortuosity of the conducting phase, respectively. Given various experimental studies of small molecule transport in cocontinuous, heterogeneous media (e.g., gas and water filtration through disordered pores,³²⁻³⁴ and tracer molecules in ordered block polymers in the gyroid phase),^{30,31} one expects τ to attain values between 1.5 and 3. As shown in Figure 2.13, the conductivities observed are consistent with Equation 2.2 and our anticipated range of τ , indicating that the conductive channels are continuous over macroscopic distances.

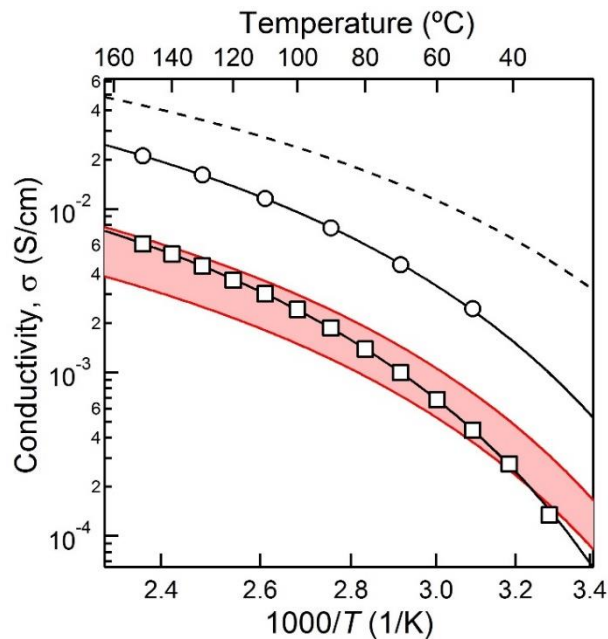


Figure 2.13 Conductivity in a heterogeneous PEM sample (\square) is reduced relative to a PEO/ionic liquid homogeneous electrolyte (\circ) of the same composition. The conductivity of pure BMITFSI (dashed line) is also shown for reference. The homogeneous electrolyte was prepared from an 8 kg mol^{-1} PEO homopolymer/BMITFSI mixture (50 vol%), and the heterogeneous PEM sample was prepared with 28 kg mol^{-1} PEO-CTA and BMITFSI at 21 overall vol%. In the conducting phase of the heterogeneous electrolyte, the resulting concentration of ionic liquid is 46 vol%. In both cases, only segmental motion contributes to ion transport.³⁵ The red region is defined by a tortuosity of 1.5 (upper bound) and 3 (lower bound).

The dynamic moduli, E' and E'' , of a representative PEM were determined as a function of frequency at temperatures up to 200 °C, and time-temperature superposition was used to generate master curves (Figure 2.14). Figure 2.15 compares E' at a fixed frequency (10 rad/s) of a representative PEM to a sample without ionic liquid in a pithy construction. The samples are glassy at room temperature and perform as high modulus solids ($\tan(\delta) = E''/E' < 0.1$) over the entire temperature range studied. The supporting crosslinked polystyrene phase allows for operation at temperatures above the glass transition temperature of a linear polystyrene-block analogue, where the conductivity can be above 10 mS/cm (Figure 2.12). Consistent with the decrease in the volume fraction of the high modulus phase, addition of ionic liquid to the PEO domain reduces E' by a factor of 2–3.

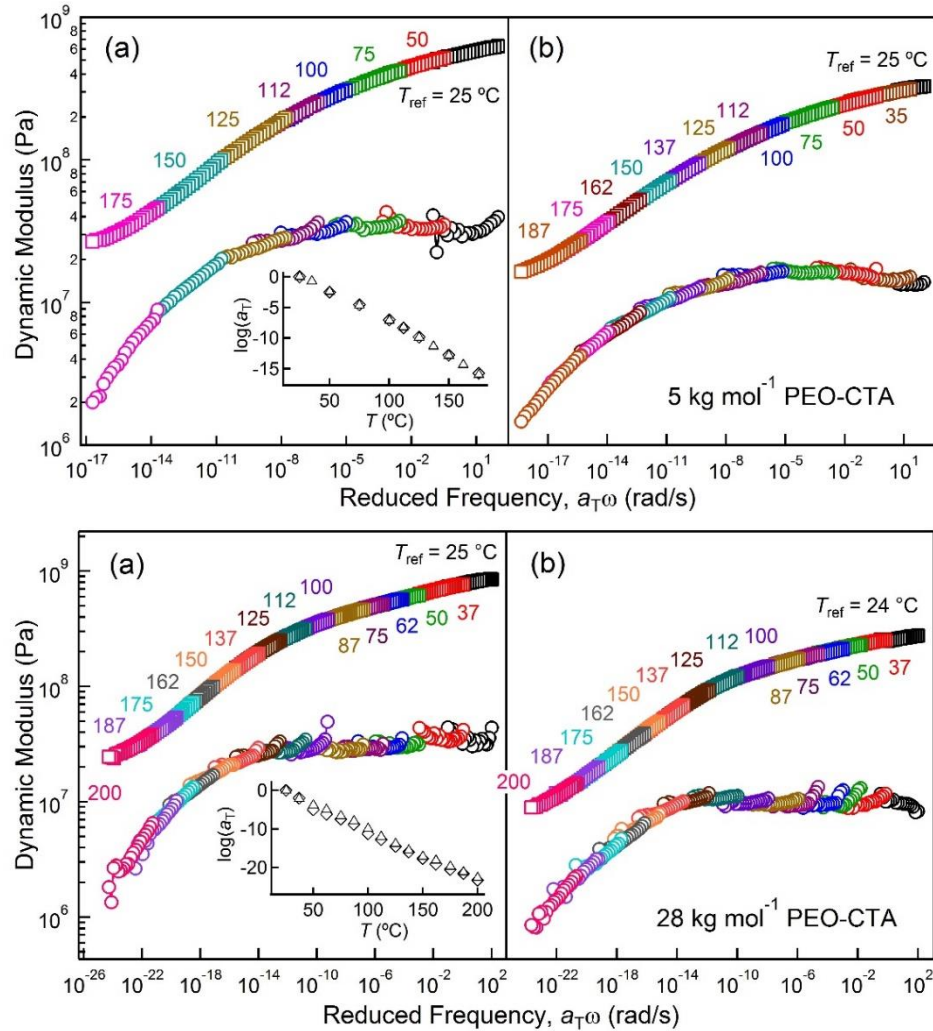


Figure 2.14 Linear viscoelastic master curves of representative polymer electrolyte membranes prepared from 5 kg mol^{-1} (upper) and 28 kg mol^{-1} (lower) PEO-CTA (a) without ionic liquid and (b) with 21 vol% BMITFSI. Frequency sweeps were collected from room temperature up to ca. $200 \text{ }^\circ\text{C}$. Colored numbers indicate the temperature of the corresponding frequency sweep. Data of (a) and (b) show the elastic modulus, E' (\square), and the viscous modulus, E'' (\circ), versus reduced frequency, $a_T\omega$, for samples without ionic liquid and samples containing 21 vol% BMITFSI, respectively. The inset graphs display the temperature-dependent shift factors, a_T , for the sample without ionic liquid (\triangle) and the sample with 21 vol% BMITFSI (\diamond).

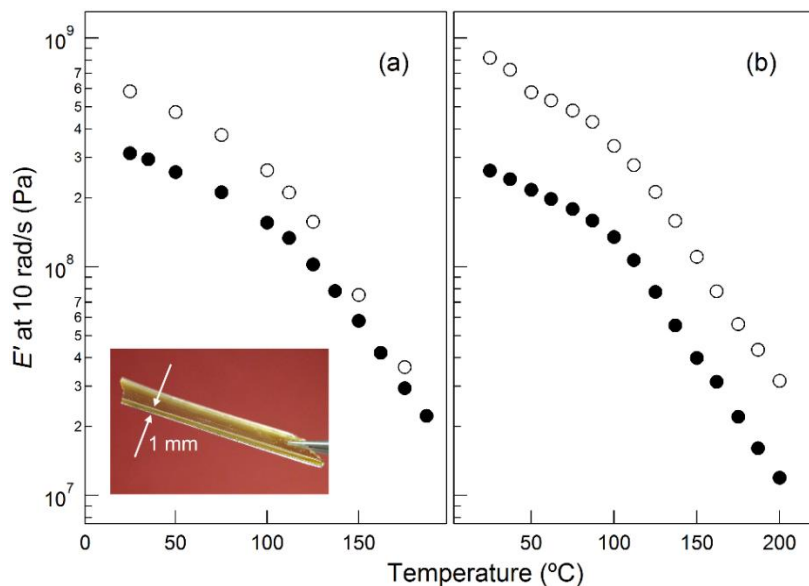


Figure 2.15 Temperature dependent linear elastic response of PIMS PEMs prepared with (a) 5 and (b) 28 kg mol⁻¹ PEO-CTA without ionic liquid (○) and with 21 vol% BMITFSI (●). The inset is a photograph of a typical tensile bar used. The data points are the elastic modulus, E' , at 10 rad/s and were extracted from isothermal frequency sweeps.

2.4 Conclusions

The preparation of polymeric networks swollen with a high fraction of ionic liquid (“ion gels”) by ABA copolymer self-assembly^{23,36-38} or by direct polymerization of monomer and crosslinker³⁹ affords some tunability of the modulus, but due to the lack of continuity of the high modulus domain, these are soft solids ($E' \leq 10^4$ Pa). Although ion gels can be easily processed in the liquid state and solidified *in situ*, increasing the modulus typically results in reduction of the ionic conductivity, illustrating the nontrivial dependence of both properties on the segmental relaxation of polymer chains. On the other hand, PEMs composed predominantly of polymer, such as the isotropically-oriented lamellae from PS-*b*-PEO and lithium bis(trifluoromethylsulfonyl)imide (LiTFSI), achieve sufficient continuity of both the conductive and glassy domains such that the modulus and conductivity can be decoupled.¹⁴ However, both modulus and conductivity fall short of the target region ($E' \approx 1$ GPa, $\sigma \geq 1$ mS/cm) because (i) grain boundaries and lack of domain

continuity reduce ion mobility, and (ii) the glassy modulus is reduced with progressive increases in temperature and suffers a precipitous drop above the glass transition of polystyrene ($T_g \approx 100\text{ }^\circ\text{C}$). Furthermore, diblock-based electrolytes are prepared from multi-step processes involving synthesis, isolation, and solution-casting, and generally exhibit rather low toughness.⁴⁰⁻⁴² In this work, the important contribution to the generation and application of solid-state electrolytes is a process that marries the processability and synthetic simplicity of a liquid precursor with the independent tunability of mechanical and mass transport properties offered by a nanostructured block polymer. The result is a material that achieves record combinations of modulus and conductivity at high temperature (Figure 2.16). This approach is very promising for the scalable production of PEMs for critical energy applications such as solid-state lithium ion batteries and high temperature fuel cells.

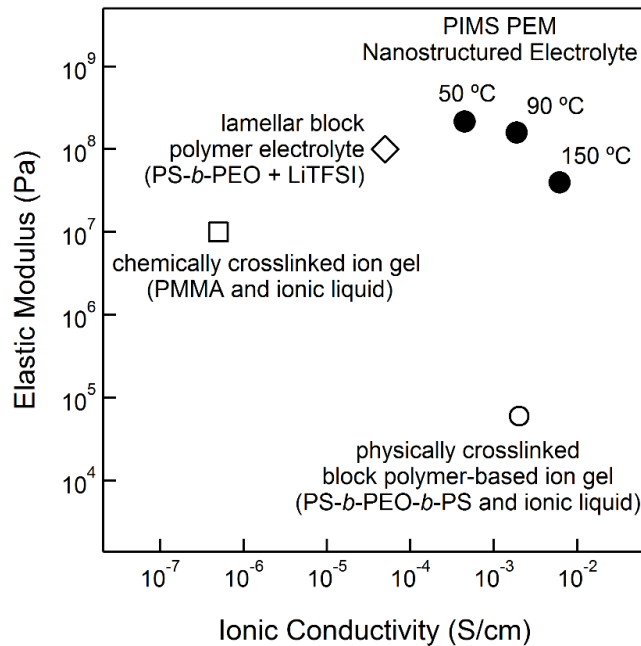


Figure 2.16 The trade-off relationship between elastic modulus and ionic conductivity in a solid electrolyte is illustrated using data from refs 14 (\diamond), 23 (\circ), and 33 (\square). Data represented by (\bullet) are from this study. All data are reported at 90 °C, unless otherwise noted. Only chemically crosslinked electrolytes remain solid at elevated temperature (> 90 °C), where conductivity is maximized.

2.5 References

- (1) Hallinan, D. T.; Balsara, N. P. *Annual Review of Materials Research* **2013**, *43*, 503.
- (2) Steele, B. C. H.; Heinzl, A. *Nature* **2001**, *414*, 345.
- (3) Tarascon, J. M.; Armand, M. *Nature* **2001**, *414*, 359.
- (4) Young, W.-S.; Kuan, W.-F.; Epps, T. H. *Journal of Polymer Science Part B: Polymer Physics* **2014**, *52*, 1.
- (5) Goodenough, J. B.; Park, K.-S. *Journal of the American Chemical Society* **2013**, *135*, 1167.
- (6) Goodenough, J. B.; Kim, Y. *Chemistry of Materials* **2009**, *22*, 587.
- (7) Noda, A.; Susan, M. A. B. H.; Kudo, K.; Mitsushima, S.; Hayamizu, K.; Watanabe, M. *The Journal of Physical Chemistry B* **2003**, *107*, 4024.
- (8) Nakamoto, H.; Watanabe, M. *Chemical Communications* **2007**, 2539.
- (9) Hoarfrost, M. L.; Tyagi, M. S.; Segalman, R. A.; Reimer, J. A. *Macromolecules* **2012**, *45*, 3112.
- (10) Monroe, C.; Newman, J. *Journal of The Electrochemical Society* **2005**, *152*, A396.
- (11) Monroe, C.; Newman, J. *Journal of The Electrochemical Society* **2004**, *151*, A880.
- (12) Monroe, C.; Newman, J. *Journal of The Electrochemical Society* **2003**, *150*, A1377.
- (13) Hallinan, D. T.; Mullin, S. A.; Stone, G. M.; Balsara, N. P. *Journal of The Electrochemical Society* **2013**, *160*, A464.
- (14) Singh, M.; Odusanya, O.; Wilmes, G. M.; Eitouni, H. B.; Gomez, E. D.; Patel, A. J.; Chen, V. L.; Park, M. J.; Fragouli, P.; Iatrou, H.; Hadjichristidis, N.; Cookson, D.; Balsara, N. P. *Macromolecules* **2007**, *40*, 4578.
- (15) Choi, I.; Ahn, H.; Park, M. J. *Macromolecules* **2011**, *44*, 7327.
- (16) Choi, J. H.; Ye, Y. S.; Elabd, Y. A.; Winey, K. I. *Macromolecules* **2013**, *46*, 5290.
- (17) Virgili, J. M.; Hoarfrost, M. L.; Segalman, R. A. *Macromolecules* **2010**, *43*, 5417.
- (18) Young, W.-S.; Epps, T. H. *Macromolecules* **2012**, *45*, 4689.
- (19) Weber, R. L.; Ye, Y.; Schmitt, A. L.; Banik, S. M.; Elabd, Y. A.; Mahanthappa, M. K. *Macromolecules* **2011**, *44*, 5727.

- (20) Scalfani, V. F.; Wiesenauer, E. F.; Ekblad, J. R.; Edwards, J. P.; Gin, D. L.; Bailey, T. S. *Macromolecules* **2012**, *45*, 4262.
- (21) Majewski, P. W.; Gopinadhan, M.; Jang, W.-S.; Lutkenhaus, J. L.; Osuji, C. O. *Journal of the American Chemical Society* **2010**, *132*, 17516.
- (22) Seo, M.; Hillmyer, M. A. *Science* **2012**, *336*, 1422.
- (23) Zhang, S.; Lee, K. H.; Frisbie, C. D.; Lodge, T. P. *Macromolecules* **2011**, *44*, 940.
- (24) Simone, P. M.; Lodge, T. P. *ACS Applied Materials & Interfaces* **2009**, *1*, 2812.
- (25) Lai, J. T.; Filla, D.; Shea, R. *Macromolecules* **2002**, *35*, 6754.
- (26) Rzyayev, J.; Hillmyer, M. A. *Journal of the American Chemical Society* **2005**, *127*, 13373.
- (27) Tokuda, H.; Hayamizu, K.; Ishii, K.; Susan, M. A. B. H.; Watanabe, M. *The Journal of Physical Chemistry B* **2004**, *108*, 16593.
- (28) Tokuda, H.; Hayamizu, K.; Ishii, K.; Susan, M. A. B. H.; Watanabe, M. *The Journal of Physical Chemistry B* **2005**, *109*, 6103.
- (29) Car, A.; Stropnik, C.; Yave, W.; Peinemann, K.-V. *Advanced Functional Materials* **2008**, *18*, 2815.
- (30) Hamersky, M. W.; Hillmyer, M. A.; Tirrell, M.; Bates, F. S.; Lodge, T. P.; von Meerwall, E. D. *Macromolecules* **1998**, *31*, 5363.
- (31) Milhaupt, J. M.; Lodge, T. P. *Journal of Polymer Science Part B: Polymer Physics* **2001**, *39*, 843.
- (32) Cussler, E. L. *Diffusion : Mass Transfer in Fluid Systems*; 3rd ed.; Cambridge University Press: Cambridge, UK, 2009.
- (33) Phillip, W. A.; Amendt, M.; O'Neill, B.; Chen, L.; Hillmyer, M. A.; Cussler, E. L. *ACS Applied Materials & Interfaces* **2009**, *1*, 472.
- (34) Chen, L.; Phillip, W. A.; Cussler, E. L.; Hillmyer, M. A. *Journal of the American Chemical Society* **2007**, *129*, 13786.
- (35) Teran, A. A.; Tang, M. H.; Mullin, S. A.; Balsara, N. P. *Solid State Ionics* **2011**, *203*, 18.

-
- (36) Gu, Y.; Zhang, S.; Martinetti, L.; Lee, K. H.; McIntosh, L. D.; Frisbie, C. D.; Lodge, T. P. *Journal of the American Chemical Society* **2013**, *135*, 9652.
- (37) Zhang, S.; Lee, K. H.; Sun, J.; Frisbie, C. D.; Lodge, T. P. *Macromolecules* **2011**, *44*, 8981.
- (38) Tang, B.; White, S. P.; Frisbie, C. D.; Lodge, T. P. *Macromolecules* **2015**, *48*, 4942.
- (39) Susan, M. A. B. H.; Kaneko, T.; Noda, A.; Watanabe, M. *Journal of the American Chemical Society* **2005**, *127*, 4976.
- (40) Bates, F. S.; Hillmyer, M. A.; Lodge, T. P.; Bates, C. M.; Delaney, K. T.; Fredrickson, G. H. *Science* **2012**, *336*, 434.
- (41) Hermel, T. J.; Hahn, S. F.; Chaffin, K. A.; Gerberich, W. W.; Bates, F. S. *Macromolecules* **2003**, *36*, 2190.
- (42) Hermel, T. J.; Wu, L.; Hahn, S. F.; Lodge, T. P.; Bates, F. S. *Macromolecules* **2002**, *35*, 4685.

Chapter 3

Evolution of Morphology, Modulus, and Conductivity in Polymer Electrolytes Prepared via Polymerization-Induced Microphase Separation^{†,‡}

Polymer electrolytes are alternatives to liquid electrolytes traditionally used in electrochemical devices such as lithium-ion batteries and fuel cells. In particular, block polymer electrolytes are promising candidates because they self-assemble into well-defined microstructures, in which orthogonal properties can be integrated into a single material (e.g., high modulus in domain A, fast ion transport in domain B). However, the performance of block polymer electrolytes often falls short, due to the lack of long-range continuity of both domains, and relatively low strength. Chapter 2 described a simple, one-pot synthetic strategy to prepare polymer electrolytes with the highest reported combination of modulus and ionic conductivity, attributes enabled by a co-continuous, crosslinked network morphology. In this chapter we aim to understand the mechanism by which this nanoscale morphology is formed by performing a series of in situ, time-resolved experiments — small-angle X-ray scattering, conductivity, rheology, and reaction kinetics — to monitor the electrolyte as it transitions from a macroscopically homogeneous liquid to a microphase-separated solid. The results suggest that the chain connectivity of the diblock gives rise to isotropic concentration fluctuations that increase in amplitude and coherence such that the network morphology is ultimately produced. The kinetic trapping of this network morphology by chemical crosslinking prior to the ordering transition is shown to be critically important to the resulting advantageous bulk electrolyte properties.

[†] This work was done in collaboration with Lucas D. McIntosh, Matthew T. Irwin and Timothy P. Lodge.

[‡] Reproduced with permission from McIntosh, L. D.;* Schulze, M. W.;* Irwin, M. T.; Hillmyer, M. A.; Lodge, T. P. *Macromolecules* **2015**, *48*, 1418–1428. Copyright 2015 American Chemical Society. (* Contributed equally)

3.1 Introduction

Polymer electrolytes^{1,2} are promising candidates to replace the small molecule, volatile solvents currently used in electrochemical devices such as lithium-ion batteries and fuel cells. Relative to liquid electrolytes, solid-state polymer electrolytes offer the advantage of mechanical integrity and can mitigate application-specific challenges such as dendrite growth in lithium-ion batteries³⁻⁷ or long-term creep in fuel cells.⁸ Independent of the application, the key challenge is to design polymer electrolytes that maximize ionic conductivity while simultaneously optimizing a mechanical property, such as modulus, fracture toughness, or creep resistance. To overcome this barrier, the polymer electrolyte community has recently focused on block polymers. For example, block polymer electrolytes can be designed to self-assemble into well-defined morphologies that exhibit both a glassy, insulating domain and a low- T_g , ion-conducting domain.⁹⁻¹⁸ Unfortunately, the measured conductivity of block polymer electrolytes is often compromised because network defects (e.g., dead ends at grain boundaries^{19,20}) in the conducting pathways increase resistance to ion transport.^{11,16,21} Additionally, although diblock-based electrolytes can exhibit relatively high moduli, they cannot compete with the toughness or high temperature stability of multiblock or crosslinked materials.^{22,23}

We recently reported a significant advance in the design of mechanically robust, high conductivity polymer electrolyte membranes (PEMs) for use in electrochemical energy storage and conversion devices.²⁴ As shown in Figure 3.1, PEMs were prepared in a simple and versatile one-pot synthetic scheme — termed polymerization-induced phase separation, or PIMS — by direct incorporation of salt into an easily processable liquid reaction mixture. The resulting PEMs exhibit an unprecedented combination of high conductivity (> 1 mS/cm at $T > 80$ °C) and high modulus (> 0.1 GPa for $T < 125$ °C) owing to the long-range, co-continuity of poly(ethylene oxide)/ionic liquid domains and highly crosslinked polystyrene domains. The liquid reaction precursor solidifies in situ by simply heating to 120 °C, allowing substantial flexibility in tailoring the sample geometry to the needs of a particular experiment or application. Furthermore, the wide parameter space that produces PEMs with the desired bicontinuous microstructure allows substantial flexibility

when choosing the identity and concentration of the salt and the concentration and molar mass of the ion-conducting block.

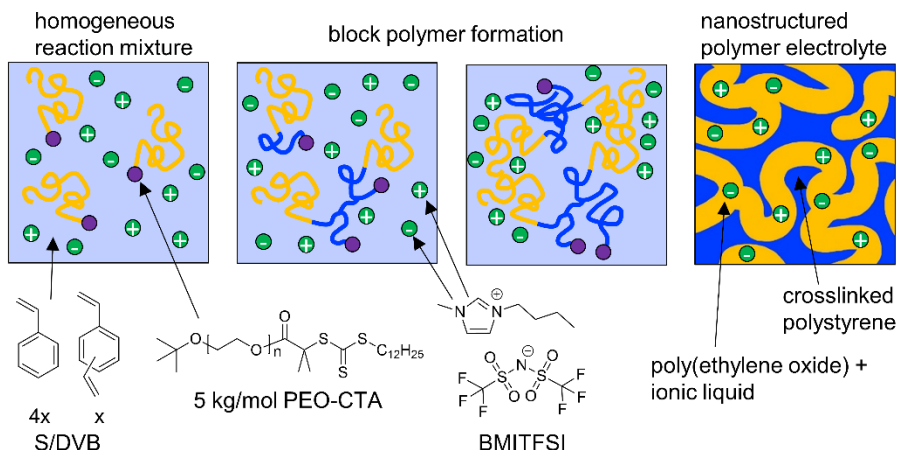


Figure 3.1 Schematic of the polymerization-induced phase separation (PIMS) strategy used to prepare polymer electrolyte membranes. Initially, a macro-CTA of poly(ethylene oxide) (yellow) is dissolved in a mixture of multifunctional monomers (light blue) and BMITFSI (green). RAFT copolymerization allows the growth of chains (dark blue) generating a block polymer architecture. Concerted in situ crosslinking arrests the emergent co-continuous structure, with percolating composite domains of PEO/BMITFSI and a mechanically robust, crosslinked polystyrene matrix.

The chemistry and microstructure of the resultant PEMS are illustrated schematically in Figure 3.1. The liquid reaction precursor is a quaternary mixture of monomer (styrene (S) and divinylbenzene (DVB)), poly(ethylene oxide) macro chain-transfer agent (PEO-CTA), and the ionic liquid (IL) 1-butyl-3-methylimidazolium bis(trifluoromethylsulfonyl)imide (BMITFSI). This liquid precursor exhibits relatively low viscosity (ca. 25 cP at room temperature) and is macroscopically homogeneous at the reaction temperature of 120 °C. Radical generation is effected by both thermal auto-initiation of styrene and homolysis of initiator. The P(S-*co*-DVB) block then grows from the PEO-CTA via reversible addition-fragmentation chain-transfer (RAFT) polymerization, in which chemical crosslinking occurs by incorporation of DVB.

Ultimately, the sample exhibits a microphase-separated morphology that lacks long-range, periodic order, as previously confirmed by a combination of small-angle X-ray

scattering (SAXS) and real space imaging (TEM and SEM).²⁴ The morphology is characterized by co-continuous networks of glassy, highly crosslinked polystyrene (P(S-*co*-DVB)) and an ion-conducting domain of poly(ethylene oxide)/ionic liquid (PEO/IL). This interpretation was supported by analyses of conductivity and calorimetry data, which indicate that during the course of the polymerization the majority of the BMITFSI segregates to the PEO-rich domains. Importantly, the PEO conducting domains are predominantly continuous, enabling ionic conductivity that achieves the theoretical maximum. The macroscopic mechanical response is, in turn, dominated by the highly crosslinked P(S-*co*-DVB) phase, which imparts both a glassy modulus and superior toughness at room temperature. PIMS PEMs also exhibit exceptional mechanical stability at high temperature ($G' \geq 10^7$ Pa at $T \leq 200$ °C) compared to linear PEO-*b*-PS electrolytes, which suffer a precipitous drop in elastic modulus above 100 °C.

The focus of the work presented here is the structural evolution through which PIMS generates the nanoscale morphology that governs the macroscopic PEM properties. The goal is to build a mechanistic understanding of how these PEMs transition from a homogeneous liquid reaction mixture to a high modulus solid that exhibits co-continuous networks of ion-conducting poly(ethylene oxide)/ionic liquid channels and crosslinked polystyrene. To this end, a series of in situ, time-resolved experiments were performed to measure reaction kinetics, ionic conductivity, modulus, and morphological development during the PIMS reaction.

3.2 Experimental Section

3.2.1 Materials

Sample preparation for in situ experiments followed the same protocol as previously reported.²⁴ Briefly, the liquid reaction mixture was prepared as a 32 wt% solution of a 5 kg/mol poly(ethylene oxide) macro chain-transfer agent (PEO-CTA) in a monomer mixture of styrene (S) and divinylbenzene (DVB) (4/1 molar ratio S/DVB). Previous studies have found that the resulting morphology is largely insensitive to the initial ratio of monomer to PEO-CTA. To prepare electrolytes, the ionic liquid 1-butyl-3-

methylimidazolium bis(trifluoromethylsulfonyl)imide (BMITFSI) was added to the PEO-CTA + S/DVB stock solution at two concentrations, 21 and 30 overall vol%. Samples prepared without ionic liquid are referred to as “neat”. Table 3.1 summarizes the resulting concentration of all species in the reaction mixtures for samples used in this study. Unless otherwise noted, samples were synthesized with the inclusion of azobisisobutyronitrile (AIBN) in the initial mixture at 0.05 *eq* to PEO-CTA.

Table 3.1 Composition (vol%) of polymer electrolyte samples. Data shown is obtained from study of the 21 vol% BMITFSI sample except where indicated.

BMITFSI	PEO-CTA ⁱ	S/DVB ⁱⁱ
0	32	68
21	25	54
30	22	48

ⁱ $M_{\text{PEO-CTA}} = 5 \text{ kg/mol}$

ⁱⁱMolar ratio of S/DVB = 4/1

3.2.2 Kinetics and Molar mass Evolution

Polymerization kinetics of styrene and divinylbenzene were investigated under the conditions utilized in the preparation of PIMS PEMs. A stock solution of S/DVB monomer, PEO-CTA, AIBN, and BMITFSI (21 vol%) was distributed into a series of vials that were simultaneously heated to 120 °C to initiate the polymerization. At various time points, the reaction was stopped by immersing the vial in liquid nitrogen. Each vial was then allowed to warm to room temperature, and ca. 1.5 mL of chloroform with *tert*-butyl catechol inhibitor was added to the reaction mixture to prevent further reaction and to ensure that all of the reaction mixture was transferred for precipitation. The dissolved solids were precipitated in hexanes, recovered by gravity filtration, and rigorously dried under dynamic vacuum (< 100 mTorr) at elevated temperature (> 80 °C) for several days. Soluble polymer recovered at early times was further characterized by size exclusion chromatography (SEC), performed using THF as the mobile phase at room temperature and a flow rate of 1 mL/min. Eluents were monitored by a Wyatt Optilab T-rEX refractive index detector. Molar mass and molar mass dispersity was determined based on a 12-point

calibration curve using polystyrene standards (Agilent Technologies). $^1\text{H-NMR}$ spectroscopy of the soluble polymers was conducted in deuterated chloroform using a Bruker Avance III HD 500 MHz spectrometer. Chemical shifts were referenced from tetramethylsilane (TMS) at 0.00 ppm.

3.2.3 Small-angle X-ray Scattering (SAXS)

Small angle X-ray scattering experiments were performed at the Argonne National Laboratory Advanced Photon Source, sectors 5-ID-D and 12-ID-B. Samples of the liquid reaction mixture were flame-sealed in boron-rich capillary tubes (Charles Supper Company). The capillaries were maintained at $-10\text{ }^\circ\text{C}$ to suppress radical formation and were warmed to room temperature shortly before the experiment. Samples were loaded in a Linkam heating stage, and the temperature was set to $120\text{ }^\circ\text{C}$. A thermocouple placed in the sample holder indicated that the temperature was within $\pm 1\text{ }^\circ\text{C}$ of the set point. Scattering data were collected at discrete time points during the PIMS reaction. Typical exposure times were of order 1 s. 2D scattering patterns were recorded on a Pilatus 2M area detector, and were isotropic in all cases. The sample-to-detector distance was calibrated with a silver behenate standard. Intensity was not reduced to absolute units; however, because the sample thicknesses were comparable and the intensities normalized by the exposure time, the intensities in relative units can be compared between samples. 2D data were reduced to intensity as a function of the magnitude of the wave vector $q = |\mathbf{q}| = 4\pi\sin(\theta/2)/\lambda$, where λ is the nominal X-ray wavelength and θ is the scattering angle.

3.2.4 Impedance Spectroscopy

Impedance spectroscopy was used to measure the bulk resistance of samples during the PIMS reaction, using a Solartron 1255B frequency response analyzer connected to a Solartron SI 1287 electrochemical interface. The conductivity cell was custom-built, within a three-neck, 25 mL round bottom flask. The two outer ports were plugged with rubber stoppers through which copper wires were inserted to connect the electrical leads. The sample electrodes were platinum wires soldered to the copper wire. The conductivity cell constant, κ , was calibrated with a known volume (typically 1 mL) of a 0.01 M KCl standard

(Fluka, 1.413 mS/cm at 25 °C). After calibration, the cell was washed 3–5 times with distilled water and dried at elevated temperature (> 80 °C) under dynamic vacuum (< 100 mTorr) for 1 d. A volume of sample equivalent to the calibration standard was loaded through the middle port, after which the port was sealed. The headspace was purged with argon for 20 min and finally pressurized with 5 psi argon. The conductivity cell held positive argon pressure throughout the course of the experiment. Impedance spectroscopy data collection began at room temperature, and the conductivity cell was immersed in an oil bath equilibrated at the reaction temperature of 120 °C. Ionic conductivity, σ , was calculated as $\sigma = \kappa/R$, where R is the bulk resistance as determined from the high-frequency plateau of the real part of impedance, Z' .

Conductivity was also measured for samples polymerized in standard glass vials. These monolithic samples were sanded down to uniform thickness (typically 0.5 mm) and dried at elevated temperature (> 80 °C) under dynamic vacuum (< 100 mTorr) for 1 d prior to measurement. The solid membranes were sandwiched between stainless steel electrodes, and impedance was measured as a function of temperature from 30 to 150 °C. These samples were measured in open atmosphere; we have previously determined that water uptake does not significantly impact the results for electrolytes containing the ionic liquid BMITFSI. For membrane samples, σ was calculated as $\sigma = l/Ra$, where l is the sample thickness and a is the superficial area.

3.2.5 Rheometry

The linear viscoelastic response was monitored during polymerization using oscillatory shear with a 40 mm diameter parallel plate geometry (TA Instruments AR-G2). Approximately 1 mL of liquid reaction precursor was loaded at room temperature on a Peltier plate for temperature control. Evaporation of styrene and divinylbenzene monomer was suppressed by enclosing the sample in a custom-built housing. The inside of the housing was lined with styrene monomer-soaked cotton to saturate the environment and further reduce monomer evaporation from the sample. Data collection was started at room temperature, and the sample was then heated over the course of 80 s to the reaction temperature of 120 °C for the duration of the experiment. Measurements of the elastic, G' ,

and viscous, G'' , moduli were performed at an angular frequency of 10 rad/s. As the sample stiffened, the strain amplitude was reduced to remain within the linear response regime.

3.3 Results

3.3.1 Reaction Kinetics and Molar mass Evolution

At early times, the RAFT-mediated polymerization of styrene and DVB using the macro chain transfer agent forms a mixture of highly asymmetric block polymer and monomer. Figure 3.2 shows the mass of solids recovered as the reaction proceeds in the presence of BMITFSI. At $t = 0$ min, the polymer collected prior to initiation should simply reflect the mass of PEO-CTA added to the reaction mixture (24 wt%). However, the recovered mass at $t = 0$ min is approximately 40% of the mass of the initial reaction mixture. The higher-than-expected mass yield could be attributed to the strong ion-dipole attractive interaction between PEO and BMI^+ cation, leading to the isolation of PEO solid wet with ionic liquid. The presence of BMITFSI was further confirmed using $^1\text{H-NMR}$ spectroscopy (Figure 3.3); the augmented mass yield can be accounted for by the calculated weight ratio of 1.2:1 PEO-CTA to BMITFSI, which reduces the estimated mass yield to 23% for PEO-CTA at $t = 0$ min.

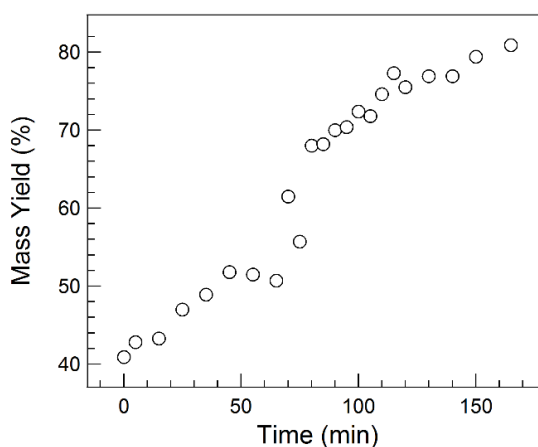


Figure 3.2 Polymerization time vs. mass yield in the polymerization of S and DVB (4/1) in the presence of PEO-CTA (25 vol%) and BMITFSI (21 vol%) at 120 °C.

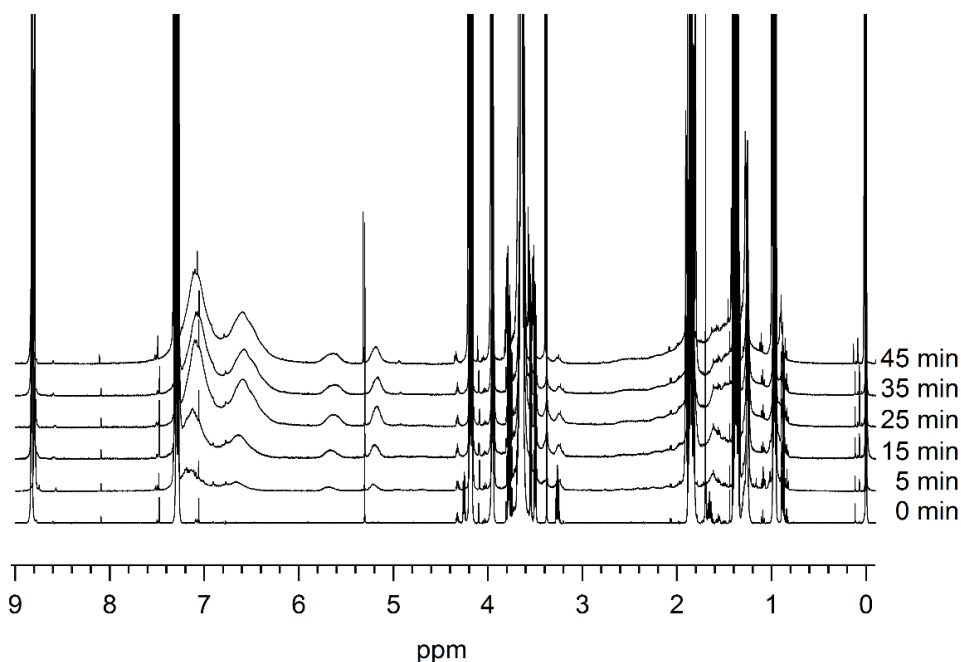


Figure 3.3 $^1\text{H-NMR}$ spectra (CDCl_3 , 500 MHz, 20 °C) of the soluble polymers obtained by precipitation in hexanes. The methine proton singlet of the imidazolium ring (8.8 ppm) and the broad multiplet of the PEO backbone (3.6 ppm) were used to calculate an approximate 1:1 weight ratio of PEO-CTA to BMITFSI in all isolated samples.

In general, the mass yield increases with time, indicating growth of the P(*S-co-DVB*) block. For $t \leq 45$ min, the solids recovered could be readily re-dissolved in THF for size exclusion chromatography analysis. For $t \geq 55$ min, small insoluble particulates were observed upon attempted dissolution in THF. The formation of these discrete flocs of crosslinked polymer, coincident with large increases in apparent molar mass via SEC, correlates with the rapid increase in the mass yield between 65 and 80 min. The SEC traces of Figure 3.4 are, in general, qualitatively indicative of the molar mass increases at early times (Table 3.2). The isolated solid at $t = 0$ min reproduces the narrow, monomodal trace of as-synthesized PEO-CTA. Within 5 min, a shoulder at lower elution volume emerges from the predominant peak of the SEC trace. This shoulder grows in intensity and indicates an increasing population of higher molar mass dimers formed by reaction through the pendant vinyl group of partially polymerized DVB.^{25,26} The distribution becomes broad

and multimodal because crosslinked, higher molar mass and remnant lower molar mass linear polymers coexist. This implicates the higher probability of coupled chains to participate in crosslinking because of the larger number of crosslinkable moieties (pendant DVB vinyl groups) relative to the uncrosslinked, linear polymer. As a result, crosslinked diblocks tend to grow more rapidly than linear diblocks, producing a mixture containing aggregates of large hydrodynamic volume that ultimately grow too large to dissolve. For comparison, a freely soluble, linear PS-*b*-PEO diblock was prepared without ionic liquid or DVB crosslinking agent, following three freeze-pump-thaw cycles. The resulting large molar mass and clear shift of the SEC trace for the linear diblock ($M_{n,NMR} = 39$ kg/mol, $\mathcal{D} = 1.30$) illustrates the utility of PEO-CTA to effect the growth of block polymer in the case of PIMS PEM preparation.

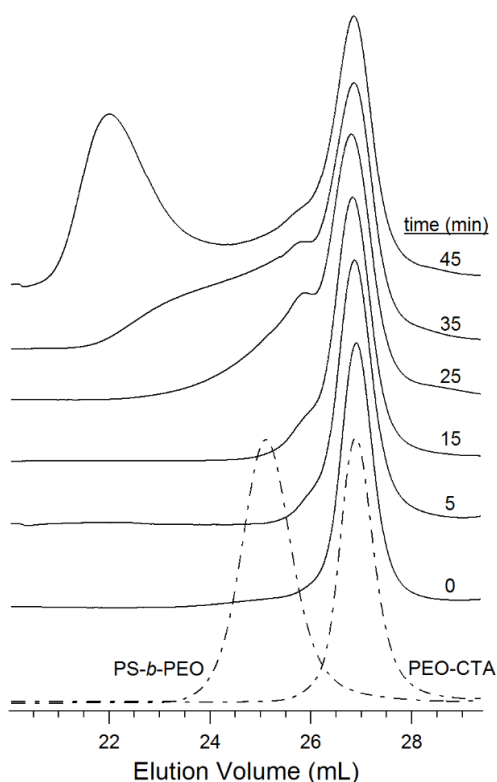
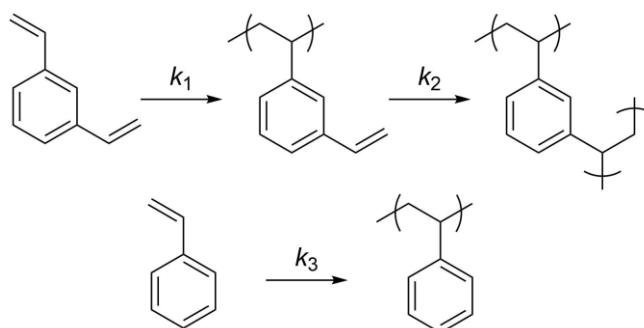


Figure 3.4 Progression of the size exclusion chromatograms of PEO-*b*-P(*S-co*-DVB) (solid) isolated at various times following initiation at $t = 0$ min. A separate polymerization (dash-dot) illustrates the utility of PEO-CTA in the controlled growth of linear of a PS-*b*-PEO diblock in the absence of crosslinker.

Table 3.2 Molar mass and dispersity for SEC traces in Figure 3.4

	PEO-CTA	PS- <i>b</i> -PEO	reaction time, <i>t</i> (min)					
			0	5	15	25	35	45
M_n (kg/mol)	6.9	26.5	7.2	7.3	7.2	9.0	9.5	14.7
\bar{D}	1.1	1.3	1.2	1.2	1.3	2.1	4.3	10.5

The ^1H NMR spectra of the soluble polymers (obtained by precipitation in hexanes) were analyzed to estimate the incorporation of repeat units of monomer per PEO-CTA. Each spectrum was normalized relative to the resonance of the methylene protons of PEO-CTA (3.6 ppm). The kinetics of polymerization were interpreted in terms of the proposed reactions of Scheme 3.1.

Scheme 3.1 Proposed reaction kinetics for polymerization of DVB and Styrene

The contributions of polymerized styrene, [PS], DVB with a pendant vinyl group, [DVB₁], and DVB with both vinyl groups polymerized, [DVB₂], to the integral of the aromatic protons (7.2–6.2 ppm) ($I_{\text{Ar-H}}$) can be expressed as:

$$I_{\text{Ar-H}} = 5[\text{PS}] + 4[\text{PDVB}_1] + 4[\text{PDVB}_2] \quad (3.1)$$

[PDVB₁] can be obtained from the integral of vinylic protons (5.2 ppm) ($I_{\text{vinyl-H}}$).

$$[\text{PDVB}_1] = I_{\text{vinyl-H}} \quad (3.2)$$

The rate of formation and consumption of [PDVB₁] is treated as an elementary series reaction of pseudo-first order with rate constants k_1 and k_2 , respectively:

$$[\text{PDVB}_1] = 2k_1/(k_2-2k_1)[\text{DVB}]_{\text{ini}}(\exp(-2k_1t)-\exp(-k_2t)) \quad (3.3)$$

[DVB]_{ini} is the initial number of DVB monomers per PEO-CTA obtained from the integral of the vinyl protons in the spectrum of the polymerization mixture at $t = 0$, assuming DVB is pure (no ethylstyrene) and the molar ratio of S/D is 4/1. Because k_1 and k_2 are estimated using Equation 3.3 and the experimentally obtained [PDVB₁], [PDVB₂] can be calculated according to:

$$d[\text{PDVB}_2]/dt = k_2[\text{PDVB}_1] \quad (3.4)$$

Equation 3.1 can then be used to determine [PS]. The concentration of each species is depicted in Figure 3.5 and summarized in Table 3.3. The fit of [PS] is calculated using a pseudo-first order rate constant, k_3 , for the consumption of styrene. Table 3.3 also provides estimates for the average molar mass of a theoretical linear polystyrene block per PEO-CTA. Table 3.4 provides the rate constants obtained from fitting the data of Figure 3.5.

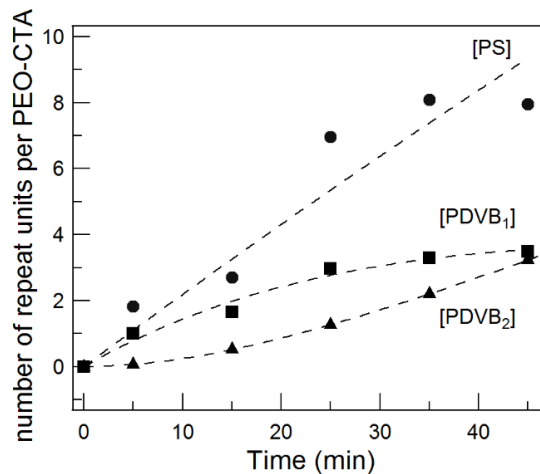


Figure 3.5 Number of repeat units per PEO-CTA represented as [PS] (circle), [PDVB₁] (square), and [PDVB₂] (triangle) versus polymerization time that were calculated from the respective contributions to the total aryl and vinyl concentration. The dashed lines indicate fits using the analytical model of a series reaction for the polymerization kinetics.

Table 3.3 Calculation of the number of styrene and DVB repeat units polymerized per PEO-CTA from $^1\text{H-NMR}$ analysis of soluble polymers precipitated at early reaction times

reaction time, t (min)	$I_{\text{Aryl-H}}$	$I_{\text{Vinyl H}}$	[PS]	[PDVB ₁]	[PDVB ₂]	$M_{n,\text{NMR}}$ (g/mol)
0	0.0	0.0	0.0	0.0	0.0	0
5	12.8	1.0	1.8	0.8	0.1	300
15	24.0	1.7	2.7	2.1	0.5	600
25	51.3	3.0	7.0	2.9	1.3	1300
35	62.6	3.3	8.1	3.3	2.2	1600
45	66.9	3.5	8.0	3.5	3.2	1700

Table 3.4 Rate constants obtained from fitting the data of Figure 3.5

constant	value ($\times 10^3 \text{ min}^{-1}$)	error ($\times 10^3 \text{ min}^{-1}$)
k_1	9.2	1.2
k_2	27.8	7.0
k_3	3.0	0.3

3.3.2 Ionic Conductivity

Time-resolved conductivity data were acquired during the PIMS reaction for a sample containing 21 vol% BMITFSI (Figure 3.6). Following initiation, the conductivity quickly decreases from the maximum obtained of ca. 6.5 mS/cm. The conductivity continues to decrease monotonically for 3–4 h before plateauing slightly below 3 mS/cm, with only an overall factor of two reduction in conductivity. This plateau is consistent with the conductivity at 120 °C of a solid membrane prepared with equivalent composition (dash-dot line in Figure 3.6). Although the nominal ionic liquid concentration is equivalent, the slight difference between the in situ end-value and the dash-dot line is likely a combination of sample-electrode contact and small compositional differences between samples.

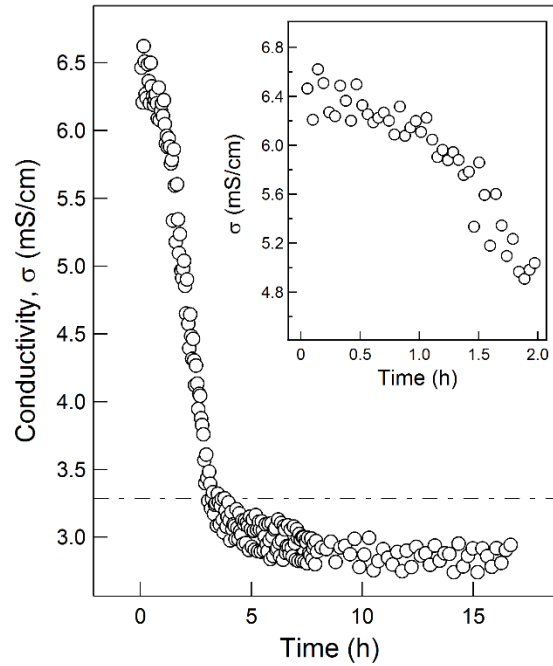


Figure 3.6 In situ conductivity for a PEO-*b*-P(S-*co*-DVB) sample prepared with 21 vol% BMITFSI. The dash-dot line is the conductivity of a previously measured solid membrane of equivalent composition. The inset shows an expanded view of the conductivity in the first 2 h.

The conductivity of charged species i in the liquid reaction mixture, σ_i , is a function of ion diffusivity, D_i , the square of ion charge, z_i , and the effective number of dissociated ions, n_i .²⁷

$$\sigma_i \sim D_i \times z_i^2 \times n_i \quad (3.5)$$

The decrease in ionic conductivity during the PIMS reaction (Figure 3.6) is the combined result of change in these parameters and morphological effects consequent to the formed microstructure.

Ion diffusivity is a strong function of the local friction imparted by the surrounding medium. As the reaction proceeds, the local ion environment transitions from a concentrated polymer solution (where S and DVB dilute the PEO chains) to PEO-rich domains, eventually forming a conducting phase that is an approximately 50 vol% mixture of PEO and BMITFSI. Within the PEO/IL domains, the rate of ion transport is comparable

to a bulk electrolyte of PEO homopolymer and ionic liquid. The local relaxation dynamics that determine BMITFSI migration are therefore expected to slow down over the course of the reaction, as polymer segmental relaxation should decrease in a polymer melt relative to a solvated mixture of polymer chains. Thus, we expect that some of the decrease in conductivity is due to an increase in the viscosity of the medium and a corresponding reduction in D_i .

The charges of the constituent ions do not change during the reaction; however, the fraction of dissociated ions (i.e., those that contribute to the measured current) will vary with the local dielectric environment. For both styrene monomer and polystyrene, the relative permittivity, ϵ_r , is ca. 2.5,²⁸ approximately half the value of PEO, for which $\epsilon_r \approx 6$.²⁹ As the ions partition from a mixture of PEO + S/DVB in the homogeneous liquid to PEO-rich domains in the microphase-separated solid electrolyte, ions experience an increase in the relative permittivity of the medium. Higher relative permittivity would lead to an enrichment of dissociated ions. Thus, the decrease in ionic conductivity due to reduction in D_i is mitigated by an increase in n_i .

The final factor influencing the conductivity of the electrolyte is microphase separation. In the case of PIMS PEMs, the emergent microstructure imposes additional resistance through an increase in tortuosity, τ , a geometric parameter that quantifies the longer average path ions must travel between electrodes in the nanostructured electrolyte relative to that in a homogeneous electrolyte of the same PEO/ionic liquid composition. In the liquid precursor, there are no insulating barriers preventing direct ion migration between the two electrodes, so $\tau = 1$. In the microphase-separated solid PEM, however, ions must migrate through tortuous conducting domains, decreasing the measured conductivity because $\tau > 1$. In our previous work,²⁴ transmission and scanning electron micrographs provided direct visualization of the tortuous conducting channels in PIMS PEMs. Although the value of τ was not directly calculated, it was found that the decrease in measured conductivity of the nanostructured PIMS PEMs relative to bulk, homopolymer-based electrolytes could be rationalized by assuming values of τ between 1.5 and 3. This range is consistent with the work of Seo and Hillmyer,²⁵ who studied a similar nanostructured PIMS

system. The authors used water and gas transport experiments to calculate values of τ of 1.4 and 1.7, respectively. More generally, Cussler³⁰ has noted that for transport of small molecules in one phase of a disordered, co-continuous composite, a physically reasonable range of τ is 1.5–3. In summary, the overall modest drop in conductivity during the PIMS process is due to a reduction in the diffusivity of the ions and an increase in the tortuosity of the conducting paths. An increase in the fraction of dissociated ions due to localization of the ionic liquid in the more polar PEO phase likely counteracts these effects to a small extent.

3.3.3 Rheometry

Figure 3.7 shows in situ rheology data for PIMS PEMs containing 21 and 30 vol% BMITFSI in comparison with a neat sample containing no BMITFSI. (Note that for the 30 vol% sample, the strain amplitude was purposely set too low to obtain reliable data at early times ($t < 100$ min) to ensure that the sample remained inside the linear response regime as the apparent gel point was approached.) In general, at early times, all samples exhibit a predominantly liquid-like response, with $G'' > G'$. The dip in G'' within the first few minutes occurs because data collection began at room temperature, and the viscosity decreased by approximately a factor of 3 (from 25 to 8 cP) as the sample was heated to 120 °C over the course of 80 s.

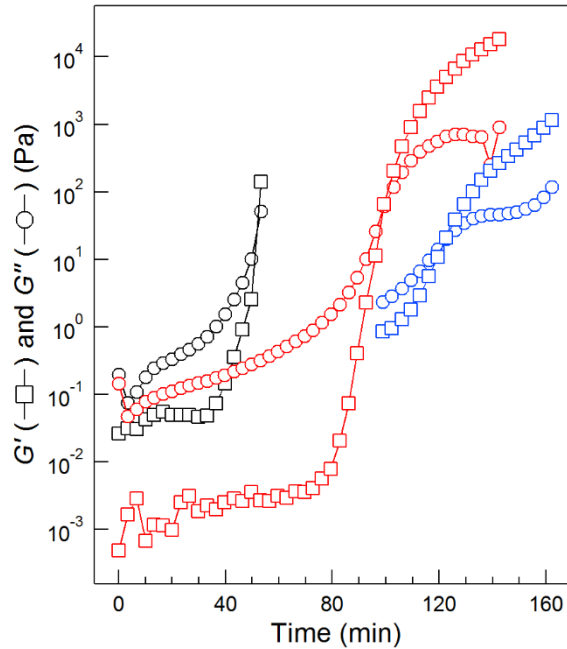


Figure 3.7 Evolution of the elastic, G' , and viscous, G'' , shear moduli measured at $T_{\text{rxn}} = 120$ °C and an angular frequency of 10 rad/s. The concentration of BMITFSI increases from 0 (black), to 21 (red) and 30 (blue) vol%. Note that the magnitude of G' before the sharp upturn is likely not quantitatively accurate; the raw phase angle for early time data was $> 150^\circ$, suggesting that instrument inertial effects dominated the response.³¹

Following thermal equilibration, the viscosity monotonically increases — as evidenced by the increase in G'' — consistent with the predominantly linear growth of the P(S-*co*-DVB)-*b*-PEO diblock before a significant degree of crosslinking has occurred. During this initial stage, G' exhibits only a modest increase, as the sample response is dominated by viscous dissipation. After some time, however, the elastic response quickly grows, beginning with a sharp upturn in G' . The rate of increase in G' outpaces that of G'' , and the subsequent crossover of G' and G'' indicates an apparent rheological transition from liquid-like to solid-like response. After the apparent gel point, G' continues to increase and eventually plateaus at a value of 0.1 GPa at 120 °C, as reported in our earlier work.²⁴ However, the samples did not adhere to the rotating parallel plate after stiffening to G' values above 10^3 – 10^4 Pa, as evidenced by a drastic decrease in the instrument torque. As a

result, the rheometer used for the in situ experiments could not be used to measure the mechanical response at later stages of the polymerization.

As shown in Figure 3.7, increasing the concentration of ionic liquid increases the time required to reach the apparent gel point ($G' = G''$). This increase in the time to gel is most likely a dilution effect; that is, a result of the decreasing concentration of macro chain-transfer agent (Table 3.1). In contrast to the time required to reach the apparent gel point, the value of the modulus at the crossover of G' and G'' does not vary appreciably with ionic liquid concentration; for all samples, the modulus at the apparent gel point is quite low, ranging from 20–60 Pa.

3.3.4 Synchrotron SAXS

Figure 3.8 presents the results of in situ, time-resolved small-angle X-ray scattering (SAXS) for a PIMS PEM prepared with 21 vol% BMITFSI. Figure 3.9 shows the raw I versus q scattering data for this composition, as well as neat samples for comparison. In general, the scattering for both neat and ionic liquid-containing samples is characterized by a single broad peak with a local maximum at a wavevector between 0.3 and 0.5 nm⁻¹. One notable difference between neat and ionic liquid-containing samples is the development of a higher order peak late in the reaction when ionic liquid is present. We have attributed this higher order peak to an increase in the structural correlation length, although the microphase-separated PIMS PEMs lack crystallographic symmetry.

The primary structure factor peaks were fit to a Lorentzian function to extract values for the maximum in scattered intensity, I_m , located at wavevector q_m . This primary structure factor peak grows in intensity and shifts first to higher, and then lower q as the reaction proceeds. Figure 3.8 reveals an exponential increase in I_m for the first 2 h of the PIMS reaction, during which q_m becomes progressively smaller. The decrease in q_m during the course of the reaction — which corresponds to an increase in the d -spacing of 2 nm — could be explained by the combination of chain growth and chain stretching as the segregation strength increases during the reaction. Presumably, the SAXS experiments were terminated too early to observe a clear plateau in the value of q_m ; the experiment was

discontinued upon observing a decrease in intensity at $t \approx 2$ h, most likely resulting from sample degradation due to extended high intensity irradiation.

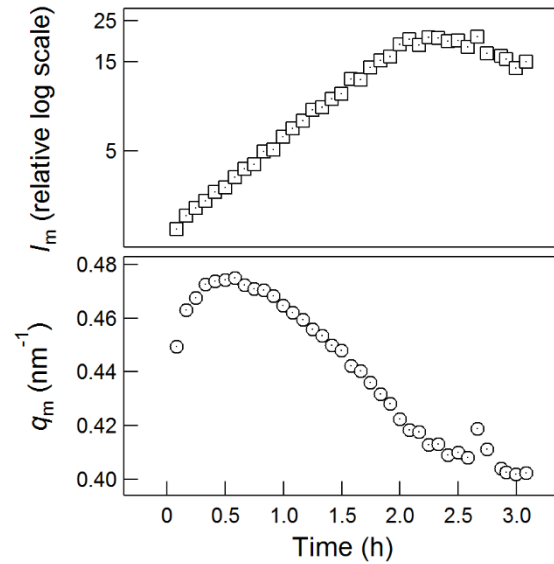


Figure 3.8 Time-resolved evolution of the maximum scattered intensity, I_m , of the primary structure factor peak located at wave vector q_m , for a sample prepared with 21 vol% BMITFSI.

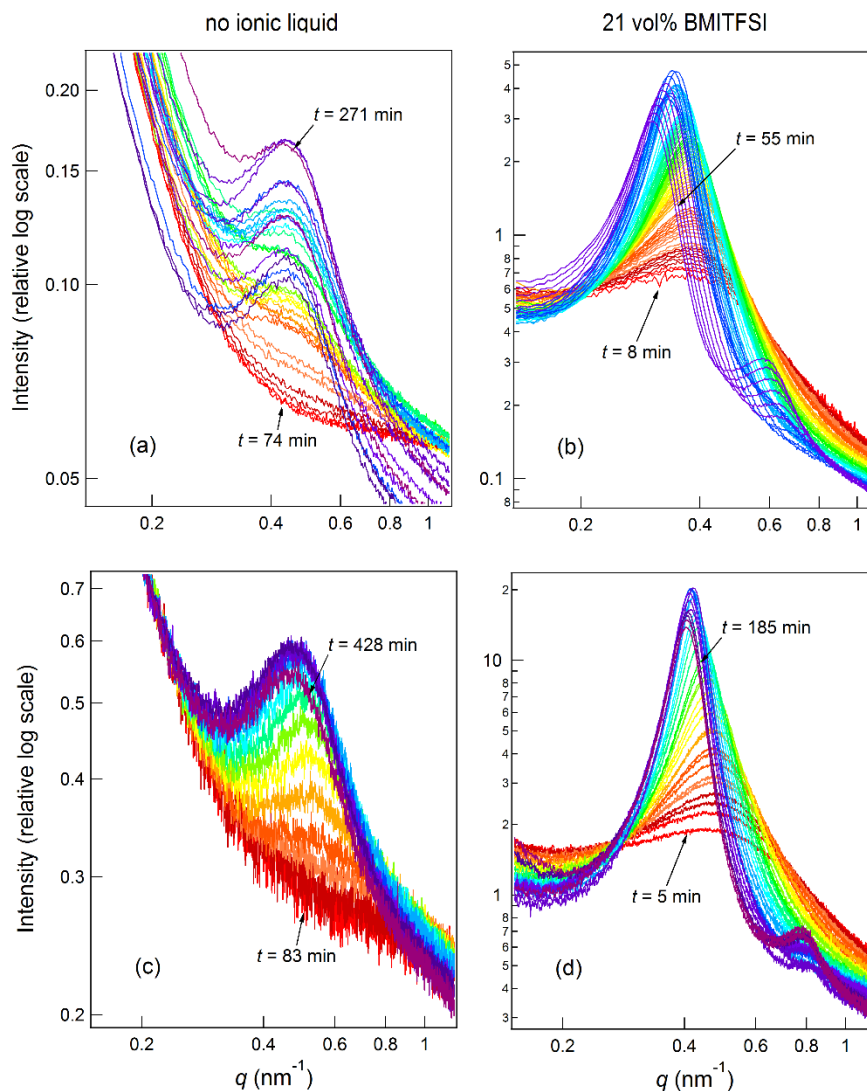


Figure 3.9 (a)–(d) Replicate in situ time-resolved small angle X-ray scattering data for samples prepared with 0 (left column) and 21 (right column) vol% BMITFSI. The traces are color-coded according to ROYGBIV, where early time data are red and late time data are violet. The first and last collected traces are labeled with the time after initiation at $T_{\text{rxn}} = 120$ °C. The scattered intensity is on a common scale for all samples, but was not reduced to absolute units. That is, samples with ionic liquid scatter ca. 10–20 times stronger than neat samples. To show the relative change in intensity during the polymerization, traces were not shifted vertically.

3.4 Discussion

3.4.1 Segregation Strength

As shown in Figures 3.8 and 3.9, the scattering profile develops a weak local maximum within minutes of heating the liquid reaction mixture to 120 °C. This peak indicates the growth of block polymer and, accordingly, can result from a number of phenomena — including correlations in the molecularly disordered growing block polymer³²⁻³⁴ or microphase separation between globally disordered domains.³⁵ Here, we distinguish the term microphase separation transition (MST), which characterizes isotropic compositional fluctuations in a state of weak-to-intermediate segregation, from the order-disorder transition (ODT), a thermodynamic transition to a periodic ordered phase as evidenced by one or more sharp Bragg reflections.³⁶ We have shown on the basis of real space images that PIMS PEMs are ultimately arrested in a microphase-separated microstructure lacking long-range periodic order. We therefore interpret the emergence of a scattering peak as the onset of microphase separation between the P(S-*co*-DVB) and PEO/IL domains. As the P(S-*co*-DVB) block continues to grow off the PEO-CTA, the segregation strength — the product of an effective interaction parameter, χ^{eff} , and the average volumetric degree of polymerization, N — increases, both due to the increasing molar mass of the block polymer and the increasing incompatibility of BMITFSI+PEO with the P(S-*co*-DVB) block. Previously, He et al.³⁷ and Zhang et al.³⁸ have shown that an imidazolium-based ionic liquid (EMITFSI) similar to BMITFSI is immiscible with polystyrene with $M \geq 3$ kg/mol.

There is a large literature exploring the effect of salt-doping on χ^{eff} , as well as the resulting microstructure.^{9,17,39-43} Despite quantitative differences among these studies, likely attributable to the different methods used to calculate χ^{eff} , the common lesson is that doping one phase of a block polymer with salt results in a drastic increase in the interaction parameter relative to the neat diblock. Furthermore, the effect of salt doping often pushes the T_{ODT} outside the experimentally accessible window through substantive increases in χ^{eff} . It is therefore not surprising that adding a strongly selective salt to the PIMS reaction

mixture induces microphase separation even when N of the growing block polymer is small (see the $^1\text{H-NMR}$ analysis).

The effective interaction parameter, χ^{eff} , was not directly calculated for the P(S-*co*-DVB)-*b*-PEO/BMITFSI system studied here. However, Simone et al.⁴¹ reported scattering data at 150 °C for lamellae-forming PS-*b*-PEO/EMITFSI blends that can provide a reasonable estimate for χ^{eff} in the PIMS system. As shown in Figure 3.10, Simone et al.⁴¹ measured the increase in d -spacing with increased salt loading for four lamellae-forming PS-*b*-PEO/EMITFSI blends. Salt-doping is analogous to blending diblocks with a selective solvent^{44,45} and increases the d -spacing both by simple volume addition to one phase and by increasing chain stretching at the interface. The concentration of EMITFSI was reported in terms of r , defined as the molar ratio of cations (EMI⁺) to ethylene oxide (EO) repeat units. An equivalent concentration in terms of volumetric units is given in Figure 3.10.

Linear extrapolation of the four lamellae-forming data points was used in Figure 3.10(a) to estimate the d -spacing of a hypothetical neat diblock, for which $d^* \approx 25$ nm. The relation between the d -spacing and χ^{eff} in the strong segregation limit (defined as $\chi N \gg 10$) was then used to determine the increase in the interaction parameter upon salt doping, $\chi_{\text{salt}}^{\text{eff}}$, relative to that for a neat diblock, $\chi_{\text{neat}}^{\text{eff}}$.⁴⁶

$$\chi_{\text{salt}}^{\text{eff}} = \chi_{\text{neat}}^{\text{eff}} \left(\frac{d_{\text{salt}}^*}{d_{\text{neat}}^*} \right)^6 \quad (3.6)$$

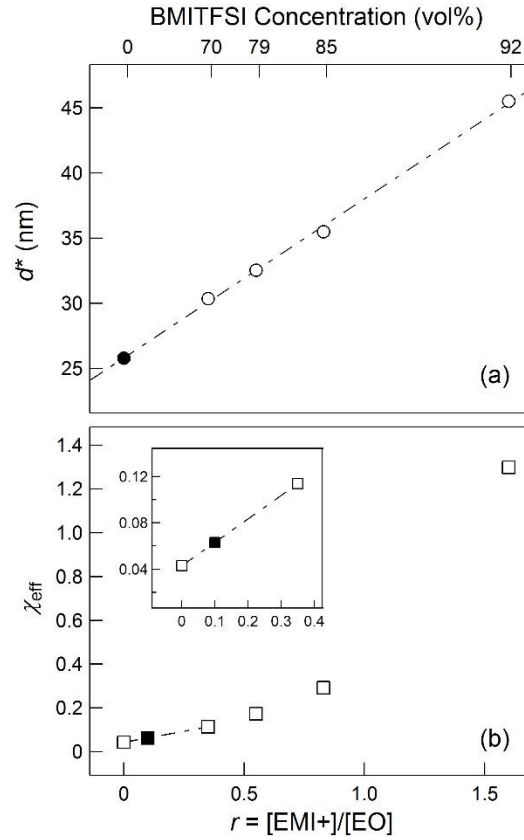


Figure 3.10 (a) Lamellar d -spacing at 150° C for PS-*b*-PEO/EMITFSI blends (open circles, data from reference 41 and linear extrapolation to a hypothetical neat ($r = 0$) diblock (filled circle). (b) Estimation of the effective interaction parameter, $\chi_{\text{salt}}^{\text{eff}}$, at 150° C for PS-*b*-PEO/EMITFSI as a function of salt loading, r . The filled square represents a PIMS PEM with 21 overall vol% BMITFSI. The inset shows an expanded view of the low- r data and the linear interpolation used to determine $\chi_{\text{salt}}^{\text{eff}}$ of the sample.

Zhu et al.⁴⁷ used the structure factor of the Random-phase Approximation (RPA) to fit the scattering profile of a disordered PS-*b*-PEO diblock and calculate the effective interaction parameter of neat PS-*b*-PEO. Using a reference volume of 100 Å³, the temperature dependence of $\chi_{\text{neat}}^{\text{eff}}$ is given by

$$\chi_{\text{neat}}^{\text{eff}}(T) = \frac{21.3}{T} - 7.05 \times 10^{-3} \quad (3.7)$$

The concentration of BMITFSI in PIMS electrolytes prepared with 21 overall vol% corresponds to $r \approx 0.1$; linear interpolation was used in Figure 3.10(b) to estimate at $r = 0.1$ an increase in χ^{eff} of 1.5 relative to the neat diblock ($\chi_{\text{neat}}^{\text{eff}} = 0.043$ at 150 °C), or $\chi_{\text{salt}}^{\text{eff}} = 0.065$. This value of $\chi_{\text{salt}}^{\text{eff}}$ is strictly valid at 150 °C, but because salt doping has a much stronger effect on the interaction parameter than temperature, the factor of 1.5 increase in χ^{eff} for $r = 0.1$ is approximate at 120 °C.

Figure 3.11 is based on a simplified model for the evolution of segregation strength of the growing diblock in the presence of BMITFSI. For a neat diblock, the combination of χN and the volume fraction, f , of one of the blocks defines the equilibrium morphology on the classic phase portrait.⁴⁸ One of the challenges in modeling the PIMS system is the concurrent dynamic progression of both χN and f as the reaction proceeds. Figure 3.11 therefore makes important simplifying assumptions about the PIMS system. (i) The growth of the P(S-co-DVB) block off a 5 kg/mol PEO-CTA is modeled by calculating the value of χN assuming a neat, linear diblock at discrete values of the molar mass of the polystyrene block, M_{PS} . In reality, the P(S-co-DVB)-*b*-PEO diblock is growing in a monomer mixture of S/DVB. At 120 °C, the S/DVB mixture is effectively a neutral solvent and screens some of the net repulsive interactions between P(S-co-DVB) and PEO. (ii) Relative to the neat, linear diblock, the addition of ionic liquid increases the magnitude of χ^{eff} by a factor of 1.5. We estimated this increase in χ^{eff} using the increase in d -spacing with increasing ionic liquid concentration in PS-*b*-PEO/EMITFSI electrolytes, as described above assuming EMITFSI and BMITFSI exhibit similar thermodynamic incompatibility with polystyrene;⁴¹ the volume addition of the ionic liquid to the PEO phase is not accounted for. (iii) $(\chi N)_{\text{ODT}}$ was calculated using mean field theory, which ignores spontaneous concentration fluctuations that exist in the disordered melt in the vicinity of the T_{ODT} . As in the case of growing the diblock in a neutral solvent, fluctuations will screen net unfavorable interactions. The values of χN in Figure 3.11(a) therefore represent an upper limit, as both the neutral solvent and fluctuations will stabilize the disordered phase, pushing $(\chi N)_{\text{ODT}}$ higher than the mean field prediction.

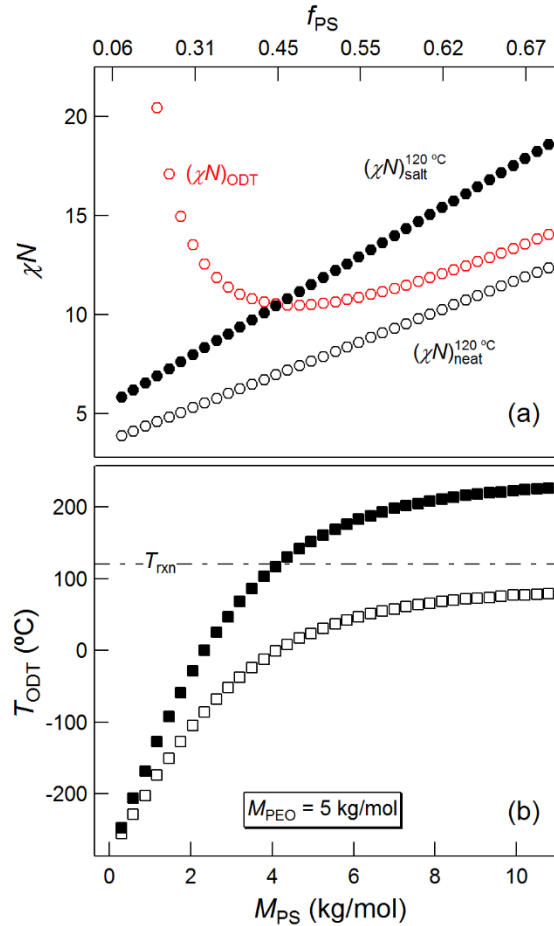


Figure 3.11 Segregation strength, χN , as a function of the molar mass of a polystyrene (PS) block growing from a 5 kg/mol PEO block. The top axis indicates the equivalent volume fraction of the PS block calculated with a reference volume of 100 \AA^3 . $(\chi N)_{ODT}$ is the mean field prediction for segregation strength at the order-disorder transition temperature. $(\chi N)_{neat}^{120^\circ C}$ is the calculated segregation strength of a neat PS-*b*-PEO diblock at $120^\circ C$, calculated using data from Zhu et al.⁴⁷ $(\chi N)_{salt}^{120^\circ C}$ is the segregation strength with the addition of 21 overall vol% BMITFSI, calculated assuming $\chi_{salt}^{eff} = 1.5\chi_{neat}^{eff}$, based on the analogous system of PS-*b*-PEO/EMITFSI. (b) Mean field prediction for the T_{ODT} as a function of PS molar mass for a neat PS-*b*-PEO diblock (open squares) and PS-*b*-PEO/BMITFSI (filled squares).

Despite these simplifications, Figure 3.11 provides valuable insight into the PIMS reaction. In a sense, the time variable in the PIMS experiments is analogous to inverse temperature for a diblock melt. Early in the reaction (or equivalently, high temperature for a diblock melt) the diblock is disordered, and the local composition can be described by

the mean field. In Figure 3.11(b) — which re-casts the segregation strength in terms of the mean field prediction for the T_{ODT} — this corresponds to low M_{PS} , where the value of χN for both growing neat and salt-doped diblock is much lower than $(\chi N)_{\text{ODT}}$. As the reaction progresses and M_{PS} increases, T_{ODT} and χN increase, producing a thermodynamic drive to develop concentration fluctuations. When the T_{ODT} is higher than the reaction temperature (120 °C), there is a thermodynamic drive to order.

The segregation strength of the neat sample without ionic liquid is always much lower than that of the sample with ionic liquid, consistent with the much later emergence of scattering peaks in the reaction for the neat sample relative to the electrolyte (see Figure 3.9). For $M_{\text{PS}} \geq 4$ kg/mol, the segregation strength for the ionic liquid-containing sample is larger than the estimated $(\chi N)_{\text{ODT}}$, indicating a strong thermodynamic drive to order. If the system were at equilibrium, the value of f_{PS} at the crossover would place the diblock in the lamellae-forming region of the diblock phase portrait. It is worth noting that the segregation strength of the neat diblock at 120 °C is always lower than $(\chi N)_{\text{ODT}}$, even for a fully polymerized (and uncrosslinked) diblock. That is, even if all the styrene monomer were incorporated into the neat PS-*b*-PEO diblock — for which $M_{\text{tot}} \approx 16$ kg/mol and $f_{\text{PS}} \approx 0.7$ — the system would be disordered. This is not surprising, as $\chi_{\text{neat}}^{\text{eff}}$ is rather low (0.046 at 120 °C),⁴⁷ requiring a relatively high chemical degree of polymerization (> 300) to place PS-*b*-PEO inside the ordered window at 120 °C.

3.4.2 Morphology

The morphology of PIMS PEMs is a microphase-separated state *without* long-range order, reminiscent of the fluctuation-induced, disordered bicontinuous structure known to exist in neat diblock melts in the vicinity of the T_{ODT} .^{48,49} The connectivity of the diblock restricts the compositional heterogeneity to length scales of order of the radius of gyration, R_{g} . It is likely that the long-range domain continuity observed in PIMS PEMs is a direct result of arresting (via chemical crosslinking) a similar disordered network structure prior to an ODT.⁵⁰⁻⁵²

To illustrate that the PIMS strategy kinetically arrests a disordered, bicontinuous morphology prior to ordering, samples were prepared while varying the mole fraction of the crosslinking agent (DVB) in the monomer mixture from 0 (pure styrene) to 100 mol% (pure DVB) at fixed concentrations of PEO-CTA and BMITFSI, respectively 25 and 21 vol%. Figure 3.12(a) shows SAXS data of the electrolytes prepared, noting the DVB concentration routinely used in this work is 20 mol%. Samples prepared with DVB concentrations between 10 and 100 mol% exhibit a broad primary peak. At moderate concentrations of DVB, the primary peak is accompanied by a relatively weak higher order correlation peak, a scattering signature signifying greater structural coherence of the compositionally heterogeneous microstructure.

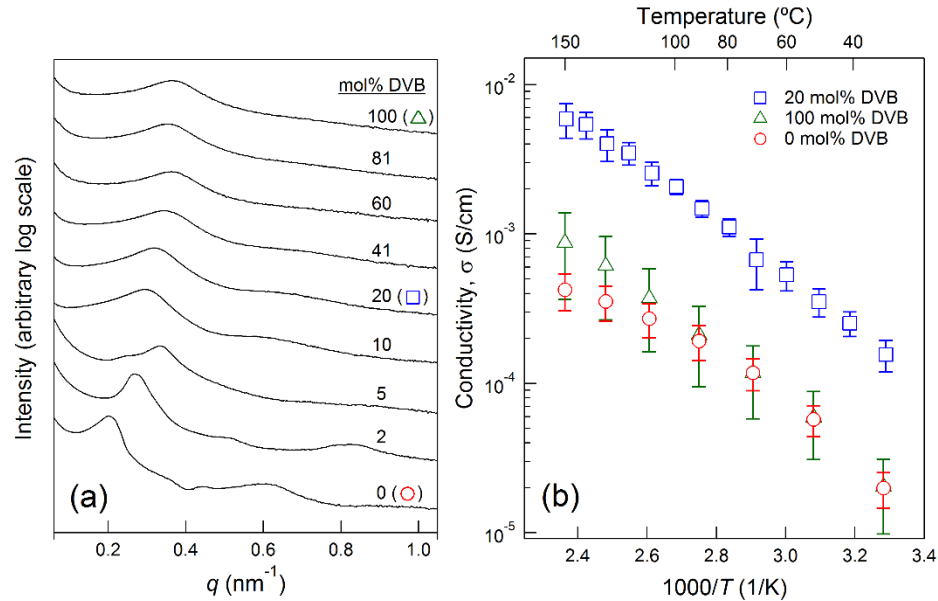


Figure 3.12 (a) SAXS data for samples prepared with 5 kg/mol PEO-CTA, 21 vol% BMITFSI, and S/DVB, with varying concentration of DVB. Note that the radical initiator AIBN was not used in the preparation of these samples. Reduced crosslinker content leads to materials exhibiting Bragg-like diffraction and long-range order. (b) Temperature-dependent conductivity as a function of DVB concentration. Error bars represent one standard deviation based on three or more samples.

In contrast, samples prepared with 5 mol% DVB or less exhibit relatively sharp Bragg peaks, suggesting some degree of long-range, periodic order. The higher order reflections do not appear to correspond to any of the common equilibrium morphologies (lamellae,

BCC spheres, HCP cylinders, gyroid) for neat diblocks. However, with the exception of the linear diblock (i.e., the 0 mol% DVB sample), chemical crosslinking likely prevents relaxation to morphological equilibrium. Nevertheless, Figure 3.12(a) demonstrates that the PIMS reaction mixture is *en route* to an order-disorder transition into a state with long-range periodic order, and some threshold concentration of crosslinking agent is required to prevent the growing diblock from undergoing a transition from a disordered network to an ordered morphology.

From the viewpoint of the resulting membrane performance, trapping the bicontinuous network structure prior to the ordering of well-segregated domains is critically important, as illustrated by the conductivity experiment in Figure 3.12(b). At equal concentrations of ionic liquid, the conductivities of samples prepared without DVB and with 100 mol% DVB are approximately a factor of 10 lower than a sample prepared with 20 mol% DVB. As we previously reported, the conductivity of the sample prepared with 20 mol% DVB achieves the theoretical maximum, based on volume fraction and geometric arguments. The reduction in conductivity in the 0 mol% DVB sample therefore implies loss of long-range continuity of the conducting pathways. Alternatively, the lower conductivity of the 100 mol% DVB sample and a coinciding attenuation of the secondary shoulder observed via SAXS (Figure 3.12(a)) suggest that early onset of extensive crosslinking and gelation may produce broad interfaces that hinder ion diffusivity.^{6,53}

The result for the 0 mol% DVB sample is qualitatively similar to a recent report by Chintapalli et al.,²¹ who showed that the conductivity of LiTFSI in a nearly symmetric PS-*b*-PEO diblock decreased after the polymer underwent an ordering transition from a disordered, co-continuous network into isotropically-oriented grains of lamellae. Although the authors interpreted their results in the context of diffusion resistance at grain boundaries, the important similarity with our work appears to be a loss in continuity of the conducting channels in electrolytes that exhibit an ordered microstructure. Unfortunately, attempts to obtain TEM micrographs to illustrate this lack of continuity were unavailing. The exceptionally soft mixture of ionic liquid and polymer was easily manipulated and flowed at high temperature, signifying a concomitant loss of mechanical integrity and

conductivity. The PIMS strategy therefore presents a unique opportunity to increase both the mechanical properties and conductivity of a PEM simultaneously.

3.4.3 Overall PIMS Mechanism

The PIMS process is characterized by a competition between polymerization (crosslinking) and ordering. Consequently, several outcomes following reaction of the PIMS mixture can be envisioned: (i) macrophase separation; (ii) homogenous gelation of the mixture; (iii) long-range ordering of a swollen block polymer; and (iv) a bicontinuous nanostructure with high conductivity and modulus. Therefore, we examine the in situ data in an attempt to discern the relative and critical timescales that restrict the outcome to the desired fourth possibility, thereby maximizing electrolyte performance. Figure 3.13 summarizes the results of the four in situ, time-resolved experiments — SAXS, conductivity, reaction kinetics, and rheology — following the course of the PIMS reaction. From each experiment, a characteristic timescale is extracted, denoted in Figure 3.13 by a dash-dot line and summarized in Table 3.5. Within minutes of initiation, the presence of ionic liquid induces microphase separation, i.e., strong, isotropic compositional fluctuations, evidenced by the emergence of the structure factor peak in the SAXS data. Increases in scattering intensity during the reaction reflect increases in the amplitude of the fluctuations, growing at a rate determined by chemical reaction kinetics and the effective mutual diffusion coefficient of the growing diblock.⁵⁴⁻⁵⁶ This is consistent with an increase in local enrichment as the segregation strength increases with diblock growth and ionic liquid partitioning to the PEO domains. The decrease in q_m indicates growth of the size of the block polymer and the preferred lengthscale of heterogeneity. The scattering intensity and preferred lengthscale appear to saturate at $t \approx 2.5$ h, indicating a “locking in” of the structure. This could be the result of either (i) an ODT to a lamellar phase, or (ii) gelation (in this case, gelation of one microphase). Through the following discussion, we establish the latter as the predominant mechanism.

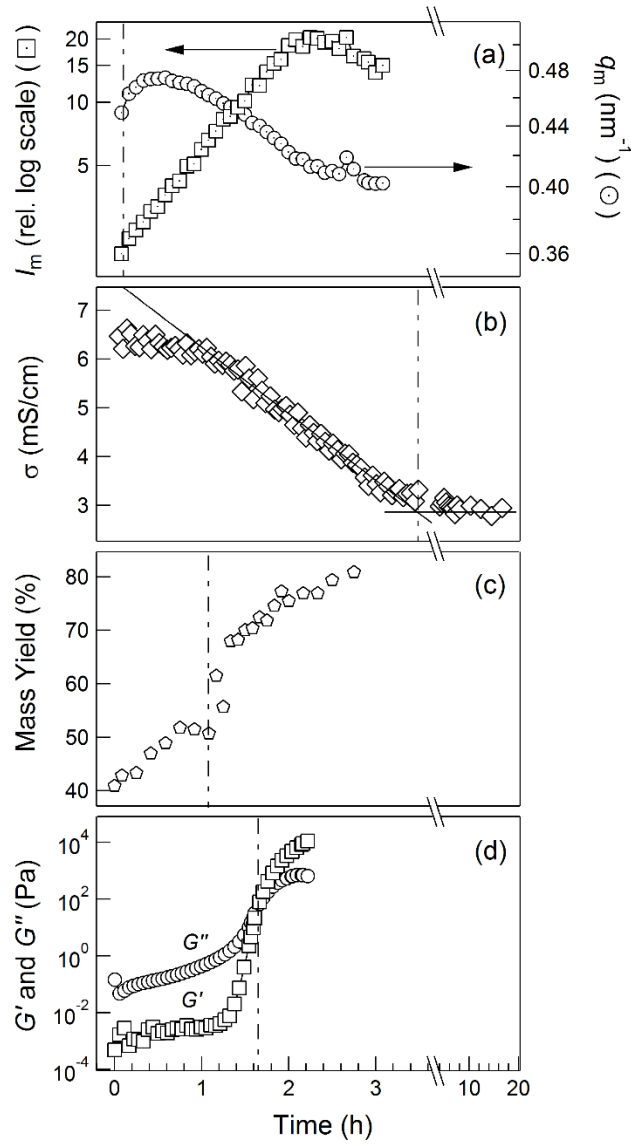


Figure 3.13 Comparison of (a) SAXS, (b) conductivity, (c) mass yield, and (d) rheology in situ experiments for a sample prepared with 21 vol% BMITFSI. I_m is the maximum scattered intensity of the structure factor peak at wave vector q_m . The solid black lines in panel (b) were used to determine time at which conductivity plateaus. The dash-dot lines indicate the characteristic timescale associated with each experiment.

Table 3.5 Characteristic timescales associated with the *in situ* experiments in Figure 3.13

experiment	characteristic timescale, t_x (h)
SAXS	0.08
conductivity	3.5
kinetics	1.08
rheology	1.65

At $t \approx 1$ h, the sharp increase in mass yield, attributed to the formation of discrete flocs of crosslinked polymer, correlates well with an upturn in G' . The onset of the decrease in conductivity also begins at approximately 1 h, likely resulting from increases in the local viscosity concurrent with floc formation. Shortly thereafter, this increase in the elastic modulus is followed by the apparent gel point at $t \approx 1.7$ h. It is important that the growing block polymer forms long-range domains prior to the rheological gel point, as most individual chains would not be able to rearrange after gelation. Although it is worth noting that the crossover of G' and G'' might not represent a true rheological gel point, as the experiment was performed at a fixed frequency (10 rad/s), it is clear from the mass yield data that microphase separation precedes gelation. As discussed above, shortly after the apparent rheological gel point, the SAXS peak intensity and the peak position saturate, indicative of the arrest of all long-range structural rearrangements.

Over the course of 3–4 h, the conductivity exhibits a gradual, continuous decrease from that of the liquid precursor at 120 °C to its plateau at approximately 3 mS/cm. The decrease in conductivity at early times is most likely a result of the increase in local viscosity and concomitant decrease in diffusivity of the ionic liquid. The ionic liquid remains relatively homogeneously distributed for some amount of time before ultimately segregating to the PEO domains, so ions experience an increase in viscosity as the polystyrene block grows. The final value of conductivity reflects a combination of the local viscosity of the PEO environment and the tortuosity of the conducting pathways. Therefore, conductivity is perhaps the most informative experiment to probe formation of the disordered, co-continuous network structure. The conductivity reaches its plateau value at a reaction time

of 3–4 h, suggesting that this is the timescale for full development of the PEO/IL domains in terms of composition. The fact that the conductivity decreases by only a nominal factor of two without discontinuity over the course of the PIMS reaction indicates (i) long-range continuity of the conducting domain is always present, which supports the conclusion that there is no loss of domain continuity associated with an ODT, and (ii) gelation, which would slow ion transport, occurs predominately in the insulating phase.

In general, the data elucidates the growth of a P(S-*co*-DVB)-*b*-PEO diblock forming an isotropic, bicontinuous network after the onset of microphase separation early in the reaction. The estimated values of χN during the reaction indicate that the electrolyte does not pass through the order-disorder transition prior to gelation, although there is significant uncertainty in the estimated value of χ^{eff} . In addition, we observe no experimental evidence (i.e., a discontinuous increase in intensity and/or sharp, higher order Bragg peaks) to suggest an ODT. For this reason, *if* PIMS PEMs do pass through the ODT, the morphology is due to persistent compositional fluctuations of the disordered state and chemical crosslinking prior to nucleation of the ordered phase. For example, Sakamoto et al.^{50,57} studied the ordering kinetics of a nearly symmetric poly(styrene)-*b*-poly(isoprene) diblock when quenched from a disordered melt to below the T_{ODT} . The authors provided direct visualization (via TEM) of samples quenched from the disordered state, which revealed an isotropic network morphology similar to that observed in solid, microphase separated PIMS PEMs. This disordered network structure persisted for a period of time at temperatures slightly below the T_{ODT} , until the equilibrium lamellar morphology had sufficient time to nucleate and grow. It is plausible that chemical crosslinking in PIMS PEMs prevents nucleation and growth of the equilibrium, well ordered morphology.

Alternatively, if gelation occurs prior to crossover of the ODT, but within the fluctuation regime, it requires that the domains are defined and maintain long-range continuity prior to ordering. This would be consistent with the “pattern transition” recently reported by Lee et al.,⁵⁸ in which the authors studied a nearly symmetric poly(1,4-isoprene)-*b*-poly(lactide) diblock, and showed that the amplitude of fluctuations does not change through the T_{ODT} . Instead, the authors offer a physical interpretation of the ODT as

retention of high domain purity through the transition, and an ordering process that simply corresponds to a rearrangement of the interfaces between domains. Although that particular diblock was not amenable to real space imaging, the heat flow upon ordering was consistent with a transition from domains with hyperbolic interfaces (consistent with a disordered network) to the flat interfaces characteristic of the equilibrium lamellar morphology.

Previously, Yamamoto et al.⁵⁹ also studied polymerization-induced phase separation of a system with block architecture, via growth of *N,N*-dimethylacrylamide off a telechelic poly(dimethylsiloxane). These authors similarly observed an exponential increase in scattering intensity while the diblock grew in a monomer mixture, and interpreted this observation as evidence that the system underwent phase separation via spinodal decomposition. Although it is true that models for spinodal decomposition^{60,61} predict scattering signatures such as an exponential increase in intensity and a transient, preferred wavelength of composition fluctuations, observation of these phenomena does not necessarily imply that spinodal decomposition is the operative mechanism. Several studies have likened the self-similar structure observed in the fluctuating, disordered state of block polymers to the late-stage spinodal patterns of binary mixtures,^{36,48} however, in contrast to spinodal decomposition, where the characteristic wavelength ultimately diverges to infinity, the characteristic length scale of PIMS PEMs is closely tied to that of the diblock. The average center-to-center distance for the domains of PIMS PEMs is between 13–16 nm. The unperturbed radius of gyration, R_g , of a linear PS-*b*-PEO diblock – taking $N \approx 200$ and a statistical segment length, b , of 0.6 nm – is ca. 4 nm. However, chains will be stretched relative to a random coil at the interface, so locally, the d -spacing can approximate that of lamellae. Using the relation developed by Leibler³² for the d -spacing in the weak segregation limit (WSL) and the estimate of R_g , the mean-field WSL predicts $d^* \approx 3.23R_g \approx 13$ nm, in agreement with the measured d -spacing.³⁶ The calculation suggests that the 13–16 nm size scale is the result of chain stretching of a perturbed diblock across a domain interface. Furthermore, in our system the time scale for structural evolution, which is closely tied to polymerization kinetics, is much slower (i.e., hours) than the

timescale for molecular motion on the 10 nm lengthscale; thus spinodal decomposition is likely not playing a role in this system.

3.5 Conclusions

Long-range continuity of both the ion-conducting and high modulus domains is critical to maximizing the composite properties of block polymer electrolytes. We performed a series of in situ, time-resolved experiments — small-angle X-ray scattering, conductivity, rheology, and kinetics — to study structural development during the PIMS reaction for samples prepared with the ionic liquid BMITFSI. It appears that the network morphology is a direct result of concentration fluctuations in the reaction medium due to the increasing segregation strength of the growing diblock. These results highlight the delicate balance required to form the desired bicontinuous network morphology during the PIMS reaction: gelation must occur after the domains achieve high purity (to avoid detrimental interfacial effects), but prior to ordering, which could result in a loss of domain continuity. In terms of membrane performance, it is worth noting that while the conductivity decreases by only a factor of two over the course of the PIMS reaction, the modulus increases by many orders of magnitude, from that of a low viscosity liquid to 0.1 GPa. This remarkable result is a direct consequence of the maintenance of the long-range continuity of the disordered, network morphology. The PIMS strategy therefore enables the substantial independent tuning of the mechanical properties and the conductivity of polymer electrolytes.

3.6 References

- (1) Hallinan, D. T.; Balsara, N. P. *Annual Review of Materials Research* **2013**, *43*, 503.
- (2) Young, W.-S.; Kuan, W.-F.; Epps, T. H. *Journal of Polymer Science Part B: Polymer Physics* **2014**, *52*, 1.
- (3) Monroe, C.; Newman, J. *Journal of The Electrochemical Society* **2003**, *150*, A1377.
- (4) Monroe, C.; Newman, J. *Journal of The Electrochemical Society* **2004**, *151*, A880.
- (5) Monroe, C.; Newman, J. *Journal of The Electrochemical Society* **2005**, *152*, A396.
- (6) Singh, M.; Odusanya, O.; Wilmes, G. M.; Eitouni, H. B.; Gomez, E. D.; Patel, A. J.; Chen, V. L.; Park, M. J.; Fragouli, P.; Iatrou, H.; Hadjichristidis, N.; Cookson, D.; Balsara, N. P. *Macromolecules* **2007**, *40*, 4578.
- (7) Hallinan, D. T.; Mullin, S. A.; Stone, G. M.; Balsara, N. P. *Journal of The Electrochemical Society* **2013**, *160*, A464.
- (8) Steele, B. C. H.; Heinzl, A. *Nature* **2001**, *414*, 345.
- (9) Young, W.-S.; Epps, T. H. *Macromolecules* **2009**, *42*, 2672.
- (10) Young, W.-S.; Albert, J. N. L.; Schantz, A. B.; Epps, T. H. *Macromolecules* **2011**, *44*, 8116.
- (11) Young, W.-S.; Epps, T. H. *Macromolecules* **2012**, *45*, 4689.
- (12) Virgili, J. M.; Hoarfrost, M. L.; Segalman, R. A. *Macromolecules* **2010**, *43*, 5417.
- (13) Hoarfrost, M. L.; Segalman, R. A. *Macromolecules* **2011**, *44*, 5281.
- (14) Choi, J. H.; Ye, Y. S.; Elabd, Y. A.; Winey, K. I. *Macromolecules* **2013**, *46*, 5290.
- (15) Ye, Y.; Choi, J.-H.; Winey, K. I.; Elabd, Y. A. *Macromolecules* **2012**, *45*, 7027.
- (16) Weber, R. L.; Ye, Y.; Schmitt, A. L.; Banik, S. M.; Elabd, Y. A.; Mahanthappa, M. K. *Macromolecules* **2011**, *44*, 5727.
- (17) Wanakule, N. S.; Virgili, J. M.; Teran, A. A.; Wang, Z.-G.; Balsara, N. P. *Macromolecules* **2010**, *43*, 8282.
- (18) Yuan, R.; Teran, A. A.; Gurevitch, I.; Mullin, S. A.; Wanakule, N. S.; Balsara, N. P. *Macromolecules* **2013**, *46*, 914.
- (19) Gido, S. P.; Thomas, E. L. *Macromolecules* **1994**, *27*, 6137.

- (20) Gido, S. P.; Gunther, J.; Thomas, E. L.; Hoffman, D. *Macromolecules* **1993**, *26*, 4506.
- (21) Chintapalli, M.; Chen, X. C.; Thelen, J. L.; Teran, A. A.; Wang, X.; Garetz, B. A.; Balsara, N. P. *Macromolecules* **2014**, *47*, 5424.
- (22) Seo, M.; Amendt, M. A.; Hillmyer, M. A. *Macromolecules* **2011**, *44*, 9310.
- (23) Hermel, T. J.; Hahn, S. F.; Chaffin, K. A.; Gerberich, W. W.; Bates, F. S. *Macromolecules* **2003**, *36*, 2190.
- (24) Schulze, M. W.; McIntosh, L. D.; Hillmyer, M. A.; Lodge, T. P. *Nano Letters* **2013**, *14*, 122.
- (25) Seo, M.; Hillmyer, M. A. *Science* **2012**, *336*, 1422.
- (26) Koh, M. L.; Konkolewicz, D.; Perrier, S. b. *Macromolecules* **2011**, *44*, 2715.
- (27) Newman, J. *Electrochemical Systems*; 2nd ed.; Prentice-Hall, 1991.
- (28) Haynes, W. M. *CRC handbook of chemistry and physics : a ready-reference book of chemical and physical data*; CRC Press: Boca Raton, Florida, 2014.
- (29) Fanggao, C.; Saunders, G. A.; Lambson, E. F.; Hampton, R. N.; Carini, G.; Di Marco, G.; Lanza, M. *Journal of Polymer Science Part B: Polymer Physics* **1996**, *34*, 425.
- (30) Cussler, E. L. *Diffusion : Mass Transfer in Fluid Systems*; 3rd ed.; Cambridge University Press: Cambridge, UK, 2009.
- (31) Arvidson, S. A.; Lott, J. R.; McAllister, J. W.; Zhang, J.; Bates, F. S.; Lodge, T. P.; Sammler, R. L.; Li, Y.; Brackhagen, M. *Macromolecules* **2012**, *46*, 300.
- (32) Leibler, L. *Macromolecules* **1980**, *13*, 1602.
- (33) Bates, F. S.; Hartney, M. A. *Macromolecules* **1985**, *18*, 2478.
- (34) Bates, F. S. *Macromolecules* **1987**, *20*, 2221.
- (35) Lodge, T. *Mikrochim Acta* **1994**, *116*, 1.
- (36) Bates, F. S.; Fredrickson, G. H. *Annual Review of Physical Chemistry* **1990**, *41*, 525.
- (37) He, Y.; Boswell, P. G.; Bühlmann, P.; Lodge, T. P. *The Journal of Physical Chemistry B* **2006**, *111*, 4645.

- (38) Zhang, S.; Lee, K. H.; Frisbie, C. D.; Lodge, T. P. *Macromolecules* **2011**, *44*, 940.
- (39) Nakamura, I.; Balsara, N. P.; Wang, Z.-G. *ACS Macro Letters* **2013**, *2*, 478.
- (40) Teran, A. A.; Balsara, N. P. *The Journal of Physical Chemistry B* **2013**, *118*, 4.
- (41) Simone, P. M.; Lodge, T. P. *ACS Applied Materials & Interfaces* **2009**, *1*, 2812.
- (42) Thelen, J. L.; Teran, A. A.; Wang, X.; Garetz, B. A.; Nakamura, I.; Wang, Z.-G.; Balsara, N. P. *Macromolecules* **2014**, *47*, 2666.
- (43) Huang, J.; Tong, Z.-Z.; Zhou, B.; Xu, J.-T.; Fan, Z.-Q. *Polymer* **2013**, *54*, 3098.
- (44) Lodge, T. P.; Pudil, B.; Hanley, K. J. *Macromolecules* **2002**, *35*, 4707.
- (45) Simone, P. M.; Lodge, T. P. *Macromolecules* **2008**, *41*, 1753.
- (46) Semenov, A. N. *Macromolecules* **1993**, *26*, 6617.
- (47) Zhu, L.; Cheng, S. Z. D.; Calhoun, B. H.; Ge, Q.; Quirk, R. P.; Thomas, E. L.; Hsiao, B. S.; Yeh, F.; Lotz, B. *Polymer* **2001**, *42*, 5829.
- (48) Bates, F. S.; Rosedale, J. H.; Fredrickson, G. H. *The Journal of Chemical Physics* **1990**, *92*, 6255.
- (49) Fredrickson, G. H.; Helfand, E. *The Journal of Chemical Physics* **1987**, *87*, 697.
- (50) Sakamoto, N.; Hashimoto, T. *Macromolecules* **1998**, *31*, 3292.
- (51) Jinnai, H.; Nishikawa, Y.; Koga, T.; Hashimoto, T. *Macromolecules* **1995**, *28*, 4782.
- (52) Gomez, E. D.; Das, J.; Chakraborty, A. K.; Pople, J. A.; Balsara, N. P. *Macromolecules* **2006**, *39*, 4848.
- (53) Ganesan, V.; Pyramitsyn, V.; Bertoni, C.; Shah, M. *ACS Macro Letters* **2012**, *1*, 513.
- (54) Hashimoto, T.; Kowsaka, K.; Shibayama, M.; Suehiro, S. *Macromolecules* **1986**, *19*, 750.
- (55) Hashimoto, T.; Kowsaka, K.; Shibayama, M.; Kawai, H. *Macromolecules* **1986**, *19*, 754.
- (56) Hashimoto, T. *Macromolecules* **1987**, *20*, 465.
- (57) Sakamoto, N.; Hashimoto, T. *Macromolecules* **1998**, *31*, 3815.
- (58) Lee, S.; Gillard, T. M.; Bates, F. S. *Aiche J* **2013**, *59*, 3502.

- (59) Yamamoto, K.; Ito, E.; Fukaya, S.; Takagi, H. *Macromolecules* **2009**, *42*, 9561.
- (60) Cahn, J. W.; Hilliard, J. E. *The Journal of Chemical Physics* **1958**, *28*, 258.
- (61) Cahn, J. W. *The Journal of Chemical Physics* **1965**, *42*, 93.

Chapter 4

Crosslinked Nanoporous Polymer Monoliths from Polymerization-Induced Microphase Separation

In this chapter the synthetic strategy of polymerization-induced microphase separation is extended to the preparation of mesoporous crosslinked polymer monoliths from the bulk polymerization of styrene and DVB in the presence of macromolecular PLA-CTA. The morphology and porosity of the crosslinked matrix are characterized through a combination of small-angle x-ray scattering, scanning electron microscopy and nitrogen sorption. Variation of the crosslinker-to-monomer ratio, temperature, molar mass of the PLA-CTA and choice of DVB isomer are shown to strongly influence the porous properties of the matrix.

4.1 Introduction

Porous polymers are highly valued materials in separations, catalysis, ion-exchange, and templating.^{1,2} Although inorganic porous media, such as metal oxides or silica^{3,4} have shown longstanding utility, porous organic polymers engender unrivaled opportunities to tune porosity, surface chemistry, structure, and properties through material design and myriad preparative strategies. Such diverse application can leverage the processibility, mechanical integrity, and versatile surface functionality and composition afforded by an organic framework.

Block polymers naturally form materials structured on the nanometer length scale due to the covalent connectivity of incompatible segments.⁵ Tailoring the minority block to exploit selective chemical or thermal degradation techniques can convert self-assembled periodic nanostructures (5-100 nm) to well-ordered matrices of nanopores.⁶ However, block polymer materials producing a percolating pore structure and a continuous matrix structure (i.e., bicontinuous structures) are few.⁷⁻⁹ Typically, the long-range order needed for pore accessibility is achieved by employing a macroscopic alignment procedure, such as shear aligning or extrusion.¹⁰⁻¹² In addition, limited pore stability in thermally or chemically challenging environments requires the post-polymerization introduction of crosslinks within the matrix to form a robust thermoset, but these post-polymerization steps can become synthetically cumbersome.^{13,14}

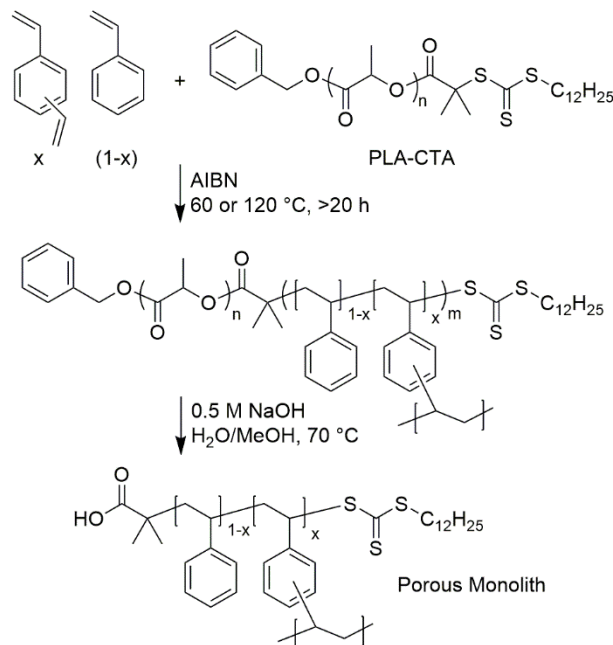
Alternative routes to porous materials have relied on facile free radical chemistries that deliver a permanent pore structure by crosslinking solids in situ.¹⁵⁻¹⁹ In such elaborations, a homogeneous monomer mixture containing large quantities of crosslinking agent and a nonreactive diluent, e.g. a polymer or solvent, is reacted in a conduit or mold. Simultaneous crosslinking and copolymerization lead to phase separation of an incipient polymer network. After removal of the solvent or macromolecular porogen, macropores (> 50 nm) are found within a three-dimensional inter-adhered globule morphology fixed via crosslinking. Well-developed empiricisms by Svec and Frechet^{17,20} and others,^{21,22} have enabled the porosity and pore size distribution to be predictably tuned using synthetic

variables such as the solvent (diluent) quality and amount, crosslinker-to-monomer ratio, initiator concentration, and polymerization temperature.

In a new approach, Seo and Hillmyer²³ combined the facile preparative methods of monolithic macropores with block copolymer self-assembly in a synthetic route generating a robust bicontinuous network of mesopores. The chemistry as highlighted in Scheme 1 utilizes an initially homogeneous liquid reaction precursor comprising a polylactide macromolecular chain transfer agent (PLA-CTA) in a multifunctional monomer mixture of styrene and divinylbenzene (DVB). Following thermal initiation, a P(S-*co*-DVB) block grows from the PLA-CTA via reversible addition fragmentation chain transfer (RAFT) polymerization, generating a block polymer architecture in situ. As the polymerization proceeds, crosslinking prevents the coarsening of locally segregated domains of PLA and polystyrene, retaining a microphase-separated morphology. Subsequent hydrolysis of the PLA block produces a porous monolith of interconnected voids.

The development of mesoscopic structure in this process coined polymerization-induced microphase separation (PIMS) relies on the kinetic competition of block polymer ordering and the gelation of a network within a single domain. Various parameters of the reaction, such as temperature, monomer-to-crosslinker ratio, and molar mass of the PLA CTA can potentially control the morphology of the monolith and the resulting porous properties. This chapter presents the preliminary results that probe and exploit reaction parameters that control the porosity of PIMS monoliths during their preparation. Porous monoliths were characterized in the dry state by SEM imaging, nitrogen sorption, and small-angle x-ray scattering. We find that simple variation of the reaction temperature and the relative composition of monofunctional and difunctional monomer mixtures can offer additional control over the resulting surface area and pore size distributions. These convenient synthetic manipulations help elucidate the fundamental controlling parameters for mesoporous and hierarchical pore structures formed using PIMS.^{24,25}

Scheme 4.1 Synthetic route to porous polymer monolith via polymerization-induced microphase separation.



4.2. Experimental Procedures and Characterization

4.2.1 Materials

All reagents were purchased from Sigma Aldrich and used as received unless otherwise noted. Styrene ($\geq 99\%$, stabilized) and divinylbenzene (80% technical grade consisting of 56% *m*-DVB, 24% *p*-DVB and 20% ethylstyrene) were filtered over basic alumina prior to use. Toluene was passed through a home-built solvent system comprising columns of activated alumina and molecular sieves. Azobisisobutyronitrile (AIBN) (98%) was recrystallized from methanol and dried under vacuum. (\pm)-lactide was provided by Altasorb, stored under a N_2 atmosphere and used as received.

4.2.2 Synthesis of *para*-divinylbenzene (*p*-DVB)

Preparation of the *p*-DVB isomer followed a previously reported procedure utilizing the Wittig reaction of the corresponding aldehyde.²⁶ Under argon, potassium *tert*-butoxide (21.3 g, 190.2 mmol) and methyltriphenylphosphonium bromide (64.7 g, 181.2 mmol)

were mixed to readily form the ylide as a bright neon yellow solution in dry THF at room temperature. The reaction was then cooled to 0 °C and stirred for 25 min. Terephthalaldehyde (12.0 g, 89.5 mmol) was dissolved in 100 mL of dry THF and added dropwise over 25 min as the solution turned to a deep royal blue. The reaction was allowed to warm to room temperature and stirred for 2h. The resulting purple mixture was poured into a separation funnel containing 300 mL of water, and the organic phase formed from the addition of diethyl ether was removed. The water phase was washed three times with *n*-hexane. The organic portions were combined, washed with brine and dried over anhydrous magnesium sulfate. The mixture was rotovapped and then distilled under vacuum at 40 °C. The final product solidified on standing (2.57 g, 22%). ¹H-NMR (500 MHz; CDCl₃): δ 7.37 (s, 4H, -C₆H₄-), 6.70 (dd, *J* = 11.0 and 17.7 Hz, H, CH₂=CH-), 5.75 (d, *J* = 17.4 Hz, 2H, cis-CHH=CH-), 5.24 (d, *J* = 11.0 Hz, 2H, trans-CHH=CH-).

4.2.3 Synthesis of polylactide macro-chain transfer agent (PLA-CTA)

The synthesis of hydroxyl-terminated polylactide was carried out according to a previously reported procedure.¹¹ Briefly, benzyl alcohol (anhydrous) initiator (110 μL, 1.1 mmol) and triethylaluminum catalyst (0.54 mL, 1.0 M in hexanes) were mixed in toluene (105 mL) and stirred in a pressure vessel overnight under inert atmosphere. (±)-lactide (15.05 g) was added, and the sealed vessel was heated in an oil bath at 90 °C for 2.6 h. The reaction was quenched with the addition of ca. 4 mL of 1 M HCl and isolated following precipitation in methanol and re-precipitation in hexanes (8.95 g PLA, 78 % conversion, 60 % yield).

(*S*)-1-dodecyl-(*S'*)-(α,α'-dimethyl-α''-acetic acid) trithiocarbonate, the chain transfer agent (CTA), was synthesized as previously reported.²⁷ The esterification of the CTA (2.7 eq) and hydroxyl terminus of the PLA followed the generation of the acid chloride intermediate through reaction with oxalyl chloride (98%, 4.0 eq) in dichloromethane.¹¹ Quantitative end-functionalization was assessed using ¹H NMR end-group analysis and SEC analysis of linear, low dispersity PLA-*b*-PS block polymers produced in the bulk polymerization of styrene monomer (120 °C, 5 h) using PLA-CTA as the macroinitiator.

4.2.4 Synthesis of nanoporous polymer monoliths

The four PLA-CTAs used in this study to initiate the copolymerization of styrene and divinylbenzene (DVB) in the presence of AIBN are described in Table 4.1. Polymer monoliths were prepared by dissolution of PLA-CTA in a single dram vial (ca. 2 mL) in a mixture of styrene and DVB previously prepared at a specified relative concentration. Following dissolution, AIBN (0.4 molar equivalents to PLA-CTA) was added as a 2 wt% solution in toluene. Reactions proceeded for 24 or 48 h in vials sealed with electrical tape and stirred in an oil bath at temperatures of 120 or 60 °C, respectively, without degassing. Monoliths produced were obtained as transparent yellow solids, unless otherwise indicated, and dried under reduced pressure for ~20 h. Monoliths were etched in a 0.5 M NaOH solution in 6/4 water/methanol (v/v) sealed within polypropylene bottles and heated for 3 d at 70 °C. Etched monoliths were well rinsed with water and methanol. The resulting porous monoliths were generally transparent solids. Complete removal of the PLA was confirmed by gravimetric analysis and IR spectroscopy. Because there is no simple or unambiguous method to determine the real crosslink ratio of the network, each monolith is referred to by the nominal molar content of technical grade DVB in the monomer feed unless otherwise specified.

Table 4.1 Molecular characterization of PLA-CTA precursors

Precursor ^a	$M_{n,NMR}$ (kg/mol) ^b	$M_{n,SEC}$ (kg/mol) ^c	$M_{m,SEC}$ (kg/mol) ^c	\bar{D}^c
PLA-CTA-8	6.0	8.0	9.0	1.21
PLA-CTA-18	22	18	19	1.02
PLA-CTA-19	19	19	20	1.02
PLA-CTA-35	38	34	36	1.04

^aPLA-CTA-X corresponds to the PLA-CTA of number-average molar mass X kg/mol as determined by SEC light scattering analysis. ^bNumber-average molar mass of PLA calculated from ¹H NMR spectroscopy based on the relative integration of the methine proton of the PLA backbone at 5.2 ppm and the aromatic protons of the benzyl alcohol initiator. ^cAbsolute molar-mass and dispersity were determined using SEC chromatography and laser light scattering analysis ($dn/dc = 0.049 \text{ mL g}^{-1}$).

4.2.5 Instrumentation

Solution state ¹H nuclear magnetic resonance (NMR) spectra were recorded on a Bruker Avance III HD 500 MHz spectrometer. Chemical shifts are reported in deuterated

chloroform and downfield relative to tetramethylsilane (TMS) at 0.0 ppm. Size exclusion chromatography (SEC) was performed in tetrahydrofuran (25 °C, 1 mL/min) using an Agilent 1260 Infinity liquid chromatograph equipped with three Waters Styragel HR columns, a Wyatt DAWN Heleos II 18-angle laser light scattering detector, and a Wyatt OPTILAB T-rEX refractive index detector. Absolute molar mass of PLA precursors was determined using laser light scattering analysis ($dn/dc = 0.049 \text{ mL/g}$).²⁸ Thermogravimetric analysis (TGA) was performed on a TA Instruments Q500 under nitrogen atmosphere at a heating rate of 10 °C/min with typical sample size of 10–15 mg. Differential scanning calorimetry (DSC) experiments were performed on a TA Instruments Discovery DSC. Heating and cooling ramps were applied at 10 °C/min to samples of 5-10 mg sealed in aluminum hermetic T-zero pans. Glass transition temperatures (T_g) were estimated on the second heating. Small-angle X-ray scattering (SAXS) data was acquired at the DND-CAT (5-ID-D beamline) at the Advanced Photon Source (APS) located at the Argonne National Laboratory (Argonne, IL). Two-dimensional SAXS patterns were collected on a Mar CCD area detector exposed using a wavelength of 0.7293 Å and a sample-to-detector distance of 3968 or 5680 mm. Samples were exposed without prior annealing at room temperature and adhered to the sample stage using Kapton tape. Azimuthal integration of the 2-D patterns provided the one-dimensional form of intensity as a function of the scattering vector, q , where $q = (4\pi/\lambda) \sin(\theta/2)$ (θ is the scattering angle and λ is the X-ray wavelength). Scanning electron microscopy data was acquired on a Hitachi S-4700 cold FEG-SEM using an accelerating voltage of 3 kV and the upper secondary electron detector. Samples were cryo-fractured and sputter coated with ca. 1-2 nm of Pt prior to imaging. Nitrogen sorption isotherms were obtained on a Quantachrome Autosorb iQ²-MP at liquid nitrogen temperature (77 K). Samples were degassed for 20 h at room temperature prior to measurement using a turbomolecular pump. Specific areas were obtained from BET analysis of the absorption branch ($p/p_0 = 0.05-0.35$).²⁹ Total specific pore volumes were determined from the distinct plateau at high relative pressure at $p/p_0 = 0.95$. Mesopore size distributions were estimated using a quenched solid density functional theory (QSDFT) kernel for the adsorption branch of nitrogen on carbon using a cylindrical pore model.³⁰

4.3 Results and Discussion

4.3.1 Crosslinker Content

Whereas microphase-separated states of a diblock copolymer at equilibrium primarily depend on the volume fraction, f , and the segregation strength given as χN , where χ is a measure of the incompatibility of the two blocks and N is the degree of polymerization, the PIMS morphology results from a kinetic competition between crosslinking and *microphase* separation. Monoliths formed using PIMS at compositions containing 20 mol% DVB have been previously shown to produce a disordered co-continuous morphology, attributed to the covalent arresting of a block polymer fluctuating in the disordered state.^{23,31,32} The premise of PIMS implies that should the polymerization proceed in the absence of crosslinker, a periodic ordered phase will nucleate as the systems crosses the order-disorder transition due to concurrent increases in N from the N of the PLA block and f of styrene from 0. Conversely, monomer mixtures containing larger quantities of DVB (> 20 mol%) may prematurely crosslink, arresting a spatially homogeneous structure prior to microphase separation that generates no pore structure.

The SAXS data of Figure 4.1a illustrate the dependence of the PIMS monolith morphology on the crosslinker-to-monomer ratio. Samples were prepared at fixed concentration of PLA-CTA-18 (32 ± 2 wt%) while varying the mole fraction of the crosslinking agent (DVB) in the monomer from 0 (pure styrene) to 100 mol% (technical grade DVB). Monoliths of ≤ 2 mol% DVB exhibit distinctive patterns with prominent scattering maxima at $q/q^* = 1, 2, 3, 4$ consistent with a lamellar microstructure. Although a cylindrical morphology is expected for block polymers of $f_{\text{PLA}} \approx 0.3$, termination reactions at high conversion may lead to increased molar mass dispersity that shifts the lamellar phase window to higher compositions of the disperse block.³³ In contrast, compositions at ≥ 5 mol% DVB lack periodic order but retain a broad scattering maximum that is characteristic of a disordered, microphase-separated state with structural heterogeneities between 20 and 27 nm. At moderate crosslinker compositions of 10-40 mol% DVB, a weak higher-order maximum at $q/q^* \approx 2$ signifies a greater extent of local order.³⁴ However, broadening of the primary peak and coincident attenuation of the

secondary shoulder as the DVB concentration is increased further (> 40 mol%) suggest that extensive crosslinking at low segregation strength (at low N) may preclude the development of a steep compositional profile and well-defined interface; the decrease of the Porod exponent from ca. 4 to 3 as the DVB content increases from 20 to 100 mol% further supports the transition from a flat and sharp interface to one that is rough and diffuse.³⁵

Treatment of the monolith with basic solution at 70 °C results in hydrolytic degradation of the PLA domain within 3 d, generating a porous structure that retains the structural heterogeneities of the unetched material for samples containing ≥ 5 mol% DVB (Figure 4.1b). Notably, the scattering pattern of the etched 2 mol% sample may suggest that below some critical crosslink density partial pore collapse can be induced at temperatures below the glass transition temperature of bulk polystyrene, a result common to lamellar microstructures.^{36,37}

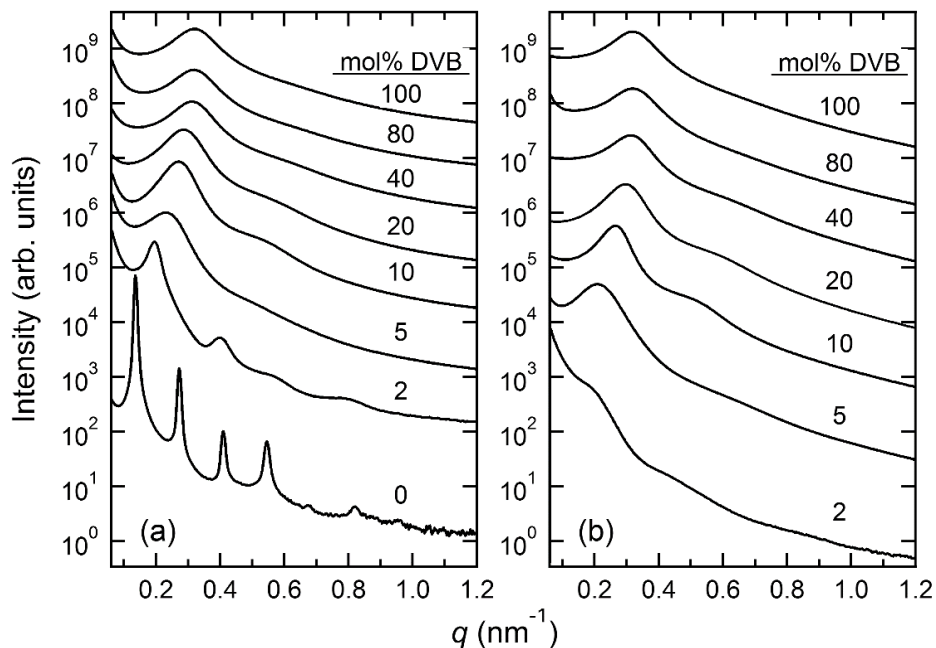


Figure 4.1 Small angle x-ray scattering of monoliths prepared via PIMS from PLA-CTA-18 (a) before and (b) after etching of the PLA. Curves have been vertically shifted for clarity. The crosslinking agent DVB prevents nucleation of an ordered phase retaining the cocontinuity of the disordered, microphase-separated state. High crosslink densities (> 40 mol% DVB samples) show reduction in the local order with the suppression of the higher order correlation peak at $q/q^* \approx 2$. SAXS data has not yet been obtained for the etched 0 mol% DVB sample.

Nitrogen sorption isotherms at 77 K of the etched sample series are shown in Figure 4.2. The specific surface area of each sample determined using the Brunauer-Emmett-Teller (BET) method is indicated.²⁹ Although correct analysis of the pore size distribution requires careful consideration of the model assumptions used to interpret the isotherm, known qualitative correlations between the shape of the hysteresis loop and mesoporous features can suggest changes in pore structure as the crosslinker content is varied. The isotherm of the 2 mol% DVB sample exhibits type H3 hysteresis indicative of slit-shaped pores consistent with the notion of partial collapse of lamellae suggested from SAXS.^{38,39} Conversely, samples of >5 mol% DVB show a comparable isotherm shape and a well-defined H2 hysteresis indicative of disordered mesopores. Additionally, the gradual rise of

the adsorption branch at lower relative pressures evinces a broad distribution of smaller pores as DVB concentration is increased for samples of 40 and 100 mol% DVB. Although the initial volume of PLA in the crosslinked monoliths is approximately constant (0.38 mL/g, based on the density of PLA, $\rho_{\text{PLA}} = 1.25 \text{ g/mL}$), greater crosslink densities result in more nitrogen absorbed at high relative pressure; according to the summarized data of Table 4.2, for all samples $\geq 40 \text{ mol\%}$, the total pore volume exceeded the anticipated pore volume and reached a maximum of 0.54 mL/g in the 100 mol% DVB sample. This pore volume can not be accounted for by the presence of ethylstyrene in commercial DVB, and furthermore, near closure of the low-pressure hysteresis loop for the samples of highest DVB content suggests that matrix swelling or N_2 dissolution within the polymeric walls cannot account for this excess volume.^{39,40}

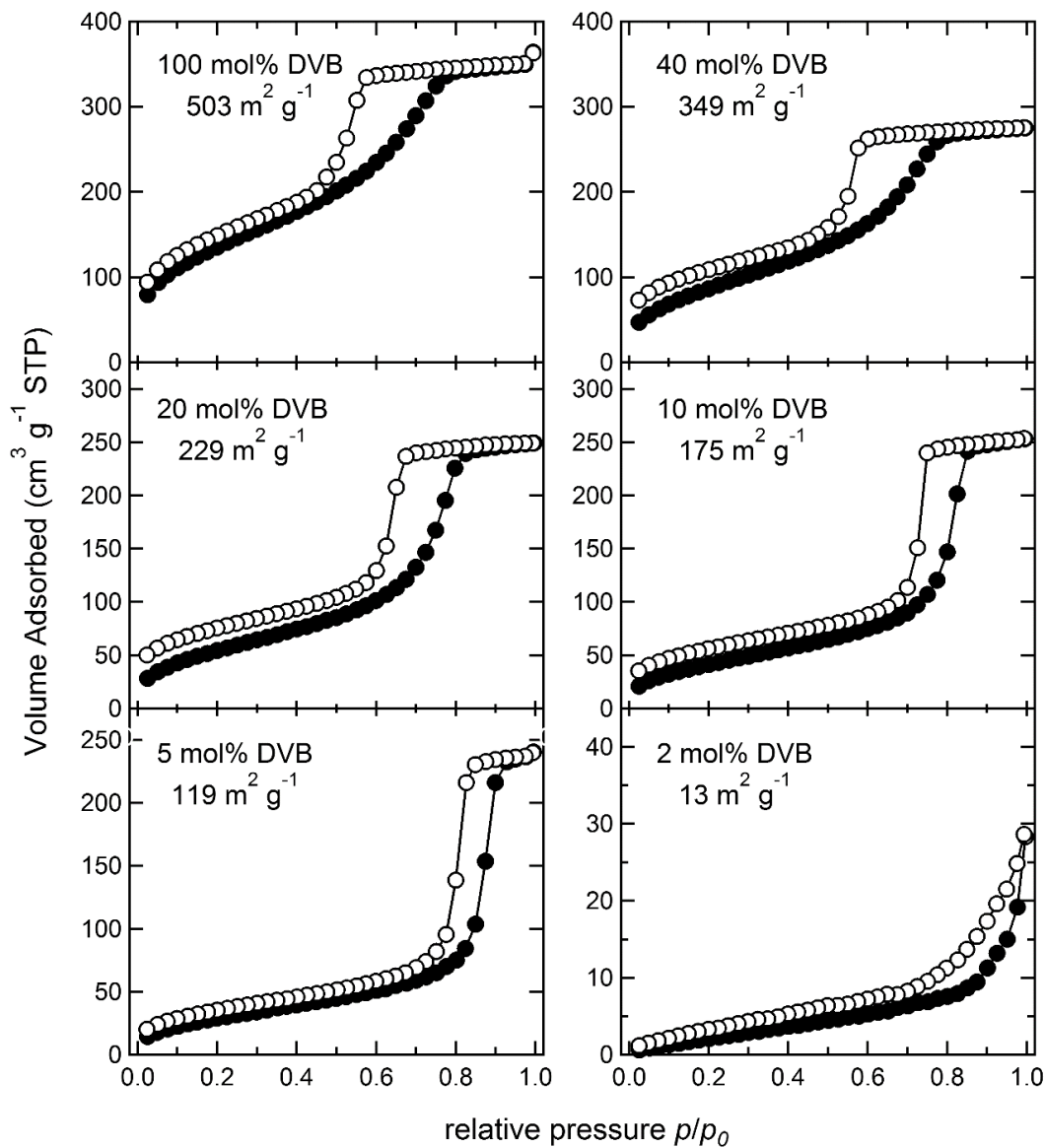


Figure 4.2 Nitrogen sorption isotherms obtained under adsorption (\bullet) and desorption (\circ) for monoliths prepared using PLA-CTA-18 and various compositions of the styrene/divinylbenzene monomer mixture expressed as mol% DVB. The BET specific surface areas are indicated.

Table 4.2 Porous characteristics of samples prepared using precursor PLA-CTA-18

DVB content (mol%)	W_{PLA}	SA_{BET} (m ² /g)	$V_{\text{p}}^{\text{total}}$ (cm ³ /g)	Pore mode (nm)
100	0.32	503	0.54	6.8
80	0.32	392	0.42	6.8
40	0.32	349	0.42	7.1
20	0.30	229	0.38	8.1
10	0.32	175	0.39	9.6
5	0.32	119	0.37	11.8
2	0.31	13	-	-
0	0.33	-	-	-

In disordered porous materials, a convolution of effects may prevent evaporation from occurring at equilibrium, such as adsorbate metastability, pore blocking, network percolation, and cavitation, and thus the desorption branch shape and position becomes uncorrelated to pore size.³⁹ We therefore chose to fit experimental adsorption isotherms using a kernel for cylindrical pores obtained using quenched solid density functional theory (QSDFT) to calculate the pore size distribution (PSD). Although commonly employed in the literature, we avoided the use of macroscopic models like the Barret-Joyner-Haleda (BJH) method in our analysis as such models have been shown to significantly underestimate pore size.^{30,39} The resulting PSDs are shown in Figure 4.3. The average pore size decreases and the distribution becomes multimodal as the crosslinker content is increased; a result consistent with the substantial increases in specific surface area obtained from BET analysis. Variation of the DVB content fine-tunes the largest mode of the distribution, likely attributable to the voided co-continuous channels resulting from the removal of the PLA domain, but high crosslink densities (≥ 40 mol%) also generate sub-structural voids that approach the microporous lengthscale (< 2 nm). It is unlikely that PLA removal is linked to the generation of these small mesopores because the total pore volume exceeds the original PLA volume as determined using TGA and gravimetric analysis after etching.

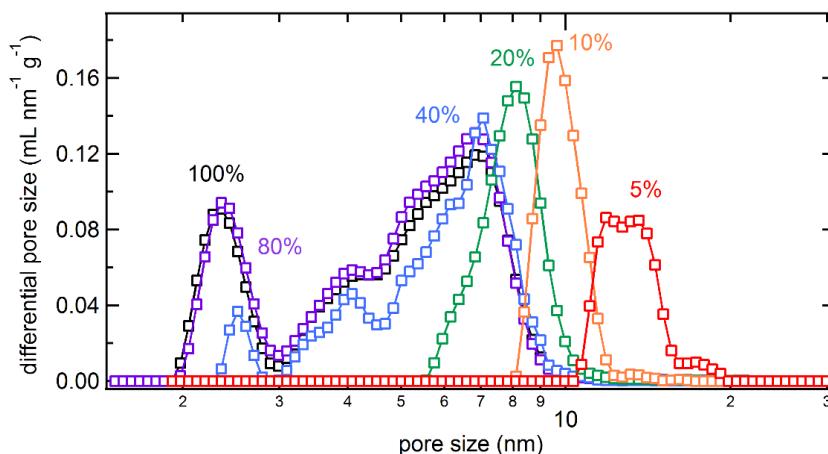


Figure 4.3 Mesopore size distributions based on QSDFT analysis of the adsorption branch of monoliths prepared from ≥ 5 mol% DVB monomer mixtures at 120 °C.

Scanning electron micrographs (Figures 4.4a-b and 4.5a-b) show that samples with crosslinker contents of 10 and 20 mol% comprise a porous skeleton of elongated and interlaced globules. As the crosslinker content exceeds 40 mol% (Figures 4.4c-d and 4.5c-d), the mesoporous voids shrink in a morphology of compact semi-spherical nodules. This is consistent with the sorption measurements of the high DVB content samples in which the larger surface areas indicated smaller globules and pores. The concomitant broadening of the PSD and excess pore volume suggest some additional levels of internal organization within the globules or between their clusters, but it is unclear if this evolving pore structure is due to some underlying aspect of phase separation or a molecular architecture that produces greater free volume.

In the growth of the second block, the propagating S/DVB radical participates in the competitive reactions of intra- and intermolecular crosslinking. An increased propensity for intramolecular cyclization accompanies the extensive branching that occurs with increasing amounts of crosslinker. At high DVB concentrations, the accumulation of intramolecularly-cyclized microgels may ultimately cause macrogelation through loose bridging of the microgels in the cocontinuous P(S-co-DVB) matrix, leading to the formation of the observed compact semi-spherical nodes.^{15,16} Connectivity between the microgels at high DVB concentrations is primarily due to an interparticular crosslinking

reaction between pendant vinyl groups of the neighboring microgel particles. The cross-linked character of the particles prevents them from mutual penetration. Evidence of this loose-bridging has been shown by separation of the monolith into macroglobules upon swelling a monolith in good solvent for polystyrene. A monolith prepared from 20 mol% DVB immersed in dichloromethane for 3 d could not be isolated as one continuous piece as it had fragmented into swollen and dispersed portions of polymer

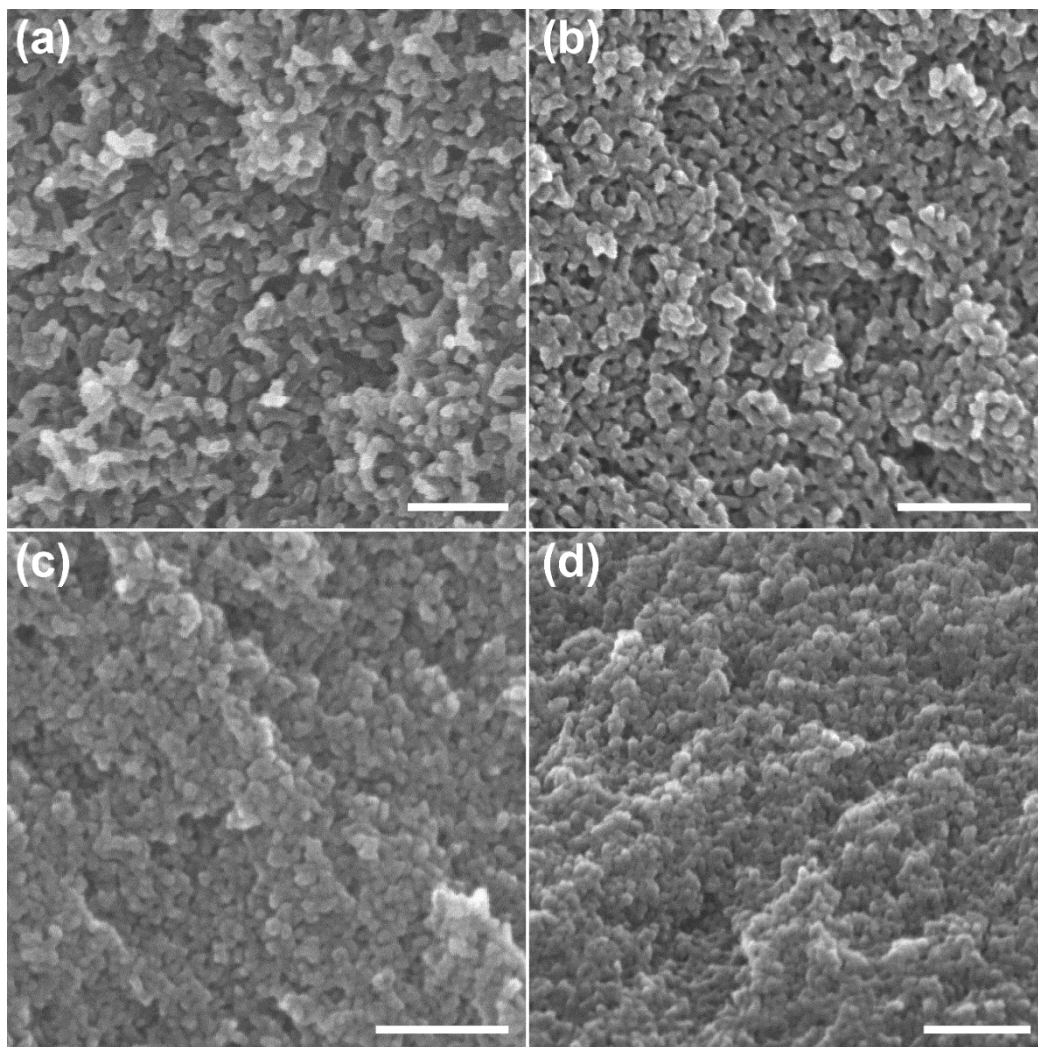


Figure 4.4 Scanning electron micrographs of etched monoliths derived from PLA-CTA-18 and monomer mixtures of (a) 10, (b) 20, (c) 40, and (d) 80 mol% DVB synthesized at 120 °C. Samples were coated with 1-2 nm of Pt prior to imaging. Scale bars represent 200 nm.

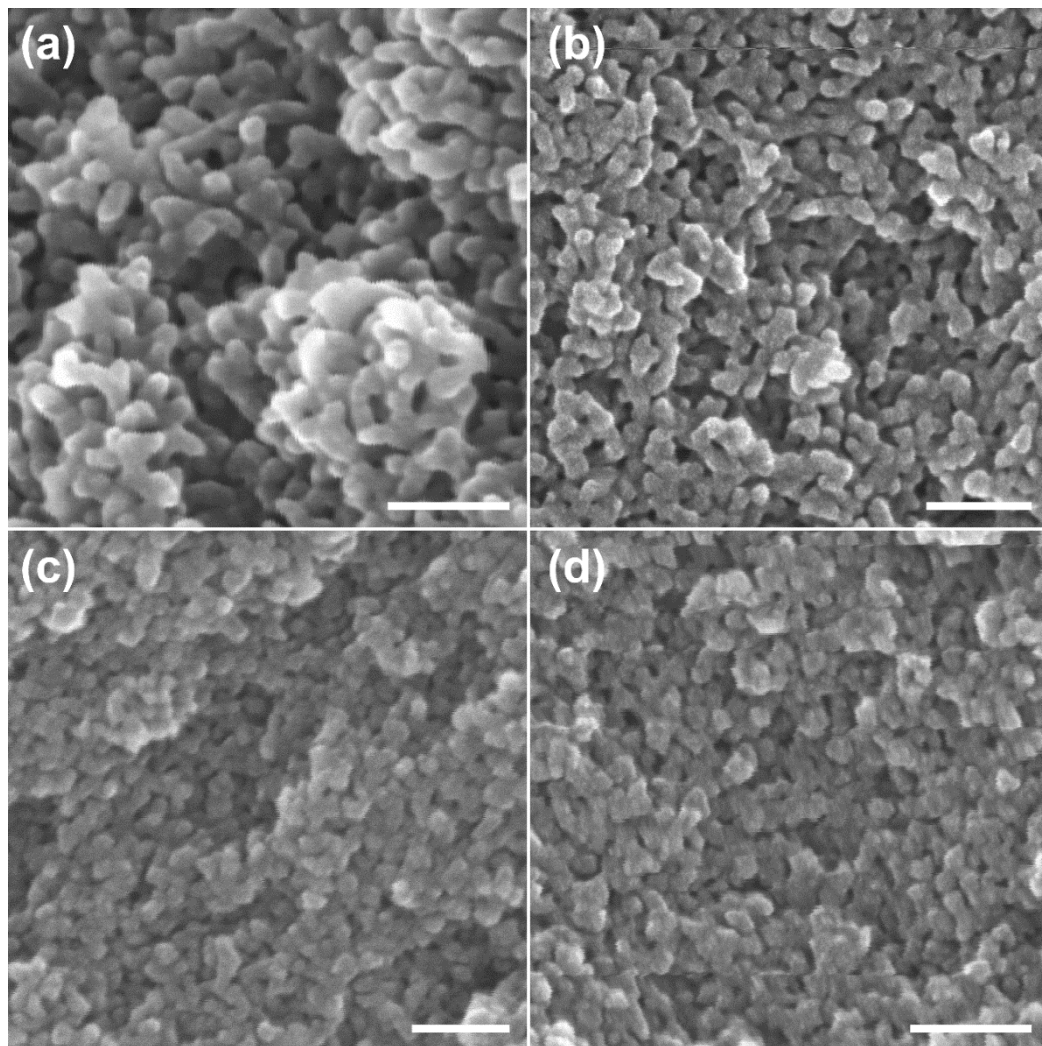


Figure 4.5 Scanning electron micrographs of Figure 4.4 visualized at higher magnification. Etched monoliths were prepared from PLA-CTA-18 and monomer mixtures of (a) 10, (b) 20, (c) 40, and (d) 100 mol% DVB. Samples were coated with 1-2 nm of Pt prior to imaging. Scale bars represent 100 nm.

4.3.2 Effect of PLA-CTA Molar Mass and Content

Chain extension from the PLA macroinitiator leads to a block polymer architecture that restricts local composition fluctuations to a length-scale proportional to the radius of gyration of the growing polymer. At a fixed mass-fraction of PLA-CTA in the monomer mixture, the degree of polymerization of styrene and DVB per molecule at fixed conversion will increase for higher molar mass PLA-CTAs because of a lower number of propagating

chains, thereby increasing the produced block polymer size. Figure 4.6 shows the small-angle X-ray scattering profiles of crosslinked monoliths synthesized from 8, 19, and 34 kg mol⁻¹ PLA-CTA at 120 °C. As the molar mass of the PLA-CTA increases roughly fourfold, the principal scattering maxima shifts towards lower q , increasing the domain spacing from ca. 13 to 29 nm. A more intense and narrow primary peak observed for samples produced from 34 kg mol⁻¹ PLA-CTA for crosslink densities of 20 and 100 mol% DVB indicate that stronger segregation at larger N results in stronger composition fluctuations prior to arrest. These results suggest that higher domain purity and narrower interfacial width is produced from higher molar mass macro-CTAs, which, notably, may be leveraged for improved domain functionality in applications using PIMS.^{32,41}

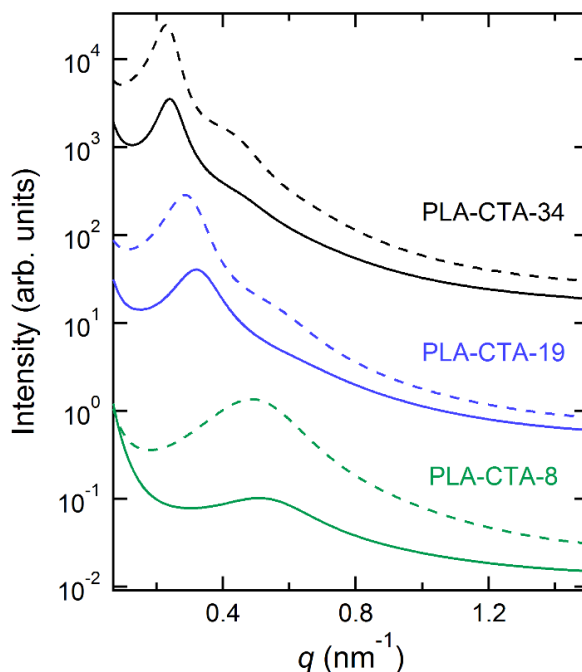


Figure 4.6 Small angle X-ray scattering of monoliths prepared using 20 (dashed lines) and 100 mol% DVB (solid lines) at 120 °C, illustrating the dependence of the domain periodicity on the molar mass of the PLA-CTA precursor.

In principle, monoliths derived from the lowest molar mass precursor, PLA-CTA-8, should produce exceptionally small mesopores. Although the reaction of PLA-CTA-8 in

styrene and DVB at 120 °C and subsequent etching in basic solution produced monoliths of similar consistency and color as the PLA-CTA-18 monoliths, nitrogen sorption analysis revealed contrasting features (Figure 4.7). Crosslinker contents that produced well-defined and continuous pores in samples derived from PLA-CTA-18 proved inadequate for PLA-CTA-8, resulting in essentially nonporous samples as indicated by low adsorption and surface areas for compositions ≤ 20 mol% DVB. Observation of some porosity at higher crosslink density suggests that the generation of smaller pores from PLA-CTA-8 leads to high Laplace pressure and matrix instabilities, thus requiring increased DVB contents to prevent pore collapse. These observations are consistent with previous work which has shown that increased crosslink density stiffens the nanoporous matrix to counterbalance the internal stresses that accompany pore size reduction.^{13,14,42} With the number of crosslinks increasing, at a composition 60 mol% DVB the surface area rises to 446 m²/g, but the total pore volume remains slightly less than expected given the initial volume of PLA-CTA, implicating some persistent pore collapse (see Table 4.3). Ultimately, the use of pure DVB (100 mol%) is required to sufficiently crosslink the matrix and retain the expected total pore volume, a result that suggests a lower limit on the pore size obtainable through reduced molar masses of PLA-CTA. Interestingly, sorption isotherms of monoliths derived from PLA-CTA-8 exhibit concavity to the p/p_0 axis, resembling that of the type I isotherms characteristic of micropores (pore width < 2 nm), yet application of so-called t -plot analysis did not reveal any micropore volume.^{39,43} Additional features in the isotherm data, including the small hysteresis loop and closure at ca. $p/p_0 = 0.42$, do not reflect the porous properties of the matrix; this closure point is currently understood to represent the limit of metastability for condensed N₂ at 77 K in disordered porous materials.³⁹

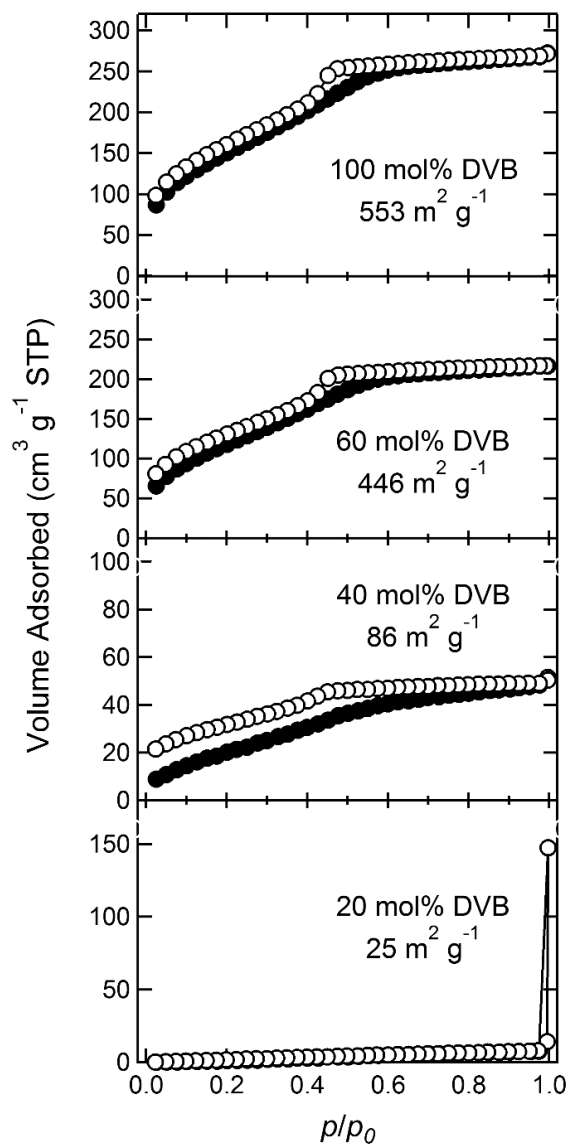


Figure 4.7 Nitrogen sorption isotherms obtained under adsorption (●) and desorption (○) for monoliths prepared using 8 kg mol^{-1} PLA-CTA-8 dissolved in various styrene/divinylbenzene monomer mixtures with compositions expressed as mol% DVB. The measured BET surface areas are indicated.

Table 4.3 Porous characteristics of samples prepared using precursor PLA-CTA-8

DVB content (mol%)	W_{PLA}	S_{ABET} (m ² /g)	$V_{\text{p}}^{\text{total}}$ (cm ³ /g)	Pore mode (nm)
100	0.32	553	0.41	4.5
60	0.34	446	0.34	4.5
40	0.32	86	0.07	4.4
20	0.32	25	0.01	-

Examination of the small-angle X-ray scattering data of the PLA-CTA-8 samples may indicate a scattering signature for monoliths that suffer pore collapse. A single broad scattering maximum indicates that as-prepared samples assume microphase separated but disordered state (Figure 4.8, dashed curves). Upon etching, an additional scattering component at low angle emerges, reminiscent of the macrophase separation induced in binary blends of block polymer and added homopolymer.⁴⁴ We speculate that this low-angle component reflects a structure of coexistent long-range concentration fluctuations and residual microstructure resulting from partial pore collapse. The reduction of the low angle scattering component as increased loadings of DVB stiffen the matrix and prevent pore collapse supports this interpretation.

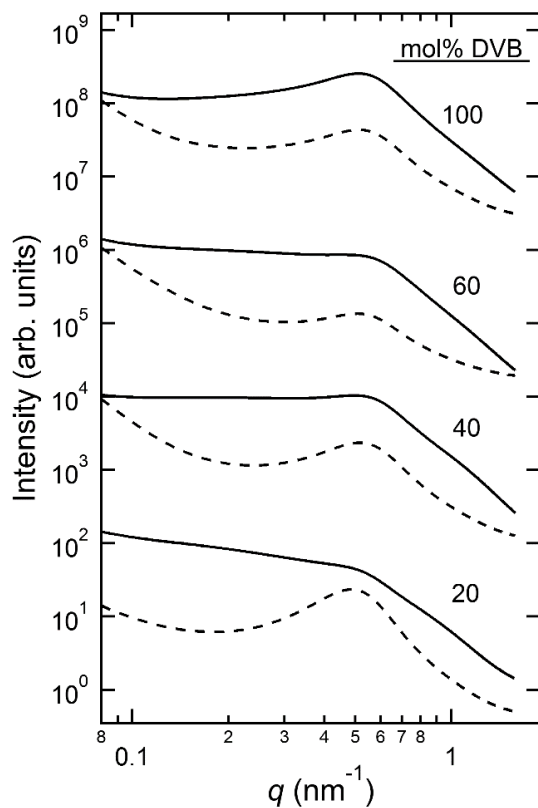


Figure 4.8 Small angle x-ray scattering of monoliths prepared from PLA-CTA-8 before (dashed line) and after etching (solid line) of the PLA. A signature of pore collapse may be the growth of a scattering component at low-angle after etching.

The PSD calculated from the adsorption branch of the isotherm using the QSDFT cylindrical kernel illustrates the retention of the porous structure as the DVB content increases (Figure 4.9a). We note that although QSDFT can provide an estimate of the PSD over the entire range of micro- and mesopores, the range of measured relative pressures limits estimation of the PSD down to 2 nm. For PLA-CTA-8 etched monoliths, the void channels produced from the removal of the percolating PLA domains increase in number and give rise to the principal pore mode at ca. 4.5 nm. At higher concentrations of DVB (≥ 60 mol%), the distribution evolves a shape similar to that observed for the PLA-CTA-18 monoliths exhibiting multiple pore modes. The consistent populations of smaller pores centered around 2.1 and 3.2 nm produced in samples from two different molar masses of

PLA-CTA as compared in Figure 4.9b suggest that the pores originate from the crosslinked matrix rather than the sacrificial component.

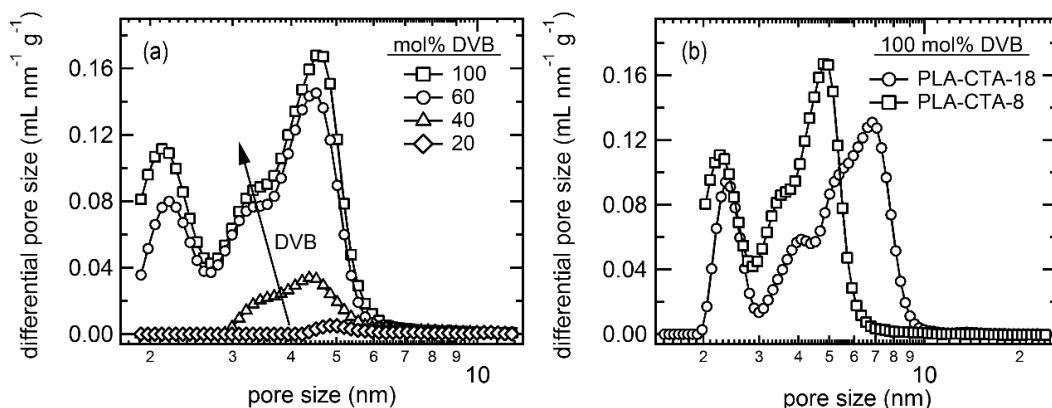


Figure 4.9 (a) Mesopore size distributions of monoliths prepared from PLA-CTA-8 at 120 °C based on QSDFT analysis of the adsorption branch show a better retention of a porous structure with increased amounts of crosslinking. (b) Comparison of the pore structures produced using solutions of PLA-CTA-18 and PLA-CTA-8 in 100 mol% DVB at 120 °C.

In the block copolymerization of styrene and DVB from PLA-CTA, an inhomogeneous distribution of crosslinks is inherently produced. Assuming equal reactivity, the presence of two vinyl groups ensures that the crosslinker is consumed at twice the rate as the monovinyl monomer. Reactivity ratios of styrene-DVB copolymerization in particular bias the initially formed blocks to be far more enriched with crosslinker than the initial monomer mixture.^{45,46} Therefore, a high local concentration of pendant vinyl groups surround the macroradical of the initial growing DVB coil, increasing its probability to form an intramolecular loop. This intramolecular cyclization begins to shrink the coil and convert it to a densely crosslinked microgel. The remaining monomer swells the formed microgels, which continue to grow leading to a nonporous, highly crosslinked region of network. As the P(S-co-DVB) and PLA domains locally segregate, however, the microgels aggregate but cannot coalesce at high concentrations of DVB due to the rigidity of their networks. Although mechanistically similar to crosslinked macroporous styrenic monoliths, the diblock architecture covalently links the PLA to the growing crosslinked

network and confines structure formation to the mesoporous lengthscale. We posit that the agglomeration of these microgels forms the porous interstices of the etched PLA-*b*-P(S-*co*-DVB) monoliths observed in the PSDs at high concentrations of crosslinker. Moreover, the bulky nature of the increasingly cyclized and crosslinked microgels reduce the PLA chain density at the interface, and these chains must therefore contract to fill space uniformly, leading to the slight decrease in the domain spacing (Figures 4.1 and 4.9) and principal pore mode with increased crosslinker content.

4.3.3 Effect of isomer content

All PIMS-based materials reported to-date have utilized mixtures of styrene and technical grade DVB, which contains 20 mol% monofunctional ethylstyrene and a mixture of *m*-DVB and *p*-DVB isomers. Given their relative reactivity, DVB constituents are more tightly embedded in the incipient network at early reaction times. In particular, *p*-DVB is unequivocally more reactive than *m*-DVB, and studies have shown that *p*-DVB/styrene networks swell less than resins composed of other isomer mixtures, implicating a more inhomogeneous distribution of crosslinker and a greater propensity for intramolecular cyclization.⁴⁶ Consequently, use of pure *p*-DVB in lieu of other isomer mixtures in PIMS monoliths may result in higher surface areas due to smaller globules and smaller interstices within the crosslinked domain. Furthermore, previous studies on the homopolymerization of DVB have shown the pendant vinyl group of *p*-DVB to be less reactive, and therefore, the use of pure *p*-DVB may offer additional advantages, including higher monomer conversions prior to gelation and a higher content of unreacted pendant vinyl groups useful for post-polymerization surface functionalization.⁴⁷⁻⁴⁹

We explored the influence of the enhanced reactivity of *p*-DVB on the porosity of PIMS monoliths using PLA-CTA-8 and PLA-CTA-19. Each macro-CTA was dissolved in mixtures of styrene and pure *p*-DVB and reacted at 120 °C. Subsequent etching in mild basic solution produced the porous materials summarized in Table 4.4. Their isotherms (Figure 4.10) reiterate findings that both the surface area and the amount of N₂ adsorbed increase as the crosslinker concentration increases. Fair comparisons to monoliths prepared from technical grade DVB must account for the presence of ethylstyrene in the commercial

product; therefore, PLA-CTA-18 monoliths composed of 100 mol% DVB and 80 mol% *p*-DVB show that the use of pure *p*-DVB increases the specific surface area and pore volume ca. 80 m²/g and 0.1 mL/g, a result supporting our hypothesis that greater intramolecular cyclization yields a smaller globule and hence smaller interstice. In fact, the use of *p*-DVB alone produces the highest surface areas obtained in exclusively mesoporous PIMS monoliths, reaching 641 and 796 m²/g PLA-CTA-19 and PLA-CTA-8 monoliths, respectively.

Table 4.4 Porous characteristics of samples prepared using *p*-DVB

Precursor	<i>p</i> -DVB content (mol%)	W_{PLA}	S_{ABET} (m ² /g)	$V_{\text{p}}^{\text{total}}$ (cm ³ /g)	Pore mode (nm)
PLA-CTA-19	20	0.33	305	0.44	7.6
PLA-CTA-19	80	0.33	584	0.61	7.1
PLA-CTA-19	100	0.33	641	0.67	7.1
PLA-CTA-8	100	0.32	796	0.62	4.7

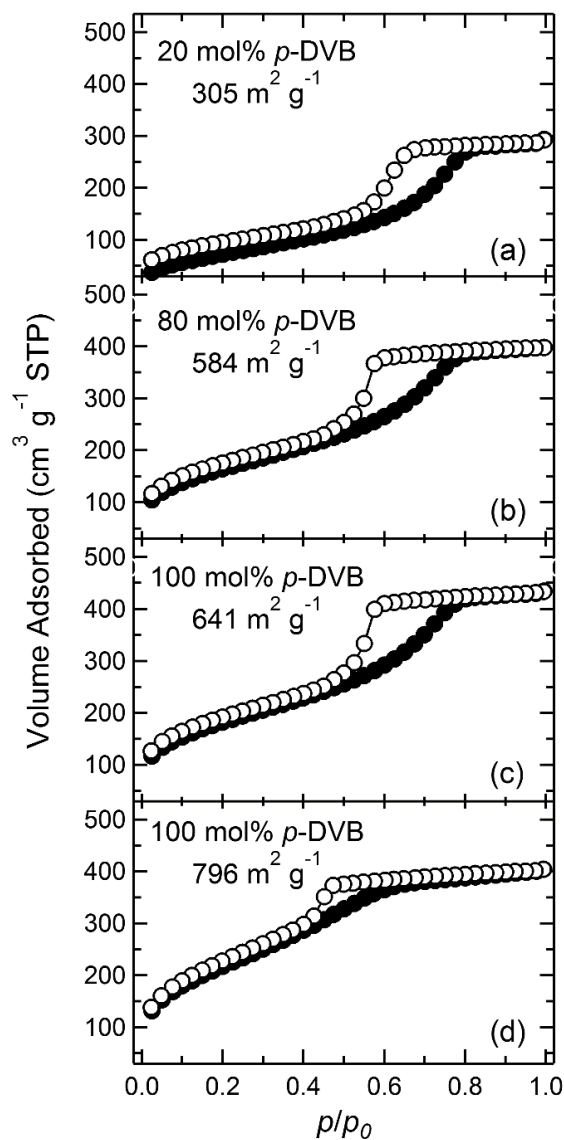


Figure 4.10 Nitrogen sorption isotherms obtained under adsorption (●) and desorption (○) for monoliths prepared using (a, b, c) PLA-CTA-18 and (d) PLA-CTA-8 dissolved in monomer mixtures using only the *p*-DVB isomer with compositions expressed as mol% *p*-DVB. The corresponding BET surface area for each sample is indicated.

4.3.2 Effect of polymerization temperature

The effect of polymerization temperature was probed by comparison of the microstructure and porous properties of monoliths prepared at 60 and 120 °C using varied concentrations of crosslinking agent. Polymerizations were run for 2 d at 60 °C and 24 h

at 120 °C to ensure high conversion of monomer at each temperature. All reactions using PLA-CTA-8 produced a monolith yielding a broad principal scattering maximum characteristic of the disordered bicontinuous morphology (Figure 4.11). A comparison of the primary peak position shows that the PIMS system does not conform to the strong segregation regime, in which the scaling of domain spacing with $\chi^{1/6}$ would estimate a 1.05 factor increase at 60 °C relative to 120 °C using the interaction parameter for PS-*b*-PLA; on the contrary, the decreased reaction temperature leads to only minute variation of q^* with a typical decrease in domain spacing of < 0.3 nm.^{10,50} The result suggests that, notwithstanding the narrowed peak breadth at 60 °C, the final microstructure is dictated primarily by reaction kinetics rather than thermodynamic incompatibility.

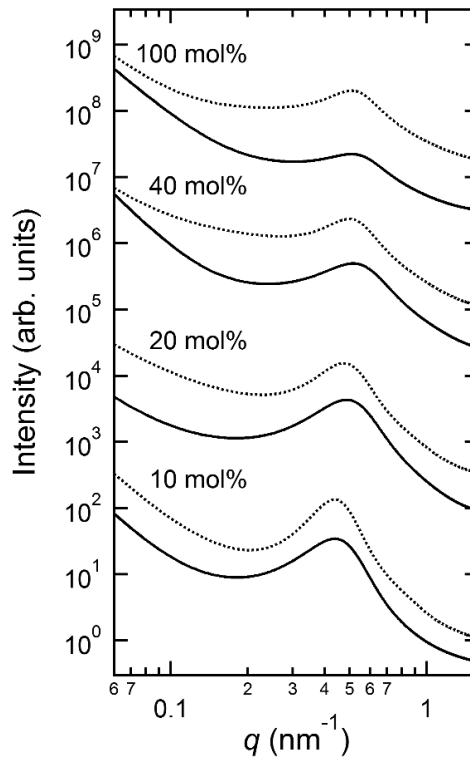


Figure 4.11 Small angle X-ray scattering of monoliths prepared from PLA-CTA-8 at 60 and 120 °C (dashed and solid lines, respectively). A higher polymerization temperature results in a minute variation in the location of q^* , indicating a weak dependence of the primary length-scale on temperature. The increase in segregation strength is captured by the reduction in primary peak width for monoliths synthesized at 60 °C.

Figure 4.12 maps the porous properties of produced monoliths in terms of their BET surface areas as a function of DVB content and temperature, illustrating that greater crosslink densities and higher reaction temperatures produce larger surface areas. At 120 °C, thermal dissociation of AIBN and autoinitiation of styrene contribute to a greater number of PLA-CTA propagating radicals that compete with the remaining monomer. This may suggest that a larger number of chains grow into globules such that their overall sizes and interstitial voids remain relatively small, however, the pore sizes remain approximately unchanged. In fact, the determined PSDs only reflect a greater number of pores. Therefore, elevated crosslinking rates at high temperature may primarily contribute to the observed increases in surface areas and pore volumes by creating a more rigid matrix that limits pore collapse.⁵¹

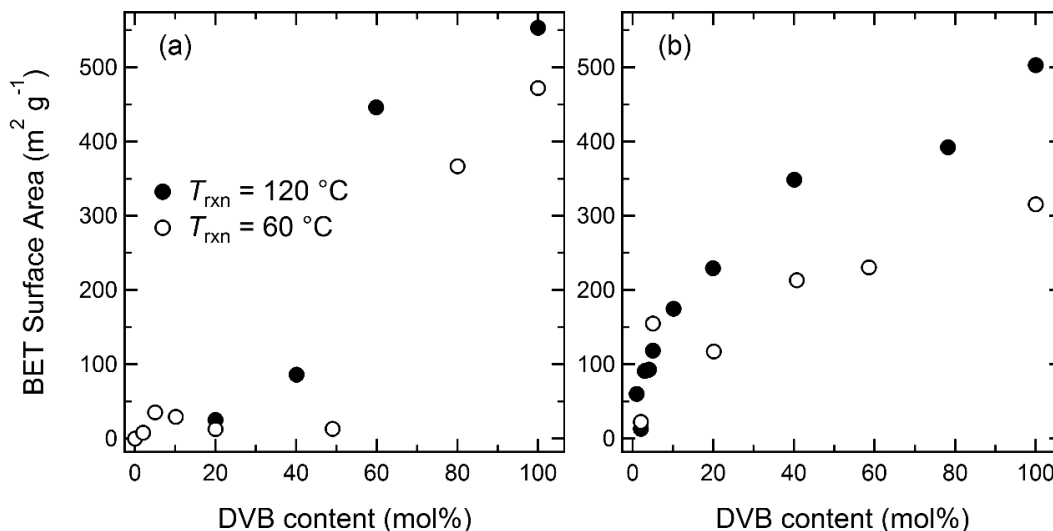


Figure 4.12 BET equivalent surface area of porous monoliths as a function of DVB content for (a) PLA-CTA-8 synthesized at 60 and 120 °C and (b) PLA-CTA-18 and PLA-CTA-19 synthesized at 60 and 120 °C, respectively. Matrix instability leads to pore collapse and low surface areas for PLA-CTA-8 monoliths formed using ≤ 50 mol% DVB.

4.4 Conclusions

The preparation of mesoporous crosslinked polymer monoliths from the bulk polymerization of styrene and DVB in the presence of macromolecular PLA-CTA was investigated. The morphology and porosity of the crosslinked matrix was tuned through variation of the crosslinker-to-monomer ratio, temperature, molar mass of the PLA-CTA and choice of DVB isomer. The crosslinked framework provides two distinct pore populations derived from the bicontinuous channels of the hydrolyzed PLA and small interstitial voids formed within the matrix, with the latter increasing in number at high crosslink densities. Higher temperatures lead to higher surface areas and pore volumes, a result likely attributable to greater crosslink densities. Use of the *p*-DVB isomer in lieu of technical grade DVB increases the porosity of the network. These observations will facilitate the implementation of PIMS in applications where mesoporous or hierarchical pore structures^{24,25} are needed.

4.5 References

- (1) Lu, G. Q.; Zhao, X. S.; World Scientific.
- (2) Todd, E. M.; Hillmyer, M. A. In *Porous Polymers*; John Wiley & Sons, Inc.: 2011, p 31.
- (3) Schüth, F. *Chemistry of Materials* **2001**, *13*, 3184.
- (4) *Monolithic Silicas in Separation Science : Concepts, Syntheses, Characterization, Modeling and Applications*; Wiley-VCH: Hoboken, NJ, USA, 2010.
- (5) Bates, F. S.; Fredrickson, G. H. *Physics Today* **1999**, *52*, 32.
- (6) Hillmyer, M.; Abetz, V., Ed.; Springer Berlin / Heidelberg: 2005; Vol. 190, p 137.
- (7) Pitet, L. M.; Amendt, M. A.; Hillmyer, M. A. *Journal of the American Chemical Society* **2010**, *132*, 8230.
- (8) Chen, L.; Phillip, W. A.; Cussler, E. L.; Hillmyer, M. A. *Journal of the American Chemical Society* **2007**, *129*, 13786.
- (9) Li, L.; Schulte, L.; Clausen, L. D.; Hansen, K. M.; Jonsson, G. E.; Ndoni, S. *ACS Nano* **2011**, *5*, 7754.
- (10) Zalusky, A. S.; Olayo-Valles, R.; Wolf, J. H.; Hillmyer, M. A. *Journal of the American Chemical Society* **2002**, *124*, 12761.
- (11) Rzayev, J.; Hillmyer, M. A. *Journal of the American Chemical Society* **2005**, *127*, 13373.
- (12) Bailey, T. S.; Rzayev, J.; Hillmyer, M. A. *Macromolecules* **2006**, *39*, 8772.
- (13) Cavicchi, K. A.; Zalusky, A. S.; Hillmyer, M. A.; Lodge, T. P. *Macromolecular Rapid Communications* **2004**, *25*, 704.
- (14) Guo, F.; Andreasen, J. W.; Vigild, M. E.; Ndoni, S. *Macromolecules* **2007**, *40*, 3669.
- (15) Okay, O. *Progress in Polymer Science* **2000**, *25*, 711.
- (16) Nischang, I.; Teasdale, I.; Brüggemann, O. *Anal Bioanal Chem* **2011**, *400*, 2289.
- (17) Svec, F.; Frechet, J. M. J. *Chemistry of Materials* **1995**, *7*, 707.
- (18) Xie, S.; Allington, R.; Fréchet, J. J.; Svec, F. In *Modern Advances in Chromatography*; Freitag, R., Ed.; Springer Berlin Heidelberg: 2002; Vol. 76, p 87.

- (19) Kanamori, K.; Nakanishi, K.; Hanada, T. *Advanced Materials* **2006**, *18*, 2407.
- (20) Viklund, C.; Svec, F.; Fréchet, J. M. J.; Irgum, K. *Chemistry of Materials* **1996**, *8*, 744.
- (21) Kanamori, K.; Hasegawa, J.; Nakanishi, K.; Hanada, T. *Macromolecules* **2008**, *41*, 7186.
- (22) Barlow, K. J.; Hao, X.; Hughes, T. C.; Hutt, O. E.; Polyzos, A.; Turner, K. A.; Moad, G. *Polymer Chemistry* **2014**, *5*, 722.
- (23) Seo, M.; Hillmyer, M. A. *Science* **2012**, *336*, 1422.
- (24) Saba, S. A.; Mousavi, M. P. S.; Bühlmann, P.; Hillmyer, M. A. *Journal of the American Chemical Society* **2015**, *137*, 8896.
- (25) Seo, M.; Kim, S.; Oh, J.; Kim, S.-J.; Hillmyer, M. A. *Journal of the American Chemical Society* **2015**, *137*, 600.
- (26) Tanaka, S.; Matsumoto, M.; Goseki, R.; Ishizone, T.; Hirao, A. *Macromolecules* **2012**, *46*, 146.
- (27) Lai, J. T.; Filla, D.; Shea, R. *Macromolecules* **2002**, *35*, 6754.
- (28) Brutman, J. P.; Delgado, P. A.; Hillmyer, M. A. *ACS Macro Letters* **2014**, *3*, 607.
- (29) Brunauer, S.; Emmett, P. H.; Teller, E. *Journal of the American Chemical Society* **1938**, *60*, 309.
- (30) Gor, G. Y.; Thommes, M.; Cychosz, K. A.; Neimark, A. V. *Carbon* **2012**, *50*, 1583.
- (31) Lee, S.; Gillard, T. M.; Bates, F. S. *Aiche J* **2013**, *59*, 3502.
- (32) McIntosh, L. D.; Schulze, M. W.; Irwin, M. T.; Hillmyer, M. A.; Lodge, T. P. *Macromolecules* **2015**.
- (33) Lynd, N. A.; Hillmyer, M. A.; Matsen, M. W. *Macromolecules* **2008**, *41*, 4531.
- (34) Bates, F. S.; Wiltzius, P. *The Journal of Chemical Physics* **1989**, *91*, 3258.
- (35) Hammouda, B. *Journal of Applied Crystallography* **2010**, *43*, 716.
- (36) Bertrand, A.; Hillmyer, M. A. *Journal of the American Chemical Society* **2013**, *135*, 10918.
- (37) Seo, M.; Amendt, M. A.; Hillmyer, M. A. *Macromolecules* **2011**, *44*, 9310.

- (38) Sing, K. S. W.; Everett, D. H.; Haul, R. A. W.; Moscou, L.; Pierotti, R. A.; Rouquerol, J.; Siemieniewska, T. *Pure Appl. Chem.* **1985**, *57*, 603.
- (39) Lowell, S.; Shields, J. E.; Thomas, M. A.; Thommes, M. *Characterization of porous solids and powders: surface area, pore size and density*; Springer Science & Business Media, 2012; Vol. 16.
- (40) Weber, J.; Bergström, L. *Macromolecules* **2009**, *42*, 8234.
- (41) Schulze, M. W.; McIntosh, L. D.; Hillmyer, M. A.; Lodge, T. P. *Nano Letters* **2013**, *14*, 122.
- (42) Muralidharan, V.; Hui, C.-Y. *Macromolecular Rapid Communications* **2004**, *25*, 1487.
- (43) Zhou, X.; Huang, J.; Barr, K. W.; Lin, Z.; Maya, F.; Abbott, L. J.; Colina, C. M.; Svec, F.; Turner, S. R. *Polymer* **2015**, *59*, 42.
- (44) Roe, R. J.; Nojima, S. *MRS Online Proceedings Library Archive* **1986**, *79*, null.
- (45) Schwachula, G. *Journal of Polymer Science: Polymer Symposia* **1975**, *53*, 107.
- (46) Davankov, V.; Tsyurupa, M. In *Comprehensive Analytical Chemistry*; Vadim, A. D., Maria, P. T., Eds.; Elsevier: 2011; Vol. Volume 56, p 2.
- (47) Nyhus, A. K.; Hagen, S.; Berge, A. *Journal of Polymer Science Part A: Polymer Chemistry* **1999**, *37*, 3345.
- (48) Koh, M. L.; Konkolewicz, D.; Perrier, S. b. *Macromolecules* **2011**, *44*, 2715.
- (49) Nyhus, A. K.; Hagen, S.; Berge, A. *Journal of Polymer Science Part A: Polymer Chemistry* **2000**, *38*, 1366.
- (50) Bates, F. S.; Fredrickson, G. H. *Annual Review of Physical Chemistry* **1990**, *41*, 525.
- (51) Mikos, A. G.; Takoudis, C. G.; Peppas, N. A. *Macromolecules* **1986**, *19*, 2174.

Chapter 5

Poly(cyclohexylethylene)-*block*-poly(ethylene oxide) Block Polymers for Metal Oxide Templating^{†, ‡}

A series of poly(cyclohexylethylene)-*block*-poly(ethylene oxide) (CEO) diblock copolymers were synthesized through tandem anionic polymerizations and heterogeneous catalytic hydrogenation. Solvent-annealed CEO diblock films were used to template dense arrays of inorganic oxide nanodots via simple spin coating of an inorganic precursor solution atop the ordered film. The substantial chemical dissimilarity of the two blocks enables (i) selective inclusion of the inorganic precursor within the PEO domain and (ii) the formation of exceptionally small feature sizes due to a relatively large interaction parameter, estimated from mean-field analysis of the order-disorder transition temperatures of compositionally symmetric samples. UV/ozone treatment following incorporation produces an ordered arrangement of oxide nanodots and simultaneously removes the block polymer template.

[†] This work was done in collaboration with Christophe Sinturel.

[‡] Reproduced with permission from Schulze, M. W.; Sinturel, C.; Hillmyer, M. A. *ACS Macro Lett.* **2015**, *4*, 1027–1032. Copyright 2015 American Chemical Society.

5.1 Introduction

Dense arrays of nanostructured metal oxides offer diverse functionality for a broad range of technologies, including optoelectronics,^{1,2} magnetic storage,^{3,4} and photocatalysis.^{5,6} Their utility motivates the investigation of tractable, low-cost strategies to produce precision nanostructure arrays. Block polymer (BP) nanolithography has emerged as a powerful bottom-up patterning technique in which synthetically controllable variables, such as the overall degree of polymerization (N), the block incompatibility (χ), and the composition (f) dictate the morphology and lengthscale of the patterned structures.⁷⁻⁹ The ability of block polymers to produce well-defined features for ultra-high density arrays is dictated by the segregation strength (χN). At reduced values of N needed for very small feature sizes, the diffuse interfaces of weakly segregated block polymers result in significant line edge roughness, an issue exacerbated by the limited etch-contrast of typical organic blocks.⁷⁻¹⁰

The need to simultaneously increase χ and the block etch-contrast has motivated the introduction of segments containing inorganic elements.¹⁰ Although often high- χ materials, inorganic-organic diblocks can be difficult to prepare and have limited versatility in terms of the product metal oxide. New, high- χ diblocks reliant on “etch-less” technology are attractive alternatives to inorganic-organic block polymers. In the etch-less approach, selective inclusion of inorganic additives into a single domain occurs upon exposure of a self-assembled film to a dilute solution of inorganic precursors. Subsequent UV/ozone, thermal, or plasma treatment of the film removes the organic polymer scaffold and generates a metal oxide in situ, thereby readily replicating the structure of the initial template. Previous demonstrations of this selective inclusion technique have relied on the combination of a hydrophobic block, typically polystyrene (PS), and a more polar metallophilic block such as poly(vinylpyridine) (PVP)¹¹⁻¹⁵ or poly(ethylene oxide) (PEO).¹⁶⁻²⁰ Although these polar candidates offer exceptional flexibility and imbibe both sol-gel reactants and metal ions, their relatively low incompatibility with the hydrophobic blocks typically used places a lower limit on the accessible particle dimensions.

To enable ultra-small etch-less particle formation, the ideal block polymer would combine two highly incompatible low molar mass segments distinguished by marked differences in hydrophobicity and hydro(metallo)philicity. Although it has been shown that high- χ , low- T_g polyolefin-PEO block polymers can adopt domain sizes below 10 nm at synthetically accessible molar masses, their mechanical and thermal properties are likely inadequate for nanopatterning purposes.²¹⁻²³ Poly(cyclohexylethylene) (PCHE), however, is a simple polymeric hydrocarbon that is attractive due to its exceptionally high glass transition temperature.^{24,25} In this study, we prepared a new highly incompatible block polymer system, poly(cyclohexylethylene)-*block*-poly(ethylene oxide) (CEO), and utilized it in thin films to template metal oxides of exceptionally small dimensions.

5.2 Experimental Procedures and Characterization

5.2.1 Materials

Ethylene oxide ($\geq 99.5\%$), styrene ($\geq 99\%$, stabilized), di-*n*-butylmagnesium (1.0 M in heptane), butylmagnesium chloride (2.0 M in THF), *n*-butyllithium (2.5 M in hexanes) and *sec*-butyllithium (1.4 M in cyclohexane) were obtained from Sigma Aldrich. Each purification reagent was rigorously dried prior to use to remove solvent. Palladium on calcium carbonate (Pd/CaCO₃, 5%) was purchased in both reduced and unreduced forms from suppliers as available. Solvents utilized in anionic syntheses were passed through a home-built solvent system comprising columns of activated alumina and molecular sieves prior to distillation. Deuterated chloroform (CDCl₃) was purchased from Cambridge Isotope Laboratories. All other reagents were purchased from Sigma Aldrich and used without further purification.

5.2.2 Synthesis of end-capped polystyrene (PSOH)

Styrene was freeze-pump-thawed three times and then twice distilled over di-*n*-butylmagnesium. The monomer was stirred for at least 1 h over the purification reagent prior to distillation and the final transfer to a flame-dried burette. Ethylene oxide (3–5 equivalents to *sec*-butyllithium initiator) was purified similarly by two successive

distillations over *n*-butylmagnesium chloride and transfer to a flame-dried burette. Cyclohexane was twice distilled over *n*-butyllithium. Polymerization was performed in a custom-made 1-L glass reactor with 5 ACE-threaded ports and Teflon-coated stir bar. Details regarding equipment for anionic synthesis are provided elsewhere.^{21,26}

A thermocouple well, a glass Y-connector with two Chemglass stopcock 0-4 connections in series, a flask of purified cyclohexane, and the burette of purified styrene monomer (32.05 g, 0.31 mol, 12.3 eq) were fitted to the ports using Teflon ferrules and Nylon bushings. A glass T-connector was connected to the center port and fitted with a Teflon-coated septum and two separate ports with 0-4 connections leading respectively to the Schlenk line and a pressure gauge via flexible Cajon tubing. Purified ethylene oxide monomer was connected to the Y-connector using Cajon tubing and stored in an adjacent dewar containing dry ice/isopropanol mixture at -78 °C. The sealed reactor and glass connections were evacuated (≈ 10 mtorr), flame-dried, and back-filled with Argon five times. The reactor was then sealed under 3 psig of positive Ar pressure, and the flask of cyclohexane opened, generating a slow drip of solvent into the reactor. Following the addition of 17.94 mL (25.1 mmol) of *sec*-butyllithium via an airtight gas syringe through the septum, the mixture was allowed to stir for 15 min to ensure homogeneity as the flask was warmed to 40 °C. The burette of styrene was slowly opened and the monomer added drop-wise. Within minutes, the light yellow solution converted to an intense deep red color, indicating the formation of poly(styryllithium) anions. The polymerization proceeded 4–5 h at 40 °C. The burette of ethylene oxide was then opened and added in one portion to end-cap the polymer chains, and the solution rapidly turned colorless. The mixture stirred for 12 h. The reaction was terminated with the addition of excess methanol and vented. Precipitated salts were removed via filtration. The solution was then concentrated *in vacuo*, precipitated in 10-fold volume excess of methanol and dried at 100 °C to afford 29.34 g of PSOH (92%, $M_n = 1.4$ kg/mol, $D = 1.05$).

5.2.3 Synthesis of Hydroxyl-terminated Poly(cyclohexylethylene) (PCHEOH)

To preserve the hydroxyl moiety, previous reports on the catalytic hydrogenation of PSOH utilized both palladium on calcium carbonate (Pd/CaCO₃) and the Dow

Hydrogenation Catalyst (DHC)^{26,27} at reduced temperature relative to previous heterogeneous hydrogenation techniques.^{25,28} Catalytic hydrogenation of PSOH was performed in a 1 L stainless steel high-pressure reactor (Parr Instrument Company, Model 4523) under 500 psig H₂ at 120 °C. Dried and reduced Pd/CaCO₃ (15.1 g, 2.5 g catalyst/g polymer) was added to a solution of 6.6 g of PSOH in ca. 250 mL cyclohexane (reagent grade) to form a heterogeneous suspension within the reactor. The mixture was sealed and degassed with Ar for 15 min through the dip-tube connection under mild agitation. All valves were then closed and the contents subsequently heated to 120 °C. H₂ was introduced and the pressure was maintained at 500 psig as the mixture stirred vigorously over the course of the reaction. Aliquots were periodically obtained from the reactor via the dip tube outlet to monitor conversion once the pressure remained constant. Complete saturation was typically achieved within ~ 48 h and determined by zero residual aromatic resonance in the ¹H-NMR spectrum. Catalyst was removed by filtration using 0.22 micron filter paper (Millipore, PVDF membrane) and recycled by washing in hexane and drying under vacuum and high temperature. The cyclohexane/polymer solution was concentrated and subsequently precipitated in 10-fold volume excess of methanol and dried under vacuum at 100 °C. The mass of polymer recovered was 6.1 g (92%, $M_n = 1.5$ kg/mol, $D = 1.09$).

5.3.4 Synthesis of CEO Block Polymers

Potassium naphthalenide solutions were prepared 24 h prior to use and discarded within 2 weeks. Briefly, freshly cleaved potassium metal (1.2 g) washed with cyclohexane was transferred to a custom flame-dried graduated cylinder with 0–4 side-arm connection and glass stir bar under a purge of argon. Naphthalene (recrystallized 3 times in diethyl ether) was then added in 10% molar excess to the vessel followed by cannulation of ca. 100 mL of freshly distilled THF to produce a dark green solution of roughly 0.3 M. The polymerization of ethylene oxide (EO) was performed in a reactor setup similar to that utilized in the polymerization of styrene in cyclohexane. A pre-weighed portion of PCHE-OH, previously dried at 100 °C overnight, was added to a flame-dried 1 L glass reactor fitted with a glass stir bar. The reactor was then simultaneously cycled with Ar and mildly heated with a heat gun. Distilled THF was then added via its connected flask to dissolve

the PCHEOH under a blanket of Ar (1–2 psig). The solution was stirred at room temperature and titrated by cannulation with potassium naphthalenide until a light green color persisted for 30 min. The solution was then warmed to 40 °C, and the connected burette of EO was opened and added in one portion. The reaction was heated for 48 h to ensure complete conversion. The reaction was then terminated with excess methanol, and the reactor vented. The resulting block copolymer solutions were filtered to remove potassium salt precipitates and freeze-dried in benzene. PEO-rich polymers were easily isolated through precipitation in *n*-pentane/cyclohexane.

5.3.5 Molecular Characterization

Molar mass and compositions were determined from ¹H Nuclear Magnetic Resonance (NMR) spectra (Bruker Avance HD 500) using a 10 s relaxation delay between pulses for quantitative end-group analysis. All spectra were obtained in CDCl₃ using TMS as an internal reference. Size-exclusion chromatography was performed on an Agilent 1260 Infinity LC employing THF as the mobile phase (25 °C, flow rate 1 mL/min) equipped with three Waters Styragel HR columns and Optilab T-rex RI and Dawn Heleos II Light Scattering detectors (Wyatt Technology). Mass-average molar masses of polystyrene precursors were determined using the asymptotic dn/dc value 0.185 mL/g for PS in THF at 25 °C. PCHE–PEO block polymers were analyzed on a separate instrument using THF with 1 wt% *N,N,N',N'*-tetramethylethylenediamine as the eluting solvent to mitigate issues of tailing and detector signal misalignment observed with PEO-containing polymers. The SEC is equipped with a DAWN DSP multiangle laser light scattering (MALLS) detector in addition to a Wyatt Optilab EX RI detector (Wyatt Technology). Size exclusion was performed with three successive Phenomenex Phenogel-5 columns. Thermogravimetric analysis (TGA) was performed on a TA Instruments Q500 under nitrogen atmosphere at a heating rate of 10 °C/min with typical sample size of 10–15 mg. Glass transition (T_g) and melting transition (T_m) temperatures were determined using the final heating result obtained on a TA Q1000 differential scanning calorimeter (DSC). Samples (5–10 mg) loaded in aluminum hermetic pans were analyzed by DSC within the temperature range of –80 °C to 170 °C, at a ramp rate of 10 °C/min. In addition, some high molar mass samples

were cycled to higher temperature as needed in order to observe the endotherm of the order-disorder transition. The onset temperature of the endotherm was used to identify T_{ODT} . Crystallinity of the diblocks was calculated using the enthalpy of fusion of pure crystalline PEO (213.4 J/g).²⁹

5.3.6 Rheological Analysis

The low-frequency rheological response of CEO block polymers was evaluated on a Rheometrics ARES mechanical spectrometer equipped with 25 mm parallel plates. Order-disorder transition temperatures (T_{ODTS}) of CEO block polymers were determined from isochronal ($\omega = 1$ rad/s) linear dynamic temperature sweeps acquired using a heating rate of 1 or 5 °C/min as denoted in Table S2. A precipitous drop in G' indicates the transition of the ordered microstructure to a disordered state. Error in the determination of the T_{ODT} was taken as the temperature increment over which the modulus drop occurred determined between the point of onset and the modulus plateau at T_{ODT} (typically 5 °C).

5.3.7 Small-angle X-ray Scattering

Synchrotron small-angle X-ray scattering (SAXS) measurements were performed at sectors 5-ID-D and 12-ID-B of the Advanced Photon Source (Argonne, IL). Sample-to-detector distances were calibrated using a silver behenate standard. CEO samples were hermetically sealed in Tzero DSC pans (TA Instruments) in a glovebox under a N₂ atmosphere. DSC pans were mounted in a Linkam heating stage for variable temperature measurements. Samples equilibrated 1–3 min at each temperature prior to data collection. Typical exposure times were of order 1 s. 2D scattering patterns were recorded on an area detector. These isotropic 2D patterns were azimuthally integrated to the one-dimensional form of intensity as a function of the magnitude of the scattering wave vector $q = |\mathbf{q}| = 4\pi\sin(\theta/2)/\lambda$, where λ is the nominal x-ray wavelength and θ is the scattering angle.

5.3.8 Thin-film Preparation and Analysis

CEO thin films were prepared by spin-coating a filtered polymer solution (1 wt% in amyl acetate) at 3000 rpm for 60 s on 4 cm² silicon substrates. The resulting CEO films obtained thicknesses between 18 and 20 nm as determined with a J. A. Woollam VASE

spectroscopic ellipsometer using 65° and 75° angles of incidence within a wavelength range of 400 to 900 nm. Substrates were subsequently solvent annealed for 5 min at room temperature in a 50 mL glass chamber containing 20 mL of a 1:1 (v/v) THF/cyclohexane mixture; samples were positioned 1 cm above the surface of the liquid. Annealed samples were removed, cleaved into four 1 cm^2 squares, and used without further treatment prior to the incorporation of inorganic precursors.

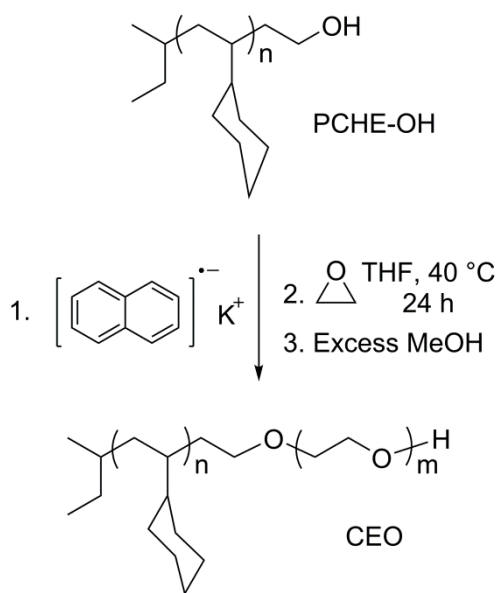
Preparation of the precursor solutions follows methods similarly described elsewhere.¹³ A silica precursor solution was formulated from tetramethoxysilane (TEOS), 1 M HCl, and anhydrous ethanol (EtOH) and prepared with a molar proportion of 1:46:5.6:0.006 TEOS:EtOH:H₂O:HCl. The solution was allowed to stir for 16 h at room temperature. The exothermic formation of the titania precursor, prepared at a 1:4.65 TiCl₄:EtOH molar ratio, required the dropwise addition of TiCl₄ to EtOH with continuous stirring in an ice-bath (at least 0.5 h following complete addition). Both of these two master solutions were then further diluted with EtOH to a final concentration of 0.005 M of Si and Ti, respectively. For the deposition of iron oxide particles, a 0.2 wt% solution of iron (III) nitrate nonahydrate (Fe(NO₃)₃·9H₂O) in EtOH was prepared. Impregnation of the annealed block polymer was achieved by spin-coating two drops of the inorganic precursor solutions on the surface of the CEO films at 2500 rpm for 60 s. Simultaneous oxidation of the precursors and removal of the polymer scaffold was achieved within 3 h at room temperature using UV/ozone treatment (Jelight UVO-Cleaner 42) and a sample-to-lamp distance of 8 cm. Samples were also subjected to thermal treatment in air to confirm the stability of the particles. Although some sintering was possible, this 500 °C calcination step likely results in amorphous material.

Scanning electron microscope (SEM) images were obtained on a Hitachi SU8230 High Resolution SEM under a 1 kV landing energy resulting from an applied 3 kV accelerating voltage in deceleration mode. All atomic force microscopy (AFM) images were collected at ambient temperature and pressure using a Bruker Nanoscope V Multimode 8 operated in tapping mode. NanoWorld NCSTR AFM probes (reported tip radius < 8 nm) with a resonant frequency of 160 kHz and a force constant of 7 N/m were used for the surface

characterization of both polymer films and nanoparticle arrays of 10 nm feature size or greater. Smaller features were imaged using Bruker Sharp Microlever Nitride Probes (MSNL) of 2 nm nominal tip radius with specified 0.6 N/m force constant and 125 kHz resonant frequency.

5.3 Results and Discussion

The route to CEO materials shown in Scheme 1 starts with functionalized polystyrene precursors synthesized by end-capping polystyryllithium anions with ethylene oxide to give hydroxyl terminated polystyrene (PSOH). The relatively low degrees of polymerization (DP) enabled precise $^1\text{H-NMR}$ spectroscopy determination of the molar mass and end-capping efficiency from the molar ratio of the *sec*-butyllithium initiator fragment ($-\text{CH}_3$, 0.7 ppm) to the aromatic backbone (6.3–7.1 ppm) and ethoxy end-group ($-\text{CH}_2\text{-OH}$, 3.3 ppm), respectively (Figure 5.1). Using Pd/CaCO₃ at 120 °C for the catalytic hydrogenation of PSOH,^{26,27} we found that no residual aromatic resonances remained in the $^1\text{H-NMR}$ spectra after 48 h (conversion > 99%), and quantitative retention of the hydroxyl functionality was achieved (i.e., DP(PSOH)/DP(PCHEOH) \approx 1). The narrow molar-mass distributions of the hydrogenated PCHEOH products also indicated saturation without significant side-reaction (Figure 5.2). Table 5.1 summarizes the molecular characteristics of the PCHEOH samples and their corresponding PSOH precursors. The molar masses of the PCHEOH samples are reported as the hydrogenous equivalent molar mass of the PSOH precursor and account for end-groups. Even though the PCHE precursors are of very low molar mass, the T_g values are still relatively high (75–118 °C) (Figures 5.3 and 5.4).

Scheme 5.1 Synthesis of Poly(cyclohexylethylene)-*block*-poly(ethylene oxide) (CEO)**Table 5.1** Hydroxyl-terminated poly(cyclohexylethylene) (PCHEOH) and the corresponding polystyrene (PSOH) precursor data

entry ^a	PCHEOH				PSOH Precursor				
	$M_{n, \text{NMR}}$ (kg/mol) ^b	\bar{D} ^c	F (%) ^d	T_g (°C) ^e	$M_{n, \text{NMR}}$ (kg/mol) ^f	$M_{m, \text{SEC}}$ (kg/mol) ^g	\bar{D} ^c	[OH]/ [<i>s</i> -Bu] ^h	T_g (°C) ^e
PCHEOH (1.2)	1.0	1.04	1.17	75	1.2	1.5	1.05	1.06	43
PCHEOH (1.5)	1.5	1.09	1.01	78	1.4	1.6	1.05	1.00	55
PCHEOH (1.6)	1.6	1.03	0.99	85	1.5	1.8	1.07	0.99	58
PCHEOH (2.0)	2.0	1.07	1.01	97	1.9	2.6	1.09	0.95	68
PCHEOH (2.7)	2.8	1.04	0.95	107	2.6	2.8	1.03	0.97	76
PCHEOH (3.1)	3.1	1.02	0.95	113	2.9	3.2	1.01	1.00	79
PCHEOH (3.3)	3.4	1.02	0.96	114	3.1	3.1	1.02	0.96	80
PCHEOH (3.7)	3.7	1.01	0.99	118	3.5	3.7	1.08	0.97	84

^aPCHEOH (X) is hydroxyl-terminated poly(cyclohexylethylene) with the number-average molar mass X in kg/mol given as a homogeneous equivalent of the PSOH starting material. ^bNumber-average molar mass calculated from ¹H-NMR spectroscopy and integration of the backbone with respect to the methylene protons adjacent to the hydroxyl-terminus. ^cMolar mass dispersity determined using LS-SEC. ^dFunctionality is calculated using DP(PSOH)/DP(PCHEOH) to estimate the retention of hydroxyl functionality post hydrogenation. ^eDetermined using DSC. ^fEnd-group analysis is based on the *sec*-butyllithium initiator fragment. ^gMass-average molar mass is estimated using LS-SEC and $dn/dc = 0.185$ ml/g for polystyrene. ^hA measure of the extent of functionalization described by the ratio the integrated end-groups, i.e. methylene protons (adjacent to the hydroxyl) of the ethoxy end-group relative to the *sec*-butyllithium initiator fragment.

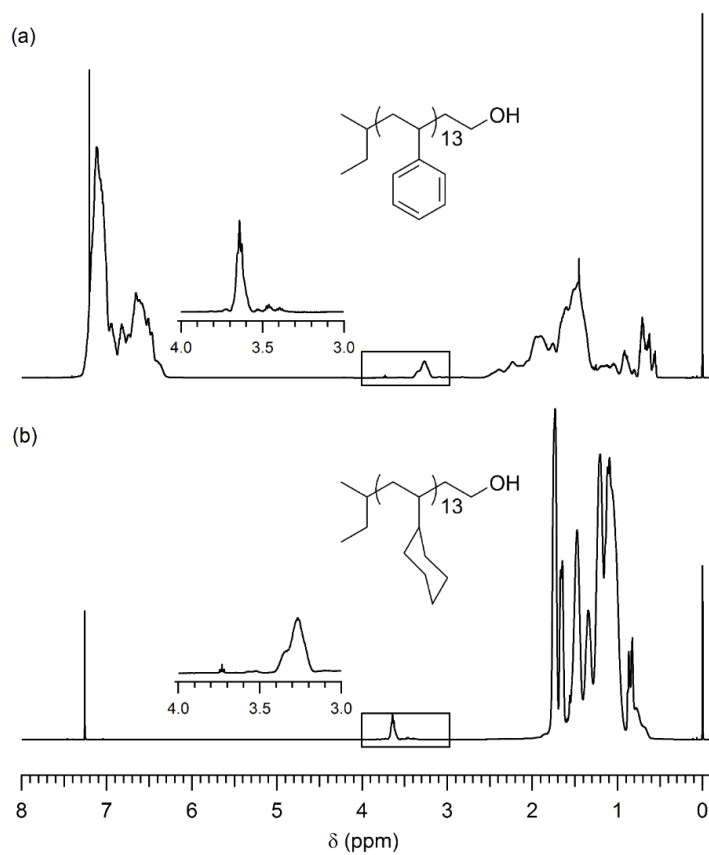


Figure 5.1 $^1\text{H-NMR}$ spectra of (a) PSOH (1.5) and (b) PCHEOH (1.6). The inset provided within the range of 3–4 ppm indicate the shift in the methylene protons of the hydroxyl end-group following hydrogenation.

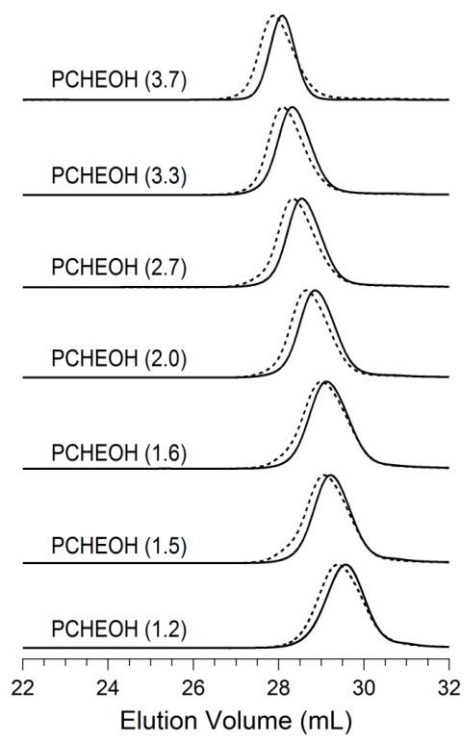


Figure 5.2 Series of representative SEC traces of PCHEOH polymers (solid lines) and the corresponding PSOH precursors (dashed lines).

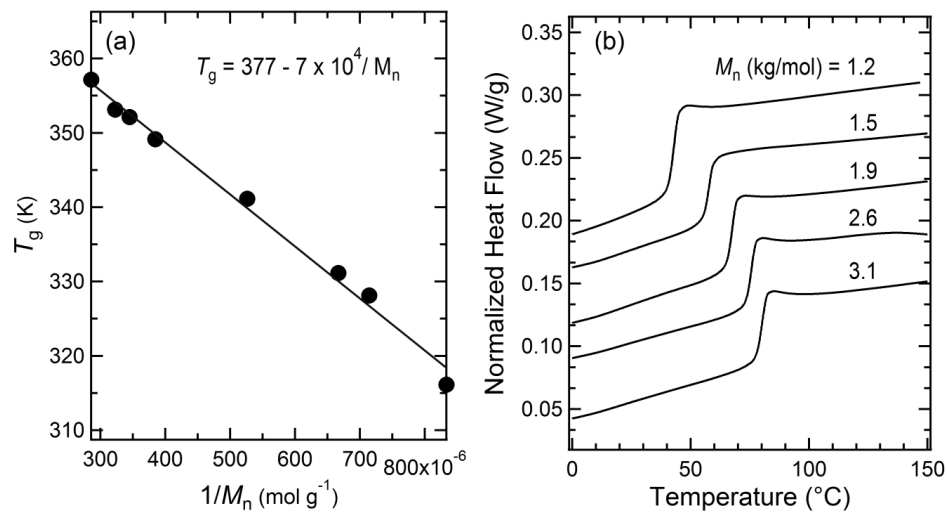


Figure 5.3 Dependence of the T_g on molar mass of the PSOH precursors is shown in (a), and representative DSC thermograms obtained on the second heating at 10 °C/min are provided in (b). The intercept of the linear regression T_g vs. $1/M_n$ provides the effective molar mass independent T_g (for PSOH, $T_{g,\text{inf}} = 104$ °C) at the high molar mass limit determined here as approximately $M_n > 7000$ g/mol.

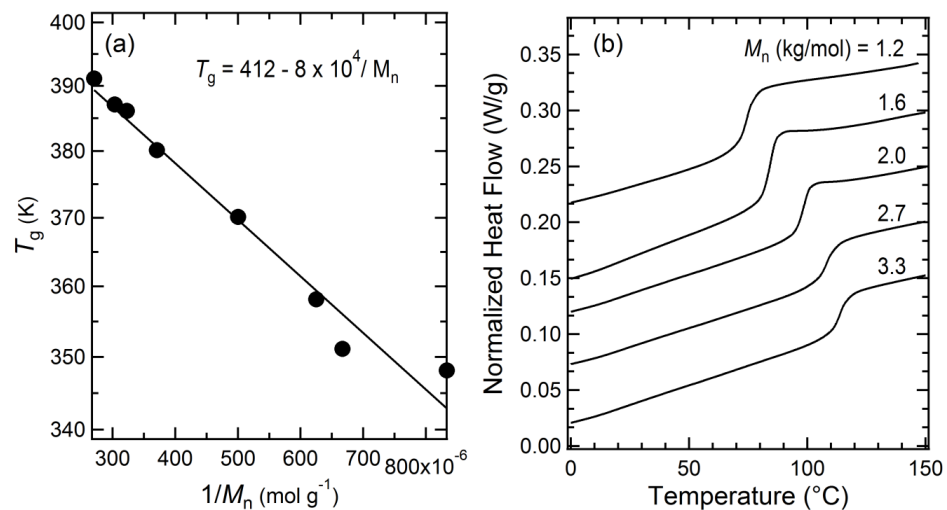


Figure 5.4 Dependence of the T_g on molar mass of the PCHEOH precursors is shown in (a), and representative DSC thermograms obtained on the second heating at 10 °C/min are provided in (b). The intercept of the linear regression T_g vs. $1/M_n$ provides the effective molar mass independent T_g for PCHEOH, $T_{g,\text{inf}} = 139$ °C, which agrees with literature precedent.^{24,25}

Potassium naphthalenide was used to convert macromolecular PCHEOH alcohols into potassium alkoxides for EO initiation.²¹ Block polymer compositions were determined from the ¹H-NMR spectra of the CEO block polymers (Figure 5.5) and spanned a broad range of volume fractions ($0.17 \leq f_{\text{PEO}} \leq 0.82$) (see Tables 5.2). SEC analysis (Figure 5.6 and 5.7) shows the shift to lower elution volumes upon formation of diblocks. From the overlay of block polymer and precursor traces, some unreacted starting material is evident implying, in fact, some minor loss of hydroxyl functionality in the hydrogenation step, a result nearly undetectable using ¹H-NMR analysis alone.^{26,27} However, peak-fitting analysis generally indicated approximately 3–5 wt% homopolymer where contamination was evident; this low level of homopolymer contamination was neglected in subsequent analysis.

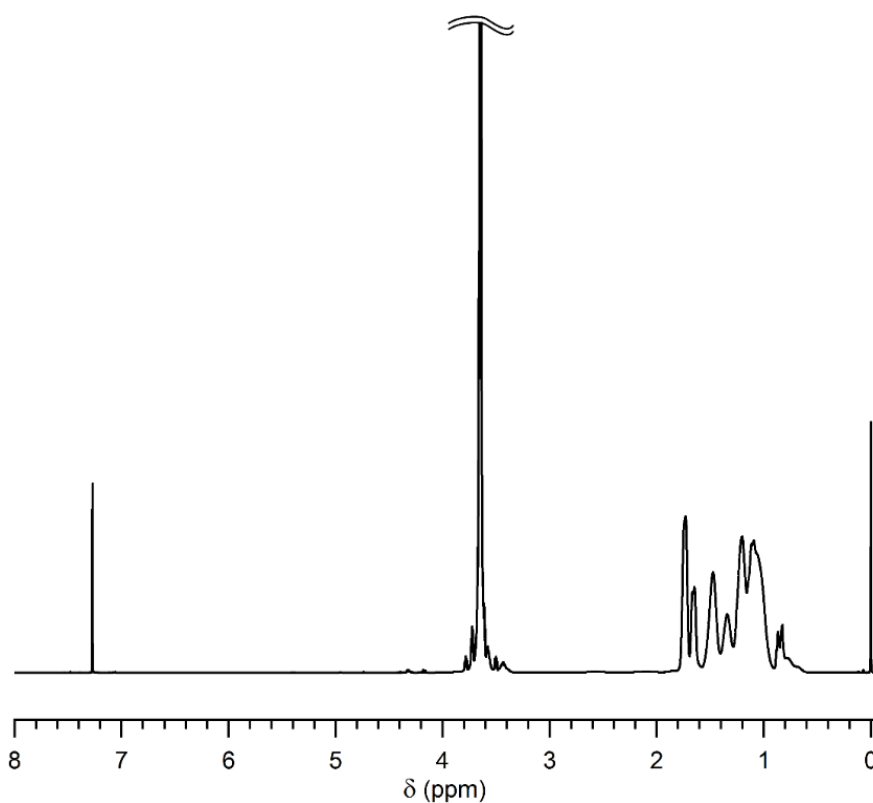
Table 5.2 Molecular characteristics of all synthesized PCHE–PEO diblock copolymers

entry ^a	precursor ^b	$M_{n, \text{PEO}}$ (kg/mol) ^c	D^d	f_{PEO}^e	N^f	T_{ODT}^g (°C)
CEO (2.7, 0.55)	PCHEOH (1.2)	1.5	1.14	0.55	39	114 (114)
CEO (3.1, 0.51)	PCHEOH (1.5)	1.6	1.12	0.51	44	130 (133)
CEO (8.9, 0.82)	PCHEOH (1.5)	7.4	1.07	0.82	121	145 (144)
CEO (3.1, 0.49)	PCHEOH (1.6)	1.6	1.12	0.49	44	132 (131)
CEO (4.3, 0.50)	PCHEOH (2.0)	2.2	1.07	0.50	61	194 (195)
CEO (5.7, 0.62)	PCHEOH (2.0)	3.6	1.07	0.62	79	204 (204)
CEO (5.6, 0.51)	PCHEOH (2.6)	2.9	1.09	0.51	79	258
CEO (3.8, 0.17)	PCHEOH (3.1)	0.7	1.10	0.17	56	disordered
CEO (4.1, 0.24) ⁱ	PCHEOH (3.1)	1.1	1.05	0.24	61	-
CEO (5.9, 0.42) ^h	PCHEOH (3.2)	2.6	1.10	0.42	85	240
CEO (7.9, 0.52) ^{h,i}	PCHEOH (3.6)	4.0	1.13	0.52	112	>300

^aCEO (X, Y) corresponds to PCHE–PEO of total molar mass X, including *s*-butyllithium end-group, and f_{PEO} (Y). ^bSee Table S1. ^cNumber-average molar mass of PEO was calculated from ¹H-NMR spectra. ^dDetermined using LS-SEC. ^eCalculated volume fraction of PEO using bulk densities of PCHE (0.92 g/cm³) and PEO (1.06 g/cm³) at 140 °C. ^fNumber-average degree of polymerization calculated using a reference volume of 118 Å³. ^g T_{ODT} was determined by DMS. Values indicated in parentheses were determined from DSC. ^hFor these samples, the DMS heating ramp rate was 5 °C/min. ⁱODTs were inaccessible or not clearly observed via DMS.

Table 5.3 Thermal characteristics of all PCHE–PEO block polymers

entry	T_c (°C)	T_m (°C)	ΔH_m (J/g)	Crystallinity (wt%)
CEO (2.7, 0.55)	-9	36	52.0	41.7
CEO (3.1, 0.51)	-3	39	45.5	39.1
CEO (8.9, 0.82)	30	59	117.8	65.7
CEO (3.1, 0.49)	-2	32	45.7	40.8
CEO (4.3, 0.50)	9	35	48.6	42.6
CEO (5.7, 0.62)	21	46	69.2	49.7
CEO (5.6, 0.51)	17	38	53.0	47.3
CEO (5.9, 0.42)	10	41	45.7	40.8
CEO (7.9, 0.52)	21	46	52.5	47.8

**Figure 5.5** ^1H -NMR spectrum of a PCHE–PEO block copolymer CEO (3.1, 0.49) in CDCl_3 .

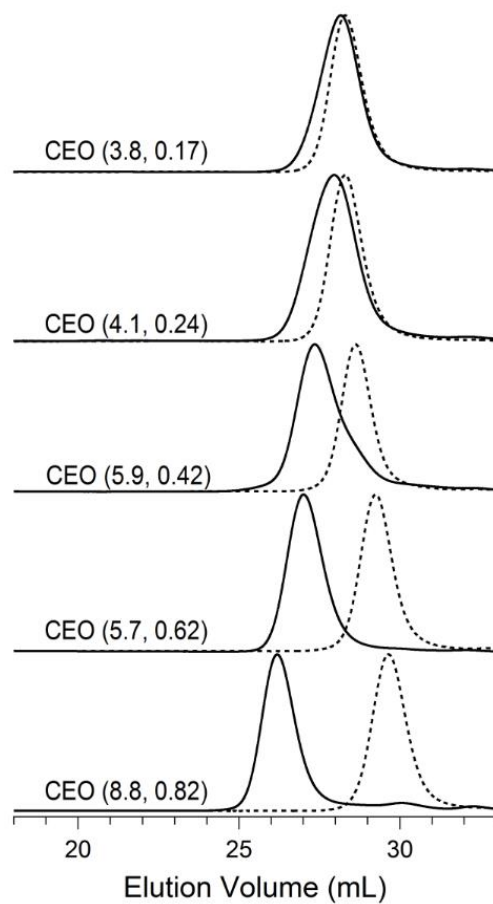


Figure 5.6 SEC traces of compositionally asymmetric PCHE-PEO block polymers (solid lines) and the corresponding PCHE-OH precursor (dashed lines).

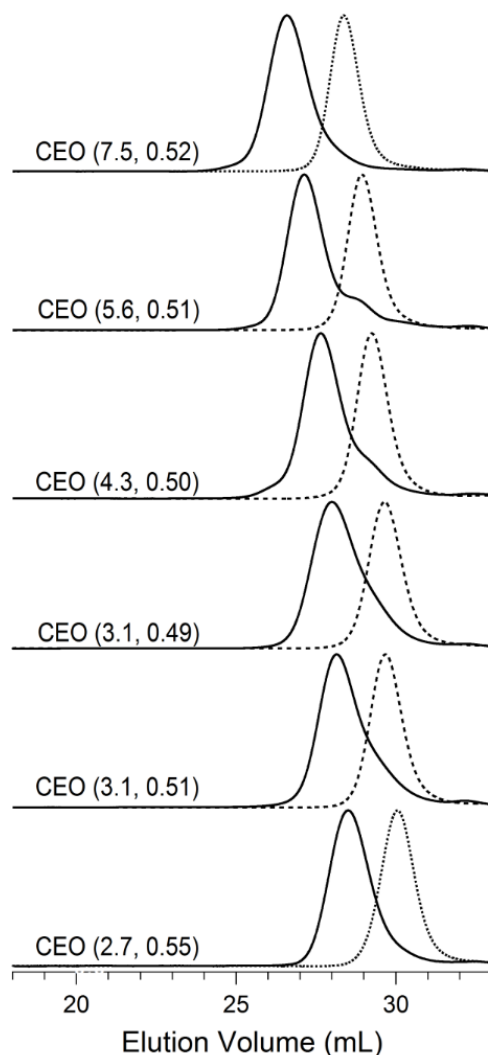


Figure 5.7 SEC traces of compositionally symmetric PCHE–PEO block polymers (solid lines) and the corresponding PCHE-OH precursor (dashed lines).

In general, the use of fully saturated PCHE hydrocarbons as initiators for the polymerization of EO produces block polymer amphiphiles with exceptional thermal stability as determined by thermal gravimetric analysis (TGA) ($T_{d,CEO} = 349\text{ }^{\circ}\text{C}$, Figure 5.8). Previous reports on polyalkane-poly(ethylene oxide)s have shown that crystalline breakout results when the poly(ethylene oxide) microdomains are surrounded by a rubbery matrix.³⁰ Although by differential scanning calorimetry (DSC) the EO blocks retain high crystallinity (41 wt%) at molar masses as low as 1.5 kg/mol (Figure 5.9), PCHE

vitrification above T_c leads to hard nano-confinement and preserves the amorphous melt morphology at low temperature in all samples.^{31,32}

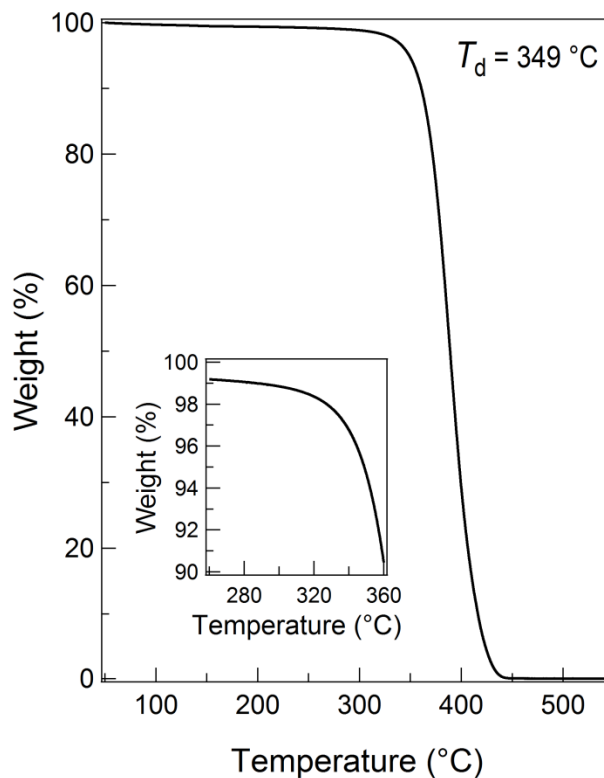


Figure 5.8 Representative TGA thermogram of CEO (3.1, 0.51) heated under nitrogen at a ramp rate of 10 °C/min. The decomposition temperature, T_d , is defined as 5% weight loss of the sample.

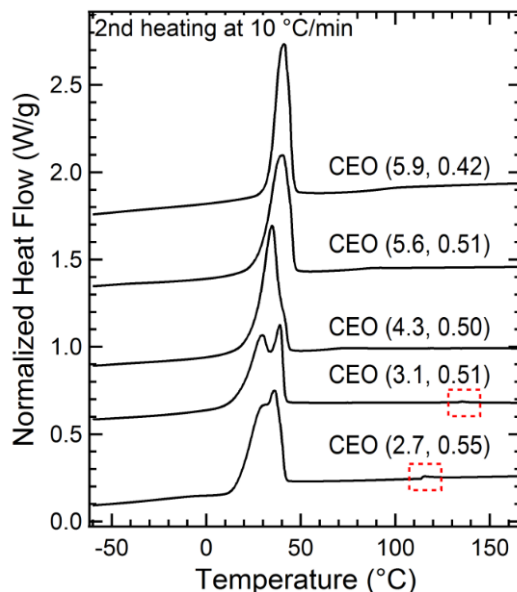


Figure 5.9 Representative DSC thermograms (*exo*-down) of CEO block copolymers obtained on the second heating. At low molar masses, the EO block is highly crystalline. Glass transition temperatures for the respective blocks are not clearly discernible, and no distinct feature of T_g is observed in the second derivative of heat flow with respect to temperature. For most CEO block polymers, T_g of the PCHE block is likely obfuscated by the large PEO melting endotherm. Red boxes indicate the latent heat of the ODT observed in samples CEO (2.7, 0.55) and CEO (3.1, 0.51).

Dynamic mechanical spectroscopy (DMS) experiments performed by slowly heating from the ordered state were used to determine the order-disorder transition (ODT) temperature, T_{ODT} , identified as a discontinuous drop in the dynamic elastic modulus (G') resulting in a liquid-like response (Figure 5.10). Weak latent heats associated with the ODT and observable in the DSC thermograms of several CEO block polymers are consistent with T_{ODT} determined by DMS (Figure 5.9, onset temperatures are indicated in parentheses in Table 5.2).⁹ Moreover, the ODT was verified by small-angle X-ray scattering experiments (Figure 5.11); the inset of Figure 1 shows a representative transition for $N = 44$ upon cooling at $T \approx 130$ °C in close agreement with T_{ODT} determined by DMS. The DMS data for the $N = 61$ and 79 samples suggest the presence of an order-order transition (OOT) prior to the ODT even though these samples are compositionally symmetric (Table 5.2).

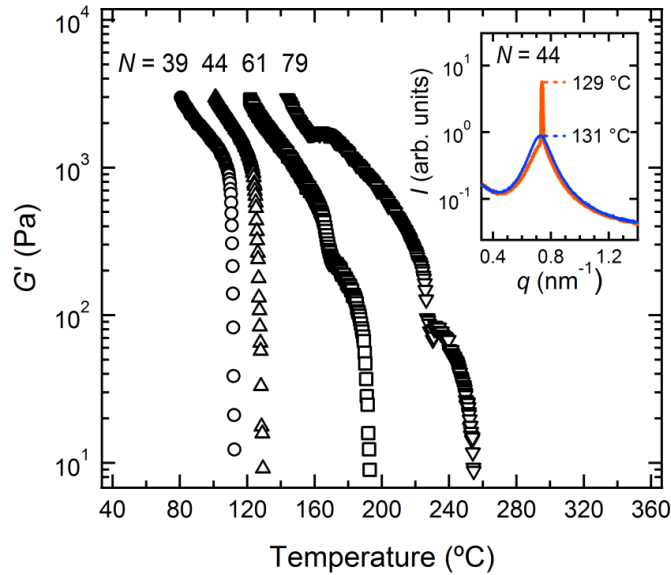


Figure 5.10 Temperature dependence of the low-frequency dynamic elastic shear modulus (G') for four compositionally symmetric samples and the determination of T_{ODT} . Samples were loaded onto a parallel plate fixture, heated above the order-disorder transition in an N_2 atmosphere, and subsequently quenched and annealed at reduced temperature for 1 h prior to measurement. The data were then obtained at a ramp rate of $1\text{ }^\circ\text{C}/\text{min}$ under relatively small strain ($\leq 1.2\%$) and a frequency of 1 rad/s . The inset shows the transition from a disordered-to-ordered phase upon cooling via SAXS for $N = 44$ at $T \approx 130\text{ }^\circ\text{C}$.

In the determination of $\chi_{\text{CEO}}(T)$, we have utilized the mean field value of $(\chi N)_{\text{ODT}} = 10.5$, thus knowing N the value of χ can be estimated at a given ODT temperature. Rigorously, this applies only to compositionally ($f = 1/2$) and conformationally symmetric (i.e., equal statistical segment lengths $b_a = b_b$) and monodisperse ($D = 1.0$) block polymers in the limit of infinitely large N .^{9,33} However, these criteria are typically relaxed in the experimental analysis of real block polymers so that estimates of χ can be made for comparative purposes. Within self-consistent field theory (SCFT), $(\chi N)_{\text{ODT}}$ for conformationally symmetric, monodisperse samples is approximately equal to 10.5 at the moderately asymmetric compositions $f = 0.45$ or 0.55 .^{34,35} Similarly, extreme conformational asymmetry ($b_a/b_b = 2$) accounts for an increase in $(\chi N)_{\text{ODT}}$ by less than 5% at $f = 0.50$.³⁵ For real block polymers with $D > 1$, calculated values of $(\chi N)_{\text{ODT}}$ also do not

vary appreciably provided \mathcal{D} is not too large.^{36,37} Lastly, SCFT suggests only small Gibbs free energy differences between different ordered states at the same composition near the ODT. Thus we posit that consistent estimation of χ by applying $(\chi N)_{\text{ODT}} = 10.5$ for CEO diblock polymers that are approximately symmetric ($f = 0.5 \pm 0.05$), and of low dispersity ($\mathcal{D} < 1.2$), will allow for useful comparisons recognizing errors associated with the differences between real systems and mean field predictions. We note in our analysis that all samples exhibit the same apparent morphology in the vicinity of the ODT by SAXS (Figure 5.11), and the OOT prior to the ODT for $N = 61$ and 79 (both nearly symmetric) occur at near equivalent values of χN given the estimate of χ we make below. Definitive morphological identification of the phases present in these materials is ongoing.

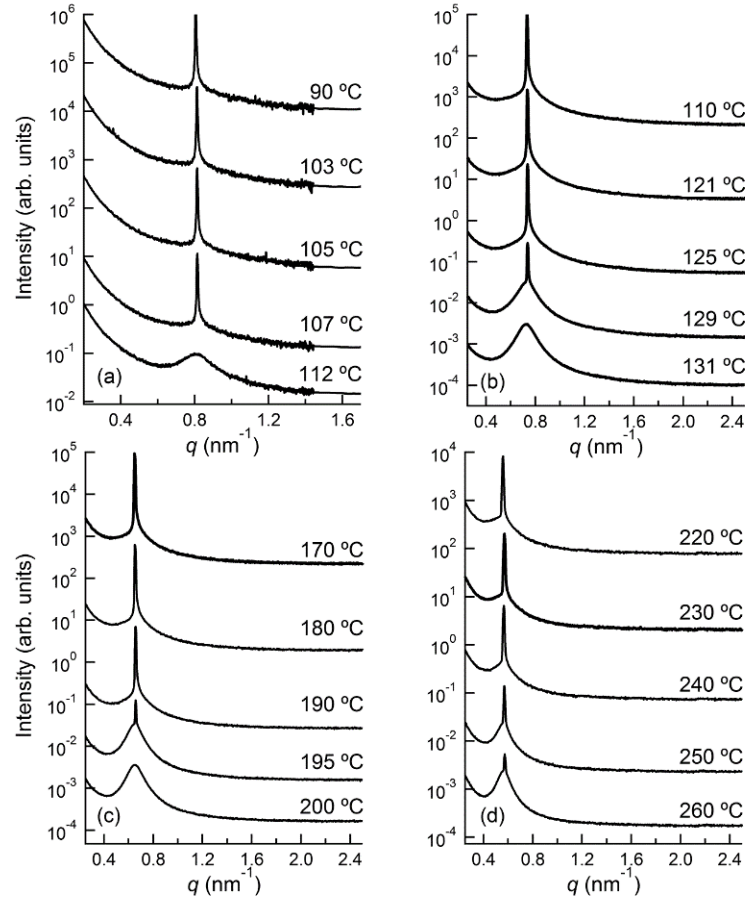


Figure 5.11 SAXS on cooling through the ODT for the four polymers used to determine the interaction parameter for $N = 39$ (a), 44 (b), 61 (c), and 79 (d). In the case of $N = 79$, a small calibration offset between the SAXS and DMS sample environments at high temperature could contribute to the apparent incomplete disordering of the polymer.

Using the values of T_{ODT} for the four symmetric samples in Table 5.2, applying $(\chi N)_{\text{ODT}} = 10.5$ and $\chi = \alpha/T + \beta$ we determined the temperature dependence of χ_{CEO} as

$$\chi_{\text{CEO}}^{118} = \frac{(192 \pm 13)}{T} - (0.23 \pm 0.03) \quad (5.1)$$

The linearity of the data is evident in Figure 5.12.

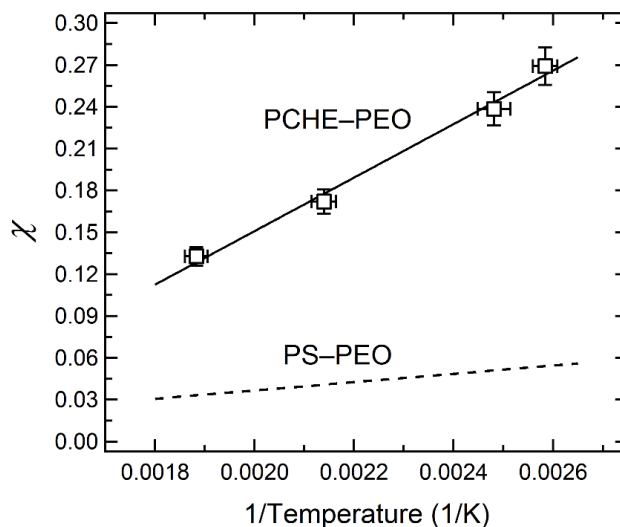


Figure 5.12 $\chi(T)$ for compositionally symmetric diblock copolymers determined using the first four entries of Table 5.1. The interaction parameter of PS-PEO is provided by Cochran et al.³⁸ Data are reported using an equivalent monomer reference volume ($v_0 = 118 \text{ \AA}^3$).

Based on the above analysis we have developed a highly segregated block polymer to direct the nanoscale structure of inorganic materials through selective metal inclusion in the PEO domains. DMS and SAXS experiments show that one sample in particular CEO (5.9,0.42) produces a hexagonally-packed cylindrical microstructure that transitions to the gyroid phase before disorder (Figure 5.13), similar to related systems.³⁰ Bulk SAXS measurement of the hexagonal unit cell spacing reveals 10 nm diameter features and a 15 nm center-to-center distance at room temperature. As-cast CEO films give an ill-defined structure and display a mixed orientation of domains with respect to the substrate surface. Furthermore, disparate interfacial energies of each block-interface combination promote a parallel domain orientation upon thermal annealing (Figure 5.14a).

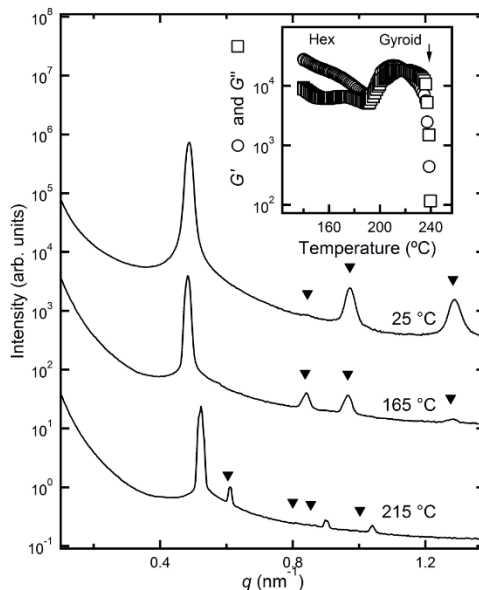


Figure 5.13 SAXS data and (inset) the temperature dependence of the dynamic moduli G' and G'' of CEO (5.9, 0.42) obtained on heating (5 °C/min, 1 rad/s, 1 % strain). Conformational asymmetry produces a hexagonally-packed cylindrical microstructure at low temperature. An order-order transition to a gyroid microstructure is observed just prior to the order-disorder transition, $T_{\text{ODT}} = 240$ °C.

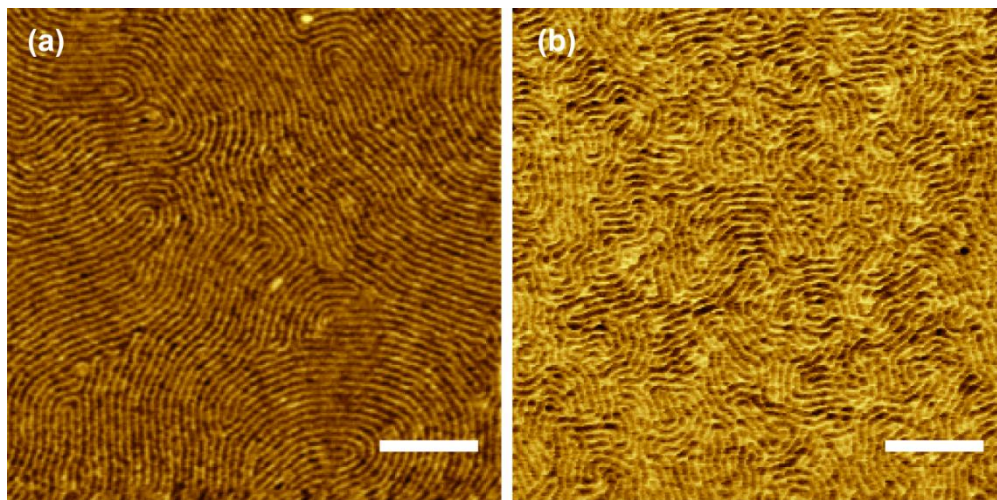


Figure 5.14 1 x 1 μm AFM phase images of CEO (5.9, 0.42) obtained in tapping mode following (a) thermal annealing and (b) solvent annealing with THF. Although there is likely a thin PCHE wetting layer, parallel cylinders may be used as templates;^{11,12,15} their utility was not explored in this work. Scale bar represents 200 nm.

Solvent vapor annealing can simultaneously induce chain mobility and circumvent preferential surface interactions. As solvent evaporates from the swollen film, a rapid evaporation front perpendicular to the plane of the substrate can nucleate a potentially non-equilibrium orientation of the ordered phase.^{39,40} Here, a 5 min exposure of CEO films to a 50/50 (v/v) mixture of cyclohexane/THF produced a hexagonal arrangement of features perpendicular to the free surface (Figure 5.15a). These data contrast the parallel orientation of PEO cylinders observed after either thermal annealing or solvent annealing with other non-selective solvents (Figure 5.14b); however, we note that this solvent mixture produced a parallel orientation for lamellar block polymer films. AFM measurements of these features, which may be spheres or perpendicular cylinders, yield a center-to-center distance estimate of 22 ± 3 nm and a diameter of 13 ± 3 nm, a significant increase in feature size relative to those observed in bulk. Cushen et al.^{41,42} previously showed similar domain enlargement (~30%) following selective solvent vapor annealing, attributable to (i) an effective increase in the segregation strength between the domains, and (ii) an effective increase in the occupied volume of the swollen block at appreciable concentrations. In our case, annealing with a single strongly-preferential solvent (cyclohexane) resulted in an overall domain increase of ~70% under comparable exposure times. We suspect that selective inclusion of cyclohexane into the PCHE domains increases χ_{eff} and induces chain-stretching, and this state is then trapped during rapid evaporation. Hence, the miscible, binary mixture of THF and cyclohexane significantly mitigates domain enlargement. The result may imply that THF, the more volatile component of the non-ideal mixture,⁴³ significantly reduces the vapor pressure of cyclohexane relative to pure solvent, resulting in a less swollen PCHE domain. Secondly, the addition of THF, a non-selective solvent enriched in the vapor phase, may screen block-block interactions and lead to an overall reduction of the effective χ of the swollen film.

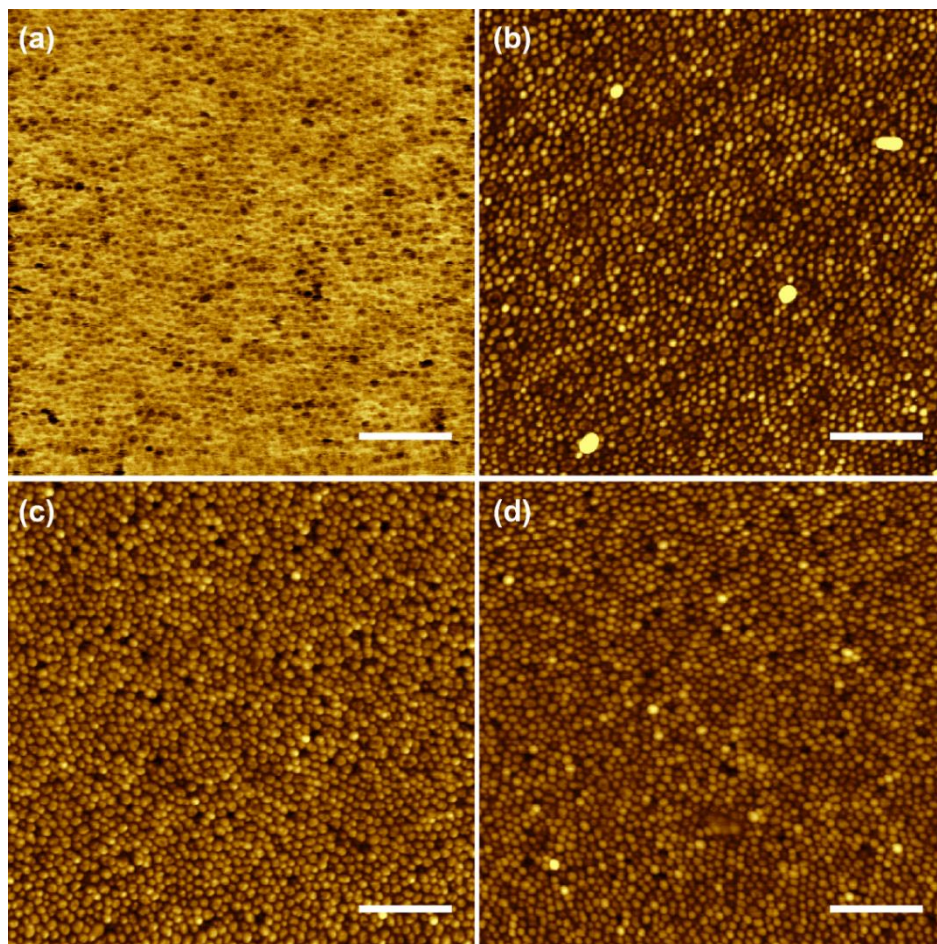


Figure 5.15 $1 \times 1 \mu\text{m}$ AFM images of the (a) CEO (5.9, 0.42) thin film after a 5 min solvent vapor anneal using a THF/cyclohexane mixture (phase image) and the templated (b) silica, (c) titania, and (d) iron oxide nanoparticles (height images). Images are acquired in tapping mode. Scale bars represent 200 nm.

Annealed and dried films were then impregnated using a simple process of spin-coating alcoholic solutions of inorganic precursors onto the film surface. Through selective interactions and rapid diffusion, these precursors are localized within the PEO domain whereas the hydrophobic nature of PCHE precludes metal ion inclusion. The organic/inorganic composites were then subjected to UV/O₃ exposure to oxidize the inorganic precursors and degrade the polymer scaffold. Originally developed by Morris et al. using PS-*b*-PEO,¹⁶⁻¹⁸ this versatile procedure templates inorganic nanodot arrays from the metal salt iron nitrate and the sol-gel precursors tetraethyl orthosilicate (TEOS) and

titanium ethoxide to produce arrays of iron oxide, silica and titania nanoparticles, respectively (Figure 5.15b-d). The procedure employed herein was simplified and no ‘activation step’, i.e., immersion of the film in ethanol prior to incorporation, was performed. Additional details regarding particle compositions resulting from this generic process are described in the literature.^{13,16-18}

The robust nature of the particles was confirmed upon thermal treatment at high temperature (500 °C for 0.5 h); each sample exhibited only a small reduction in the particle size likely due to some sintering (Figure 5.16). From image analysis, we estimate center-to-center distances and diameters that closely match the initial dimension of the block polymer templates (see Table 5.4). The heights of the particles range from 1 to 3 nm, depending on the precursor identity. For example, a typical height profile for silica particles obtained from an 18 nm thick polymer film is shown in Figure 5.17, in which the dot heights vary between 2 and 3 nm. This height reduction of the templated nanodots relative to initial block polymer film thickness is in line with previous work and attributed to the small volume fraction of the metal precursors in the PEO phase.¹⁶⁻¹⁸

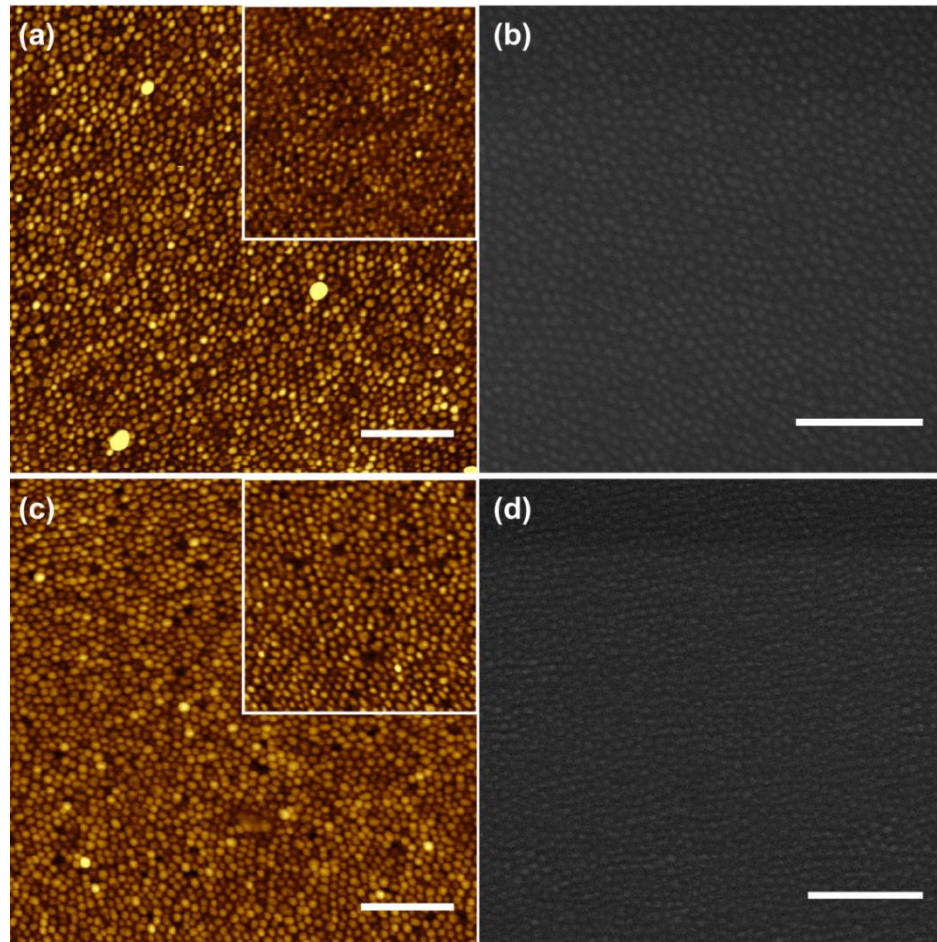


Figure 5.16 $1 \times 1 \mu\text{m}$ AFM height images of (a) silica and (b) iron oxide nanoparticles obtained in tapping mode and the corresponding SEM images (c) and (d), respectively. The insets of (a) and (b) show each array after thermal treatment at $500 \text{ }^\circ\text{C}$ for 0.5 h. Scale bars represent 200 nm.

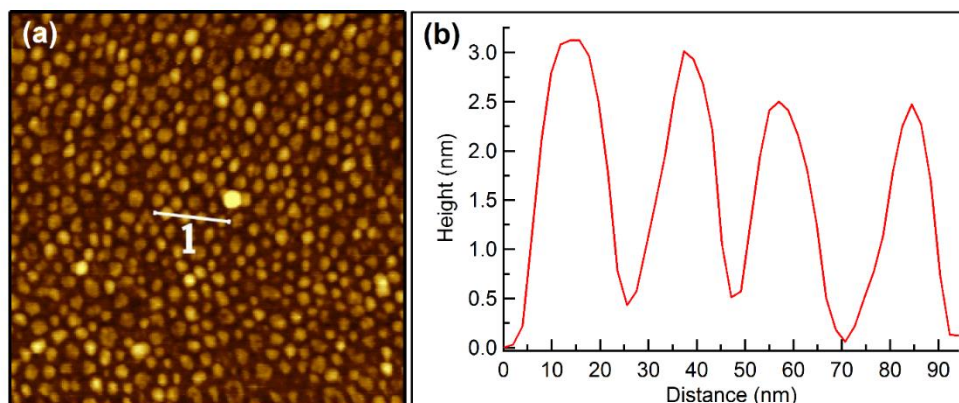


Figure 5.17 (a) AFM height image of the silica nanoparticle array templated using CEO (5.9, 0.42). (b) The line scan provides a height profile of the silica nanoparticles prepared by this method.

Table 5.4 Summary of domain dimensions of the templating block polymer film, CEO (5.9, 0.42), and deposited precursors as observed via AFM.

Material	Center-to-center (nm)	Diameter (nm)	Height (nm)
CEO (5.9, 0.42)	22±3	13±3	-
silica	20±3	13±3	2–3
titania	21±3	13±2	1–2
iron oxide	20±3	13±3	1–2

Because the size of the metal oxide dots matches closely the initial diameter of the PEO domains in the previous examples, reduction of the PEO volume fraction and/or overall molar mass can enable the formation of smaller particles. We took advantage of our selective solvent annealing process to organize a very low molar mass sample [CEO (4.1, 0.24), see Table 5.2]. A thin film of CEO (4.1, 0.24) was annealed in an 80:20 cyclohexane/THF mixture and small circular features were apparent (Figure 5.16). Applying the same process to this film, the templated nanoparticle arrays shown in Figures 5.19 and 5.20 demonstrate a significant reduction in feature size. Although minor height variations and heterogeneities, ascribed to localized deposition of agglomerated sol-gel precursors and/or potential overfilling of the PEO domains, obscure the overall image

clarity, the apparent oxide nanodots formed measure 6 ± 1 nm and represent the smallest particles templated from selective precursor insertion into a block polymer scaffold to-date.

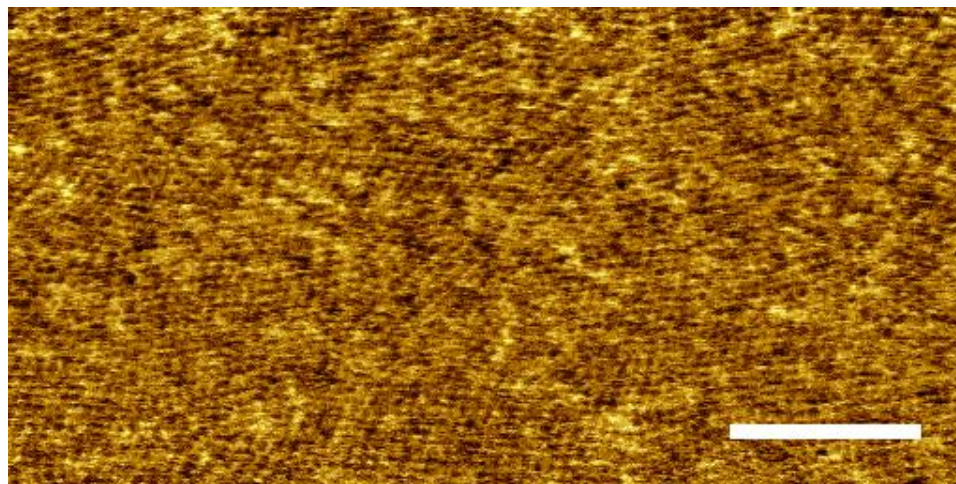


Figure 5.18 $1 \times 0.5 \mu\text{m}$ AFM phase image of the CEO (4.1, 0.24) thin film after a 4 min solvent vapor anneal using a THF/cyclohexane mixture. Scale bar represents 200 nm.

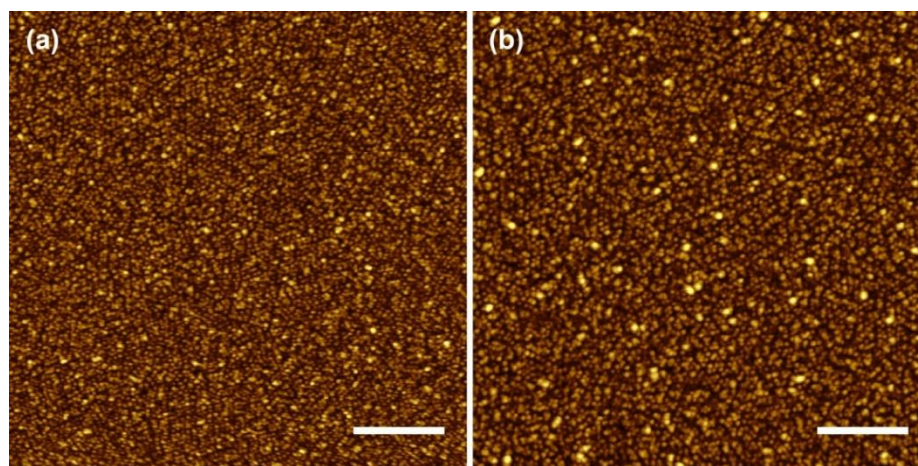


Figure 5.19 (a) Iron oxide and (b) silica nanoparticles templated from CEO (4.1, 0.24) following a selective solvent annealing. The resulting features are 6 ± 1 nm. Scale bars represent 200 nm.

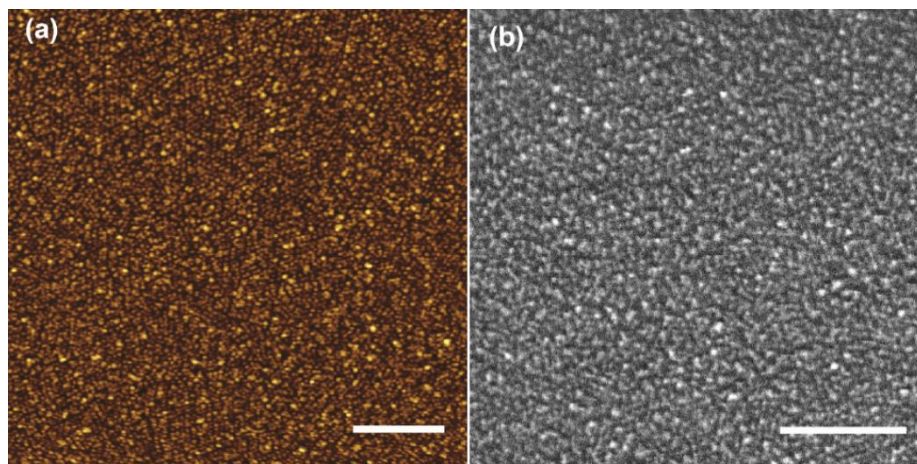


Figure 5.20 (a) AFM height image and (b) SEM image of iron oxide nanoparticles templated from CEO (4.1, 0.24). Scale bars represent 200 nm.

5.4 Conclusions

In summary, the synthesis of new CEO block polymers by tandem anionic polymerizations and catalytic hydrogenation has been demonstrated. Here, we have illustrated the utility of Si, Ti, and Fe precursors to reproducibly form oxide nanodots on a silicon substrate via a simple and versatile templating process. We have effectively shown a general proof-of-concept for advanced patterning of metal oxides of reduced feature size. Consequently, CEO block polymers represent a valuable system that can be utilized to template a wide breadth of materials through the addition of appropriate inorganic additives. Further work can be done using directed self-assembly for improved long-range order in nanotemplating applications.

5.5 References

- (1) Wang, X.; Li, Z.; Shi, J.; Yu, Y. *Chemical Reviews* **2014**, *114*, 9346.
- (2) Cui, Y.; Björk, M. T.; Liddle, J. A.; Sönnichsen, C.; Boussert, B.; Alivisatos, A. P. *Nano Letters* **2004**, *4*, 1093.
- (3) Baruth, A.; Rodwogin, M. D.; Shankar, A.; Erickson, M. J.; Hillmyer, M. A.; Leighton, C. *ACS Applied Materials & Interfaces* **2011**, *3*, 3472.
- (4) Park, S.; Lee, D. H.; Xu, J.; Kim, B.; Hong, S. W.; Jeong, U.; Xu, T.; Russell, T. P. *Science* **2009**, *323*, 1030.
- (5) Peng, J.; Li, X.; Kim, D. H.; Knoll, W. *Macromolecular Rapid Communications* **2007**, *28*, 2055.
- (6) Li, Y.; Sasaki, T.; Shimizu, Y.; Koshizaki, N. *Journal of the American Chemical Society* **2008**, *130*, 14755.
- (7) Gu, X.; Gunkel, I.; Russell, T. P. *Philosophical Transactions of the Royal Society A: Mathematical, Physical and Engineering Sciences* **2013**, *371*.
- (8) Bang, J.; Jeong, U.; Ryu, D. Y.; Russell, T. P.; Hawker, C. J. *Advanced Materials* **2009**, *21*, 4769.
- (9) Lee, S.; Gillard, T. M.; Bates, F. S. *Aiche J* **2013**, *59*, 3502.
- (10) Nunns, A.; Gwyther, J.; Manners, I. *Polymer* **2013**, *54*, 1269.
- (11) Chai, J.; Buriak, J. M. *ACS Nano* **2008**, *2*, 489.
- (12) Sweat, D. P.; Kim, M.; Larson, S. R.; Choi, J. W.; Choo, Y.; Osuji, C. O.; Gopalan, P. *Macromolecules* **2014**, *47*, 6687.
- (13) Roulet, M.; Vayer, M.; Sinturel, C. *European Polymer Journal* **2013**, *49*, 3897.
- (14) Chinthamanipeta, P. S.; Lou, Q.; Shipp, D. A. *ACS Nano* **2011**, *5*, 450.
- (15) Chaudhari, A.; Ghoshal, T.; Shaw, M. T.; Cummins, C.; Borah, D.; Holmes, J. D.; Morris, M. A. 2014; Vol. 9051, p 905110.
- (16) Mayeda, M. K.; Hayat, J.; Epps, T. H.; Lauterbach, J. *Journal of Materials Chemistry A* **2015**, *3*, 7822.
- (17) Ghoshal, T.; Maity, T.; Godsell, J. F.; Roy, S.; Morris, M. A. *Advanced Materials* **2012**, *24*, 2390.

- (18) Ghoshal, T.; Shaw, M. T.; Bolger, C. T.; Holmes, J. D.; Morris, M. A. *Journal of Materials Chemistry* **2012**, *22*, 12083.
- (19) Kim, D. H.; Kim, S. H.; Lavery, K.; Russell, T. P. *Nano Letters* **2004**, *4*, 1841.
- (20) Varghese, J.; Ghoshal, T.; Deepak, N.; O'Regan, C.; Whatmore, R. W.; Morris, M. A.; Holmes, J. D. *Chemistry of Materials* **2013**, *25*, 1458.
- (21) Hillmyer, M. A.; Bates, F. S. *Macromolecules* **1996**, *29*, 6994.
- (22) Hillmyer, M. A.; Bates, F. S.; Almdal, K.; Mortensen, K.; Ryan, A. J.; Fairclough, J. P. A. *Science* **1996**, *271*, 976.
- (23) Hajduk, D. A.; Takenouchi, H.; Hillmyer, M. A.; Bates, F. S.; Vigild, M. E.; Almdal, K. *Macromolecules* **1997**, *30*, 3788.
- (24) Cochran, E. W.; Bates, F. S. *Macromolecules* **2002**, *35*, 7368.
- (25) Gehlsen, M. D.; Bates, F. S. *Macromolecules* **1993**, *26*, 4122.
- (26) Wolf, J. H.; Hillmyer, M. A. *Langmuir* **2003**, *19*, 6553.
- (27) Kennemur, J. G.; Yao, L.; Bates, F. S.; Hillmyer, M. A. *Macromolecules* **2014**, *47*, 1411.
- (28) Ness, J. S.; Brodil, J. C.; Bates, F. S.; Hahn, S. F.; Hucul, D. A.; Hillmyer, M. A. *Macromolecules* **2001**, *35*, 602.
- (29) Car, A.; Stropnik, C.; Yave, W.; Peinemann, K.-V. *Advanced Functional Materials* **2008**, *18*, 2815.
- (30) Hillmyer, M. A.; Bates, F. S. *Macromolecular Symposia* **1997**, *117*, 121.
- (31) Zhu, L.; Cheng, S. Z. D.; Calhoun, B. H.; Ge, Q.; Quirk, R. P.; Thomas, E. L.; Hsiao, B. S.; Yeh, F.; Lotz, B. *Polymer* **2001**, *42*, 5829.
- (32) Loo, Y.-L.; Register, R. A.; Ryan, A. J. *Macromolecules* **2002**, *35*, 2365.
- (33) Gillard, T. M.; Medapuram, P.; Morse, D. C.; Bates, F. S. *Macromolecules* **2015**, *48*, 2801.
- (34) Matsen, M. W. *Macromolecules* **2012**, *45*, 2161.
- (35) Matsen, M. W.; Bates, F. S. *Journal of Polymer Science Part B: Polymer Physics* **1997**, *35*, 945.
- (36) Lynd, N. A.; Hillmyer, M. A.; Matsen, M. W. *Macromolecules* **2008**, *41*, 4531.

-
- (37) Cooke, D. M.; Shi, A.-C. *Macromolecules* **2006**, *39*, 6661.
- (38) Cochran, E. W.; Morse, D. C.; Bates, F. S. *Macromolecules* **2003**, *36*, 782.
- (39) Phillip, W. A.; Hillmyer, M. A.; Cussler, E. L. *Macromolecules* **2010**, *43*, 7763.
- (40) Sinturel, C.; Vayer, M.; Morris, M.; Hillmyer, M. A. *Macromolecules* **2013**, *46*, 5399.
- (41) Ellison, C. J.; Cushen, J. D.; Willson, C. G. *Journal of Photopolymer Science and Technology* **2013**, *26*, 45.
- (42) Cushen, J. D.; Wan, L.; Pandav, G.; Mitra, I.; Stein, G. E.; Ganesan, V.; Ruiz, R.; Grant Willson, C.; Ellison, C. J. *Journal of Polymer Science Part B: Polymer Physics* **2014**, *52*, 36.
- (43) Wu, H. S.; Sandler, S. I. *Journal of Chemical & Engineering Data* **1988**, *33*, 157.

Chapter 6

Influence of Conformational Asymmetry on the Formation of Frank-Kasper Phases in Diblock Copolymer Melts[†]

Geometries assumed by block polymer mesophases have been a subject of intensive experimental and theoretical investigation. Discovery of the complex, low-symmetry Frank-Kasper σ phase in compositionally asymmetric diblock copolymers emphasized a non-trivial relationship between melt thermodynamics and domain geometry not captured by previous theoretical frameworks. This chapter presents preliminary experimental findings to support recent theoretical conclusions that conformational asymmetry underpins the formation of new complex phases in block polymer materials. Through the synthesis and characterization of two different block polymers systems of low molar mass, far below the entanglement molar mass of either block segment, we enable facile assembly that is poised to probe the effect of conformational asymmetry and offer new insights into nanostructure formation in soft materials.

[†] This work was done in collaboration with Ronald M. Lewis, III and Frank S. Bates.

6.1 Introduction

Despite a plethora of block chemistries, diblock copolymer self-assembly has been reduced to a simple, single scheme of periodic nanostructures principally determined by the composition, f , and segregation strength, χN . With remarkable success, SCFT calculations have utilized these two parameters to validate the experimental findings of a small number of equilibrium ordered phases, including lamellae (LAM), hexagonally ordered cylinders (HEX), a body-centered cubic arrangement of spheres (BCC), and network structures (e.g., gyroid and O^{70}).¹⁻³

Recent discovery of the complex low-symmetry Frank-Kasper σ phase in asymmetric poly(isoprene)-*b*-poly(lactide) (IL)⁴⁻⁶ has motivated a review of the theoretical frameworks that govern block polymer self-assembly, predominantly in the formation of spherical phases which were thought to be simple packings of identical particles. In fact, the Frank-Kasper σ phase is a tetrahedrally close-packed structure defined by 5 spheres in unique coordination environments within a large tetragonal unit cell containing 30 spheres in total. In consideration of sphere-forming materials, it is important to note that the micellar particles of segregated block polymers are not truly spherical; conforming to the geometry of a lattice compresses the micellar shape such that each forms a multi-faceted soft polyhedron, or a Wigner-Seitz cell of the lattice.^{7,8} Theoretical and experimental efforts must combine in order to develop new insights into the formation of these complex structures.

Xie et al.⁹ have identified conformational asymmetry as the key additional parameter that influences the stability of the σ phase in linear block polymers. Using SCFT calculations, it was found that the σ phase becomes a stable equilibrium ordered phase within a narrow composition window as the conformational asymmetry, quantified as $\varepsilon = (b_A/b_B)^2$ where b_i is the statistical segment length of the i block, increases to 2.25. Through precise synthetic techniques, we have generated a library of polymer systems (Figure 6.1) to experimentally probe the effect of conformational asymmetry on the formation of complex phases in linear AB diblock copolymers. Building upon the discovery of the σ phase in IL block polymers, we have paired the polymeric hydrocarbons, poly(ethylene-

alt-propylene) (P) and poly(ethylethylene) (E), with polylactide to produce two highly incompatible block polymer systems of low molar mass and varied conformational asymmetry as indicated in Figure 6.1. The following presents a preliminary investigation into the phase behavior of these materials.

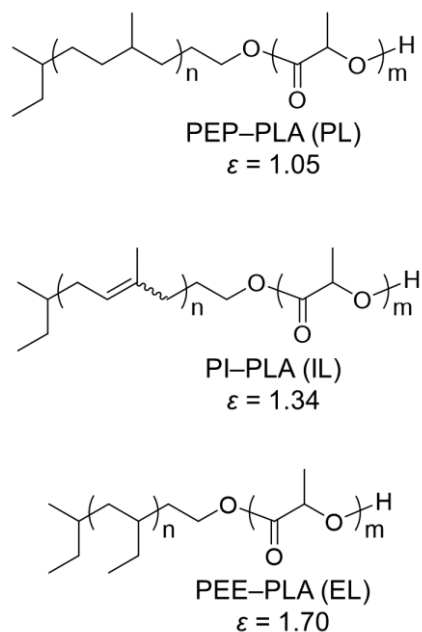


Figure 6.1 Molecular architecture of the three block polymer systems of varied conformational asymmetry studied and compared in this work. The conformational asymmetry parameter is defined as $\varepsilon = (b_A/b_B)^2$ and calculated using the statistical segment lengths (7.0, 6.8, 6.1 and 5.4 Å for L, P, I, and E, respectively) from reported¹⁰⁻¹² SANS-based values of the unperturbed mean-square end-to-end distances and densities at 140 °C.

6.2 Experimental Section

6.2.1 Materials

The synthesis of poly(ethylethylene) (PEE) is a well-described two-step procedure that combines anionic polymerization and heterogeneous catalytic hydrogenation.¹³ The anionic polymerization glassware and setup employed in its synthesis are presented in detail in a recent report.¹⁴ Briefly, the anionic polymerization of 1,3-butadiene was carried out in tetrahydrofuran (THF) at -60 °C for 4–5 h using *sec*-butyl lithium as an initiator.

Polymerization in polar solvent favors a predominantly 1,2-microstructure ($\geq 90\%$), while cold temperatures are required to limit proton abstraction from the weakly acidic solvent that would terminate the reaction. End-functionalization was achieved by the addition of excess ethylene oxide to a stirring peach-colored mixture of living polybutadienyl carbanions to produce a colorless solution of hydroxyethylated poly(1,2-butadiene) (PBOH). Following isolation, hydrogenation of PBOH was achieved using Dow 5% Pt/SiO₂ hydrogenation catalyst (3: 1 catalyst to PBOH by mass) at 80 °C in cyclohexane for 12–16 h to produce $\geq 98\%$ saturated poly(ethylethylene) (PEEOH). Poly(ethylene-*alt*-propylene) precursors (PEPOH) were obtained from the anionic synthesis of poly(isoprene) in cyclohexane at 40 °C and subsequent catalytic hydrogenation using a similar procedure.

Polymerizations of (\pm)-lactide were performed using triethylaluminum (Et₃Al) catalyst in dry toluene at 90 °C with monomer concentrations fixed at 1 M. A molar ratio of PEEOH (or PEPOH) to Et₃Al of 0.5 was used to form the aluminum alkoxide macroinitiator. Reaction mixtures were assembled in a dry box under nitrogen and sealed in high-pressure vessels. Reaction times were based on the relative ratio of macroinitiator to monomer to complete ca. 80 % conversion of lactide, and the reactions were quenched with 1 M HCl and precipitated in a 10-fold volume excess of methanol.

6.2.2 Molecular Characterization

Molar mass and composition of each polymer were estimated using ¹H Nuclear Magnetic Resonance (NMR) spectra (Bruker Avance HD 500 or Varian VI-500) obtained using a 10 s relaxation delay between pulses. Resonances are reported in ppm (δ) downfield from tetramethylsilane (0.0 ppm) in CDCl₃. Size exclusion chromatography was performed on an Agilent 1260 Infinity LC employing THF as the mobile phase (25 °C, flow rate 1 mL/min) equipped with three Waters Styragel HR columns and Optilab T-rex RI and Dawn Heleos II Light Scattering detectors (Wyatt Technology). Thermal properties were characterized using a TA Q1000 differential scanning calorimeter (DSC). Glass transition temperatures (T_g) were determined on the second heating within the temperature range of –100 to 200 °C at a ramp rate of 10 °C/min.

6.2.3 Dynamic Mechanical Spectroscopy (DMS)

Dynamic mechanical spectroscopy (DMS) measurements were performed on a strain controlled ARES-G2 (TA instruments) or ARES-1 (Rheometrics). Samples were loaded on 8 or 25 mm diameter parallel plates, and temperature was controlled using a forced convection oven equipped with an inert nitrogen purge. For all experiments, oscillatory shear was applied within the linear viscoelastic regime and utilized strain amplitudes of $\gamma \leq 2\%$. The order-disorder transition temperature (T_{ODT}) was evaluated from linear isochronal (1 rad/s) measurement of the dynamic storage moduli G' upon heating at 1 °C/min.

6.2.4 Small and medium-angle X-ray Scattering (SAXS/MAXS)

Synchrotron SAXS and MAXS was performed at the DND-CAT 5-ID-D beamline of the Advanced Photon Source (Argonne National Laboratory, Argonne, IL) using a dual detector system for simultaneous data collection of an augmented scattering wave vector range (0.02–1.74 and 1.45–8.26 nm⁻¹). Experiments employed sample-to-detector distances of 8500 and 1010 mm, respectively, and an X-ray wavelength of $\lambda = 0.729 \text{ \AA}$. The temperature was controlled using a Linkam DSC stage cooled with liquid nitrogen. Bulk samples were hermetically sealed under nitrogen in aluminum DSC pans to limit oxygen exposure. All samples were first heated above the order-disorder transition (ODT) and then quenched to the target temperature below T_{ODT} , unless otherwise specified. Two-dimensional (2D) data were collected on Rayonix CCD area detectors using an exposure time of ca. 1 s. Scattering data were azimuthally averaged to a 1D profile of intensity (arbitrary units) versus the magnitude of the scattering wave vector $q = |q| = 4\pi\sin(\theta/2)/\lambda$, where λ is the nominal X-ray wavelength and θ is the scattering angle.

6.3 Results and Discussion

In this section, the experimental results obtained for EL block polymers, the most conformationally asymmetric system studied, will be presented, and the physical characteristics of sphere-forming block polymers obtained from SAXS and DMS will be emphasized. Following a summary of their molecular characteristics, the EL interaction

parameter will be estimated and compared to that of the IL and PL systems. Phases observed in these materials at long annealing times (typically, ≥ 7 d) as a function of temperature will be identified. Then the kinetics of ordering for two representative EL polymers will be presented as a function of temperature in an attempt to gain insight into the dynamics of structure formation and the relationship between the σ phase and conventional BCC and HEX morphologies. These results in total will then be compared with a summary of the SAXS experiments performed on PL block polymers.

6.3.1 Characterization of EL Diblock Copolymers

A series of 14 EL block polymers was synthesized from 3 PEEOH precursors over a range of PLA volume fractions, $0.17 \leq f_L \leq 0.66$ (Table 6.1). Block polymers of specified molar mass and composition were synthesized to have ODT temperatures below 200 °C to limit thermally-induced degradation.

Table 6.1 Molecular characterization data for EL block polymers

entry ^a	$M_{n,E}$ ^b	$M_{n,L}$ ^b	M_n ^b	N^c	f_L ^d	\bar{D}^e	$T_{g,E}$ (°C) ^f	$T_{g,L}$ (°C) ^f	T_{ODT} (°C) ^g
EL-23-52	1300	1900	3300	46	0.52	1.06	-37	26	165
EL-23-54	1300	2000	3400	48	0.54	1.06	-36	28	169
EL-23-66	1300	3400	4800	65	0.66	1.04	-35	41	166
EL-28-37	1600	1300	3000	45	0.37	1.08	-34	15	128
EL-28-49	1600	2100	3800	54	0.49	1.05	-34	29	195
EL-44-17	2500	700	3200	52	0.17	1.07	-34	-12	44
EL-44-21	2500	900	3500	55	0.21	1.05	-35	-5	81
EL-44-24	2500	1100	3700	57	0.24	1.08	-34	3	95
EL-44-26	2500	1200	3800	58	0.26	1.03	-35	16	149
EL-44-29	2500	1400	4000	61	0.29	1.02	-36	11	169
EL-63-17	3500	1000	4700	75	0.17	1.05	-31	5	122
EL-63-21	3500	1400	5000	80	0.21	1.02	-31	16	154
EL-63-25	3500	1600	5300	83	0.25	1.04	-31	19	181

^aSamples are referred to as EL-XX-YY where “XX” specifies N_E , the volumetric degree of polymerization of the PEE block, and “YY” specifies the percentage of the polymer molecular volume that constitutes the PLA block (i.e., $f_L \times 100$). ^bNumber-average molar mass reported in (g/mol) from ¹H NMR end-group analysis of the precursor. Total molar mass of the block polymer includes the *s*-butyl end-group. ^cVolumetric degree of polymerization based on reported^{10,11} homopolymer densities at 140 °C (0.807 and 1.152 g/cm³ for E and L, respectively) and a reference volume of 118 Å³. ^dVolume fraction of L based on reported homopolymer densities at 140 °C and ¹H NMR. ^eMolar mass dispersity determined using LS-SEC in THF. ^fGlass transition temperatures determined from DSC. ^gOrder-disorder transition temperature determined from DMS performed on heating at a rate of 1 °C/min.

Symmetric samples were synthesized to evaluate $\chi(T)$ using mean-field analysis ($\chi N)_{ODT} = 10.5$ and the associated T_{ODT} values determined using DMS. Due to the exceptionally high incompatibility of these materials, only PEEOH precursors of 1300 and 1600 g/mol were appropriate macroinitiators to synthesize symmetric materials with $T_{ODT} \leq 200$ °C. Figure 6.2(a) shows the temperature dependence of the low-frequency dynamic elastic shear modulus (G') for three compositionally symmetric samples, and Figure 6.2(b) graphically compares the determined interaction parameter for EL

$$\chi = \frac{(208 \pm 32)}{T} - (0.25 \pm 0.07) \quad (6.1)$$

with the interaction parameter reported for PL¹⁵ and IL¹⁶ block polymers using a common reference volume ($v_o = 118$ Å³).

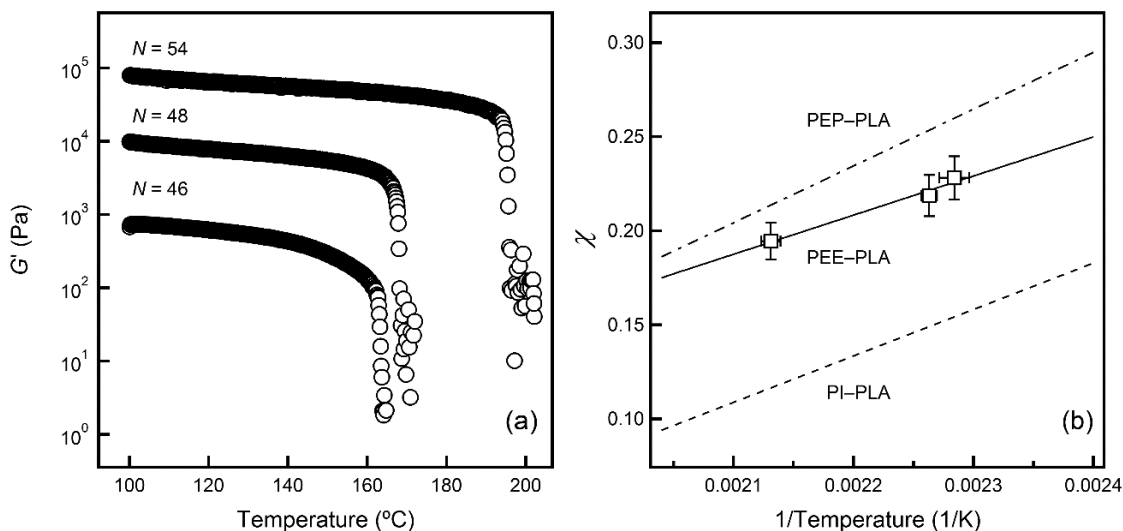


Figure 6.2 (a) Temperature dependence of the low-frequency dynamic elastic shear modulus (G') for three compositionally symmetric EL samples and the determination of T_{ODT} . Data were obtained at a ramp rate of $1\text{ }^{\circ}\text{C}/\text{min}$ under relatively small strain ($\leq 1\%$) and a frequency of 1 rad/s . Data obtained for block polymers $N = 48$ and 54 are vertically shifted for clarity by factors of 10 and 10^2 , respectively. (b) $\chi(T)$ for compositionally symmetric EL diblock copolymers estimated using the samples shown in (a). The interaction parameter of PEP-PLA¹⁵ and PI-PLA¹⁶ are shown for comparison using an equivalent reference volume ($v_0 = 118\text{ \AA}^3$).

The polyolefin-containing systems PL and EL illustrate how simple variations in molecular architecture can augment enthalpic penalties manifest in χ . Because the PEP conformational volume is greater than that of PEE, PEP chains form more intermolecular segment contacts than equal molar mass PEE chains, leading to an increase in the effective χ .¹⁷ The smaller χ of IL relative to the polyolefin systems suggest that the unsaturated and more polarizable backbone mediates segment-segment interactions with the PLA block to some extent.

Classical phases of hexagonally close-packed cylinders (HEX), lamellae (LAM), and gyroid (GYR) were assigned in block polymers of volume fraction $f_L \geq 0.26$ using SAXS. A representative series of scattering signatures of these structures is shown in Figure 6.3.

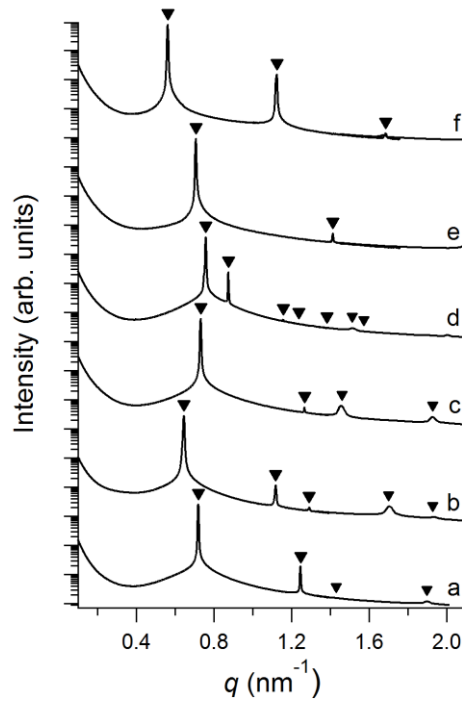


Figure 6.3 Representative isothermal synchrotron SAXS patterns obtained from EL block polymers for compositions $f_L \geq 0.26$. The HEX phase is identified by the relative peak positions $(q/q^*)^2 = 1, 3, 4, 7, 9$, where q^* is the primary peak, in samples (a) EL-44-26 at 100 °C, (b) EL-44-29 at 125 °C, and (c) EL-28-37 at 100 °C. (d) EL-28-37 adopts a GYR morphology at 125 °C as indicated by the reflections located at $(q/q^*)^2 = 6/6, 8/6, 14/6, 16/6, 20/6, 22/6, 24/6$. A LAM morphology is identified by the higher order reflections $(q/q^*)^2 = 1, 4, 9$ in samples (e) EL-23-54 and (f) EL-23-66 at 100 °C. Curves are shifted vertically for clarity.

Some materials within this study that are referred to as HEX are later shown to form the σ phase. At present, it is unclear if these materials form hexagonally close-packed cylinders or a hexagonal columnar phase of spheres. We will tentatively classify these materials as a HEX phase without distinction, and samples that form HEX and σ will be included in the discussion of sphere-forming samples that contain $f_L \leq 0.25$.

The order-disorder transition temperature, T_{ODT} , of each polymer was measured using DMS on slow (1 °C/min) heating as presented in Figure 6.4. The ODT is evident as a precipitous drop in linear storage (G') and loss (G'') moduli as the material transitions from an ordered soft solid to a disordered material with a liquid-like response. Notably, in multiple samples, a broad upturn is evident in the loss modulus (G'') on heating that may

potentially signify an order-order transition, or a simple transition to more liquid-like behavior.

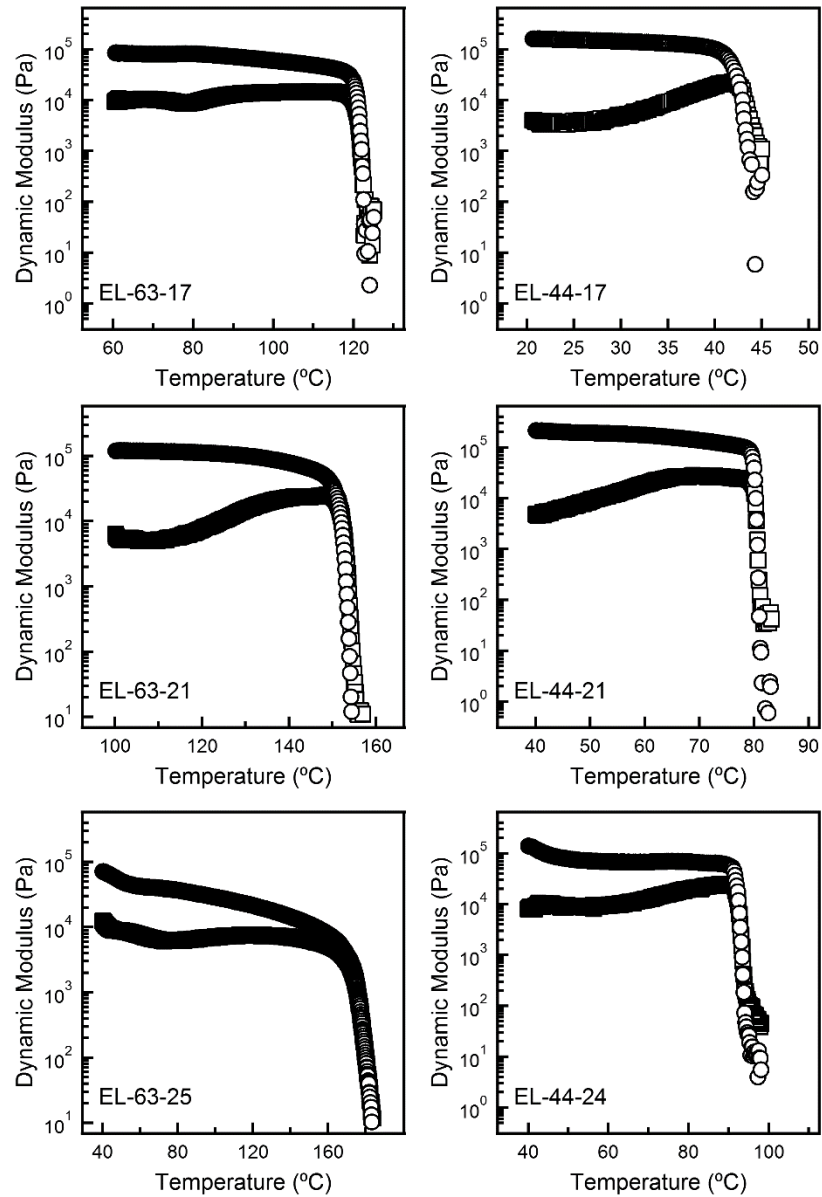


Figure 6.4 Measurement of the T_{ODT} for EL block polymers of $f_L \leq 0.25$. Linear ($\gamma \leq 1\%$) isochronal (1 rad/s) dynamic shear storage (G' , \circ) and loss (G'' , \square) were monitored on heating at a rate of 1 °C/min. Prior to measurement, the samples were cooled from the disordered state and annealed at the initial temperature for ca. 30 min. The ODT is evident as the precipitous drop in modulus. The characteristic upturn in the loss modulus on heating may indicate an order-order transition or transition to liquid-like behavior.

6.3.2 Ordered states in the sphere-forming window

SAXS experiments were performed in order to determine the stability of ordered phases in EL block polymers. In these experiments, samples contained in hermetically sealed DSC pans were equilibrated in the disordered state (~ 1 min) and then rapidly quenched to a target temperature below T_{ODT} and annealed. The results of this section summarize the temperature-dependent behavior of each sample. Phase identification is typically limited to long annealing times required to achieve a well-ordered state. Selected samples annealed at high temperature (>100 °C) were analyzed by SEC and NMR to confirm that no change in dispersity or reduction in molar mass occurred due to sample degradation.

Two poly(ethylene) precursors of distinct molar mass were used to generate two homologous series of EL block polymers within the sphere-forming window. EL-44-21, a polymer formed from the lower molar mass poly(ethylene) precursor and $f_{PLA} = 0.21$, displays a rich phase behavior presented in Figure 6.5. When EL-44-21 is annealed at 70 °C, the material orders into a body-centered cubic (BCC) phase. The BCC structure produces a unique scattering pattern with Bragg diffraction peaks at positions relative to the primary (low q) scattering peak, q^* , of $(q/q^*)^2 = 1, 2, 3, 4, 5, 6, 7 \dots$. However, when EL-44-21 is annealed at a slightly lower temperature of 55 °C, the ordered phase that forms at long times is the Frank-Kasper σ phase, a low-symmetry structure with a large tetragonal unit cell of $P4_2/mnm$ symmetry containing 30 spherical particles. Lee et al. recently discovered this phase in a closely related work on asymmetric PI-PLA (IL) block copolymers.^{4-6,16} As demonstrated in Figure 6.6, the distinctive SAXS pattern of EL-44-21 collected at 55 °C can be indexed to space group $P4_2/mnm$ with lattice parameters a and c of 35.0 and 18.3 nm.

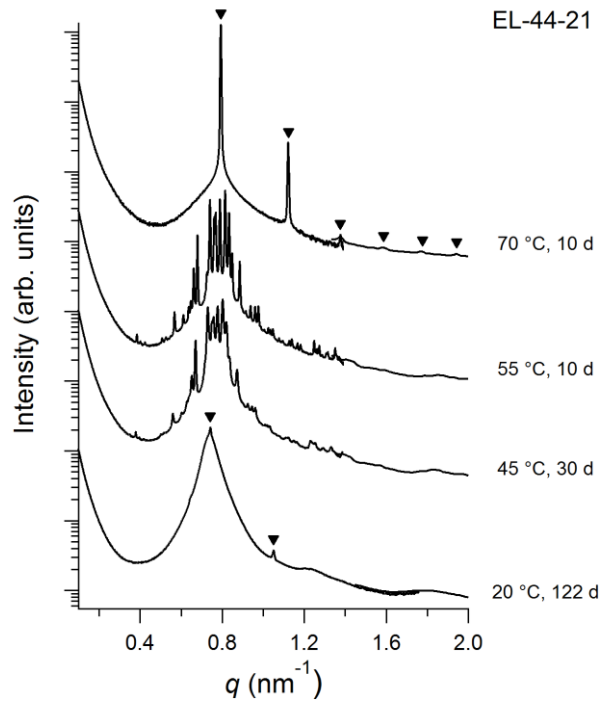


Figure 6.5 Representative SAXS patterns of the phases observed in EL-44-21 collected after a rapid quench from above T_{ODT} and annealed for the times indicated. The BCC phase is identified at 70 °C by the relative peak positions of $(q/q^*)^2 = 1, 2, 3, 4, 5, 6$ marked with filled triangles. Samples annealed at 45 and 55 °C exhibit patterns consistent with the Frank-Kasper σ phase. The sample annealed at 20 °C displays two very weak Bragg reflections indicative of the BCC phase that nucleated at early times and persists within the broad peaks of a LLP state. Curves are shifted vertically for clarity. Note that overlap of two distinct traces in each scattering pattern reflects a common q -range captured by the SAXS and MAXS detectors.

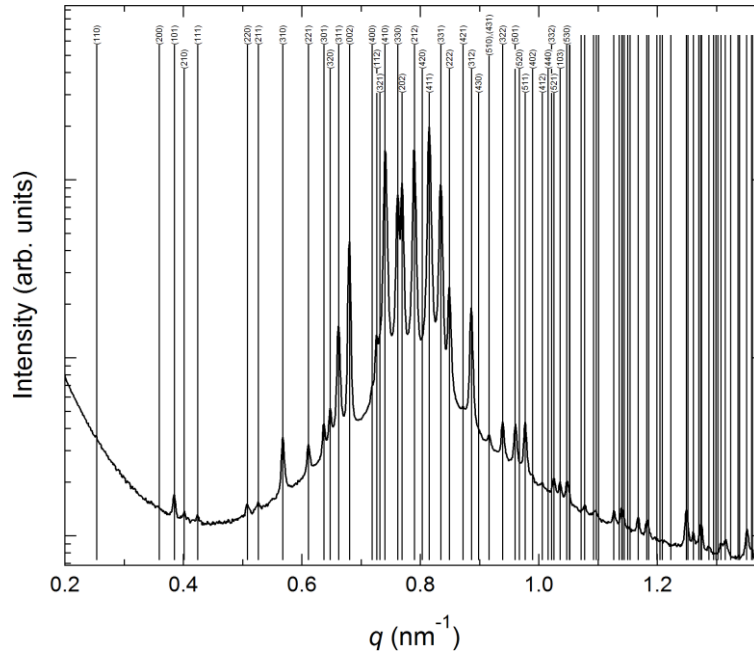


Figure 6.6 Indexing of the EL-44-21 SAXS pattern collected at 55 °C, confirming the formation of the Frank-Kasper σ phase. All allowed Bragg reflections of the σ phase (space group $P4_2/mnm$) for lattice parameters a and c of 35.0 nm and 18.3 nm, respectively, are shown as vertical lines within the experimental q range. Miller indices of the low q planes are indicated.

For EL-44-21, the σ phase also forms at 45 °C and is shown to remain stable over an extended 30 day annealing period (Figure 6.5). Notably, the phase sequence with temperature for EL-44-21 coincides with that observed by Lee et al.,^{6,16} in which the IL sample transitioned from the σ phase to BCC as temperature was increased. At room temperature ($T = 20$ °C), the sample exhibits minor reflections of a BCC microstructure, as evidenced by the small peak at $q/q^* = \sqrt{2}$ within a predominantly broad peak. Such weak Bragg reflections are indicative of the ordered state that rapidly nucleated upon quenching and gradually disappears as the sample is annealed. The broad peak and associated higher order correlations observed at 20 °C indicate a limited long-range structural order that can be attributed to a state of liquid-like packing (LLP) of micellar spheres. Although the detailed structure of the LLP state is not well-understood, it is thought to be characterized by regions of short-range-correlated packings of spheres within a macroscopically disordered structure.¹⁸

EL-44-24 was synthesized from the same poly(ethylene) precursor but has a slightly higher PLA content than the EL-44-21 sample shown to form both BCC and the σ phase. In lieu of BCC, this sample of higher composition shows evidence of weak Bragg reflections of a HEX morphology within the predominantly broad peak of the LLP state at room temperature (Figure 6.7). Assignment of a HEX microstructure is aided by observation of the sample at intermediate times where more intense higher order reflections were apparent. After 30 days of annealing at an elevated temperature of 45 °C, a minute shoulder is observed to grow in at low q along the broad peak of a persistent LLP. This shoulder corresponds to the discernible peak formed after 10 days of annealing at 55 °C. Although lack of additional reflections preclude definitive phase assignment at both 45 and 55 °C, annealing at a higher temperature of 70 °C clearly results in the formation of the σ phase. Tetrahedrally close-packed structures like the Frank-Kasper σ phase can be decomposed into two-dimensional layers of spheres that lie in planes orthogonal to the z -axis. If related to the σ phase, the developing peak observed at 45 and 55 °C is coincident with the (002) reflection, and the patterns observed may indicate the evolution of a layered structure that eventually becomes the σ phase after sufficient time.⁶ At 85 °C, the presence of the Frank-Kasper phase is also evident but after only 306 min of annealing. There are, however, two noticeable reflections, $(q/q^*)^2 = 1, 3$, that indicate that a HEX structure and the σ phase simultaneously nucleate after quenching below T_{ODT} and both persist for this short time of annealing at 85 °C.

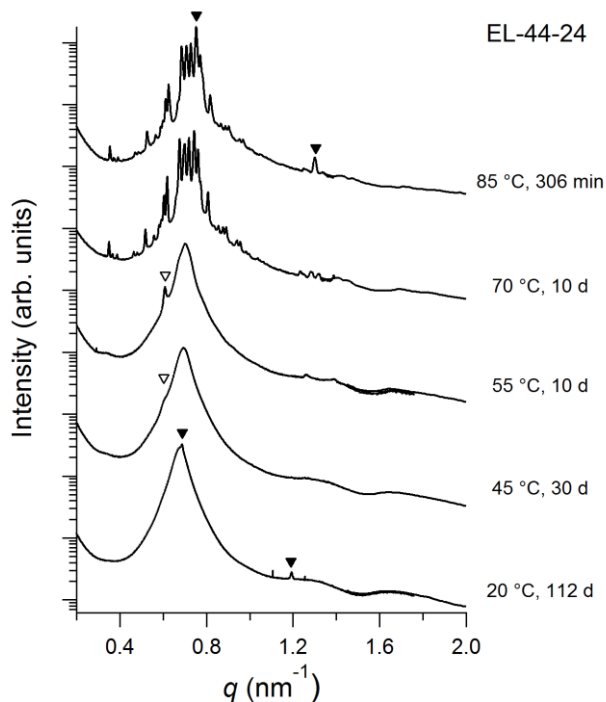


Figure 6.7 Representative SAXS patterns of the phases observed in EL-44-24 collected after a rapid quench from above T_{ODT} and annealed for the times indicated. Samples annealed at 20 and 45 °C exhibit broad scattering peaks indicative of LLP. The patterns of the samples annealed at 45 and 55 °C suggest some local organization into a layered structure due to the formation of a peak coincident with the (002) reflection of the σ phase as marked by the open triangles. Samples annealed at 70 and 85 °C display a pattern consistent with the σ phase. Weak Bragg reflections marked with filled triangles at $(q/q^*)^2 = 1, 3$ are indicative of a HEX phase that nucleated at early times and persists within the time of observation for samples annealed at 20 and 85 °C. Curves are shifted vertically for clarity.

EL-63-21 has a higher poly(ethylene) block molar mass and approximately equivalent composition as sample EL-44-21. At 45 and 70 °C, EL-63-21 displays a similar LLP state to that observed at room temperature in the previously described samples of lower molar mass (Figure 6.8). Unlike the previous samples, however, no Bragg reflections of an ordered state that nucleated on cooling below T_{ODT} are apparent, i.e., the temperature was reduced rapidly enough to prevent nucleation and growth of an ordered phase in EL-63-21. After annealing 8 d at 70 °C, however, a shoulder begins to emerge at low q as indicated by the open triangle of Figure 6.8, and at an elevated annealing temperature of 100 °C, EL-63-21 forms the σ phase. Although BCC is the accepted equilibrium phase

adjacent to the ODT for sphere-forming block polymers,^{6,18} this sample does not form a BCC microstructure at the highest annealing temperature of 150 °C, which lies within four degrees of the T_{ODT} . The disparate behavior of this sample and EL-44-21 may be accounted for by the slightly higher PLA composition of EL-63-21 (containing ~0.8 vol% more PLA), as determined from ^1H NMR analysis. The result suggests that these two materials may narrowly border a curved phase boundary between the BCC and σ phases in close proximity to the order-disorder transition.

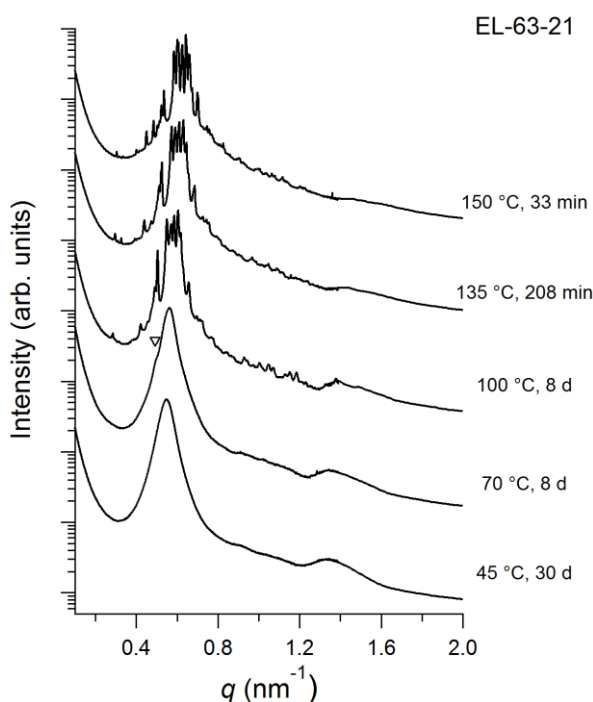


Figure 6.8 Representative SAXS patterns of the phases observed in EL-63-21 collected after a rapid quench from above T_{ODT} and annealed for the times indicated. The broad peaks observed at 45 and 70 °C are indicative of a disordered LLP. EL-63-21 produces the σ phase for $T > 100$ °C. Curves are shifted vertically for clarity.

EL-63-25 was also prepared from the larger molar mass PEE precursor and contains a larger volume fraction than the previous sample EL-63-21. At 135 °C, the sample forms the σ phase within 27 h of annealing (Figure 6.9). At a lower temperature of 100 °C, an unidentified layered structure similar to that observed in EL-44-24 and EL-63-2 is produced, as evidenced by the narrow peak at low q . It is possible that this layered structure

is a transient intermediate to the σ phase. The data suggest that cooling below some critical temperature produces a strongly segregated state (i.e., $(\chi N) > (\chi N)_{crit}$) that inhibits chain diffusion, leading to strongly temperature (and time) dependent behavior. At temperatures ≤ 70 °C, a HEX morphology was identified from Bragg diffraction peaks at positions $(q/q^*)^2 = 1, 3, 4, 7, 9, 12, 13$, but it is worth noting that the system could not be cooled at a sufficiently rapid rate to prevent nucleation of this ordered phase prior to reaching the target temperature. Therefore, the HEX phase may be a kinetically trapped state formed as the disordered system becomes unstable upon rapid cooling below the ODT.

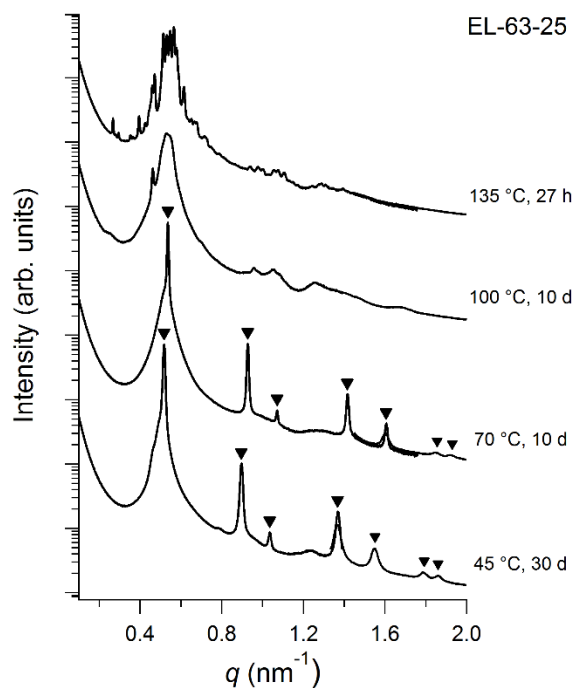


Figure 6.9 Representative SAXS patterns of the phases observed in EL-63-25 collected after a rapid quench from above T_{ODT} and annealed for the times indicated. The samples annealed at 45 and 70 °C exhibit a pattern consistent with the HEX phase $(q/q^*)^2 = 1, 3, 4, 7, 9, 12, 15$. The pattern of the sample annealed at 100 °C may be attributable to the growth of an intermediate layered structure. Curves are shifted vertically for clarity.

EL-63-17 was produced from the largest molar mass poly(ethylethylene) precursor and has the second lowest PLA composition of the samples studied. (Note that calculations of the composition from ^1H NMR analysis indicate that another sample, EL-44-17, also

nominally contains 17 vol% PLA, i.e. the compositions of EL-44-17 and EL-63-17 are 0.167 and 0.170, respectively.) At all temperatures studied, EL-63-17 (Figure 6.5) is shown to form the BCC phase, as indicated by the Bragg diffraction peaks at positions $(q/q^*)^2 = 1, 2, 3, 4, 5, 6, 7, 8, 9$. Although a BCC morphology may be expected for the block polymer of lowest composition based on previous results and recent SCFT calculations, more temperatures may be worth probing as the ODT for this polymer occurs at $T_{ODT} = 122$ °C, and the observed phase behavior of other EL materials has been shown to be strongly temperature dependent.

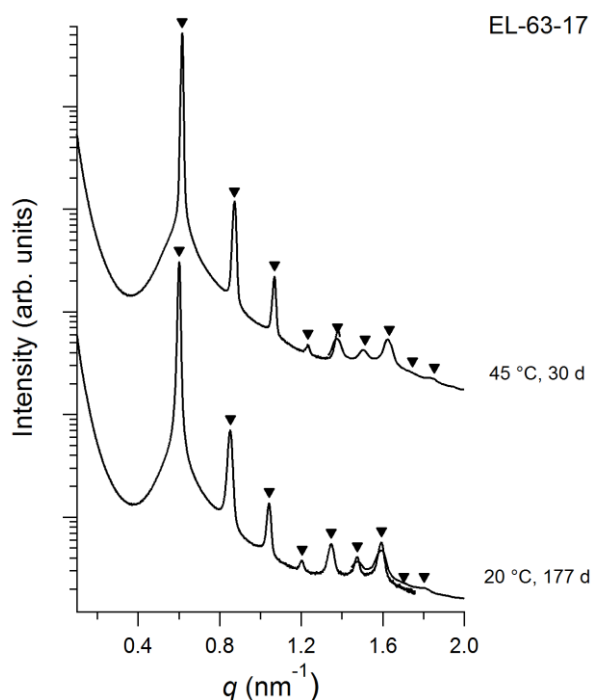


Figure 6.10 Representative SAXS patterns observed in EL-63-17 collected at 20 and 45 °C following a rapid quench from above T_{ODT} and annealed for the times indicated. The BCC phase is identified by the relative peak positions of $(q/q^*)^2 = 1, 2, 3, 4, 5, 6, 7, 8, 9$ marked with filled triangles. Curves are shifted vertically for clarity.

EL-44-17 has the lowest PLA composition of the polymers explored and was prepared from the lowest molar mass precursor employed in the synthesis of materials in the sphere-forming window. This exceptionally short and compositionally asymmetric diblock has a T_{ODT} of 44 °C, which limited our probing annealing experiments to room temperature. The

kinetic data obtained upon quenching from the disordered state to room temperature is presented in Figure 6.11.

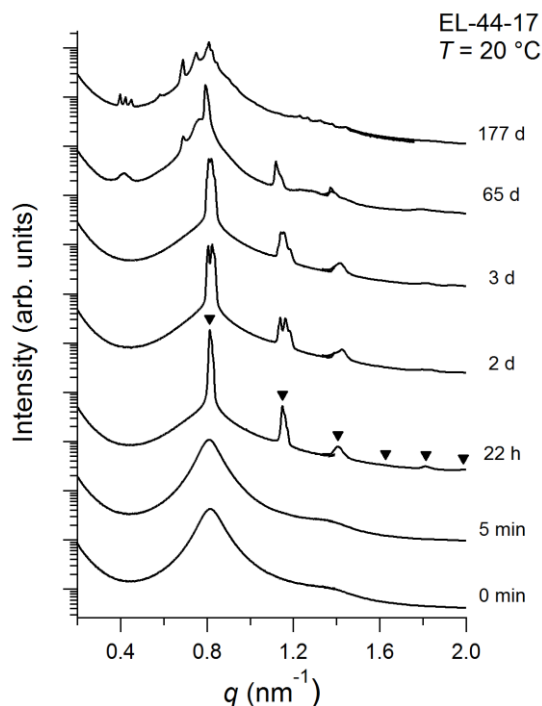


Figure 6.11 Kinetics of ordering of EL-44-17 at 20 °C as measured by SAXS. Patterns were collected after annealing for the times indicated following a rapid quench from above T_{ODT} . The BCC phase is identified by the relative peak positions of $(q/q^*)^2 = 1, 2, 3, 4, 5, 6$ marked with filled triangles above the curve obtained after 22 h of annealing. The BCC phase is replaced by the gradual formation of the C14 phase observed after 177 days.

At room temperature, an ordered BCC nucleates from a LLP state. Over time, the structure evolves through an initial distortion of the BCC microstructure. As shown in Figure 6.12(b), the diffraction pattern after 177 days of annealing contains a series of peaks that can be indexed to the Frank-Kasper C14 phase with $P6_3/mmc$ symmetry.¹⁹

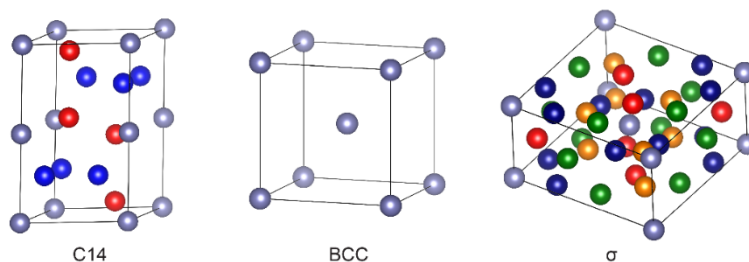


Figure 6.13 Unit cell representation of the C14 ($P6_3/mmc$) hexagonal, BCC ($Im\bar{3}m$) cubic, and σ ($P4_2/mnm$) tetragonal phases observed in EL block polymers. Different colors represent the spheres of three and five different sizes present in the Frank-Kasper C14 and σ phases, respectively.

Further experimental investigation into the stability of the C14 phase is therefore warranted, and synthesis of new materials of lower PLA composition may be necessary to determine if there is a broad window of stability. Fortunately, this result has been reproduced in another sample annealed for only two weeks at room temperature, suggesting that the times required for observation of the C14 phase may be experimentally feasible (Figure 6.14). Note that the 2D image of Figure 6.13a differs because the data was acquired at a different beamline of the Advanced Photon Source (Beamline 12-ID-B).

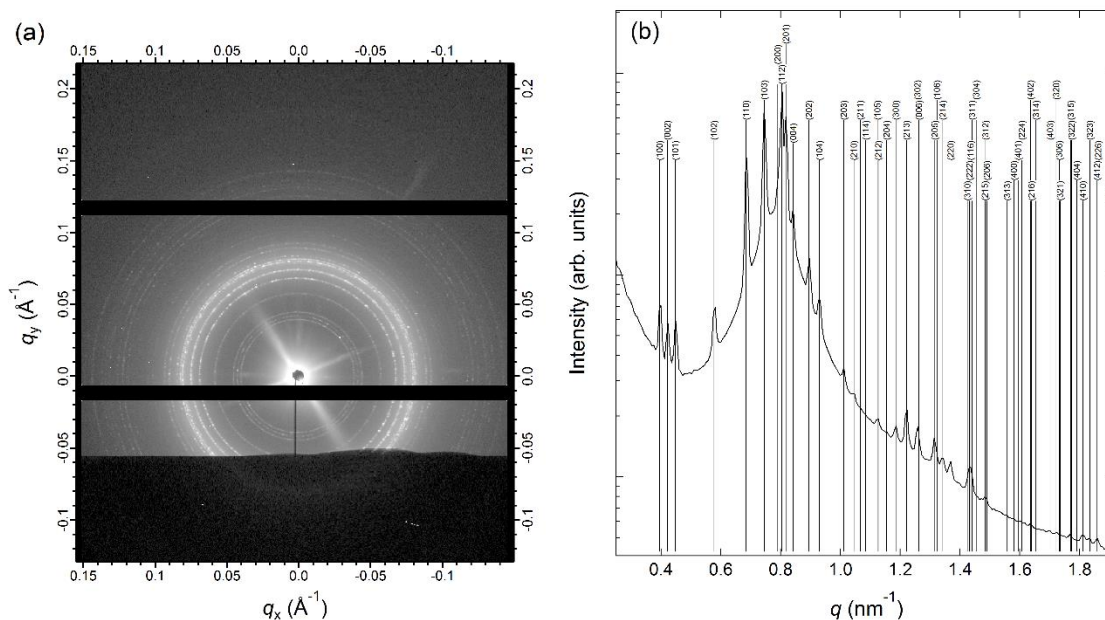


Figure 6.14 (a) The 2D powder diffraction pattern obtained for sample EL-44-17 after two weeks of annealing at 20 °C. (b) Indexing of the 1D SAXS profile, confirming the formation of the C14 phase. All allowed Bragg reflections of the C14 phase (space group $P6_3/mmc$) for lattice parameters a and c of 18.3 nm and 29.2 nm, respectively, are shown as vertical lines within the experimental q range. Miller indices of the planes are indicated.¹⁹

6.3.2 Kinetics of ordering in EL Diblock Copolymers

Block polymers of high incompatibility that self-assemble at low N are excellent candidates for the study of complex structure formation. The overall low molar mass, below the onset of molecular entanglements, and low glass transition temperatures of EL and PL ensure tractable kinetics such that the system can approach equilibrium on experimentally accessible timescales. In this section, SAXS experiments are described that follow the kinetics of ordering and the evolution of structure during the formation of the BCC, HEX and σ phases as a function of temperature for two representative polymers, EL-63-21 and EL-44-24. In these experiments, the samples were disordered ($T > T_{ODT}$), and then rapidly quenched using a Linkam DSC stage of the SAXS beamline to the temperature of interest.

For EL-63-21, ordering at temperatures at or below 70 °C appears to be kinetically limited. A representative example is shown in Figure 6.15. Some nucleation of a layered

structure is apparent from the shoulder formed on the broad peak as the sample reaches the target temperature ($t = 0$ min). However, curiously, this layered structure seems to vanish and a liquid-like packing persists. It is possible that at this temperature, although far above the glass transition of either block, increases in χN limit the coarsening of domain structures.²⁰

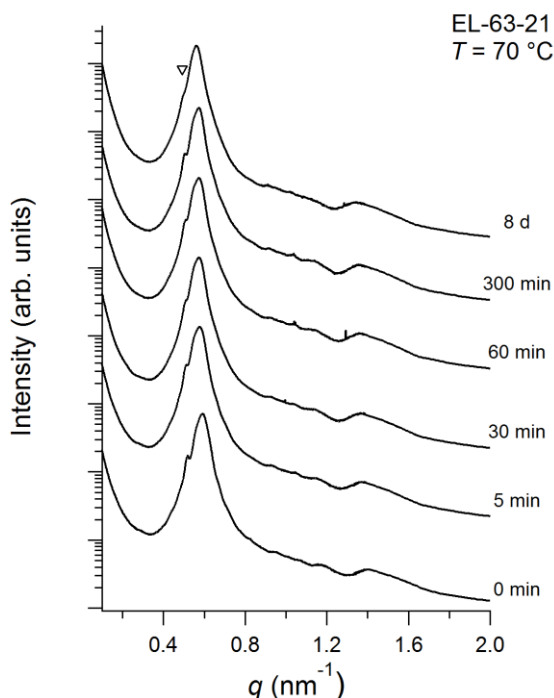


Figure 6.15 Kinetics of ordering of EL-63-21 at 70 °C as measured by SAXS. Patterns were collected after annealing for the times indicated following a rapid quench from above T_{ODT} . Some nucleation of a layered structure is evident from the shoulder at low q marked with an open triangle. Curves are shifted vertically for clarity.

When EL-63-21 is quenched to an ordering temperature of 100 °C (Figure 6.16), a layered structure and a BCC structure with reflections at $(q/q)^2 = 1, 2$ nucleate simultaneously as shown by the SAXS pattern acquired immediately after reaching the target temperature ($t = 0$ min). Within 1 min, rapid reorganization results in disordering of the BCC structure, and peaks consistent with the σ phase continue to grow in over the course of 5 h (≈ 306 min) and persist for at least 8 days of observation. A preceding

nucleation of a metastable BCC structure is consistent with previous experimental studies performed on IL block polymers that form the σ phase.^{6,16}

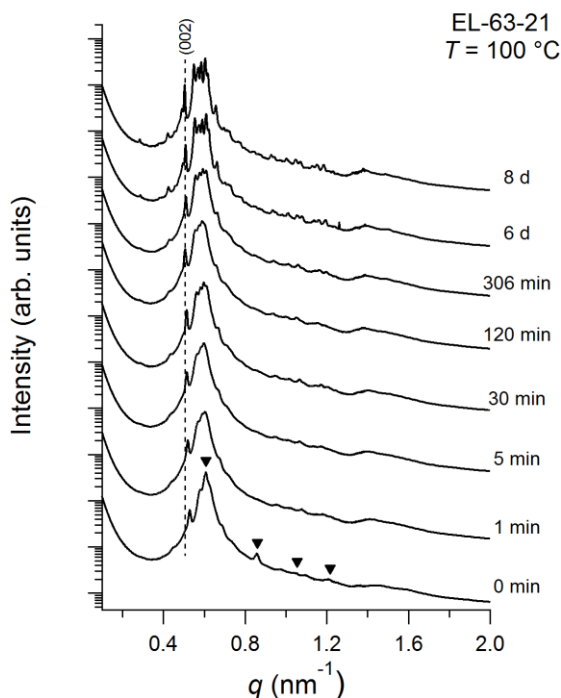


Figure 6.16 Kinetics of ordering of EL-63-21 at 100 °C as measured by SAXS. Patterns were collected after annealing for the times indicated following a rapid quench from above T_{ODT} . The BCC phase is identified by peak positions at $(q/q^*)^2 = 1, 2, 3, 4$ marked with filled triangles. Both BCC and the σ phase rapidly nucleate, but the σ phase ultimately forms. Curves are shifted vertically for clarity.

Figure 6.17 shows that while the evolution of the structure upon ordering at 135 °C is similar in appearance to that obtained at 100 °C, the time required to complete the transition to the σ phase is reduced dramatically from days to minutes.

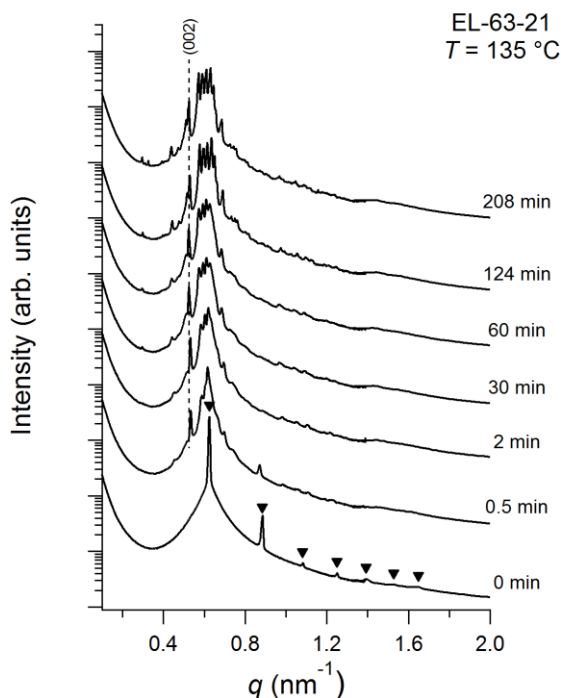


Figure 6.17 Kinetics of ordering of EL-63-21 at 135 °C as measured by SAXS. Patterns were collected after annealing for the times indicated following a rapid quench from above T_{ODT} . A BCC phase identified by peak positions $(q/q^*)^2 = 1, 2, 3, 4, 5, 6, 7$ and marked with filled triangles rapidly nucleates and grows at short time (< 30 s) but reorganizes to form the σ phase. Curves are shifted vertically for clarity.

In additional experiments, samples were annealed at low temperature following a quench from the disordered state and then heated to a target temperature of interest. These experiments give insight into the unique pathways towards equilibrium found in EL block polymers. For example, when the EL-63-21 sample is quenched to 45 °C and annealed to produce a LLP structure and then heated to 135 °C, no metastable BCC intermediate is formed. Instead, the σ phase forms slowly through an intermediate layered structure (Figure 6.18).

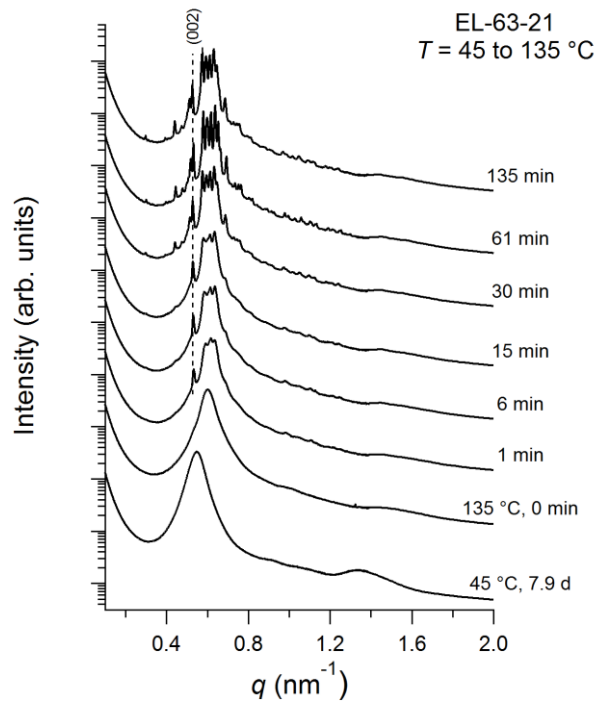


Figure 6.18 Kinetics of ordering of EL-63-21 at 135 °C following annealing of a disordered phase with LLP. In contrast to the mechanistic pathway following a direct quench to 135 °C (Figure 6.15). The dashed line marks the position of a peak related to the (002) reflection of the σ phase, which nucleates and grows through an unidentified layered intermediate. Curves are shifted vertically for clarity.

EL-44-24 is a block polymer richer in PLA and of lower molar mass than EL-63-21. For EL-44-24, ordering at 20 °C appears to produce a HEX microstructure (Figure 6.19). However, it is clear from the quick formation of the structure ($t = 0$ min) that the HEX structure nucleated and formed on cooling prior to reaching the target temperature. Utilizing a rapid and sufficient quench rate leads to a rapid stiffening of the material prior to nucleation of the ordered phase, thereby generating a disordered LLP state. Inadequate cooling rates can conversely lead to nucleation of non-equilibrium phases that become kinetically trapped as the sample is cooled further.

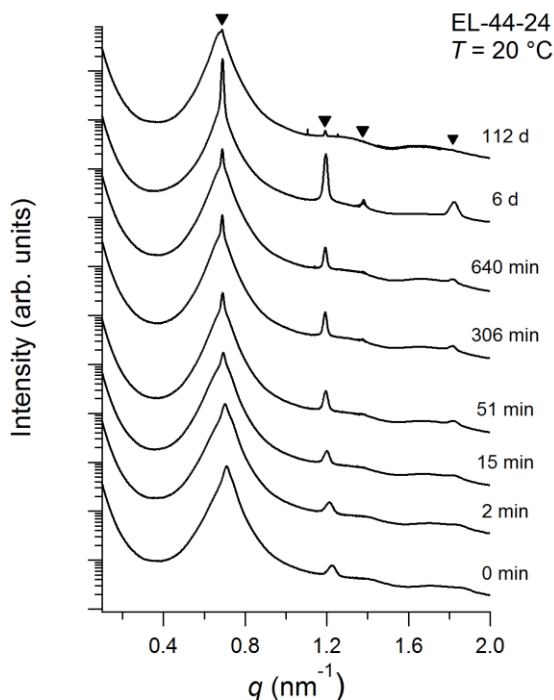


Figure 6.19 Kinetics of ordering of EL-44-24 at 20 °C as measured by SAXS. Patterns were collected after annealing for the times indicated following a rapid quench from above T_{ODT} . The HEX phase nucleates and persists at low temperature over the experimental time window. Triangles above the 112 d curve mark the first several allowed Bragg reflections at relative peak positions $(q/q^*)^2 = 1, 2, 3, 7$. Curves are shifted vertically for clarity.

The results of Figure 6.20, obtained during rapid quench of the sample from the disordered state to $T = 45$ °C, suggest that the HEX structure may not be thermodynamic equilibrium. After 30 days of annealing, a slight bump is formed at low q on top of the broad peak of the disordered LLP state, indicating the formation of a layered structure. It is likely that this structure would continue to evolve a new state with further annealing, and a similar expectation is held for the sample maintained at 20 °C, which shows very little remaining HEX microstructure after 112 days of annealing (Figure 6.19). Although kinetics of the transformation may be prohibitively slow, this result is consistent with the hypothesis made by Lee et al. that the transition to the thermodynamically favored phase likely begins with a disordering (melting) of the fast nucleating structure.⁴

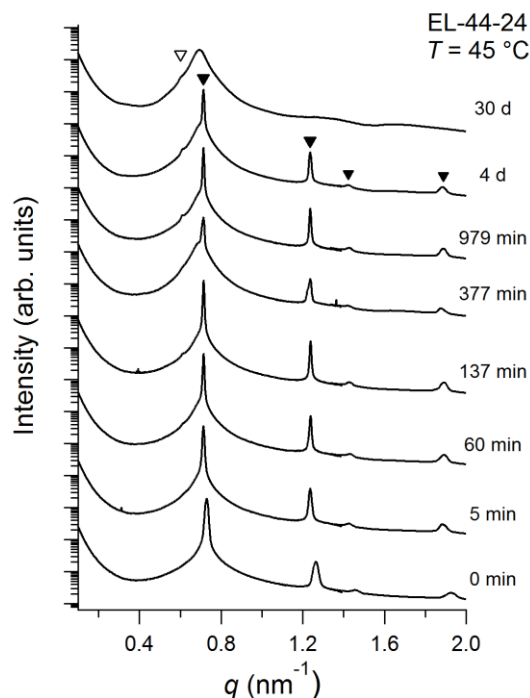


Figure 6.20 Kinetics of ordering of EL-44-24 at 45 °C as measured by SAXS. Patterns were collected after annealing for the times indicated following a rapid quench from above T_{ODT} . The HEX phase nucleates and persists at this low temperature for at least 30 days of annealing before being replaced with a LLP state. Filled triangles above the 4 d curve mark the first several allowed Bragg reflections at relative peak positions $(q/q^*)^2 = 1, 3, 4, 7$. The open triangle above the 30 d curve marks an emerging peak at low q . Curves are shifted vertically for clarity.

Annealing experiments performed at a slightly elevated temperature of 55 °C suggest that kinetic limitations play a substantial role in the observations made at low temperature (Figure 6.21). Following annealing for 4 days, HEX and a layered structure coexist. Notably, the larger HEX peaks in the sample shown at 4 days compared to earlier time points is likely due to substantial differences in quench rates between samples, as time limitations did not allow for the same sample to be followed throughout the study. Multiple samples were annealed simultaneously and monitored. The 4 day sample was quenched in the laboratory instead of on the Linkam DSC stage at the Advanced Photon Source. The disparity in the samples suggests that alternative quenching strategies may need to be employed to consistently observe a similar state of nucleation and growth at specified time. Additional experiments have demonstrated that sample EL-44-24 can be consistently

quenched to a state of LLP if immersed in liquid nitrogen. Samples heated above T_{ODT} and then immersed in liquid nitrogen did not nucleate a HEX phase upon warming to the target temperature, and, notably, the HEX phase was not observed to form upon further heating (Figure 6.22).

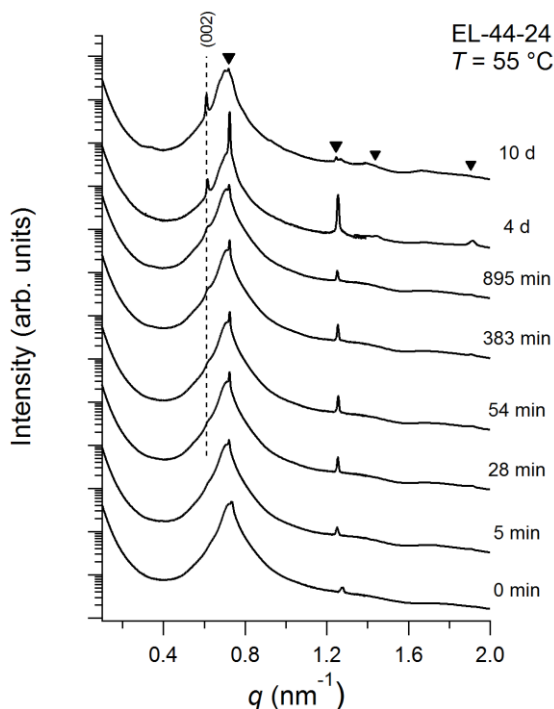


Figure 6.21 Kinetics of ordering of EL-44-24 at 55 °C as measured by SAXS. Patterns were collected after annealing for the times indicated following a rapid quench from above T_{ODT} . The HEX phase nucleates and persists at this low temperature for at least 10 d of annealing before being replaced with a layered structure. Triangles above the 10 d curve mark the first several allowed Bragg reflections of HEX at relative peak positions $(q/q^*)^2 = 1, 3, 4, 7$. The dashed line marks the position of a peak related to the (002) reflection of the σ phase indicative of a layered structure. Curves are shifted vertically for clarity.

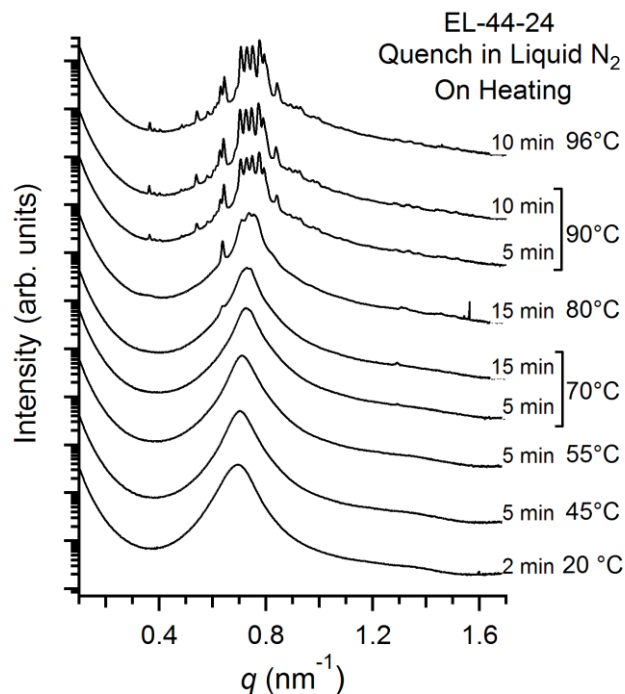


Figure 6.22 Ordering of EL-44-24 upon heating. The sample was cooled below the ODT through immersion in liquid nitrogen, thus preventing nucleation of the HEX phase. A disordered LLP state that transitions directly to the σ phase is observed. The sample was monitored and annealed at each temperature until no further change in structure was apparent. Comparison with Figure 6.19 shows that slower cooling results in a nucleation of a non-equilibrium HEX phase. Curves are shifted vertically for clarity.

The important influence of temperature (and therefore, χN) on the ordering kinetics is further illustrated by a comparison of the assembly observed at 70 °C (Figure 6.23) and 85 °C (Figure 6.24). Although EL-44-24 also nucleates the HEX phase upon quenching to 70 °C, the transition to the σ phase occurs within 4 days of annealing. Astoundingly, the σ phase forms the predominant microstructure in 30 min at temperature only 15 degrees higher ($T = 85$ °C). Interestingly, the coexistence of the HEX and σ may further support that there is not a direct transition pathway between these two phases. Rather, the σ phase can only form from a disordered state.

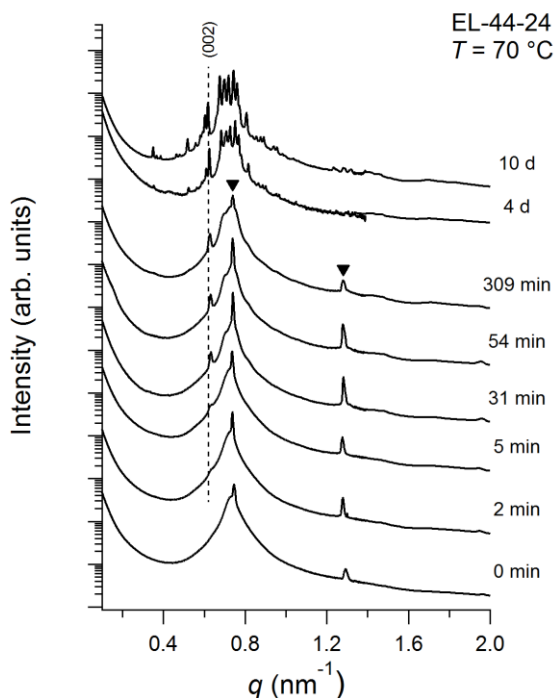


Figure 6.23 Kinetics of ordering of EL-44-24 at 70 °C as measured by SAXS. Patterns were collected after annealing for the times indicated following a rapid quench from above T_{ODT} . The HEX phase nucleates and persists for short times before being replaced by nucleation and growth of the σ phase. Triangles above the 309 min curve mark the allowed Bragg reflections of HEX at relative peak positions $(q/q^*)^2 = 1, 3$. The dashed line marks the position of the (002) reflection of the σ phase that grows in at early times. Curves are shifted vertically for clarity.

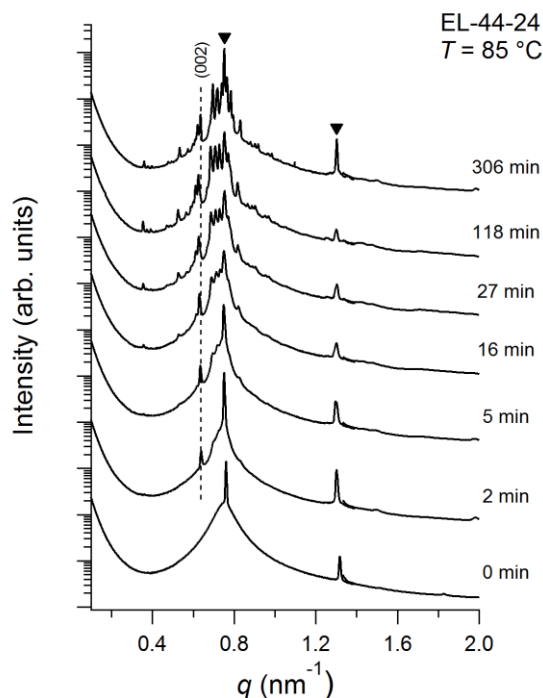


Figure 6.24 Kinetics of ordering of EL-44-24 at 85 °C as measured by SAXS. SAXS patterns were collected after annealing for the times indicated following a rapid quench from above T_{ODT} . Both HEX and the σ phase rapidly nucleate. Triangles above the 306 min curve mark the allowed Bragg reflections of HEX at relative peak positions $(q/q^*)^2 = 1, 3$. The dashed line marks the position of the (002) reflection of the σ phase that grows in at early times. Curves are shifted vertically for clarity.

It is important to understand why conventional phases such as BCC and HEX appear as metastable intermediates during the formation of the σ phase. Upon rapid quenches from the disordered phase to lower temperature, the segregation strength increases and induces a thermodynamic drive to order. There must be a clear distinction in the timescales of structure formation to account for the relative nucleation rates of the simple phases of BCC and HEX versus the σ phase. To form the σ phase, there must be sufficient exchange of polymer chains between particles to achieve the five requisite particle sizes of the various lattice sites, and further, the nucleation of the structure requires a local organization of 30 particles. These requirements are a stark contrast to a simple BCC structure, consisting of one particle size and an arrangement of only two particles per unit cell, leading to a conversely rapid nucleation. However, the scattering data suggest that following fast nucleation of the BCC or HEX phase due to instability of the disordered phase at

temperatures below T_{ODT} , the system breaks symmetry to form the σ phase as an optimal configuration that relieves any associated frustration of the lattice geometry.

6.3.4 Phase Behavior of PL Diblock Copolymers

EL and PL block polymers primarily differ in the molecular architecture of the hydrocarbon block. Similar segment-segment interactions should exist for PL and EL block polymers, and all differences observed in their phase behavior can be primarily attributed to their disparate conformational asymmetry parameters. The molecular characteristics for the PL block polymers employed in this study are specified in Table 6.2. Experiments were executed in the same manner as that described for EL block polymers, enabling fair comparisons between data sets.

Table 6.2 Molecular characterization data for PL block polymers[‡]

entry ^a	$M_{n,P}$ ^b	$M_{n,L}$ ^b	M_n ^b	N^c	f_L^d	D^e	$T_{g,P}$ (°C) ^f	$T_{g,L}$ (°C) ^f	T_{ODT} (°C) ^g
PL-26-18	1900	600	2500	40	0.18	1.11	−63	−5	63
PL-29-18	2200	700	2800	45	0.18	1.04	−62	−3	87
PL-29-21	2200	800	2900	47	0.21	1.02	−63	7	110
PL-29-32	2200	1400	3500	54	0.32	1.09	−62	19	190
PL-47-12	3400	700	4100	68	0.12	1.02	−62	−2	95
PL-47-15	3400	800	4200	70	0.15	1.07	−62	3	140

^aSamples are referred to as PL-XX-YY where “XX” specifies N_p , the volumetric degree of polymerization of the PEP block, and “YY” specifies the percentage of the polymer molecular volume that constitutes the PLA block (i.e., $f_L \times 100$). ^bNumber-average molar mass reported in (g/mol) from ¹H NMR end-group analysis of the precursor. Total molar mass of block polymer includes *s*-butyllithium end-group. ^cVolumetric degree of polymerization based on reported^{10,11} homopolymer densities at 140 °C (0.79 and 1.152 g/cm³ for P and L, respectively) and a reference volume of 118 Å³. ^dVolume fraction of L based on reported homopolymer densities at 140 °C and ¹H NMR. ^eMolar mass dispersity determined using LS-SEC in THF. ^fGlass transition temperatures determined from DSC. ^gOrder-disorder transition temperature determined from DMS performed on heating at a rate of 2 °C/min.

Unlike EL samples, PL polymers showed no temperature-dependent phase behavior, and each sample adopted only one morphology. Figure 6.25 summarizes the results of long time annealing studies for the six PL block polymers performed at fixed temperature.

[‡]These samples were prepared by Robert J. Hickey and James H. Lettow.

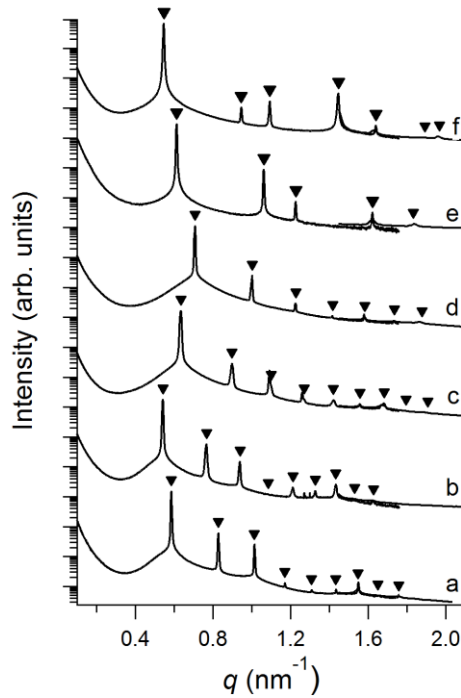


Figure 6.25 Isothermal synchrotron SAXS patterns obtained from PL block polymers annealed for 7 d at 45 °C. The BCC phase is identified by the relative peak positions $(q/q^*)^2 = 1, 2, 3, 4, 5, 6, 7, 8, 9$ where q^* is the primary peak in samples (a) PL-47-12, (b) PL-47-15, (c) PL-29-18, and (d) PL-26-18. Note that PL-47-15 was annealed at 55 °C. The HEX phase is identified by the relative peak positions $(q/q^*)^2 = 1, 3, 4, 7, 9, 12$ in samples (e) PL-29-21 and (f) PL-29-32. Bragg reflections are marked with filled triangles. Curves are shifted vertically for clarity.

In order to ensure that the equilibrium phase was obtained, each PL sample was also heated from a supercooled state at low temperature to the ODT, where the dynamics of the system are expected to become extremely fast. The representative data of PL-47-15 and PL-29-21 of Figure 6.23 summarize the results of these experiments. Each sample was heated using increments 10–20 °C and annealed at each temperature for 2–5 min. The data illustrate that the BCC microstructure of PL-47-15 (Figure 6.26a) and the HEX microstructure of PL-29-21 (Figure 6.26b) remain stable throughout the experimental temperature window.

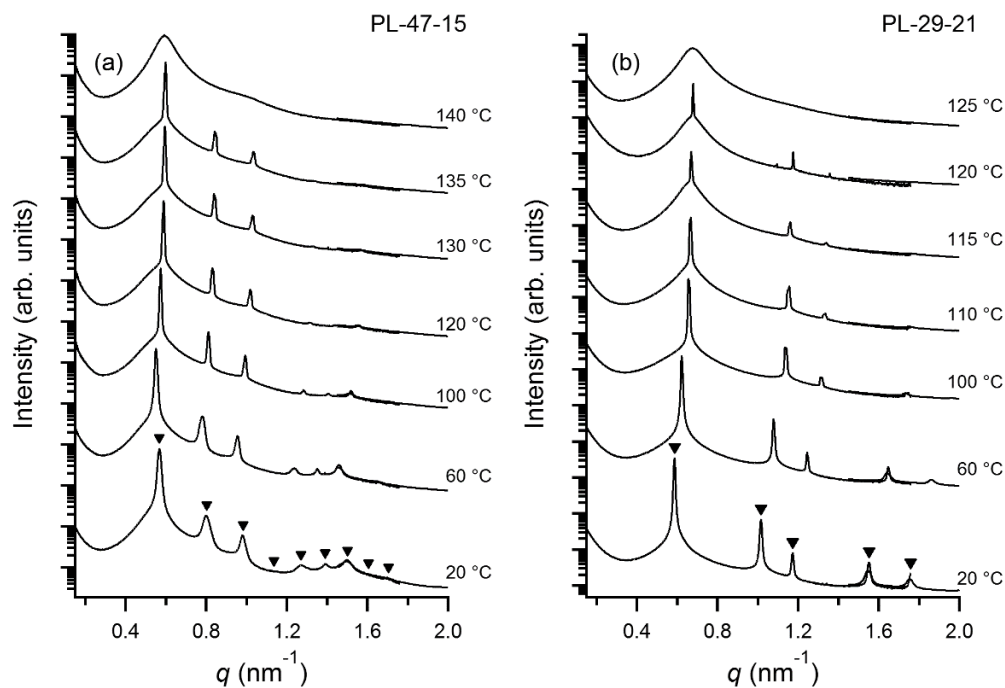


Figure 6.26 Scattering patterns of samples (a) PL-47-15 and (b) PL-29-21 obtained on heating using 10–20 °C increments to the ODT. Triangles above the 20 °C curves mark the first several allowed Bragg reflections of BCC and HEX for PL-47-15 and PL-29-21, respectively. Some data have been omitted and vertical shifts are applied to the SAXS patterns for clarity.

6.3.5 Region of stability of the σ phase

Using the previously reported interaction parameter χ for the PL system and assuming no composition dependence, the phase behavior of all asymmetric PL block polymers studied is summarized in the phase portraits of Figure 6.27. The construction is based on phase assignment after extended annealing in agreement with the dynamic heating experiments illustrated in Figure 6.26. The temperature dependence of χ for the EL system determined in Section 6.3.1 was used to construct the EL phase map. Phase assignments were limited to high temperatures where the σ phase is shown to be the equilibrium morphology through a combination of experiments involving (i) dynamic heating and (ii) annealing at high temperature in the vicinity of the ODT. The phase diagram of the IL system is included for comparison.^{6,16,21}

In EL block polymers, the σ phase is located directly between the HEX and BCC phases, emphasizing the competitive nucleation that characterizes their ordering kinetics

and the likely close free energies of each phase. As shown in Figure 6.24, this result is consistent with the work of Lee et al.⁴⁻⁶ that found the σ phase window in IL block polymers is localized to a region between the HEX and BCC phases. No σ phase window is found within the PL phase diagram, and the compositions of the spherical phase composition window agree with those previously reported on PL block polymers of larger molar mass.¹⁵ If the σ phase does exist in the PL system, it may lie between the two samples that construct the HEX-BCC phase boundary and differ by less than 3 vol% PLA.

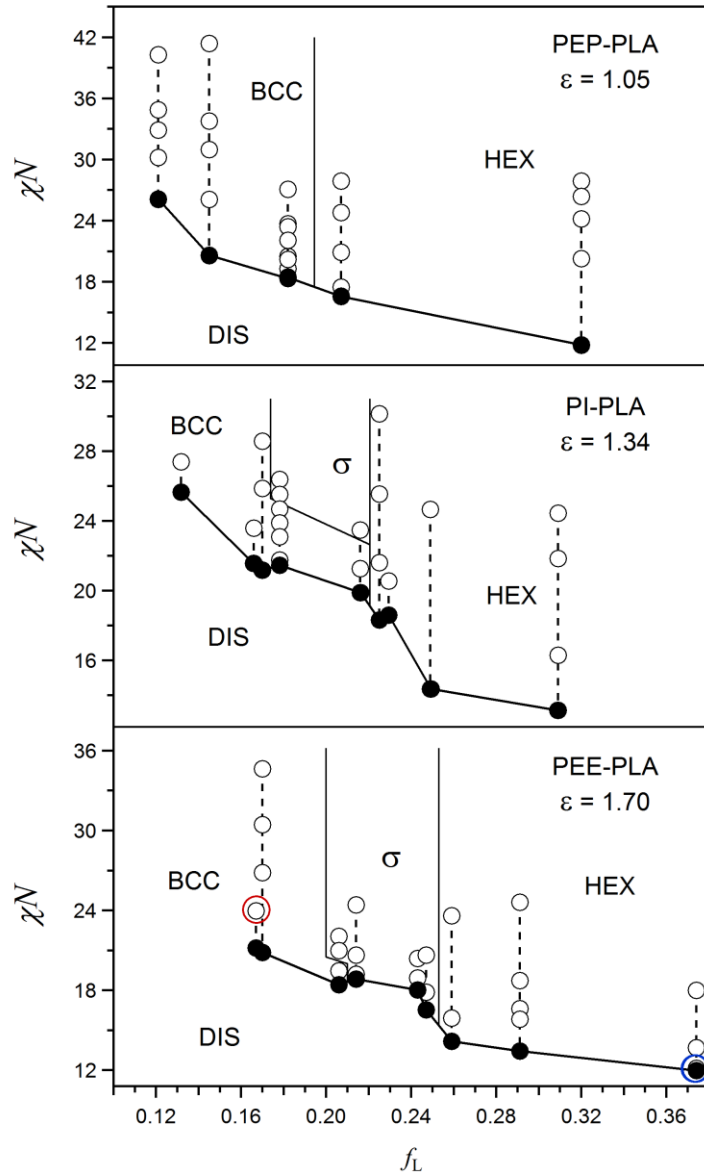


Figure 6.27 Phase portraits summarizing the phase behavior of compositionally asymmetric (a) PL, (b) IL,^{16,21} and (c) EL block polymers. Conformational asymmetry stabilizes the σ phase. Note that the data point enclosed in a red circle (EL-44-17) has been shown to also form the Frank-Kasper C14 phase. The sample enclosed in a blue circle (EL-28-37) transitions to gyroid at 109 °C prior to disorder.

Xie et al.⁹ previously identified conformational asymmetry as the key parameter to induce stability of the σ phase in linear block polymers and calculated the theoretical SCFT phase diagrams reproduced in Figure 6.25. The phase behavior was determined using

various values of the conformational asymmetry parameter. The σ phase is found to first emerge as an equilibrium morphology for an ε value of 2.25 over a narrow window of f and χN values in close proximity to and above the region of the BCC phase. As the value of ε increases, the stability window for the σ phase broadens.

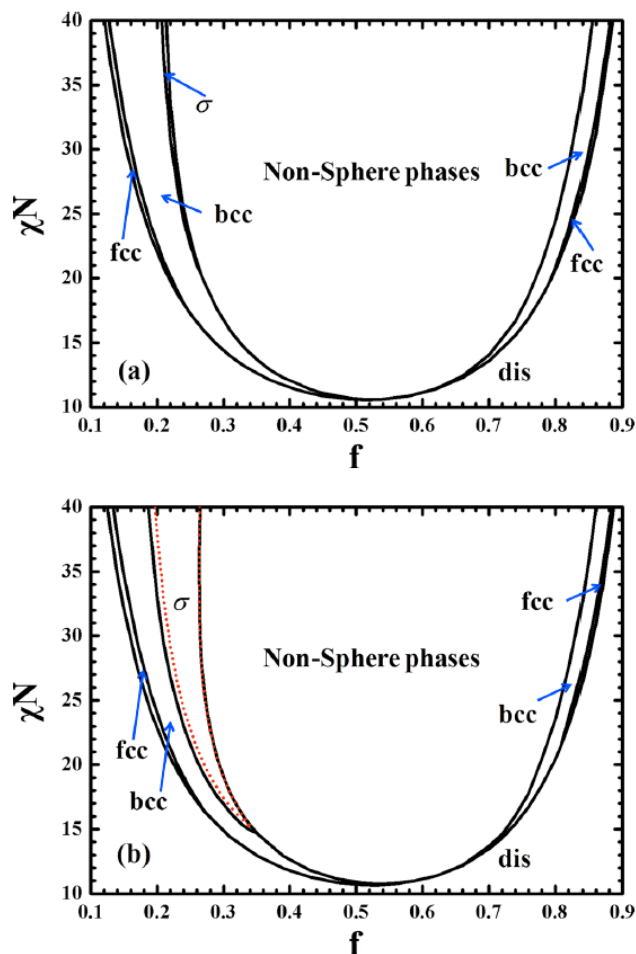


Figure 6.28 SCFT phase diagrams for conformationally asymmetric AB block polymers calculated using a conformational asymmetry parameter $\varepsilon = (b_A/b_B)^2$ of (a) 2.25 and (b) 4.0. Reproduced with permission from Xie, N.; Li, W.; Qiu, F.; Shi, A. *ACS Macro Lett.* **2014**, 3, 906–910. Copyright 2014 American Chemical Society.⁹

The EL system is estimated to have a ε value of approximately 1.70 at 140 °C, whereas the PL system is essentially conformationally symmetric ($\varepsilon = 1.05$).^{10,11,15} The large stability window of the σ phase in EL block polymers suggests that SCFT calculations

underestimate the contributions of conformational asymmetry to the formation of complex structures. Furthermore, the SCFT calculations do not account for the direct transitions from the σ phase to the disordered state observed in these materials. However, such direct transitions may be influenced by the presence of fluctuations in these low N block polymers, and therefore, their behavior cannot be quantitatively predicted nor accurately reflected in the phase diagrams calculated using SCFT.

6.4 Conclusions

A series of compositionally asymmetric block polymers were synthesized to investigate the influence of conformational asymmetry on the formation of new, low-symmetry phases in linear AB diblock copolymers. We have shown that (i) the formation of low-symmetry phases is strongly time and temperature dependent and (ii) a wide stability window of Frank-Kasper phases exist within $0.17 < f_L < 0.24$ for conformationally asymmetric EL block polymers. This composition window was augmented further due to the surprising discovery of a Frank-Kasper C14 structure adjacent to the BCC phase at the lowest compositions of PLA explored. In contrast, our preliminary findings support that there is no window of stability for the σ phase or other low-symmetry phases in the conformationally symmetric PL system.

6.5 References

- (1) Matsen, M. W. In *Soft Matter*; Wiley-VCH Verlag GmbH & Co. KGaA: 2007, p 87.
- (2) Tyler, C. A.; Morse, D. C. *Physical Review Letters* **2005**, *94*, 208302.
- (3) Leibler, L. *Macromolecules* **1980**, *13*, 1602.
- (4) Lee, S.; Leighton, C.; Bates, F. S. *Proceedings of the National Academy of Sciences* **2014**, *111*, 17723.
- (5) Lee, S.; Bluemle, M. J.; Bates, F. S. *Science* **2010**, *330*, 349.
- (6) Gillard, T. M.; Lee, S.; Bates, F. S. *Proceedings of the National Academy of Sciences* **2016**.
- (7) Grason, G. M. *Physics Reports* **2006**, *433*, 1.
- (8) Grason, G. M.; DiDonna, B. A.; Kamien, R. D. *Physical Review Letters* **2003**, *91*, 058304.
- (9) Xie, N.; Li, W.; Qiu, F.; Shi, A.-C. *ACS Macro Letters* **2014**, *3*, 906.
- (10) Fetters, L. J.; Lohse, D. J.; Richter, D.; Witten, T. A.; Zirkel, A. *Macromolecules* **1994**, *27*, 4639.
- (11) Henton, D. E.; Gruber, P.; Lunt, J.; Randall, J. *Natural fibers, biopolymers, and biocomposites* **2005**, 527.
- (12) Anderson, K. S.; Hillmyer, M. A. *Macromolecules* **2004**, *37*, 1857.
- (13) Hillmyer, M. A.; Bates, F. S. *Macromolecules* **1996**, *29*, 6994.
- (14) Schulze, M. W.; Sinturel, C.; Hillmyer, M. A. *ACS Macro Letters* **2015**, *4*, 1027.
- (15) Schmidt, S. C.; Hillmyer, M. A. *Journal of Polymer Science Part B: Polymer Physics* **2002**, *40*, 2364.
- (16) Lee, S.; Gillard, T. M.; Bates, F. S. *Aiche J* **2013**, *59*, 3502.
- (17) Almdal, K.; Hillmyer, M. A.; Bates, F. S. *Macromolecules* **2002**, *35*, 7685.
- (18) Chanpuriya, S.; Kim, K.; Zhang, J.; Lee, S.; Arora, A.; Dorfman, K. D.; Delaney, K. T.; Fredrickson, G. H.; Bates, F. S. *ACS Nano* **2016**.
- (19) Hajiw, S.; Pansu, B.; Sadoc, J.-F. *ACS Nano* **2015**, *9*, 8116.
- (20) Zhang, C.-Z.; Wang, Z.-G. *Physical Review E* **2006**, *73*, 031804.

- (21) Gillard, T. M., University of Minneosta, 2015.

Bibliography

Almdal, K.; Hillmyer, M. A.; Bates, F. S. *Macromolecules* **2002**, *35*, 7685.

Anderson, K. S.; Hillmyer, M. A. *Macromolecules* **2004**, *37*, 1857.

Arvidson, S. A.; Lott, J. R.; McAllister, J. W.; Zhang, J.; Bates, F. S.; Lodge, T. P.; Sammler, R. L.; Li, Y.; Brackhagen, M. *Macromolecules* **2012**, *46*, 300.

Bailey, T. S.; Rzayev, J.; Hillmyer, M. A. *Macromolecules* **2006**, *39*, 8772.

Balsara, N. P.; Dai, H. J.; Watanabe, H.; Sato, T.; Osaki, K. *Macromolecules* **1996**, *29*, 3507.

Bang, J.; Jeong, U.; Ryu, D. Y.; Russell, T. P.; Hawker, C. J. *Advanced Materials* **2009**, *21*, 4769.

Barlow, K. J.; Hao, X.; Hughes, T. C.; Hutt, O. E.; Polyzos, A.; Turner, K. A.; Moad, G. *Polymer Chemistry* **2014**, *5*, 722.

Baruth, A.; Rodwogin, M. D.; Shankar, A.; Erickson, M. J.; Hillmyer, M. A.; Leighton, C. *ACS Applied Materials & Interfaces* **2011**, *3*, 3472.

Baruth, A.; Seo, M.; Lin, C. H.; Walster, K.; Shankar, A.; Hillmyer, M. A.; Leighton, C. *ACS Applied Materials & Interfaces* **2014**, *6*, 13770.

Bates, C. M.; Maher, M. J.; Janes, D. W.; Ellison, C. J.; Willson, C. G. *Macromolecules* **2013**.

Bates, C. M.; Seshimo, T.; Maher, M. J.; Durand, W. J.; Cushen, J. D.; Dean, L. M.; Blachut, G.; Ellison, C. J.; Willson, C. G. *Science* **2012**, *338*, 775.

Bates, F. S. *Macromolecules* **1987**, *20*, 2221.

Bates, F. S.; Fredrickson, G. H. *Annual Review of Physical Chemistry* **1990**, *41*, 525.

Bates, F. S.; Fredrickson, G. H. *Physics Today* **1999**, *52*, 32.

- Bates, F. S.; Fredrickson, G. H. *Macromolecules* **1994**, *27*, 1065.
- Bates, F. S.; Hartney, M. A. *Macromolecules* **1985**, *18*, 2478.
- Bates, F. S.; Hillmyer, M. A.; Lodge, T. P.; Bates, C. M.; Delaney, K. T.; Fredrickson, G. H. *Science* **2012**, *336*, 434.
- Bates, F. S.; Rosedale, J. H.; Fredrickson, G. H. *The Journal of Chemical Physics* **1990**, *92*, 6255.
- Bates, F. S.; Rosedale, J. H.; Fredrickson, G. H.; Glinka, C. J. *Physical Review Letters* **1988**, *61*, 2229.
- Bates, F. S.; Schulz, M. F.; Khandpur, A. K.; Forster, S.; Rosedale, J. H.; Almdal, K.; Mortensen, K. *Faraday Discussions* **1994**, *98*, 7.
- Bates, F. S.; Schulz, M. F.; Rosedale, J. H.; Almdal, K. *Macromolecules* **1992**, *25*, 5547.
- Bates, F. S.; Wiltzius, P. *The Journal of Chemical Physics* **1989**, *91*, 3258.
- Bertrand, A.; Hillmyer, M. A. *Journal of the American Chemical Society* **2013**, *135*, 10918.
- Blanazs, A.; Armes, S. P.; Ryan, A. J. *Macromolecular Rapid Communications* **2009**, *30*, 267.
- Boudouris, B. W.; Frisbie, C. D.; Hillmyer, M. A. *Macromolecules* **2008**, *41*, 67.
- Brunauer, S.; Emmett, P. H.; Teller, E. *Journal of the American Chemical Society* **1938**, *60*, 309.
- Brutman, J. P.; Delgado, P. A.; Hillmyer, M. A. *ACS Macro Letters* **2014**, *3*, 607.
- Cahn, J. W. *The Journal of Chemical Physics* **1965**, *42*, 93.
- Cahn, J. W.; Hilliard, J. E. *The Journal of Chemical Physics* **1958**, *28*, 258.
- Car, A.; Stropnik, C.; Yave, W.; Peinemann, K.-V. *Advanced Functional Materials* **2008**, *18*, 2815.
- Cavicchi, K. A.; Zalusky, A. S.; Hillmyer, M. A.; Lodge, T. P. *Macromolecular Rapid Communications* **2004**, *25*, 704.
- Chai, J.; Buriak, J. M. *ACS Nano* **2008**, *2*, 489.
- Chanpuriya, S.; Kim, K.; Zhang, J.; Lee, S.; Arora, A.; Dorfman, K. D.; Delaney, K. T.; Fredrickson, G. H.; Bates, F. S. *ACS Nano* **2016**.

Chaudhari, A.; Ghoshal, T.; Shaw, M. T.; Cummins, C.; Borah, D.; Holmes, J. D.; Morris, M. A. 2014; Vol. 9051, p 905110.

Chen, L.; Phillip, W. A.; Cussler, E. L.; Hillmyer, M. A. *Journal of the American Chemical Society* **2007**, *129*, 13786.

Chintapalli, M.; Chen, X. C.; Thelen, J. L.; Teran, A. A.; Wang, X.; Garetz, B. A.; Balsara, N. P. *Macromolecules* **2014**, *47*, 5424.

Chinthamanipeta, P. S.; Lou, Q.; Shipp, D. A. *ACS Nano* **2011**, *5*, 450.

Cho, J. H.; Lee, J.; Xia, Y.; Kim, B.; He, Y.; Renn, M. J.; Lodge, T. P.; Daniel Frisbie, C. *Nat Mater* **2008**, *7*, 900.

Choi, I.; Ahn, H.; Park, M. J. *Macromolecules* **2011**, *44*, 7327.

Choi, J. H.; Ye, Y. S.; Elabd, Y. A.; Winey, K. I. *Macromolecules* **2013**, *46*, 5290.

Cochran, E. W.; Bates, F. S. *Macromolecules* **2002**, *35*, 7368.

Cochran, E. W.; Morse, D. C.; Bates, F. S. *Macromolecules* **2003**, *36*, 782.

Cooke, D. M.; Shi, A.-C. *Macromolecules* **2006**, *39*, 6661.

Cui, Y.; Björk, M. T.; Liddle, J. A.; Sönnichsen, C.; Boussert, B.; Alivisatos, A. P. *Nano Letters* **2004**, *4*, 1093.

Cushen, J. D.; Wan, L.; Pandav, G.; Mitra, I.; Stein, G. E.; Ganesan, V.; Ruiz, R.; Grant Willson, C.; Ellison, C. J. *Journal of Polymer Science Part B: Polymer Physics* **2014**, *52*, 36.

Cussler, E. L. *Diffusion : Mass Transfer in Fluid Systems*; 3rd ed.; Cambridge University Press: Cambridge, UK, 2009.

Davankov, V.; Tsyurupa, M. In *Comprehensive Analytical Chemistry*; Vadim, A. D., Maria, P. T., Eds.; Elsevier: 2011; Vol. Volume 56, p 2.

Ellison, C. J.; Cushen, J. D.; Willson, C. G. *Journal of Photopolymer Science and Technology* **2013**, *26*, 45.

Fanggao, C.; Saunders, G. A.; Lambson, E. F.; Hampton, R. N.; Carini, G.; Di Marco, G.; Lanza, M. *Journal of Polymer Science Part B: Polymer Physics* **1996**, *34*, 425.

Fetters, L. J.; Lohse, D. J.; Richter, D.; Witten, T. A.; Zirkel, A. *Macromolecules* **1994**, *27*, 4639.

Fredrickson, G. H.; Helfand, E. *The Journal of Chemical Physics* **1987**, *87*, 697.

- Ganesan, V.; Pyramitsyn, V.; Bertoni, C.; Shah, M. *ACS Macro Letters* **2012**, *1*, 513.
- Gehlsen, M. D.; Bates, F. S. *Macromolecules* **1994**, *27*, 3611.
- Gehlsen, M. D.; Bates, F. S. *Macromolecules* **1993**, *26*, 4122.
- Ghoshal, T.; Maity, T.; Godsell, J. F.; Roy, S.; Morris, M. A. *Advanced Materials* **2012**, *24*, 2390.
- Ghoshal, T.; Shaw, M. T.; Bolger, C. T.; Holmes, J. D.; Morris, M. A. *Journal of Materials Chemistry* **2012**, *22*, 12083.
- Gido, S. P.; Gunther, J.; Thomas, E. L.; Hoffman, D. *Macromolecules* **1993**, *26*, 4506.
- Gido, S. P.; Thomas, E. L. *Macromolecules* **1994**, *27*, 6137.
- Gillard, T. M., University of Minneosta, 2015.
- Gillard, T. M.; Lee, S.; Bates, F. S. *Proceedings of the National Academy of Sciences* **2016**.
- Gillard, T. M.; Medapuram, P.; Morse, D. C.; Bates, F. S. *Macromolecules* **2015**, *48*, 2801.
- Glaser, J.; Medapuram, P.; Beardsley, T. M.; Matsen, M. W.; Morse, D. C. *Physical Review Letters* **2014**, *113*, 068302.
- Gomez, E. D.; Das, J.; Chakraborty, A. K.; Pople, J. A.; Balsara, N. P. *Macromolecules* **2006**, *39*, 4848.
- Goodenough, J. B.; Kim, Y. *Chemistry of Materials* **2009**, *22*, 587.
- Goodenough, J. B.; Park, K.-S. *Journal of the American Chemical Society* **2013**, *135*, 1167.
- Gor, G. Y.; Thommes, M.; Cychosz, K. A.; Neimark, A. V. *Carbon* **2012**, *50*, 1583.
- Grason, G. M. *Physics Reports* **2006**, *433*, 1.
- Grason, G. M.; DiDonna, B. A.; Kamien, R. D. *Physical Review Letters* **2003**, *91*, 058304.
- Gu, X.; Gunkel, I.; Russell, T. P. *Philosophical Transactions of the Royal Society A: Mathematical, Physical and Engineering Sciences* **2013**, 371.
- Gu, Y.; Zhang, S.; Martinetti, L.; Lee, K. H.; McIntosh, L. D.; Frisbie, C. D.; Lodge, T. P. *Journal of the American Chemical Society* **2013**, *135*, 9652.
- Guo, F.; Andreasen, J. W.; Vigild, M. E.; Ndoni, S. *Macromolecules* **2007**, *40*, 3669.

- Hajduk, D. A.; Takenouchi, H.; Hillmyer, M. A.; Bates, F. S.; Vigild, M. E.; Almdal, K. *Macromolecules* **1997**, *30*, 3788.
- Hajiw, S.; Pansu, B.; Sadoc, J.-F. *ACS Nano* **2015**, *9*, 8116.
- Hallinan, D. T.; Balsara, N. P. *Annual Review of Materials Research* **2013**, *43*, 503.
- Hallinan, D. T.; Mullin, S. A.; Stone, G. M.; Balsara, N. P. *Journal of The Electrochemical Society* **2013**, *160*, A464.
- Hamersky, M. W.; Hillmyer, M. A.; Tirrell, M.; Bates, F. S.; Lodge, T. P.; von Meerwall, E. D. *Macromolecules* **1998**, *31*, 5363.
- Hammouda, B. *Journal of Applied Crystallography* **2010**, *43*, 716.
- Hashimoto, T. *Macromolecular Symposia* **2001**, *174*, 69.
- Hashimoto, T. *Macromolecules* **1987**, *20*, 465.
- Hashimoto, T.; Kowsaka, K.; Shibayama, M.; Kawai, H. *Macromolecules* **1986**, *19*, 754.
- Hashimoto, T.; Kowsaka, K.; Shibayama, M.; Suehiro, S. *Macromolecules* **1986**, *19*, 750.
- Haynes, W. M. *CRC handbook of chemistry and physics : a ready-reference book of chemical and physical data*; CRC Press: Boca Raton, Florida, 2014.
- He, Y.; Boswell, P. G.; Bühlmann, P.; Lodge, T. P. *The Journal of Physical Chemistry B* **2006**, *111*, 4645.
- Henton, D. E.; Gruber, P.; Lunt, J.; Randall, J. *Natural fibers, biopolymers, and biocomposites* **2005**, 527.
- Hermel, T. J.; Hahn, S. F.; Chaffin, K. A.; Gerberich, W. W.; Bates, F. S. *Macromolecules* **2003**, *36*, 2190.
- Hermel, T. J.; Wu, L.; Hahn, S. F.; Lodge, T. P.; Bates, F. S. *Macromolecules* **2002**, *35*, 4685.
- Hickey, R. J.; Gillard, T. M.; Lodge, T. P.; Bates, F. S. *ACS Macro Letters* **2015**, *4*, 260.
- Hiemenz, P. C.; Lodge, T. P. *Polymer Chemistry, Second Edition*; CRC Press, 2007.
- Hillmyer, M.; Abetz, V., Ed.; Springer Berlin / Heidelberg: 2005; Vol. 190, p 137.
- Hillmyer, M. A.; Bates, F. S. *Macromolecular Symposia* **1997**, *117*, 121.
- Hillmyer, M. A.; Bates, F. S. *Macromolecules* **1996**, *29*, 6994.

- Hillmyer, M. A.; Bates, F. S.; Almdal, K.; Mortensen, K.; Ryan, A. J.; Fairclough, J. P. A. *Science* **1996**, *271*, 976.
- Hoarfrost, M. L.; Segalman, R. A. *Macromolecules* **2011**, *44*, 5281.
- Hoarfrost, M. L.; Tyagi, M. S.; Segalman, R. A.; Reimer, J. A. *Macromolecules* **2012**, *45*, 3112.
- Huang, J.; Tong, Z.-Z.; Zhou, B.; Xu, J.-T.; Fan, Z.-Q. *Polymer* **2013**, *54*, 3098.
- Jinnai, H.; Nishikawa, Y.; Koga, T.; Hashimoto, T. *Macromolecules* **1995**, *28*, 4782.
- Kanamori, K.; Hasegawa, J.; Nakanishi, K.; Hanada, T. *Macromolecules* **2008**, *41*, 7186.
- Kanamori, K.; Nakanishi, K.; Hanada, T. *Advanced Materials* **2006**, *18*, 2407.
- Kataoka, K.; Harada, A.; Nagasaki, Y. *Advanced Drug Delivery Reviews* **2001**, *47*, 113.
- Kennemur, J. G.; Hillmyer, M. A.; Bates, F. S. *ACS Macro Letters* **2013**, *2*, 496.
- Kennemur, J. G.; Yao, L.; Bates, F. S.; Hillmyer, M. A. *Macromolecules* **2014**, *47*, 1411.
- Kim, D. H.; Kim, S. H.; Lavery, K.; Russell, T. P. *Nano Letters* **2004**, *4*, 1841.
- Kim, J. K.; Lee, H. H.; Gu, Q.-J.; Chang, T.; Jeong, Y. H. *Macromolecules* **1998**, *31*, 4045.
- Kim, S. H.; Hong, K.; Xie, W.; Lee, K. H.; Zhang, S.; Lodge, T. P.; Frisbie, C. D. *Advanced Materials* **2013**, *25*, 1822.
- Koga, T.; Koga, T.; Kimishima, K.; Hashimoto, T. *Physical Review E* **1999**, *60*, R3501.
- Koh, M. L.; Konkolewicz, D.; Perrier, S. b. *Macromolecules* **2011**, *44*, 2715.
- Lai, C.; Russel, W. B.; Register, R. A.; Marchand, G. R.; Adamson, D. H. *Macromolecules* **2000**, *33*, 3461.
- Lai, J. T.; Filla, D.; Shea, R. *Macromolecules* **2002**, *35*, 6754.
- Lee, J.; Kaake, L. G.; Cho, J. H.; Zhu, X. Y.; Lodge, T. P.; Frisbie, C. D. *The Journal of Physical Chemistry C* **2009**, *113*, 8972.
- Lee, S.; Bluemle, M. J.; Bates, F. S. *Science* **2010**, *330*, 349.
- Lee, S.; Gillard, T. M.; Bates, F. S. *Aiche J* **2013**, *59*, 3502.
- Lee, S.; Leighton, C.; Bates, F. S. *Proceedings of the National Academy of Sciences* **2014**, *111*, 17723.

- Leibler, L. *Macromolecules* **1980**, *13*, 1602.
- Li, L.; Schulte, L.; Clausen, L. D.; Hansen, K. M.; Jonsson, G. E.; Ndoni, S. *ACS Nano* **2011**, *5*, 7754.
- Li, Y.; Sasaki, T.; Shimizu, Y.; Koshizaki, N. *Journal of the American Chemical Society* **2008**, *130*, 14755.
- Lodge, T. *Mikrochim Acta* **1994**, *116*, 1.
- Lodge, T. P.; Pudil, B.; Hanley, K. J. *Macromolecules* **2002**, *35*, 4707.
- Loo, Y.-L.; Register, R. A.; Ryan, A. J. *Macromolecules* **2002**, *35*, 2365.
- Lowell, S.; Shields, J. E.; Thomas, M. A.; Thommes, M. *Characterization of porous solids and powders: surface area, pore size and density*; Springer Science & Business Media, 2012; Vol. 16.
- Lu, G. Q.; Zhao, X. S.; World Scientific.
- Lynd, N. A.; Hillmyer, M. A.; Matsen, M. W. *Macromolecules* **2008**, *41*, 4531.
- Majewski, P. W.; Gopinadhan, M.; Jang, W.-S.; Lutkenhaus, J. L.; Osuji, C. O. *Journal of the American Chemical Society* **2010**, *132*, 17516.
- Matsen, M. W. *Macromolecules* **2012**, *45*, 2161.
- Matsen, M. W. In *Soft Matter*; Wiley-VCH Verlag GmbH & Co. KGaA: 2007, p 87.
- Matsen, M. W.; Bates, F. S. *Journal of Polymer Science Part B: Polymer Physics* **1997**, *35*, 945.
- Matsen, M. W.; Bates, F. S. *Macromolecules* **1996**, *29*, 1091.
- Matsen, M. W.; Schick, M. *Macromolecules* **1994**, *27*, 4014.
- Matsen, M. W.; Schick, M. *Physical Review Letters* **1994**, *72*, 2660.
- Maurer, W. W.; Bates, F. S.; Lodge, T. P.; Almdal, K.; Mortensen, K.; Fredrickson, G. H. *The Journal of Chemical Physics* **1998**, *108*, 2989.
- Mayeda, M. K.; Hayat, J.; Epps, T. H.; Lauterbach, J. *Journal of Materials Chemistry A* **2015**, *3*, 7822.
- Mays, J. W.; Kumar, R.; Sides, S. W.; Goswami, M.; Sumpter, B. G.; Hong, K.; Wu, X.; Russell, T. P.; Gido, S. P.; Avgeropoulos, A.; Tsoukatos, T.; Hadjichristidis, N.; Beyer, F. L. *Polymer* **2012**, *53*, 5155.

McIntosh, L. D.; Schulze, M. W.; Irwin, M. T.; Hillmyer, M. A.; Lodge, T. P. *Macromolecules* **2015**.

Medapuram, P.; Glaser, J.; Morse, D. C. *Macromolecules* **2015**, *48*, 819.

Meuler, A. J.; Hillmyer, M. A.; Bates, F. S. *Macromolecules* **2009**, *42*, 7221.

Mikos, A. G.; Takoudis, C. G.; Peppas, N. A. *Macromolecules* **1986**, *19*, 2174.

Milhaupt, J. M.; Lodge, T. P. *Journal of Polymer Science Part B: Polymer Physics* **2001**, *39*, 843.

Monolithic Silicas in Separation Science : Concepts, Syntheses, Characterization, Modeling and Applications; Wiley-VCH: Hoboken, NJ, USA, 2010.

Monroe, C.; Newman, J. *Journal of The Electrochemical Society* **2003**, *150*, A1377.

Monroe, C.; Newman, J. *Journal of The Electrochemical Society* **2004**, *151*, A880.

Monroe, C.; Newman, J. *Journal of The Electrochemical Society* **2005**, *152*, A396.

Muralidharan, V.; Hui, C.-Y. *Macromolecular Rapid Communications* **2004**, *25*, 1487.

Nakamoto, H.; Watanabe, M. *Chemical Communications* **2007**, 2539.

Nakamura, I.; Balsara, N. P.; Wang, Z.-G. *ACS Macro Letters* **2013**, *2*, 478.

Ness, J. S.; Brodil, J. C.; Bates, F. S.; Hahn, S. F.; Hucul, D. A.; Hillmyer, M. A. *Macromolecules* **2001**, *35*, 602.

Newman, J. *Electrochemical Systems*; 2nd ed.; Prentice-Hall, 1991.

Nischang, I.; Teasdale, I.; Brüggemann, O. *Anal Bioanal Chem* **2011**, *400*, 2289.

Noda, A.; Susan, M. A. B. H.; Kudo, K.; Mitsushima, S.; Hayamizu, K.; Watanabe, M. *The Journal of Physical Chemistry B* **2003**, *107*, 4024.

Nunns, A.; Gwyther, J.; Manners, I. *Polymer* **2013**, *54*, 1269.

Nyhus, A. K.; Hagen, S.; Berge, A. *Journal of Polymer Science Part A: Polymer Chemistry* **2000**, *38*, 1366.

Nyhus, A. K.; Hagen, S.; Berge, A. *Journal of Polymer Science Part A: Polymer Chemistry* **1999**, *37*, 3345.

Okay, O. *Progress in Polymer Science* **2000**, *25*, 711.

- Park, S.; Lee, D. H.; Xu, J.; Kim, B.; Hong, S. W.; Jeong, U.; Xu, T.; Russell, T. P. *Science* **2009**, *323*, 1030.
- Peng, J.; Li, X.; Kim, D. H.; Knoll, W. *Macromolecular Rapid Communications* **2007**, *28*, 2055.
- Phillip, W. A.; Amendt, M.; O'Neill, B.; Chen, L.; Hillmyer, M. A.; Cussler, E. L. *ACS Applied Materials & Interfaces* **2009**, *1*, 472.
- Phillip, W. A.; Hillmyer, M. A.; Cussler, E. L. *Macromolecules* **2010**, *43*, 7763.
- Pitet, L. M.; Amendt, M. A.; Hillmyer, M. A. *Journal of the American Chemical Society* **2010**, *132*, 8230.
- Pochan, D. J.; Gido, S. P.; Zhou, J.; Mays, J. W.; Whitmore, M.; Ryan, A. J. *Journal of Polymer Science Part B: Polymer Physics* **1997**, *35*, 2629.
- Qin, J.; Grzywacz, P.; Morse, D. C. *The Journal of Chemical Physics* **2011**, *135*, 084902.
- Roe, R. J.; Nojima, S. *MRS Online Proceedings Library Archive* **1986**, *79*, null.
- Rosedale, J. H.; Bates, F. S.; Almdal, K.; Mortensen, K.; Wignall, G. D. *Macromolecules* **1995**, *28*, 1429.
- Roulet, M.; Vayer, M.; Sinturel, C. *European Polymer Journal* **2013**, *49*, 3897.
- Rzayev, J.; Hillmyer, M. A. *Journal of the American Chemical Society* **2005**, *127*, 13373.
- Saba, S. A.; Mousavi, M. P. S.; Bühlmann, P.; Hillmyer, M. A. *Journal of the American Chemical Society* **2015**, *137*, 8896.
- Sakamoto, N.; Hashimoto, T. *Macromolecules* **1998**, *31*, 3292.
- Sakamoto, N.; Hashimoto, T. *Macromolecules* **1998**, *31*, 3815.
- Scalfani, V. F.; Wiesenauer, E. F.; Ekblad, J. R.; Edwards, J. P.; Gin, D. L.; Bailey, T. S. *Macromolecules* **2012**, *45*, 4262.
- Schmidt, S. C.; Hillmyer, M. A. *Journal of Polymer Science Part B: Polymer Physics* **2002**, *40*, 2364.
- Schulze, M. W.; McIntosh, L. D.; Hillmyer, M. A.; Lodge, T. P. *Nano Letters* **2013**, *14*, 122.
- Schulze, M. W.; Sinturel, C.; Hillmyer, M. A. *ACS Macro Letters* **2015**, *4*, 1027.
- Schüth, F. *Chemistry of Materials* **2001**, *13*, 3184.

- Schwachula, G. *Journal of Polymer Science: Polymer Symposia* **1975**, *53*, 107.
- Segalman, R. A.; McCulloch, B.; Kirmayer, S.; Urban, J. J. *Macromolecules* **2009**, *42*, 9205.
- Semenov, A. N. *Macromolecules* **1993**, *26*, 6617.
- Seo, M.; Amendt, M. A.; Hillmyer, M. A. *Macromolecules* **2011**, *44*, 9310.
- Seo, M.; Hillmyer, M. A. *Science* **2012**, *336*, 1422.
- Seo, M.; Kim, S.; Oh, J.; Kim, S.-J.; Hillmyer, M. A. *Journal of the American Chemical Society* **2015**, *137*, 600.
- Simone, P. M.; Lodge, T. P. *Macromolecules* **2008**, *41*, 1753.
- Simone, P. M.; Lodge, T. P. *ACS Applied Materials & Interfaces* **2009**, *1*, 2812.
- Sing, K. S. W.; Everett, D. H.; Haul, R. A. W.; Moscou, L.; Pierotti, R. A.; Rouquerol, J.; Siemieniewska, T. *Pure Appl. Chem.* **1985**, *57*, 603.
- Singh, M.; Odusanya, O.; Wilmes, G. M.; Eitouni, H. B.; Gomez, E. D.; Patel, A. J.; Chen, V. L.; Park, M. J.; Fragouli, P.; Iatrou, H.; Hadjichristidis, N.; Cookson, D.; Balsara, N. P. *Macromolecules* **2007**, *40*, 4578.
- Sinturel, C.; Vayer, M.; Morris, M.; Hillmyer, M. A. *Macromolecules* **2013**, *46*, 5399.
- Steele, B. C. H.; Heinzl, A. *Nature* **2001**, *414*, 345.
- Sun, S.-S. *Solar Energy Materials and Solar Cells* **2003**, *79*, 257.
- Susan, M. A. B. H.; Kaneko, T.; Noda, A.; Watanabe, M. *Journal of the American Chemical Society* **2005**, *127*, 4976.
- Svec, F.; Frechet, J. M. J. *Chemistry of Materials* **1995**, *7*, 707.
- Sweat, D. P.; Kim, M.; Larson, S. R.; Choi, J. W.; Choo, Y.; Osuji, C. O.; Gopalan, P. *Macromolecules* **2014**, *47*, 6687.
- Tanaka, S.; Matsumoto, M.; Goseki, R.; Ishizone, T.; Hirao, A. *Macromolecules* **2012**, *46*, 146.
- Tang, B.; White, S. P.; Frisbie, C. D.; Lodge, T. P. *Macromolecules* **2015**, *48*, 4942.
- Tarascon, J. M.; Armand, M. *Nature* **2001**, *414*, 359.
- Teran, A. A.; Balsara, N. P. *The Journal of Physical Chemistry B* **2013**, *118*, 4.

- Teran, A. A.; Tang, M. H.; Mullin, S. A.; Balsara, N. P. *Solid State Ionics* **2011**, *203*, 18.
- Thelen, J. L.; Teran, A. A.; Wang, X.; Garetz, B. A.; Nakamura, I.; Wang, Z.-G.; Balsara, N. P. *Macromolecules* **2014**, *47*, 2666.
- Todd, E. M.; Hillmyer, M. A. In *Porous Polymers*; John Wiley & Sons, Inc.: 2011, p 31.
- Tokuda, H.; Hayamizu, K.; Ishii, K.; Susan, M. A. B. H.; Watanabe, M. *The Journal of Physical Chemistry B* **2004**, *108*, 16593.
- Tokuda, H.; Hayamizu, K.; Ishii, K.; Susan, M. A. B. H.; Watanabe, M. *The Journal of Physical Chemistry B* **2005**, *109*, 6103.
- Tran, H.; Gopinadhan, M.; Majewski, P. W.; Shade, R.; Steffes, V.; Osuji, C. O.; Campos, L. M. *ACS Nano* **2013**, *7*, 5514.
- Tyler, C. A.; Morse, D. C. *Physical Review Letters* **2005**, *94*, 208302.
- Varghese, J.; Ghoshal, T.; Deepak, N.; O'Regan, C.; Whatmore, R. W.; Morris, M. A.; Holmes, J. D. *Chemistry of Materials* **2013**, *25*, 1458.
- Vassiliev, O. N.; Matsen, M. W. *The Journal of Chemical Physics* **2003**, *118*, 7700.
- Vavasour, J. D.; Whitmore, M. D. *Macromolecules* **1992**, *25*, 5477.
- Viklund, C.; Svec, F.; Fréchet, J. M. J.; Irgum, K. *Chemistry of Materials* **1996**, *8*, 744.
- Virgili, J. M.; Hoarfrost, M. L.; Segalman, R. A. *Macromolecules* **2010**, *43*, 5417.
- Voronov, V. P.; Buleiko, V. M.; Podneks, V. E.; Hamley, I. W.; Fairclough, J. P. A.; Ryan, A. J.; Mai, S. M.; Liao, B. X.; Booth, C. *Macromolecules* **1997**, *30*, 6674.
- Wanakule, N. S.; Virgili, J. M.; Teran, A. A.; Wang, Z.-G.; Balsara, N. P. *Macromolecules* **2010**, *43*, 8282.
- Wang, H.; Newstein, M. C.; Krishnan, A.; Balsara, N. P.; Garetz, B. A.; Hammouda, B.; Krishnamoorti, R. *Macromolecules* **1999**, *32*, 3695.
- Wang, X.; Li, Z.; Shi, J.; Yu, Y. *Chemical Reviews* **2014**, *114*, 9346.
- Weber, J.; Bergström, L. *Macromolecules* **2009**, *42*, 8234.
- Weber, R. L.; Ye, Y.; Schmitt, A. L.; Banik, S. M.; Elabd, Y. A.; Mahanthappa, M. K. *Macromolecules* **2011**, *44*, 5727.
- Wolf, J. H.; Hillmyer, M. A. *Langmuir* **2003**, *19*, 6553.

- Wu, H. S.; Sandler, S. I. *Journal of Chemical & Engineering Data* **1988**, *33*, 157.
- Xie, N.; Li, W.; Qiu, F.; Shi, A.-C. *ACS Macro Letters* **2014**, *3*, 906.
- Xie, S.; Allington, R.; Fréchet, J. J.; Svec, F. In *Modern Advances in Chromatography*; Freitag, R., Ed.; Springer Berlin Heidelberg: 2002; Vol. 76, p 87.
- Xu, T.; Zhu, Y.; Gido, S. P.; Russell, T. P. *Macromolecules* **2004**, *37*, 2625.
- Yamamoto, K.; Ito, E.; Fukaya, S.; Takagi, H. *Macromolecules* **2009**, *42*, 9561.
- Ye, Y.; Choi, J.-H.; Winey, K. I.; Elabd, Y. A. *Macromolecules* **2012**, *45*, 7027.
- Young, W.-S.; Albert, J. N. L.; Schantz, A. B.; Epps, T. H. *Macromolecules* **2011**, *44*, 8116.
- Young, W.-S.; Epps, T. H. *Macromolecules* **2012**, *45*, 4689.
- Young, W.-S.; Epps, T. H. *Macromolecules* **2009**, *42*, 2672.
- Young, W.-S.; Kuan, W.-F.; Epps, T. H. *Journal of Polymer Science Part B: Polymer Physics* **2014**, *52*, 1.
- Yuan, R.; Teran, A. A.; Gurevitch, I.; Mullin, S. A.; Wanakule, N. S.; Balsara, N. P. *Macromolecules* **2013**, *46*, 914.
- Zalusky, A. S.; Olayo-Valles, R.; Wolf, J. H.; Hillmyer, M. A. *Journal of the American Chemical Society* **2002**, *124*, 12761.
- Zhang, C.-Z.; Wang, Z.-G. *Physical Review E* **2006**, *73*, 031804.
- Zhang, S.; Lee, K. H.; Frisbie, C. D.; Lodge, T. P. *Macromolecules* **2011**, *44*, 940.
- Zhang, S.; Lee, K. H.; Sun, J.; Frisbie, C. D.; Lodge, T. P. *Macromolecules* **2011**, *44*, 8981.
- Zhou, X.; Huang, J.; Barr, K. W.; Lin, Z.; Maya, F.; Abbott, L. J.; Colina, C. M.; Svec, F.; Turner, S. R. *Polymer* **2015**, *59*, 42.
- Zhu, L.; Cheng, S. Z. D.; Calhoun, B. H.; Ge, Q.; Quirk, R. P.; Thomas, E. L.; Hsiao, B. S.; Yeh, F.; Lotz, B. *Polymer* **2001**, *42*, 5829.